ROLES OF CLN7 IN NEURODEVELOPMENT

By

ALAMIN MOHAMMED

A thesis submitted to the University of Birmingham for the degree of DOCTOR OF PHILOSOPHY

Institute of Cancer and Genomic Sciences
College of Medical and Dental Sciences
University of Birmingham
February 2019

Abstract

The neuronal ceroid lipofuscinoses (NCLs) are group of neurodegenerative disorders with infantile or childhood onset. The NCLs result in a progressive decline in cognitive and motor functions, seizures and loss of vision that is clinically characterised by the build-up of autofluorescent storage material in lysosomes. Mutations in *CLN7* lead to a late-infantile form of NCL. *CLN7* encodes a putative lysosomal transmembrane transport protein, but its substrate remains unknown and the biology underpinning the disease is not understood. In this thesis, I used CRISPR/Cas9 genome editing in *Drosophila* to generate a YFP-CLN7 knock-in to enable the first *in vivo* localisation study of CLN7 without overexpression. Within the CNS, CLN7 was predominately expressed in glial cells that form the insect blood-brain-barrier, with neuronal expression being restricted to visual neurons. CLN7 was also found to localise to the postsynaptic site of the larval neuromuscular junction (NMJ). *CLN7*-deficient larvae showed significant reductions in synapse size with genetic studies using GAL4/UAS revealing post-synaptic expression of CLN7 in muscles being crucial for NMJ development. Autophagy and the retrograde TGF-β pathways that regulate NMJ development were unaffected by the loss of CLN7. Autofluorescent material was observed in the visual system of aged *CLN7* flies, recapitulating a key hallmark of the human disease. I also identified functional defects in vision. Taken together, dysregulation of synapses at the NMJ and the visual system indicate a fundamental role for CLN7 in neurodevelopment.

Acknowledgments

I would firstly like to thank Richard for all his support and guidance throughout my time in Birmingham. He has been an amazing supervisor who has guided and helped push me forward as a scientist. I would also like to thank all members of the Tuxworth lab who helped expand my mind and were great company in and outside of the fly room (Lucy, Emma, Kyle, Katlyn, Sotti, Matt and Niki). I would also like to thank everyone in the office for the chats and cakes, in particular, Dewi, Malgosia and Jan, the labs unsung hero. I would like to thank my friends, Atif, Shariff, Haseeb, Abdullah (Kuwati and Syrian) and Naser for helping me settle in Birmingham and showing me more to life outside the Lab.

I would greatly like to thank my family for their continual support, my wife Naz, who has had to put up with a lot, particular during the write up phase and my in-laws who made it easier. Great thanks to my Mum who has been waiting for this day for a long time. Last but most importantly, Allah swt, who has provided me with the knowledge and guidance to achieve this - Alhamdulillah.

Table of Contents

List of figures

List of Tables

List of abbreviations

3IL	Third instar larvae
ANCL	Adult NCL
AI	Artificial intron
ALS	Amyotrophic lateral sclerosis
ANCL	Adult neuronal ceroid lipofucinosis
A*tg*	Autophagy genes
BBB	Blood brain barrier
BO	Bolwig organ
Ca^{2+}	Calcium
Cl^-	Chloride
CathF	Cathepsin F
cDNA	Complimentary DNA
cGMP	3',5'-cyclic guanosine monophosphate
CLN	Ceroid lipofuscinosis neuronal
CMA	Chaperone mediated autophagy
CNS	Central nervous system
CRISPR	Clustered Regulatory Interspaced Short Palindromic Repeats
CSPα	Cysteine-string protein α
DAG	Diacylglycerol
dFz	*Drosophila* Frizzled receptor
DSB	Double strand breaks
dsDNA	Double stranded DNA
ECL	Chemiluminescence substrate
EEG	Electroencephalogram
ELAV	Embryonic lethal abnormal vision
ER	Endoplasmic reticulum
ERGIC	ER-Golgi intermediate compartment
ERG	Electroretinograms
EtOH	Ethanol
FGF	Fibroblast growth factor
FNI	Frizzled nuclear import
gDNA	Genomic DNA
GPCR	G-protein coupled receptors
gRNA	Guide RNA
GRODs	Granular osmiophilic deposits
HDR	Homology directed repair
His	Histamine
INCL	Infantile NCL
IP3	Inositol 1,4,5-trisphosphate
IP3R	Inositol 1,4,5-trisphosphate receptor
iPSC	Induced pluripotent stem cells

JNCL	Juvenile NCL
LAMP1	Lysosomal-associated membrane protein 1
LINCL	Late-infantile NCL
LSD	Lysosomal storage disorders
MEFs	Mouse embryonic fibroblasts
MeOH	Methanol
MFSD8	Major facilitator superfamily domain
MLIV	Mucolipodosis type IV
MRI	Magnetic resonance imaging
MSA	Muscle surface area
NCL	Neuronal ceroid lipofuscinoses
NEB	New England Biolabs
NMJ	Neuro muscular junction
ONL	Outer nuclear layer
OPL	Outer plexiform layer
PAM	Protospacer adjacent motif
PBS	Phosphate buffered seline
PBST	PBS containing 0.1% Tween-20
PCR	Polymerase chain reaction
PD	Parkinsons disease
PDE	Phosphodiesterase
PIP2	Phosphatidylinositol 4,5-bisphosphate
PLCβ	Phospholipase C β
PPT1	Palmitoyl protein thioesterase 1
PSD-95	Post synaptic density 95
qPCR	Quantitative PCR
RMCE	Recombinase-mediated cassette exchange
RT-PCR	Reverse transcription PCR
S6K	S6 kinase
SAPs	Saposins
SCMAS	Subunit c of mitochondrial ATP synthase
SDR	Secreted decoy of insulin receptor
SMA	Spinal muscular atrophy
SNP	Single nucleotide polymorphism
SSVEP	Steady state visually evoked potential
TAE	1x Tris/acetic acid/EDTA
TAP	Tandem affinity purification
TGF-β	Transforming growth factor β
TORC	Target of rapamycin complex
TRP	Transient receptor potential
TRPL	TRP-like
UAS	upstream activation sequence
VEP	Visual evoked potentials
VNC	Ventral nerve cord

Wg   Wingless

1. INTRODUCTION

1.1 Neuronal Ceroid Lipofuscinosis

1.1.1 Lysosomal storage disorders

Lysosomes are multifunctional membrane bound acidic organelles found in all types of nucleated cells. They contain over 50 acid hydrolase enzymes essential for the degradation and recycling of macromolecules and play a crucial role in the balance of growth signalling vs autophagy pathway via regulation of the Target of Rapamycin Complex 1 (TORC) signalling (Betz and Hall, 2013). They are also involved in stress signalling and play an important role in intracellular calcium (Ca^{2+}) signalling by acting as a Ca^{2+} store (Saftig and Klumperman, 2009, McGuinness et al., 2007). Mutations within nuclear genes encoding lysosomal proteins give rise to approximately 50 genetically inherited lysosomal storage disorders (LSDs) leading to impaired lysosomal function. LSDs are characterised by the build-up of storage material within the lysosomes of most if not all cells, however a large proportion of LSDs exhibit fundamental early-onset neural pathology, highlighting the key dependence of the nervous system on lysosomal function (Bellettato and Scarpa, 2010). The reasons for this dependence are not well understood.

1.1.2 Neuronal ceroid lipofuscinoses – historical background

The neuronal ceroid lipofuscinoses (NCLs) are a collection of progressive neurodegenerative diseases that fall into the wider group of LSDs. The NCLs are

also interchangeably referred to as Batten disease, named after an early pioneer of the field, Fredrick Batten (1865-1918), a British paediatrician and neurologist. However, the earliest description of a family who may have suffered from a form of NCLs was described by the Norwegian clinical practitioner, Otto Christian Stengel in 1826. He observed a single illness affecting four siblings and, although no autopsies were performed, the disease progression and symptoms correspond to juvenile CLN3 disease (Stengel, 1862). Unfortunately, his findings remained unnoticed in scientific community until the 1950s. In the early 20th century, independent research by Batten, German neurologist Heinrich Vogt (1875–1936) and neuropathologist Walther Spielmeyer (1879–1935), and the Swedish psychiatrist Torsten Sjögren (1896–1974) described similar familial cases. They each found patients who exhibited a progressive deterioration in vision and psychomotor which was accompanied by pathological accumulation of granular lipid-like storage material in neurons (Haltia and Goebel, 2013). They were placed under the umbrella term "amaurotic family idiocy" which included Tay–Sachs disease. In the early 1930s, studies were being carried to overthrow the generalisation of "amaurotic family idiocy" and in 1969, Wolfgang Zeman and Paul Dyken distinguished the NCLs from other diseases within the group (Zeman and Dyken, 1969). They showed that NCLs exhibited highly insoluble storage material which was largely resistant to lipid solvents. In comparison, storage material in Tay–Sachs disease could be easily extracted. The NCL storage material also showed curvilinear and fingerprint ultrastructure patterns resembling the build-up of autofluorescent lipopigments, ceroid and lipofuscin (Zeman and Dyken, 1969, Haltia

and Goebel, 2013). This led to the introduction of the term "neuronal ceroid lipofuscinosis".

The NCLs are recessively inherited and predominantly have a childhood onset, however an autosomal dominant inherited form exists which affects adults. The NCLs are clinically characterised by the build-up of autofluorescent lipofuscin-like material within lysosomes of all cell types and neurodegeneration in the cerebral cortex and cerebellum. They are fatal, and as of yet, there are no therapies to treat the disease. The NCLs share similar symptoms including: decline in visual acuity, seizures, psychomotor deterioration and a progressive decline in cognitive and motor function, and ultimately leads to premature death. Although, the different forms of NCLs are rare, collectively they represent the most common cause of childhood neurodegenerative diseases. The NCLs are found worldwide with incidences ranging from 1:67,000 in Italy and Germany to 1:14,000 in Iceland, with prevalence rates ranging from 1:100 000 to 1:1,000 000 depending on geographical location (Sara Mole, 2011).

1.1.3 Old classification system

With the introduction of the term NCL in 1969, the NCL classification system was created and sorted NCL forms by the age of onset of symptoms: infantile (INCL), late-infantile (LINCL), juvenile (JNCL) and adult onset (ANCL). They were also known by the eponym of the people who originally described them: Haltia-Santavuori (INCL), Jansky-Bielschowsky (LINCL), Spielmeyer-Vogt (JNCL), and Kufs disease (ANCL). This system ignored earlier reports of the sporadic congenital

cases. Overtime more forms of NCLs were discovered such as of variant late infantile in Finland and early Juvenile in the UK, adding to the spectrum of NCLs. Additionally, reports exclusive to Finland of cases of Northern epilepsy syndrome, an inherited childhood epilepsy accompanied by mild mental retardation, was discovered to be a novel form of NCLs. These led to additional NCLs being named after their geographical location or familial ethnicity such as 'Turkish' variant LINCL now known as late infantile CLN7. Batten disease was also used interchangeably to describe JNCL or the NCLs as a collection (Haltia, 2006) (http://www.ucl.ac.uk/ncl/newnomenclature.shtml).

1.1.3 Current NCL nomenclature

The first NCL gene was not identified until 25 years after the NCL nomenclature was established. This gene encoded palmitoyl protein thioesterase 1 (PPT1) and mutations in this gene was responsible for INCL (Haltia, 2006). Subsequently, many other NCL genes have been identified and it is clear that the NCL sub-types show genetic heterogeneity, with similar clinical disease phenotypes manifesting from mutations in different genes. They also show allelic heterogeneity, with different clinical disease phenotypes manifesting from mutations in the same gene and can also be phenotypically heterogeneous, with disease phenotypes and progression varying from mutations in the same gene even within the same family. As a result, a NCL mutations database was established in 2012 and the NCL nomenclature revised (http://www.ucl.ac.uk/ncl/). The current nomenclature uses an axial diagnostic classification system, similar to those used for epilepsy and paediatric mental health disorders (ICD-10). Importantly this combined the age of onset of

symptoms with the NCL gene affected, known as ceroid lipofuscinosis neuronal (CLN) genes, e.g. late infantile CLN7 disease (http://www.ucl.ac.uk/ncl/newnomenclature.shtml).

1.1.4 NCL genes and proteins

To date, mutations in 14 genes have been identified to cause NCLs in humans. These genes encode proteins with differing function and cellular localisation including: soluble lysosomal proteins (CLN1, CLN2, CLN10 and CLN13), a lysosomal enzyme (CLN5), cytosolic proteins (CLN4 and CLN14), an extracellular protein (CLN11), lysosomal transmembrane proteins (CLN3, CLN7 and CLN12) and ER/ER-Golgi intermediate compartment (ERGIC) membrane proteins (CLN6 and CLN8) (Carcel-Trullols et al., 2015). The protein products and their intracellular localisation are shown in figure 1.1 and summarised in table 1.1.

1.2 Symptoms and pathology of human NCLs

1.2.1 Congenital NCL

Mutations in the *CLN10* gene gives rise to the most aggressive form of NCL. It has a congenital onset and is the only form to present symptoms at birth. It is characterised poor foetal growth, microcephaly, seizures and respiratory defects. The survival of period can last from a few hours to couple days (Siintola et al., 2006). The onset of NCL symptoms are summarised in table 1.2.

Disease gene	Protein name	Biochemical product
CLN1/PPT1	Palmitoyl-protein thioesterase 1 (PPT1)	Soluble lysosomal enzyme
CLN2/TPP1	Tripeptidyl peptidase 1 (TPP1)	Soluble lysosomal enzyme
CLN3	CLN3	Lysosomal transmembrane protein
CLN4/DNAJC5	Cysteine String Protein alpha (CSPα)	Cytosolic proteins/ synaptic vesicle
CLN5	CLN5	Soluble lysosomal protein
CLN6	CLN6	ER transmembrane protein
CLN7/MFSD8	Major Facilitator Superfamily Domain Containing 8 (MFSD8)	Lysosomal transmembrane protein
CLN8	CLN8	ER transmembrane protein
CLN9	Unknown	Unknown
CLN10/CTSD	Cathepsin D (CathD)	Soluble lysosomal enzyme
CLN11/GRN	Progranulin	Extracellular protein
CLN12/ATP13A2	ATPase Cation Transporting 13A2 (ATP13A2)	Lysosomal transmembrane proteins
CLN13/CTSF	Cathepsin F (Cath F)	Soluble lysosomal enzyme
CLN14/KCTD7	Potassium channel tetramerisation domain-containing protein 7 (KCTD7)	Cytosolic proteins

Table 1.1: Protein product of CLN genes and their biochemical product

1.2.2 Infantile NCL

Symptoms of CLN1 disease presents itself at 6-18 months of age. By 2 years of age, microcephaly becomes apparent and is accompanied by a rapid psychomotor deterioration (Santavuori et al., 1993). Additionally, abnormal brain activity can be observed using an electroencephalogram (EEG) and patients becomes unresponsive by 3 years of age. The electrical activity in the visual system is also affected with abnormal electroretinograms (ERGs) readings at 2.5 years and visual evoked potentials (VEPs) failing to respond by 2-5 years of age. This leads to premature death by 8-13 years of age.

1.2.3 Late Infantile NCL

Mutations in multiple *CLN* genes lead to late infantile NCL (LINCL) with CLN2 disease often referred to as classical LINCL and the remaining known as variant-LINCL. Genes responsible for variant LINCL include: *CLN5*, *CLN6*, *CLN8* and *CLN7* which is discussed further in section 1.2.4. The age of onset in LINCL varies between 2 and 8 years with mortality usually occurring at 5-11 years of age depending on the mutation. However, in instances, mortality can occur later in life as documented by CLN5 disease patients surviving until 36 years of age (reviewed in (Jalanko and Braulke, 2009)).

All LINCL share similar symptoms including motor dysfunction, seizures, mental retardation and visual defects. However, patients with mutations in *CLN8* associated with epilepsy with mental retardation (EPMR) have atypical symptoms and do not suffer from visual failures and can survive into mid-adulthood. Patients

Disease gene	Clinical phenotype
CLN1/PPT1	CLN1 disease: infantile, late-infantile, juvenile and adult NCLs
CLN2/TPP1	CLN2 disease: late-infantile and juvenile NCL
CLN3	CLN3 disease: juvenile NCL
CLN4/DNAJC5	CLN4 disease: adult NCL
CLN5	CLN5 disease: late-infantile, juvenile and adult NCL
CLN6	CLN6 disease: late-infantile NCL and adult (Kufs type A)
CLN7/MFSD8	CLN7 disease: late-infantile NCL
CLN8	CLN8 disease: late-infantile and CLN8 disease with EPMR
CLN10/CTSD	CLN10 disease: congenital, late-infantile, juvenile and adult
CLN11/GRN	CLN11 disease: adult
CLN12/ATP13A2	CLN12 disease: juvenile
CLN13/CTSF	CLN13 disease: adult (Kufs type B)
CLN14/KCTD7	CLN14 disease: infantile

Table 1.2: Classification of human neuronal ceroid lipofuscinoses. Adapted from (Schulz et al., 2013) .

also exhibit a generalised tonic-clonic seizures that can last up to 15 min and increased in frequency to 1-2 seizures a week during puberty (Ranta and Lehesjoki, 2000). In contrast, Turkish patients with CLN8 disease show more typical NCL phenotypes including visual failure (Topcu et al., 2004).

1.2.4 Late infantile *CLN7* disease

Mutations in *CLN7/MFSD8*, which encodes a lysosomal transmembrane protein, cause late infantile CLN7 disease. CLN7 disease was originally discovered in 6 Turkish families, however at this stage, all known NCL loci were unaffected, and became known as a Turkish variant LINCL (Wheeler et al., 1999). The causative gene was first characterised in 2007 which found 6 point mutations in a group of patients (Siintola et al., 2007) and became known as CLN7 disease following changes to the NCL nomenclature. To date, 38 mutations and 2 sequence variations have been identified to cause CLN7 disease (NCL – database). The effects of these mutations, predominantly missense/nonsense, have been predicated to result in a truncated protein.

CLN7 disease is diagnosed by clinical presentations and confirmed via genetic testing. Children usually present initially with seizures or psychomotor decline between 2 and 7 years of age. This is followed by a progressive decline in motor and cognitive functions followed by visual failure leading to blindness. Ultrastructural examination of storage material in CLN7 disease exhibit a fingerprint pattern and rectilinear patterns. MRI of patients show atrophy of the cerebral and cerebellar

cortexes along with thinning of the corpus callosum reviewed in (Nita et al., 2016, Kousi et al., 2009, Siintola et al., 2007).

1.2.5 Juvenile NCL

Juvenile NCL (JNCL) is caused by mutations to *CLN3* and is the most common form of NCLs. The most common mutation throughout the world is a 1kb intragenic deletion of 2 exons, which results in the production of a severely truncated protein that has been argued may retain residual activity (Kitzmuller et al., 2008). The majority of studies, however, refute this (Chan et al., 2008). Mutations in *CLN3* normally results in ER retention of the CLN3 protein although during milder progression of the disease, the mutated CLN3 protein is released from the ER (Haskell et al., 2000, Haskell et al., 1999). CLN3 disease patients begin to exhibit symptoms at 5-10 years of age and generally survive into their 30's. Symptoms start with a decline in vision followed by mental retardation, seizures and a decline in motor function.

Two missense mutations, F229I and W383C, in the *CLN10* gene has delayed CNCL onset to early school age. In these cases, patients exhibit neurodegenerative symptoms – visual defects and ataxia. Cerebral and cerebellar atrophy was visualised by magnetic resonance imaging (MRI) scans and overtime a progressive decline in psychomotor was noted (Steinfeld et al., 2006).

Mutations in *CLN1* can also result in a form of JNCL which differs from CLN1 INCL and CLN3 JNCL. Symptoms starts at 5-10 years of age. Patients generally present

with mental retardation, seizures and may present with ataxia in the lower limbs. However, loss of vision occurs later in disease progression reviewed in (Schulz et al., 2013).

1.2.6 Adult NCL

Adult onset forms of NCL (ANCL) have the mildest form of disease progression and are relatively rare (accounting for approximately 5% of all CLN mutations). This has made it difficult to study the genetic basis of ANCL. ANCL was original named Kufs disease, with an autosomal dominant form and two autosomal recessive forms, type A and type B distinguished by symptoms. Type A presents with progressive myoclonus epilepsy, whereas type B presented with dementia and motor function decline. It was found that the *CLN4* gene was responsible for the dominant form (Noskova et al., 2011), while *CLN6* (Arsov et al., 2011) and *CLN13* (Smith et al., 2013) mutations were linked to Type A and B respectively. Adult CLN4 disease, also known as Parry disease, is the only known form of NCLs to have an autosomal dominant inheritance. The *CLN4/DNAJC5* gene encodes a synaptic vesicle protein, cysteine-string protein α (CSPα). CSPα has been shown to be involved in aiding protein folding

Additional ANCL cases have been linked to mutations in genes associated with early onset NCL, generally due to residual protein activity causing a delayed onset. CLN13 disease, also known as type B Kufs disease, is an autosomal recessively inherited form of ANCL (Smith et al., 2013, Di Fabio et al., 2014). Three patients from independent Italian and Canadian families with ANCL lacked mutations in the

CLN6 gene, another gene known to be associated with ANCL. Linkage mapping and exome sequencing found the *CLN13* gene to be responsible for the disease. Symptoms manifest around 20 years of age, including: tremors, ataxia and dysarthria, followed by dementia and motor dysfunction in later life but would rarely experience seizures. Examinations revealed diffuse cerebral atrophy and astrogliosis (Smith et al., 2013). Mutations in *CLN5* have also been shown to cause ANCL. Symptoms manifested in the mid-50s of patients including progressive motor and cognitive decline and dysarthria. Patients exhibited visual loss at an earlier age, however this was attributed to glaucoma. Brains showed extensive atrophy in the cerebellar particularly in the vermis. (Mancini et al., 2015)

1.3 Pathology and Mechanism of disease

1.3.1 Lysosomal functions of CLN proteins

The localisation of CLN proteins have mainly been localised to the lysosomes, however the function of many of the proteins remain unknown. Mutations in all CLN genes result in the inability to clear waste products, leading to the build-of undigested material within lysosomes. While the primary function of many CLN proteins are unknown, many have been known to regulate different aspects of lysosomal function. CLN2 (TPP1), CLN10 (CathD) and CLN12 (AP13A2) are thought to be involved in the lysosomal protein degradation, while CLN3 has been shown to be involved in regulation of lysosomal pH (reviewed in (Kollmann et al., 2013, Carcel-Trullols et al., 2015). A major lysosomal function emerging to be disrupted in most if not all NCLs is autophagy. Defects in autophagy has been

observed in models of CLN2, CLN3, CLN5, CLN6, CLN7 and CLN10 (reviewed in (Seranova et al., 2017) and will be discussed further in section 1.3.5.

1.3.2 Neurodegeneration

Although widespread neurodegeneration can be seen by the end of the disease, studies in humans, ovine and murine models have indicated selective regional neuronal loss. Murine models show the hippocampal neurons, thalamic relay neurons in the thalamus and Purkinje cells of the cerebellum are particularly susceptible to neuronal loss (Cooper et al., 2006, Cooper, 2003). While pathology in mice models is not as severe as in human NCL, ovine models exhibit a more evident selective loss suggesting more complex gyrencephalic brains may be more severely affected (reviewed in (Palmer et al., 2013)). Build-up of storage material in the brain was initially thought to predict forthcoming neuronal loss, however glial activation is now considered a better marker. This is supported by pharmacological studies in mice which found reducing storage material failed to affect disease progression (Griffey et al., 2006).

1.3.3 Storage material

All of the LSDs, including the NCLs, are characterised by the build-up of specific storage material in lysosomes. Unlike other LSDs, however, the CLN genes encode for proteins throughout the trans-Golgi network rather than solely lysosomal proteins. The NCLs were originally characterised by symptoms, widespread neuropathology and gliosis and distinguished from other LSDs by the clinical build-up of storage material and autofluorescent lipopigments in lysosomes of all tissues.

Determining the composition of the storage material seen in NCL models was made difficult due to its hydrophobic insoluble nature. A method to isolate and identify storage material was developed in studies of a South Hampshire *CLN6* deficient sheep model. Storage material was extracted from various tissues, including the brain, and two-thirds was found to be composed of proteins and undigested lipids. The predominant protein species identified was the N-terminal subunit *c* of mitochondrial F_1F_0 ATP synthase (SCMAS), a 75-amino acid long proteolipid. Since the discovery, SCMAS has been identified as the major storage component in many NCLs including: CLN2-, CLN3-, CLN5-, CLN6-, CLN7- and CLN8- and CLN11- diseases by immunohistochemical staining (reviewed in (Palmer, 2015), (Palmer et al., 2013), (Haltia, 2003) and (Bennett and Rakheja, 2013) summarised in table 1.3). However, sphingolipid activator proteins (saposins) A and D were the major storage material in late infantile CLN1-, adult CLN4- and congenital CLN10 disease (Palmer et al., 2013). Subunit c initially accumulates within the mitochondria before being transported into lysosomes. However, subunit c is found functionally intact within lysosomes instead of in a partially degraded state, as it lacked the N terminal import pre-sequence. This confirmed subunit c was correctly imported into the mitochondria before the N-terminal sequence got cleaved, indicating a defective lysosomal degradation/recycling machinery as opposed to mitochondrial defects (reviewed in (Palmer et al., 2013)). While storage material may primarily be composed of one protein, the presence of SCMAS was discovered in a *CLN10* deficient mouse model which predominantly accumulated saposins (Koike et al., 2000). This indicates storage material may be composed of multiple proteins with some potentially yet unidentified.

EM profiling of storage material in saposin dominant forms of NCLs exhibit granular osmiophilic deposits (GRODs), while SCMAS predominant storage material are characterised by the accumulation of curvilinear and/or fingerprint membranous profiles. No intrinsic fluorophore has been detected within storage material to explain the autofluorescence, which has been attributed to the aggregate property of non-fluorescent proteins and lipids (Palmer et al., 1993). Build-up of storage material is seen in most cells in the NCLs and acts as a marker of the neurodegenerative disease and not the cause. This is demonstrated by the selective neurodegeneration seen in patients (Palmer et al., 2013). In addition, mitochondrial dysfunction has been observed to precede SCMAS build-up in patient derived fibroblasts cultures with CLN1, CLN2 and CLN3 disease in addition to *CLN3* deficient mice (Fossale et al., 2004, Das et al., 2001).

1.3.4 Neuroinflammation

Gliosis - activation of glial cells in the brain - is now considered a key hallmark of most neurodegenerative diseases including the NCLs. Microglia, the immune cells of the CNS, can be activated by the presence of reactive oxygen species and foreign material and during disease sustained activation of glial cells results in a harmful neurotoxic environment. Hippocampal brain autopsies from CLN1, CLN2, CLN3, CLN5 and CLN8 disease patients showed reginal specific gliosis, with microglial activation rather than astrocyte activation spatially matching neuropathology (Tyynela et al., 2004). However, it was not until studies using a *CLN6* deficient sheep model were undertaken was it known whether gliosis was a neurotoxic insult or a

neuroprotective response to neuronal loss. Gliosis was detected as early as the pre-natal stage. Early glial activation was observed to occur in the cortex primarily the visual cortex but not in the cerebellum, with the former suffering future neurodegeneration (Oswald et al., 2005, Kay et al., 2006). These indicated early microglial activation spatially correlated with neuronal loss and is now considered a better marker than storage material. Early gliosis has been detected in *CLN3* deficient mouse models with early microglial and astrocyte activation preceding neuronal loss. The glial cells present abnormal morphology with microglia failing to reach full maturity indicating defective glial functions.

Consistent with an immune component to the disease, suppressing the immune system in a *CLN3* mouse model resulted in a significant reduction of gliosis, neuronal loss and marked improvement in motor functions (Seehafer et al., 2011). The mechanism behind this immune response are yet to be fully understood, although post-mortem analysis of CLN1 disease patient tissue and a respective mouse model indicated increased levels of a pro-inflammatory transcription factor, NFκB (Saha et al., 2008).

1.3.5 Autophagy

Autophagy is a key cellular pathway that utilises lysosomes and is implicated in most neurodegenerative diseases including the NCLs. Autophagy involves the cellular degradation of macromolecules and organelles into its breakdown

Disease gene	Main storage component
CLN1/PPT1	Saposins (SAPs)
CLN2/TPP1	Subunit c of mitochondrial ATP synthase (SCMAS)
CLN3	SCMAS
CLN4/DNAJC5	SAPs
CLN5	SCMAS
CLN6	SCMAS
CLN7/MFSD8	SCMAS
CLN8	SCMAS
CLN9	SCMAS
CLN10/CTSD	SAPs
CLN11/GRN	SCMAS
CLN12/ATP13A2	SCMAS
CLN13/CTSF	SCMAS
CLN14/KCTD7	SCMAS

Table 1.3: Major storage component of NCLs

products that are then recycled. There are three types of autophagy: macroautophagy (which will be referred to as autophagy), microautophagy and chaperone mediated autophagy (CMA) with the former the best understood. Multiple autophagy genes (*Atg*) are involved in the autophagy process, which initiates with the *de novo* formation of the double-membranous phagophore. Cytosolic components such as p62 are sequestered into the forming phagophore until a double membrane vesicle is formed, known as an autophagosome. Autophagosomes then mature into autolysosomes via one of two processes: firstly, by directly fusing with lysosomes; or via the second predominant pathway by fusing with late endosomes to form ampisomes, which then fuse with lysosomes. The components are broken down by the low acidic pH within the lysosomal lumen and lysosomal hydrolases before being released for recycling. The continual flow of autophagy is known as autophagic flux. As neurons are post-mitotic, they heavily rely on autophagy to removed unwanted waste and maintain good neuronal health.

Autophagy defects have been reported in several NCL mouse models including: CLN3, CLN5, CLN6, CLN10 and CLN7 with the latter being discussed below (section 1.4). Defects range from: inhibition of autophagosome formation; defects in autophagosome maturation and accumulation of autophagosomes and autophagic cargo. *CLN3*-deficient cells had increased numbers of autophagosomes indicating defects in autophagosomes maturation, while build-up of autophagic material was also observed in *CLN5* and *CLN6* disease models. A similar defect was observed in CLN3 and CLN6 patient fibroblasts, and CLN3
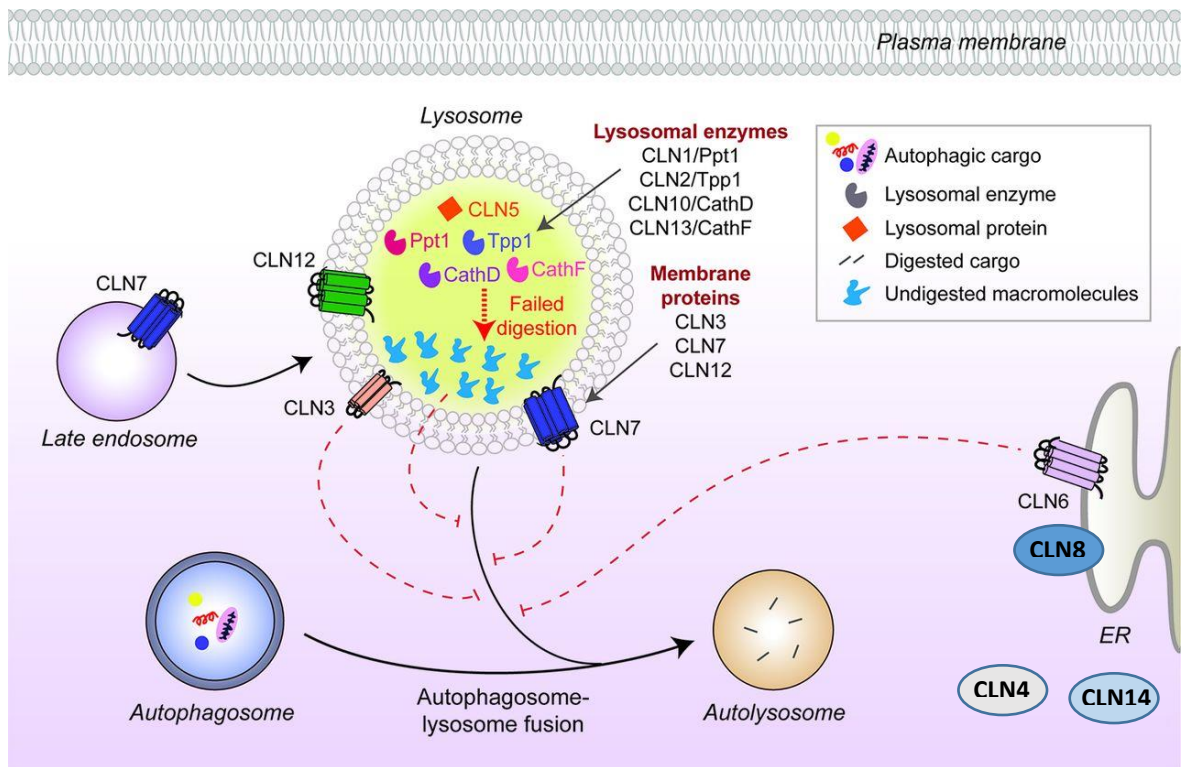
Figure 1.1: Schematic of CLN protein distribution and their effect on autophagy. CLN proteins can be found across the trans-Golgi network. CLN proteins can be found inside the lysosome (CLN1, CLN2, CLN5, CLN10 and CLN13), at the lysosomal membrane (CLN3, CLN7 and CLN12), at the ER/ERGIC membrane (CLN6 and CLN8). Mutations in lysosomal proteins/enzymes prevent degradation of autophagic cargo impairing lysosomal function. Mutations inhibiting autophagosome maturation are resulting in a block of autophagic flux are depicted as dashed lines. Roles in autophagy have not been established for cytosolic proteins (CLN4 and CLN14), extracellular protein (CLN11 - not shown) or CLN9 (localisation yet to be determined. Figure adapted from (Seranova et al., 2017).

patient induced pluripotent stem cells (iPSC) derived neuronal cells showed (reviewed in (Seranova et al., 2017)). A reduction in autophagic flux is observed in cultured neurons from *CLN10* deficient mice indicated by the build-up of autophagosomes and has also been observed *in vivo* in addition to build-up of storage material (Koike et al., 2000). A summary of how CLN proteins effect autophagy is shown in figure 1.1.

1.4   MODELS OF the NCLs

Model organisms are an excellent method to study the functions of the CLN proteins, the pathology and underlying mechanisms of diseases and for testing potential therapeutic agents. The identification of NCL disease-causing genes has allowed many naturally occurring NCLs to be identified in domesticated and farmed animals, and led to the generation of specific NCL models, many of which recapitulate the pathology of the human disease plus many engineered models. Animal models can replicate the complex biology of the human CNS much better than cell culture systems and have proved to be an invaluable tool for the study of NCL disease progression. NCL models range from large animal models such as ovine and canine models, smaller vertebrate models such as rodents and zebrafish, single cell yeast model and an invertebrate *Drosophila* model which will be discussed further in section 1.6. Each animal model has its own advantages and limitations for study of disease progression (reviewed in (Bond et al., 2013, Faller et al., 2015)).

1.4.1 Vertebrate models

1.4.1.1 Mouse models

The understanding of NCL disease pathology has been greatly improved by studies using mouse models. NCL mouse models have been generated for many *CLN* genes including: *CLN1*, *CLN2*, *CLN3*, *CLN5*, *CLN10* and *CLN7* (reviewed in (Faller et al., 2015, Bond et al., 2013, Brandenstein et al., 2016, Damme et al., 2014). In addition, naturally occurring mouse models exist for CLN6 and CLN8 disease. Each mouse model recapitulates key features of the human disease including motor and behavioural defects and shows regional specific neurodegeneration and build-up of storage material. These have highlighted the vulnerability of the thalamocortical system where gliosis and neuronal loss generally occur early in the disease. Various processes have been reportedly been affected including, autophagy, oxidative stress and apoptosis, with a number of studies also indicating synaptic failure to be common pathology of the NCLs (Partanen et al., 2008a, Kielar et al., 2009b). However, the underlying mechanism leading to neurodegeneration remains poorly understood.

1.4.1.2 Zebrafish

Zebrafish has homologues of most human *CLN* genes and strains carrying mutations have been identified for several *CLN* genes, including *CLN7*. However, only a few of these models have been studied and shown to recapitulate key pathological features, these include mutations in: *CLN2, CLN3, CLN10* and *CLN11* (reviewed in (Bond et al., 2013, Wager et al., 2016)). The *CLN2^{sa11}* larvae have a

smaller head and eyes, and like the *CLN3^{-/-}*, which was generated by morpholino injections, recapitulated key features of the human disease. These included locomotion defects and seizures, neurodegeneration and build-up of SCMAS (Mahmood et al., 2013, Wager et al., 2016). The phenotypes present during embryonic stages indicating these genes are essential for development.

1.4.2 Invertebrate models

1.4.2.1 NCLs in *Drosophila*

The short generation time, large progeny and cheap maintenance costs of *Drosophila* have made it an attractive *in vivo* model to study human disease, including the NCLs. A core of the NCL genes are conserved in *Drosophila*: CLN1, CLN3, CLN4, CLN7, and CLN10. They have high amino acid sequence homology with PPT1, CLN3, CLN7 and CathD having 75%, 60%, 56% and 65% homology to their human counterpart (Myllykangas et al., 2005, Glaser et al., 2003, Tuxworth et al., 2009, Muzaffar and Pearce, 2008). Loss of function mutants have been generated for all known NCL causing genes in *Drosophila* and all, with the exception of CLN4, has been shown to recapitulate key features of NCL pathology. (Myllykangas et al., 2005, Tuxworth et al., 2011b, Hickey et al., 2006)(Unpublished data, Richard Tuxworth). CLN4/Csp mutant has been used to study its functions at the synapse rather than as a NCL locus (Zinsmaier et al., 1994, Umbach et al., 1994). CathD and PPT1 deficient flies accumulate autofluorescent material, with the former exhibiting neurodegeneration and the *CLN3^{-/-}* and *PPT1^{-/-}* flies have reduced life span. The level of NCL proteins in cells is important as overexpression of PPT1, CLN3 or human-CLN3 in the fly visual system results in neural pathology and

abnormal eyes (Tuxworth et al., 2009, Korey and MacDonald, 2003). This was shown to be due to increased protein activity as increasing expression of a truncation form of CLN3 or non-functional form of PPT1 does not cause neural pathology.

Drosophila models have revealed roles for CLN proteins in key cellular processes regulating synaptic development or function. Larvae lacking CLN3 are able hypersensitive to oxidative stress, while PPT1 deficient larvae have defects in endocytosis, both which of regulate synaptic function (Saja et al., 2010, Tuxworth et al., 2011b). Mutations in *Spinster* (*Spin,* also known as *benchwarmer*), produce NCL-like pathology, however the human homologues has not been associated with NCLs, potentially because there are three homologues in humans (Dermaut et al., 2005). Studies of *Spin* mutants have also implicated defects in endocytosis and synapse function to NCL-like pathology at the synapse (Nakano et al., 2001, Sweeney and Davis, 2002), suggesting synaptopathology be common in the NCLs.

1.5 *Drosophila melanogaster* as a model organism

Since Thomas Hunt Morgan discovered the fruit fly over a century ago, *Drosophila melanogaster* has been used to make advances in genetics, inheritance, developmental and cell biology (Stephenson, 2013). A wide range of genetic tools have been developed and continue to do so making *Drosophila* a great model for studying human diseases. Although being a relatively simple organism, many mammalian signalling pathways and functions are conserved. The *Drosophila* CNS

shares many fundamental molecular, structural and functional properties with its mammalian counterpart: numerous neurotransmitters, including glutamate, dopamine, acetylcholine, GABA and peptidergic neurotransmitters; essential neuron-glia interactions; a blood-brain-barrier to isolate the CNS; and it exhibits synaptic plasticity during development. However, some limitations in modelling the nervous system in *Drosophila* include a lack of myelin and blood flow vessels preventing modelling of multiple sclerosis brain infarcts and haemorrhages.

1.5.1 GAL4-UAS system

The bi-partite GAL4-UAS system is a powerful genetic tool available to view and manipulate ectopic gene expression in *Drosophila* (Brand and Perrimon, 1993). It consists of a *Saccharomyces cerevisiae* (yeast) transcription activator protein, GAL4, which binds to an upstream activation sequence (UAS) inducing downstream gene expression (Figure 1.2). The GAL4 gene can be placed under any native gene promoter to induce expression exclusively in subsets of cells in which that gene is expressed, and can be visualised when linked to a UAS reporter gene such as GFP. The GAL4 and UAS components are kept apart as independent transgenic lines. Crossing a GAL4 driver line with a UAS line gives rise to progeny which possess both components. This will induce expression of the UAS gene in a GAL4 dependent expression pattern (Hartwell., et al., 2011).

The GAL4-UAS system can also be combined with RNA interference (RNAi) to induce cell specific knockdowns of gene function. Here the Gal4 drives UAS which is upstream of an inverted sequence (e.g. Gene X inverted) separated by 10-100bp of DNA. Transcription of the inverted sequences results in the formation of a double stranded RNA hairpin loop structures and ultimately silencing of gene expression (e.g. Gene X is silenced) via the RNAi pathway (Perrimon et al., 2010). This is assisted by a huge collection of Gal4 and UAS-RNAi transgenic lines that are available in *Drosophila* stock centres, allowing ectopic expression in effectively any tissue at different developmental stages. This tool can be used to re-express a wildtype copy of a gene in mutants to rescue phenotypes, or monitor the effects of knocking down gene functions in a tissue dependent manner.

1.5.2 Balancer chromosomes

Balancer chromosomes are a genetic tool used to inhibit homologous recombination during meiosis in gametes. Balancer chromosomes contain a series of inversions of different sizes along the chromosome. This results in misalignment with its sister chromosome and suppresses homologous recombination. They also carry at least one dominant mutation producing a visible phenotype that allows genetic crosses to be followed from generation to generation. Different dominant markers are found on different balancer chromosomes, including the common Curly wings (Cy) and Tubby (Tb) markers on chromosome 2 and 3 balancers respectively. Balancer chromosomes can be used to maintain stocks of recessive lethal alleles that would otherwise be lost by recombination (Hartwell., et al., 2011).
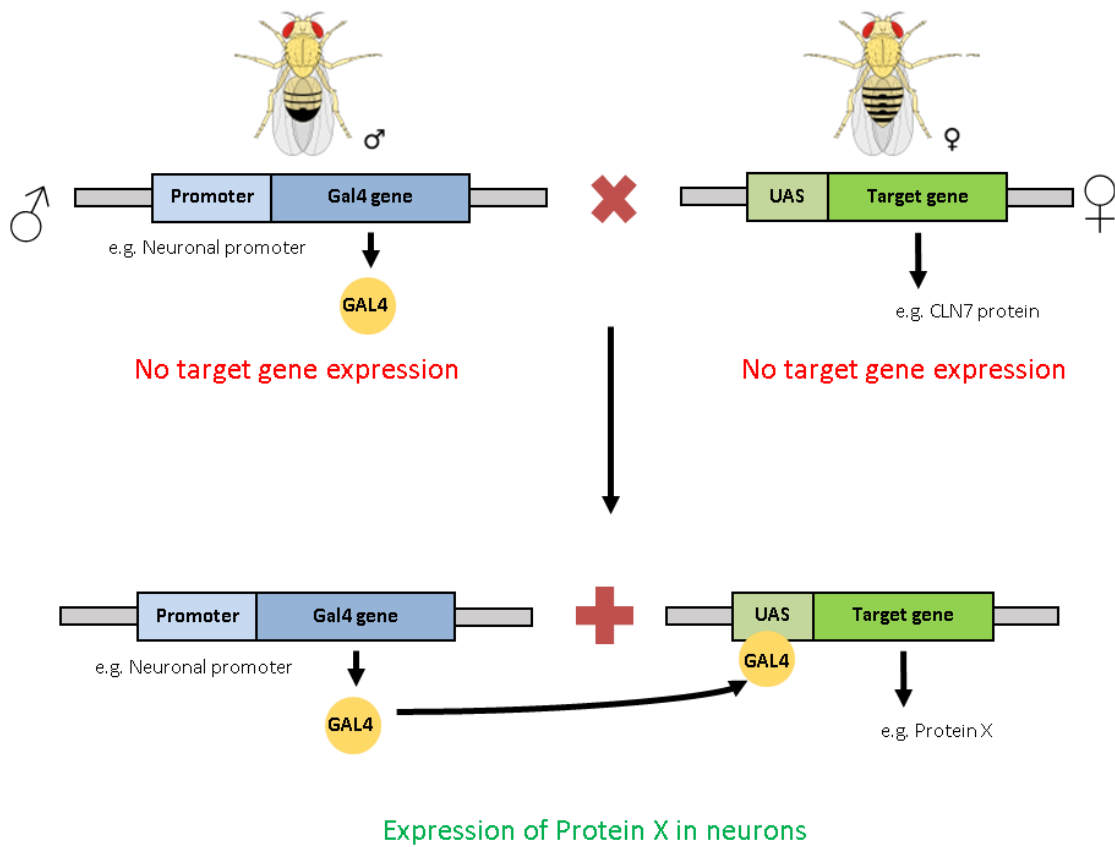
Figure 1.2: The GAL4/UAS system. The Gal4-UAS system is made up of two components, a Gal4 driver and UAS gene. The Gal4 driver lines produce ectopic expression in subsets of cells. The GAL4 gene and UAS gene are maintained on separate transgenic flies. Individually, expression of the target gene does not occur. Crossing a Gal4 driver with a UAS line produces progeny possessing both the Gal4 and UAS genes. This results in expression of the target gene in a Gal4 expression dependant manner.

1.5.3 *Drosophila* neuromuscular junction

Synaptopathy – pathology of the synapse — is an early hallmark of many, if not all neurodegenerative diseases and usually precedes neurodegeneration (Wishart et al., 2006, Gillingwater and Wishart, 2013). Synaptopathy has been observed in NCL models including *Drosophila*. The early onset of neural pathology in the NCLs, suggests the CLN genes are essential for the development of the nervous system and synapses. The late larval stage of *Drosophila* provides an established model - the neuromuscular junction (NMJ) synapse - to study synaptic development, function and plasticity (Keshishian et al., 1996). *Drosophila* motor neurons innervate the body walls muscles using excitatory glutamatergic neurons, whereas in mammals motor neurons are cholinergic. However, *Drosophila* NMJs are structurally similar to central synapses of the mammalian CNS and are often used as an accessible system to model glutamatergic synapse development and function because of the accessibility for high-resolution microscopy and electrical recording after a simple dissection (reviewed in (Andlauer and Sigrist, 2012a, Ruiz-Canada and Budnik, 2006, Menon et al., 2013)).

The larval neuromuscular system comprises of eight repeating bilaterally symmetrical abdominal segments (Figure 1.3). Each segment contains 32 motor neurons which project onto 30 multinucleated skeletal muscles and can be grouped into six major nerve branches. Each nerve branch projects towards a particular set of muscles and includes: intersegmental nerve (ISN), segmental nerve a-d (SNa -

d) and transverse nerve (TN) (Hoang and Chiba, 2001; Kim et al., 2009 and Menon et al., 2013).

Presynaptic boutons - the site of neurotransmitter release - are swellings found near the axon terminal containing active zones. Action potentials reaching boutons cause a local influx of Ca^{2+} which ultimately causes neurotransmitter containing vesicles to fuse with the membrane, emptying its contents into the synaptic cleft in order to innervate the post synaptic membrane. Motor neurons innervate muscles via synapses which can be categorised into three bouton types, type I – III. Type one boutons are surrounded by subsynaptic reticulum and are further subdivided into type Ib (big) and type Is (small) boutons. Each type of boutons can be found on different lengths of neurons and vary in size (Hoang and Chiba, 2001). For my thesis, I have studied type Ib boutons on muscle 4 due to its accessibility and the clear physical separation between type Is and Ib boutons. The muscle 4 NMJ has also been used widely in other studies allowing me to directly compare my data to other studies.

The NMJ is sculpted by three types of cells, the presynaptic motor neuron, postsynaptic muscle and peripheral glia. The plasticity and size of boutons are controlled by homeostatic mechanisms that match presynaptic innervations with the requirements of the postsynaptic muscle (Lazarevic et al., 2013). Changes in synapse size indicate an imbalance in synaptic activity. Two main pathways

involved in retrograde signalling include the transforming growth factor β (TGF-β) and Wnt signalling pathways (Wu et al., 2010).

1.5.4 Anatomy of *Drosophila* eye

The *Drosophila* brain is made up of many components involved visual processing including the compound eye/retina, lamina, medulla lobula and lobula plate. The compound eye is made up of approximately 750-800 repeating hexagonal units known as ommatidia. Each ommatidium is composed of eight photoreceptors (R1-R8), first order neurons, which forms synaptic connections in deeper regions of the brain. Phototransduction occurs in the rhabdomeres of ommatidia, which houses the light sensitive rhodopsin, of which there are approximately 50,000 within R1-6 photoreceptors. Photoreceptors R1-6 utilise the same rhodopsin most sensitive to blue light and processes achromic information. R7 and R8 have UV – and blue and green sensitive rhodopsins respectively which are utilised to process colour vision. R1-6 and R7/8 can be likened to the vertebrate rods and cones of the mammalian visual system respectively. R1-6 photoreceptors project onto first neuropil – a region highly enriched in synaptic connections – and forms connections with second order lamina neurons. R7 and R8 photoreceptors pass through the lamina region and form connections with neurons in the medulla.

1.5.5 Electroretinograms of *Drosophila* visual system

Electroretinograms (ERGs) have been used to measure the phototransduction cascade in *Drosophila* since the late 1960s and have played a role in characterising many key genes involved in the regulation of phototransduction. The ERG records

a collective field potential in response to a light stimulus, and produces transient spikes in response to lights being turned on and off corresponding to the polarisation of photoreceptors and downstream neurons. Key components of phototransduction have been correlated to ERG waves using different mutations. In particular, the on- and off-transients have been determined to be regulated by synaptic transmission onto lamina neurons, while the receptor amplitude corresponds to photoreceptor potential (Montell, 2012, Heisenberg, 1971).

1.5.6 Phototransduction signalling

The effects of a light stimulus is amplified by phototransduction, via G-protein coupled receptors (GPCR), by a mechanism similar in both flies and mammals. Phototransduction begins with the absorption of photons by rhodopsin which is linked to a retinal chromophore, 2-dehydro 11-*cis*-retinal in mammals and 3-hydroxy 11-*cis*-retinal in *Drosophila*. Absorption of light by rhodopsin photoisomerises the *cis* chromophore into an all-*trans* configuration and subsequently activates rhodopsin which transforms into metarhodopsin. In vertebrates, the all-*trans*-retinal chromophore, is released from rhodopsin and is recycled via an enzymatic pathway. However, rhodopsin is bistable in flies, and therefore absorption of a second photon will convert the all-*trans* form back in a *cis* configuration. The conversion into metarhodopsin promotes the GDP/GTP exchange and activation of a heterotrimeric G-protein, transducin in vertebrates and $G_q\alpha$ in *Drosophila* (Montell, 2012). In vertebrates, the G-protein activates phosphodiesterase (PDE) which hydrolyses 3',5'-cyclic guanosine monophosphate
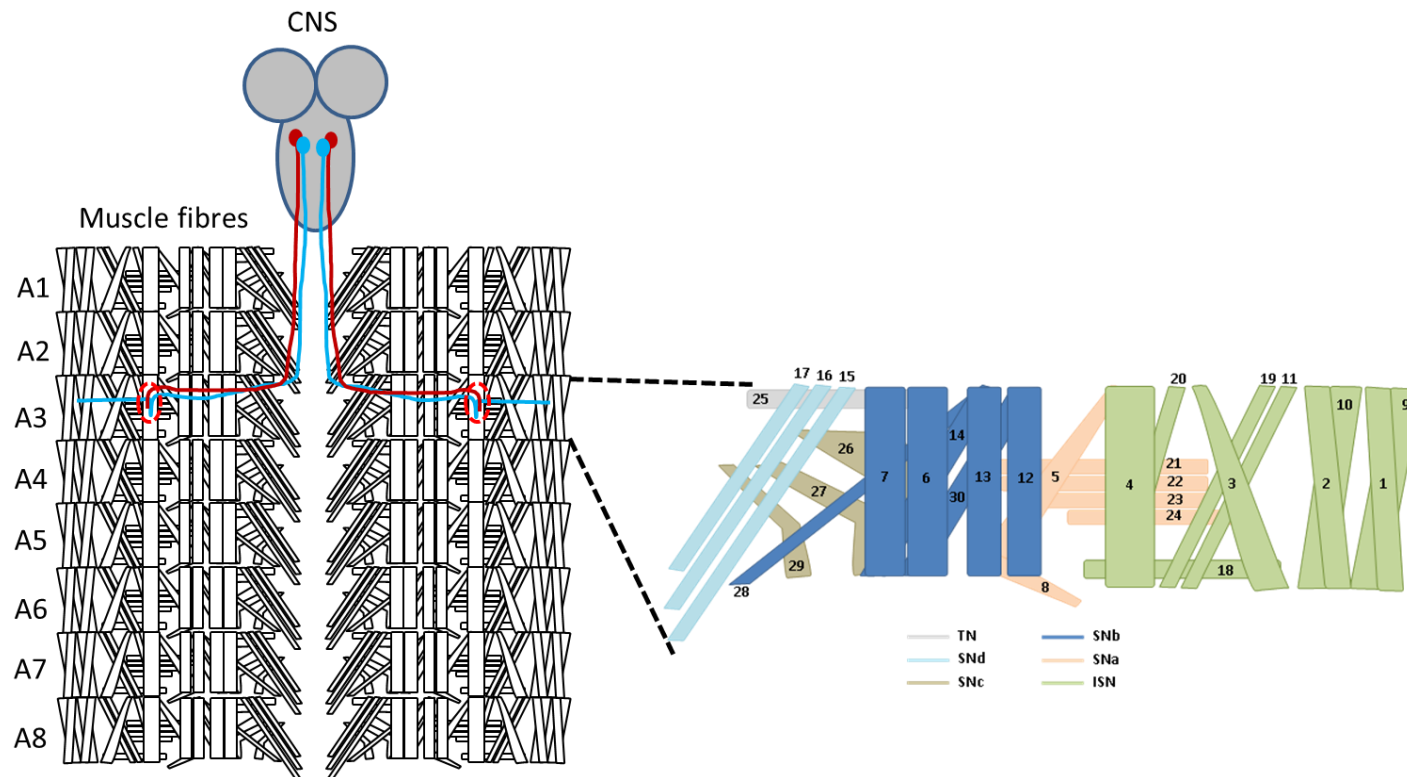
Figure 1.3: Schematic of motor neurons innervating muscle 4. Each abdominal segment is made up 30 muscles which are innervated by one of six different nerve branches. Groups of muscles innervated by different nerve branches are highlighted in different colours and include: intersegmental nerve (ISN), segmental nerve a - d (SNa - d) and transverse nerve (TN).

(cGMP) and results in the hyperpolarsation of neurons via the closing of cGMP-gated transduction channels. In flies, the G-protein in turn activates phospholipase C β (PLCβ) – encoded by *NorpA* - which hydrolyses phosphatidylinositol 4,5-bisphosphate (PIP$_2$) into soluble inositol 1,4,5-trisphosphate (IP$_3$) and membrane-bound diacylglycerol (DAG). This leads to the opening of two types of Ca^{2+}-permeable channels: transient receptor potential (TRP) and TRP-like (TRPL) channels in photoreceptors. The influx of Ca^{2+} depolarises the photoreceptor which results in the release of histamine (His) neurotransmitter at the synapse, which opens chloride channels and hyperpolarises downstream lamina and medulla neurons. The increase in cytosolic Ca^{2+} is counterbalanced by an active Na$^+$/Ca^{2+} exchanger, CalX, which extrudes Ca^{2+} ions from photoreceptors in exchange for a Na$^+$ ions (Montell, 2012). NORPA also promotes a negative feedback loop by accelerating intrinsic GTPase activity.

Polarisation of the photoreceptors and synaptic transmission in the lamina has been detected using ERGs on *Drosophila* eye with mutations along different parts of the fly visual system producing abnormal ERG readings. Although the mechanism underlying the opening of TRP and TRPL channels are unknown, DAG is thought indirectly be responsible (Hardie and Raghu, 2001, Katz and Minke, 2009). Additionally, ER Ca^{2+} stores can be released when IP$_3$ binds to ER IP$_3$ receptors (IP$_3$R), however this has been shown to have no effect on ERG readings in *Drosophila* (Acharya et al., 1997, Raghu et al., 2000, Bollepalli et al., 2017). One study using GMR-Gal4 to drive RNAi to knockdown IP$_3$R expression found reduced levels of the receptor results in abnormal ERG readings (Kohn et al., 2015).

However, this finding was later rebutted by Bollepalli et al, 2017 due to the failure to include a GMR-Gal4/+ control, which was found to exhibit a visual phenotype (Bollepalli et al., 2017). Therefore, Ca^{2+} homeostasis regulated by membrane channels are thought to regulate phototransduction.

1.6: CLN7

1.6.1 Structure of CLN7

The CLN7 protein has been predicted to encode a transmembrane protein with 12 membrane spanning domains. Northern blot analysis of various human tissue samples indicated *CLN7* mRNA is expressed in a ubiquitous expression pattern, including all regions of the brain tested including the cerebellum and cerebral cortex (Siintola et al., 2007). The subcellular localisation of CLN7 has been revealed by numerous studies that indicate CLN7 is a predominantly a lysosomal membrane protein. Tagged forms of human and mouse CLN7 expressed in COS-1 and HeLa cells presented punctate staining in the cytoplasm which co-localised with the lysosomal marker lysosomal-associated membrane protein 1 (LAMP1) and with an acidic organelle marker, LysoTracker. Additionally, no co-localisation was observed when the early endosomal or compartments of early secretory pathway were marked (Siintola et al., 2007). This is supported by proteomics analysis of rat liver which identified CLN7/MFSD8 as a novel lysosomal transport (Chapel et al., 2013) and the presence of lysosomal sorting signal motifs on CLN7: a N-terminal dileucine motif and 2 C-terminal tyrosine motifs, both of which reside on the cytoplasmic side of the lysosome. This ensures the protein is transported from the ER and trafficked

to lysosomes directly or indirectly via the plasma membrane (Steenhuis et al., 2010, Sharifi et al., 2010). There is evidence that around 22% of the N-terminally tagged GFP-CLN7 protein is localised at the plasma membrane in cells (Steenhuis et al., 2010).

1.6.2 Function of CLN7

CLN7/MFSD8 is conserved in mammals and invertebrates including rodents, *C.elegans* and *Drosophila* (Siintola et al., 2007). Sequence alignment has indicated *CLN7* shares homology with the major facilitator superfamily (MFS) proteins. CLN7 is predicted to contain a functional domain of MFS giving rise to it other name MFS-domain (MFSD). The MFS are the largest family of secondary active transporters and can transport a wide range of substrates including: ions, carbohydrates, amino acids, neurotransmitters, amongst other small molecules. However, the substrate CLN7 may transport remains unknown (Yan, 2013).

Understanding the function of CLN7 has been aided by the generation of novel CLN7 models. The first animal model for CLN7 disease was generated in 2016 by the insertion of a *LacZ* gene-trap cassette between exons 1 and 2 (Damme et al., 2014). This resulted in hypomorphic mice model which resembled many of the clinical symptoms of CLN7 disease. Subsequently a knock-out model was generated by removing exon 2 which better recapitulated key features of the human CLN7 disease, including neuropathology, gliosis and motor and neurological defects, along with clinical build-up of storage materials (Brandenstein et al., 2016). These models provide increasing evidence implicating CLN7 in mTORC/autophagy

regulation. Mouse embryonic fibroblasts (MEFs) taken from a knock-out model failed to adapt to starvation conditions by monitoring phosphorylation of S6 kinase (S6K), a downstream target of the TORC1 pathway. Levels of pS6K was abolished 2 hours after starvation and was followed by a gradual recovery under long term starvation as expected. However, by 8- and 12 hours of starvation, levels were significantly reduced in CLN7 knock-outs, indicating impaired reactivation of mTORC1 signalling during ongoing starvation (Danyukova et al., 2018). Recent data also indicates reduced TORC1 activity in a *Drosophila CLN7* model (Richard Tuxworth, unpublished data).

No defects were observed in macroautophagy or autophagic flux – determined by levels of p62 and LC3-II, an autophagy adaptor protein and autophagosome marker - during amino acid- and serum free- starved states which were comparable to control MEFs (Danyukova et al., 2018). However, impaired autophagy has been observed in *CLN7* KO mice with increased levels of LC3-II in the brains of 10 month old mice. Additionally, detergent-insoluble fractions exhibited a 10-fold increase in p62, indicating a block in autophagy. Large protein aggregates positive for p62 and ubiquitin were also detected via immunohistochemistry in different regions of the brain including: granule layer in the cerebellum, cerebral cortex, hippocampus and thalamus (Brandenstein et al., 2016), suggesting a role for CLN7 in autophagy.

1.6.3 Preliminary *CLN7$^{-/-}$* data

CLN7 Drosophila models generated by imprecise P-element excision also exhibited similar NCL-like phenotypes including motor defects and synaptopatholgy.

Unpublished observations made by Megan O'Hare and Richard Tuxworth have shown that the anatomy of NMJs in *CLN7* mutants at the third instar larval stage is altered. The study found that type Ib junctions in *CLN7* mutants were significantly smaller than wild type, while type Is junctions remained unaffected. The plasticity and size of boutons are controlled by homeostatic mechanisms which match presynaptic innervations with the requirements of the postsynaptic muscle (Lazarevic et al., 2013). Understanding the mechanism behind this was a key goal of my study.

CLN7 mutants may also share genetic interactions with autophagy related proteins as an *Atg/Df* autophagy mutant shows the same decrease in type Ib phenotype. *CLN7* mutant adults were also shown to be larger in size, with larger cells accounting for the increase in wing span, not increased number of cells. The abnormal increase in size suggests a possible shift in the homeostatic TORC signalling, which is involved in the anabolic vs catabolic pathways. This may be due to inappropriate up-regulation of TORC1 (biosynthesis) in mutants, with inhibition of TORC1 via rapamycin rescuing the mutant phenotype.

1.7 Aims

The main aim of this thesis is to uncover the functions of CLN7 and highlight potential mechanisms the underpinning CLN7 disease. The first approach was to tag the *Drosophila* CLN7 protein with a YFP marker via genome editing (Chapter 3) and subsequently use the YFP-CLN7 knock-in to carry-out the first *in vivo* localisation of the transmembrane protein (Chapter 4) in any system. Then, I

investigated the roles of CLN7 in neurodevelopment. As synaptopathology precedes neuronal loss, I quantified boutons numbers at the NMJ as means of observing neuronal health. I also used genetic tools to determine where CLN7 is required for normal NMJ development (Chapter 5). Lastly, I observed the physiological consequences for the lack of CLN7 within the adult visual system using ERGs and SSVEP in assess whether CLN7 mutant flies suffer similar retinopathy as human CLN7 disease patients (Chapter 6).

2. MATERIALS AND METHODS

2.1 *Drosophila* husbandry and stocks

2.1.1 Maintenance

Flies were housed in an automated 12 hour light/dark cycle at 25 $^{\circ}$C unless otherwise stated. They were maintained on either standard agar medium (0.8% w/v agar, 1% w/v soy flour, 5% w/v glucose and 5% w/v yeast) or "German food" (0.8% w/v agar, 8% w/v yeast, 2% w/v yeast extract, 2% w/v peptone, 3% w/v sucrose, 6% w/v glucose, 0.05% w/v magnesium sulphate and 0.05% calcium chloride) to boost egg laying. 1% v/v of 10% w/v p-Hydroxy-benzoic acid methyl ester in EtOH and 0.3% v/v propionic acid was added to both to act as antifungal agents.

2.1.2 Making fly food

Ingredients were added to water in a pressure cooker and stirred after addition of each ingredient. The pan was placed on a heating block at 500 $^{\circ}$C, stirred after 2 x 15 min and left until the pressure indicator was between two red lines. The pan moved onto tissue placed on the bench for 2 min before being placed into a 50 $^{\circ}$C water bath to cool. Once the temperature of the food reached between 50-60 $^{\circ}$C antifungal agents were added and stirred. 7 ml and 35 ml of food was pumped into vials and bottles respectively, covered with muslin and left to cool overnight at room temperature. Vials and bottles were plugged with cotton wool and stored at 4 $^{\circ}$C. Food was made fresh weekly.

2.1.3 Fly stocks

Balancer stocks and genetic markers were used to follow genetic crosses. *CLN7* mutants refer to the *CLN7^{84D}* allele unless otherwise stated. The stocks of flies used in this thesis are summarised in table 2.1.

2.1.4 CRISPR/Cas9 crossing scheme

Injected flies were crossed to a third chromosome balancer (Figure 2.1) before the injected fly was subjected to a YFP-CLN7 PCR screen. Progeny were subjected to a 37 °C heat shock for 2 hours and virgin female from successful YFP-CLN7 incorporated flies were crossed to the same third chromosome balancer. Flies were PCR screened to determine the germline transmission rate. Virgin female progeny were selected against Drop eyed for Humeral and against the P3-GFP marker. A sibling cross was then carried out to generate flies homozygous for the *YFP-CLN7* allele on chromosomes III.

2.2 Molecular biology

2.2.1 Cloning - Heat shock transformation

Approximately 20 µl of competent bacteria (Invitrogen One Shot TOP 10) was incubated with 50 ng of pCFD3 plasmid (Addgene plasmid number 49410) in a 1.5 ml Eppendorf on ice for 15 min. Cells were then heat shocked for 40 seconds at 42 °C in a water bath and then allowed to recover for 2 min on ice. 500 µl of SOC media (New England Biolabs (NEB) - prewarmed to 37 °C) was added and place in a 37 °C shaking incubator for 60 min. Cells were spun at 7,500RPM for 90

Name	Genotype	Description	Source
Wild type:			
w^{1118} (BL6326)	*w^{1118}; +/+; +/+*	White eyed wild-type	Bloomington *Drosophila* stock centre (BDSC University of Indiana)
VDRC *w^{1118}*	*w^{1118}; +/+; +/+*	White eyed wild-type	Vienna *Drosophila* Resource Centre
Vermillion	*v^1 ; +/+; +/+*	Vermillion eyed wild-type	(BDSC)
CLN7:			
CLN7^{84D}	*w^{1118} ; +/+; CLN7^{84D}*	p-element excision	Megan O'Hare, Richard Tuxworth and Guy Tear (King's College London – KCL)
CLN7^{84D} heterozygote	*w^{1118} ; +/+; CLN7$^{84D/ +}$*	*CLN7* heterozygote	Combined
CLN7^{36H}	*w^{1118} ; +/+; CLN7^{36H}*	p-element excision	Megan O'Hare, Richard Tuxworth and Guy Tear (KCL)
CLN7 transheterozygote	*w^{1118} ; +/+; CLN7$^{84D/36H}$*	*CLN7* transheterozygote	Combined
Localisation lines:			
Venus-*YFP::CLN7* (+ AI)	*w^{1118} ;+/+; Venus-YFP::CLN7*	YFP-CLN7 knock-in	Generated in this thesis

Venus-*YFP::CLN7* (-AI)	*v¹;+/+;* Venus-*YFP::CLN7*	YFP-CLN7 knock-in	Generated in this thesis
CLN7::Red Stinger	*w¹¹¹⁸ ;+/+; CLN7::Red Stinger/FM6*	RedStinger under *CLN7* promoter	Mohammad Mofatteh and Guy Tear (KCL)

CLN7 RNAi knockdowns

UAS-CLN7^{RNAi}	y1, sc, v1; UAS-CLN7^{RNAi} ; +/+	CLN7 RNAi under a UAS promoter	(BDSC)
Actin-GAL4	*w¹¹¹⁸* ;+/+; Actin-GAL4/TM6B,Tb,Hu	Ubiquitous GAL4	(BDSC)
Mef2-GAL4	*w¹¹¹⁸* ;+/+; Mef2-GAL4/TM6B,Tb,Hu	Muscle GAL4	(BDSC)
Mhc-Gal4	*w¹¹¹⁸ ;+/+;* Mhc-Gal4/TM6B,Tb,Hu	Muscle GAL4	(BDSC)
Elav-GAL4;; Dcr2	*w¹¹¹⁸,* Elav-GAL4 ; +/+ ; Dcr2/TM6B,Tb,Hu	Pan-neuronal GAL4	(BDSC)
Repo-GAL4	*w¹¹¹⁸* ;+/+; Repo-GAL4/TM6B,Tb,Hu	Pan-Glial GAL4 (except midline glia)	(BDSC)
Spin-GAL4	*w¹¹¹⁸* ;+/+; Spin-GAL4/TM6B,Tb,Hu	NMJ GAL4	Sean Sweeny (University of York)
PG-GAL4	*w¹¹¹⁸ ;+/+;* PG-GAL4/TM6B,Tb,Hu	Perineurial glia GAL4	(Kyoto stock centre, 105-188)

CLN7 re-expression:

UAS-Venus-CLN7	w^{1118} ;+/+; UAS-Venus-YFP::CLN7 /TM6B,Tb,Hu	YFP-CLN7 under UAS promoter	Megan O'Hare, Richard Tuxworth and Guy Tear (KCL)
Actin-GAL4, *CLN7*	w^{1118} ;+/+; CLN7^{84D}, Actin-GAL4/TM6B,Tb,Hu	Ubiquitous GAL4	Megan O'Hare, Richard Tuxworth and Guy Tear (KCL)
Elav-GAL4,*CLN7*	w^{1118} ; Elav-GAL4/CyO-YFP::dfd; *CLN7^{84D}*/TM6B,Tb,Hu	Pan-neuronal GAL4	Combined
Mef2-GAL4, *CLN7*	w^{1118} ;+/+; CLN7^{84D}, Mef2-GAL4/TM6B,Tb,Hu	Muscle GAL4	Recombined
Mhc-GAL4, *CLN7*	w^{1118} ;+/+; *CLN7^{36H}* , Mhc-GAL4, /TM6B,Tb,Hu	Muscle GAL4	Recombined
RepoGAL4, *CLN7*	w^{1118} ;+/+; *CLN7^{84D}*, RepoGAL4/TM6B,Tb,Hu	Pan-Glial GAL4 (except midline glia)	Megan O'Hare, Richard Tuxworth and Guy Tear (KCL)
Spin-GAL4, *CLN7*	w^{1118} ;+/+; *CLN7^{84D}*, Spin-Gal4/TM6B,Tb,Hu	NMJ GAL4	Recombined

TGFβ and wnt:

Sax^4	w^{1118} ; *Sax^4*/CyO,Dfd::YFP ; +/+	Downregulation of TGFβ signalling	(BDSC)

Sax^5	w^{1118} ; Sax^5/CyO,Dfd::YFP ; +/+	Downregulation of TGFβ signalling	(BDSC)
Sax , $CLN7$	w^{1118} ; Sax^4/ Sax^5 ; $CLN7^{84D}$	Downregulation of TGFβ signalling combined in $CLN7$	Combined
Dad	w^{1118} ;+/+; Dad^{J1E4}	Upregulation of TGFβ signalling	(BDSC)
$Dad, CLN7$	w^{1118} ;+/+ ; Dad^{J1E4}, $CLN7^{84D}$	Upregulation of TGFβ signalling in $CLN7$	Recombined
Wnt	w^{1118} ;+/+ ; $Wnt5^{400}$	Downregulation of wnt signalling	(BDSC)

Autophagy

$Atg18$	w^{1118} ;+/+ ; $Atg18$/TM6b,Tb,Hu	Autophagy mutant	(BDSC)
$Atg18$ deficiency	$Atg18$df (Df(3L)Exel6112) /TM6b,Tb,Hu	Atg18 deficient line	(BDSC)

Balancers

Second and third chromosome balancers	w^{1118} ; If/CyO-GFP; MKRS,Sb/TM6B,Tb,Hu	Fluorescent Curly wings, Stubble, Tubby and Humeral markers	(BDSC)
Second and third chromosome balancers	w^{1118} ; If/CyO-GFP; Dr,hs-hid/TM6B,Tb,Hu	Irregular facet eyed, fluorescent Curly wings, Drop eyed, Tubby and Humeral markers	(BDSC)
third chromosome balancer	w^{1118} ;+/+; MKRS,Sb/TM6B,Tb,Hu	Stubble, Tubby and Humeral markers	(BDSC)

Table 2.1: List of Drosophila stocks
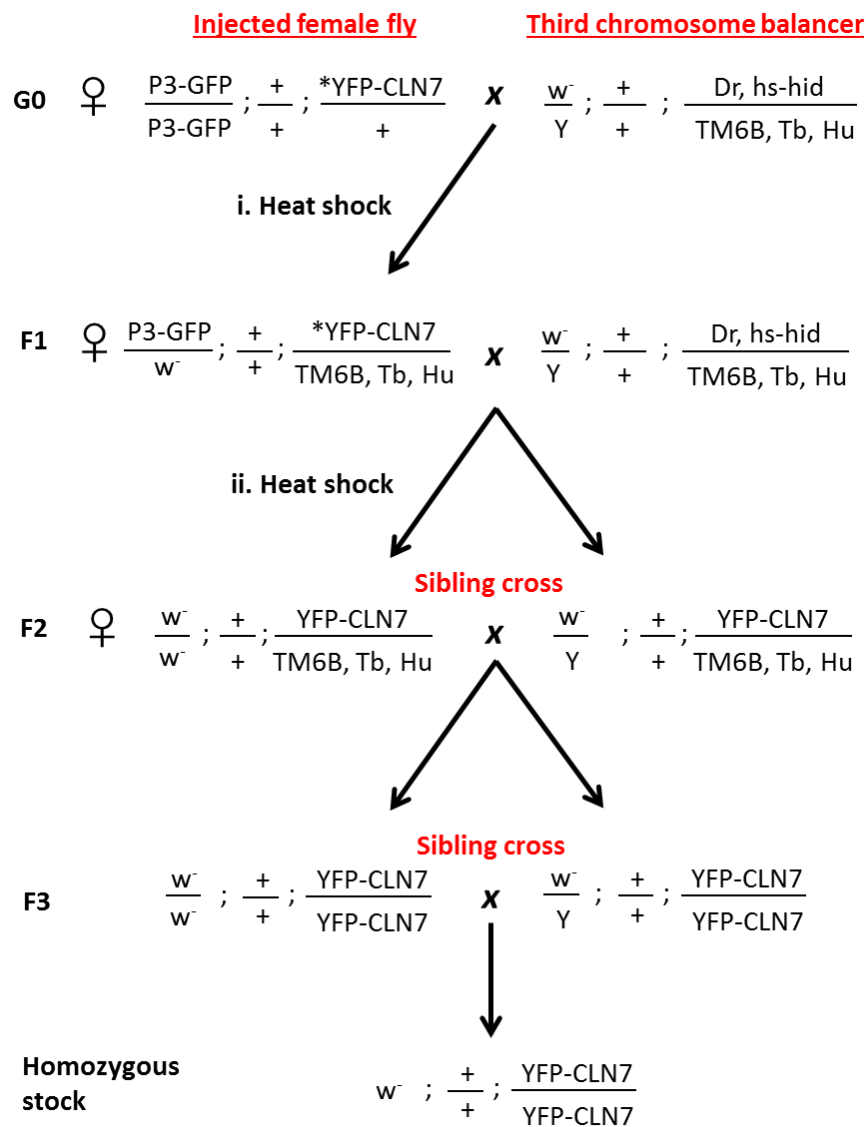
Figure 2.1: Schematic of crossing scheme. A homozygous YFP-CLN7 line was generated by crossing multiple generations of vasa injected lines with a third chromosome balancer. G0 - Individual injected flies were initially crossed with a third chromosome balancers. Genomic DNA (gDNA) was prepared from the injected parent and PCR screened for YFP-CLN7 CRISPR event. i. Larvae underwent a 90 min heat shock. F1 – Flies were selected for the Humeral (Hu) marker and crossed with a balancer. gDNA was made and screened for YFP-CLN7 in the germline. Ii. Another 90 min heat shock on larvae. F2 and F3 – A sibling cross with Hu were used to generate homozygous YFP-CLN7 flies which were used to generate a homozygous stock. This crossing scheme also shows the removal of the P3-GFP (X chromosome) marking the presence of cas9 in injected embryos. * Denotes potential insertion event of YFP-CLN7.

seconds and most of the supernatant was aspirated leaving the approximately 50 µl. Pellets were resuspended in the supernatant and plated on an LB agar plate (17.5 g/L agar) with a selective antibiotic, carbenicillin (50 µg/ml) then and incubated overnight at 37 °C (Sanyo orbital incubator).

2.2.2 Bacterial cell culture and plasmid mini preps

After overnight incubation, single colonies were picked with sterile p2 pipette tips, ejected into 2ml carbenicillin (50µg/ml) resistant LB-broth and cultured overnight in a 37 °C shaking incubator. Cultures were then mini-prepped following the Promega-Wizard Plus SV Minipreps DNA Purification System, using the centrifugation protocol. This involved pelleting cultures by spinning at 5000 x g for 5 min and resuspending in 250 µl Cell Resuspension Solution. 250 µl Cell Lysis Solution and 10 µl Alkaline Protease Solution was added and incubated at room temperature for 5 min to lyse cells which was then neutralised with 350 µl Neutralisation Solution. Cells were then centrifuged at 16,000 x g for 10 min at room temperature with the supernatant being placed into a spin column. The column was centrifuged at 16,000 x g for 1 min to bind DNA to the column and then underwent several washes at 16,000 x g with Wash Solution (EtOH added): 750 µl for 1 min, 500 µl for 1 min then 250 µl for 2 min. The empty spin column was then spun for 1 min to remove residual Wash Solution/EtOH before the plasmid DNA was eluted into a sterile 1.5ml Eppendorf tube with 30 µl nuclease free H_2O (prewarmed to 60 °C) by spinning at 16,000 x g for 1 min. The plasmid DNA was stored at -20 °C.

2.2.3 pCFD3 plasmid digestion

The pCFD3 plasmid was digested with *BbsI*: 5µl plasmid DNA, 3µl buffer2.1 (10X), 2µl BbsI (10 units) and made up to 30 µl with ddH$_2$0 before overnight incubation at 37 °C. The sample was separated on a 0.7% agarose gel then the linear plasmid band (6227bp) excised using a UV illuminator and purified using Promega-wizard SV gel and PCR clean up system. The excised gel was weighed in a weigh boat, placed back into an Eppendorf tube then 10 µl Membrane binding solution was added per 10 mg of gel mass. The mix was regularly vortexed and incubated at 55 °C until the gel fully dissolved. The solution was placed into a Minicolumn incubated at room temperature for 1 min before being spun at 16,000 x g for 1 min to bind the DNA to the column. The washing steps followed the miniprep procedure (section 2.2.2) using 700µl, 500µl and 350µl of Membrane Wash Solution provided. Residual EtOH was removed with an additional 1 min spin. 30µl nuclease free H$_2$0 was added to the column and incubated at room temperature for 1 min before eluting the DNA by spinning at 16,000 x g for 1 min and storing at -20 °C.

2.2.4 pCDF3 cloning with gRNAs

The Fly CRISPR Optimal Target Finder tool (http://tools.flycrispr.molbio.wisc.edu/targetFinder/) and CRIPSR fly design cloning protocol (http://www.crisprflydesign.org/wp-content/uploads/2014/05/Cloning-with-pCFD3.pdf) was used to design a pair of gRNA oligonucleotides with BbsI overhangs to clone into the plasmid. Oligonucleotides targeting the ATG transcription start site of *CLN7* were chosen (Section 2.2.12, table 2.2). Sense and anti-sense gRNA oligonucleotides were phosphorylated and annealed by adding 1

µl of each oligonucleotide (100µM), 1µl 10X T4 Ligation Buffer (NEB), 6.5 µl ddH$_2$O and 0.5 µl T4 polynucleotide kinase (NEB). Samples were placed in a thermocycler at 30 °C for 30 min followed by 95°C for 5 min, and then ramped down to 25 °C by 5 °C/min. Annealed oligonucleotides were diluted 1:200 in ddH$_2$O and 1 µl was added to 1 µl BbsI digested plasmid, 1.5 µl 10X T4 Ligation Buffer (NEB), 1 µl T4 DNA ligase and made up to 15 µl with ddH$_2$O and was then incubated at room temperature for 30 min. Ligated plasmid and oligonucleotide was then transformed into competent bacteria and grown on carbenicillin resistant plates overnight.

2.2.5 Colony PCR

Colony PCR was performed on individual bacterial colonies the day after transformation to identify successful clones. A single colony was picked with a 1µl pipette tip, dipping it into a PCR reaction mix and then ejecting the tip into 2ml carbenicillin resistant LB broth and grown overnight. The following day, 1.5ml from cultures that were positive in the PCR for bands for pCFD3 and gRNA incorporation was miniprepped and sent to Source Bioscience (www.sourcebioscience.com) for Sanger sequencing. Cultures were stored at 4 °C until sequencing results were returned.

2.2.6 Plasmid maxiprep

0.5 ml of overnight bacterial cultures was added to 100 ml LB broth + carbenicillin and cultured overnight at 37 °C. 1 ml of culture was used to generate a glycerol stock and the Qiagen Plasmid Maxi kit used to purify DNA from the remainder. The culture was divided between two 50ml falcon tubes (Corning) and pelleted at 5000

x g for 10 min at 4 °C. Both cultures were resuspended and combined into 10ml buffer P2 and incubated at room temperature for 5 min. Solution was transferred into ultracentrifuge tubes and 10ml of prechilled Buffer P3 was added and inverted vigorously 6 times and incubated on ice for 20 min. Cells were then centrifuged at 20,000 x g (Beckman Coulter Avanti J-E centrifuge) for 15 min at 4 °C. The QIAGEN-tip 500 was equilibrated by adding 10ml Buffer QBT allowed to empty via gravity flow before being replaced by supernatant. Once the supernatant had flowed through, the tip was washed 2 times with 30ml Buffer QC via gravity flow. 15ml Buffer QF was added to elute DNA into a sterile 50ml falcon and then precipitated by adding 10.5ml isopropanol and mixed. This was centrifuged at 15,000 x g for 30 min, supernatant aspirated and the remaining pellet was washed with 5ml 70% EtOH followed by another spin at 15,000 x g for 10 min. The supernatant was removed and the DNA pellet was air dried for 5 min and redissolved in 50µl nuclease free H_2O. DNA was transferred into a sterile 1.5ml Eppendorf and the concentration was measured on a nanodrop and H_2O was added to give a final concentration of 1000 µg/µl.

2.2.7 HDR template and CRISPR/Cas9 microinjections

An insect codon-optimised Flag-YFP-CLN7 Homology Directed Repair (HDR) template sequence was designed to include an artificial intron taken from the *white* gene to split the YFP sequence into two exons. This was surrounded by 500bp homology arms corresponding to the *CLN7* locus either side of the ATG start codon. The resulting construct was synthesised by GenScript and inserted a pUC57 plasmid and supplied as purified DNA. The HDR template-containing plasmid was

transformed and cultured in competent bacteria before being Maxi prepped as above.

2.2.8 Gibson Cloning

Gibson cloning (Gibson et al., 2009) was used to remove the artificial intron from the HDR template. The NEBuilder assembly tool (http://nebuilder.neb.com) was used to design primers to PCR amplify fragments upstream and downstream of the artificial intron for insertion into an ApaI and SacI digested pDB896 vector. Each primer contained complimentary overhang sequences to the plasmid at one end and adjacent fragment on the other end. 5' and 3' fragments were PCR amplified, purified and then quantified on a Nanodrop spectrometer. The concentration of each fragment and the vector were calculated using the formula: pmol = (concentration in ng) X 1000 / (length of fragment base pairs X 650 Daltons). The Gibson Assembly® (New England Biolabs, E5510) kit and protocol was used to ligate the two fragments and vector in a single reaction mixed in a 3:1 pmol ratio respectively. Samples were incubated at 50 °C for 15 min and then transformed overnight into competent bacteria. Individual colonies were cultures independently, underwent colony PCR, miniprep and sequencing to confirm successful artificial intron removal. A single successful culture was prepped using a maxiprep kit and made up to 1000 ng/µl.

2.2.9 Embryo microinjections

A mix of 750 µg/µl and 250 µg/µl of HDR template (plus or minus artificial intron) and gRNA respectively was mixed in 20µl volume for injections into *nanos/vasa*

cas9 embryos. Injections were carried out by The University of Cambridge Department of Genetics Fly Facility into a w^{1118} strain and transformants identified by the presence of red eyes in the F1 generation.

2.2.10 Genomic DNA preparation

Genomic DNA (gDNA) was prepared for use in a polymerase chain reaction (PCR) to follow genes and for subsequent sequencing reactions. Individual flies were anesthetised on CO_2 pads, placed in 1.5ml Eppendorf tubes and kept on ice. Flies were homogenised in 50µl of squishing buffer and Proteinase K (see appendix table 2.4) using the P200 pipette tip. Samples were heated for 10mins at 65 ^{o}C aiding protein denaturation and PK activity before being incubated at 37 ^{o}C for 30-40 min. PK activity was deactivated by boiling at 100 ^{o}C for 2-3 min prior to centrifugation at 13,800 rpm for 1 min to pellet debris. The subsequent supernatant was used for PCR reactions.

2.2.11 Polymerase Chain Reaction

PCR was used amplify specific regions of DNA and performed using the Go Taq DNA Polymerase (Promega) and supplied Go Taq buffer. Each reaction contained 0.5 µl of gDNA template or 4 µl of complimentary DNA (cDNA), 1 µM forward primer, 1 µM reverse primer (200 µM each), 0.2mM dNTP mix, 1.2U polymerase in 5x Go Taq buffer and made up to 20 µl with ddH_20. A thermal cycler (Bio Rad Tetrad 2) was used with the following settings: 5 mins of initial denaturing at 94 ^{o}C, 35 cycles of: 30 secs of denaturing at 94 ^{o}C, 30 secs of annealing with temperature depending on primers used, and then elongation at 72 ^{o}C with length of time depending on

expected product size (1 min/kb) followed by a final elongation of 2 mins before being held at 10 °C.

2.2.12 Gel electrophoresis

PCR products were run on a 1% agarose gel (unless specified) containing 1:100,000 v/v Ethidium bromide in 1x Tris/acetic acid/EDTA (TAE) buffer (recipe in appendix). 5 µl of 1kb GeneRuler ladder (Thermo Scientific) was loaded alongside as a reference and the gel run at 120V using a BioRad Power Pac 200. DNA bands were imaged on a GelDoc under UV light (Syngene InGenius). For sequencing, bands were excised quickly on a UV illuminator and purified with the Wizard® SV Gel and PCR Clean-Up System (promega) using the centrifugation protocol. DNA concentrations were measured using a nanodrop (NanoDrop Lite spectrophotometer) and sent to Source Biosciences for Sanger sequencing.

2.2.13 RNA extraction

RNA was extracted from wandering third instar larvae (3IL) in an RNAase-free area using sterile filter pipette tips. Five larvae were placed into individual autoclaved 1.5ml Eppendorf tubes and RNA was extracted following the TRIzol® Reagent (life technologies) protocol, homogenising in 0.5ml of TRIzol using a sterile micropestle. Homogenised samples were centrifuged at 12,000 x g at 4 °C for 10 min and the subsequent clear supernatant was transferred into a new tube.

	Primer name	**Sequence**
gRNA 1 oligonucleotides	Sense Strand (FP1) Reverse Strand (RP1)	gtcgCGGCGGGCAAACTCCATAAT aaacATTATGGAGTTTGCCCGCCG
gRNA 2 oligonucleotides	Sense Strand (FP2) Reverse Strand (RP2)	gtcgTTCACATGCGTAACGACGGC aaacGCCGTCGTTACGCATGTGAAC
Sequencing gRNA 1	CRISPR seq FP1 CRISPR Seq RP1	ACCTACTCAGCCAAGAGGC TGCATACGACTTAAGCGAAC
Gibson's assembly 5' and 3' fragments	5' CYFP2_pDB896	ccgtcgtcCTTGAAGAAGATTGTCCTCTC caacgcgttgggagctGACGTTCTGTACGAACCTTATC
	3' CYFP2_AI_FP 3'	acaatcttcttcaagGACGACGGCAATTACAAG ctatagggcgaattgggccGCAATATTCGCCGAGCTG
Artificial intron screening	CLN7 KO confirm FP CLN7 Positive	CCATCGCAGCCAACCAACCCA GTGGGGCAACAAGCTGGGCA
YFP::CLN7 fusion	CLN7 KO confirm FP CYFP_RP	CCATCGCAGCCAACCAACCCA GCCGGCAGCTGTCACGAACT
	CYFP2_FP CLN7 Positive RP	TGGTGGAGTCCAGCTTGCGG GTGGGGCAACAAGCTGGGCA
***CLN7* primers**	CLN7 Positive FP CLN7 KO	CGGGTTGTCTGTCCCGCGTC CCAAGGCGGCAGCCACAGTT
	CLN7 KO confirm FP CLN7 Positive	CCATCGCAGCCAACCAACCCA GTGGGGCAACAAGCTGGGCA
	CLN7 qPCR FP CLN7 qPCR	GGCCTGGAGACGCTGGAGGA TTGTCCCAGCGGATTGGCGG

CLN7[84D] **screening**	31 bp (p-element) CG8596 rev2	CGACGGGACCACCTTATGTTATTTCATCATG GTGGTGGAGCGGATACCCAA
qPCR (TaqMan)	RpL32 housekeeping	RpL32 probe (Dm02151827_g1)
	CLN7	CLN7 Probe (Dm01840591_g1)

Table 2.2: List of primers

Samples were incubated on ice for 5 min to allow complete dissociation of the nucleoprotein complex. 100µl of chloroform was added to samples which was then vigorously shaken for 15 seconds, incubated at room temperature for 2-3 min and the centrifuged again at 12,000 x g for 15 min at 4 °C. 200µl of the upper aqueous phase (exclusively containing RNA) was transferred into sterile Eppendorf tubes. 250µl 100% isopropanol was added and incubated for 10 min at room temperature before centrifugation at 12,000 x g for 10 min at 4 °C forming an RNA pellet. The supernatant was removed and 500 µl of 70% Ethanol (EtOH) was added to wash the pellet. Samples were briefly vortexed and then centrifuged at 7,500 x g for 5min at 4 °C. The supernatant was removed and the RNA pellets were air dried for 5 min, resuspended in 30 µl nuclease free water and incubated at 60 °C for 10-15 min in a heating block. RNA yield and quality was quantified on a Nanodrop spectrometer. Some RNA was used for the subsequent DNase treatment while the remainder was stored at -80 °C.

2.2.14 DNase treatment and complimentary DNA synthesis

2000ng of RNA was treated with RQ1 RNase-Free DNase (promega) for 40 min in a 10µl reaction following the standard protocol. 1µl EDTA was added to stop the DNase reaction prior to heat inactivation by incubating at 65°C for 10 min. Samples were briefly spun to collect condensation to the bottom of the tube. 10µl was used for the complimentary DNA (cDNA) synthesis reaction using the SensiFAST™ cDNA Synthesis Kit (Bioline) in a 20µl reaction volume in RNase free PCR tubes (Star lab) following the given protocol. The following program was used in a thermal cycler for first strand synthesis: 10 min at 25 °C (primer annealing), 60 min at 42 °C

(reverse transcription), 5 min at 85 °C (termination) and held at 4 °C. Samples were moved into a new 1.5ml Eppendorf tube and 40µl of nuclease free water was added to make a total volume of 60µl (50ng/µl). cDNA was either kept on ice and used immediately or stored at -20 °C.

2.2.15 Reverse transcription PCR

Reverse transcription PCR (RT-PCR) was carried out similar to PCR (Section 2.2.11) but using intron-spanning primers. This was used to check for successful removal of the artificial intron via Gibson cloning assembly and was confirmed via Sanger sequencing.

2.2.16 Quantitative PCR

Quantitative PCR (qPCR) was used to measure *CLN7* transcription levels in CRISPR generated YFP::CLN7 knock-ins. TaqMan probes (Applied Biosystems) for *CLN7* and *RpL32* as the housekeeping gene (Table 2.2) was used with all steps being carried out on ice. Each 20µl reaction mix contained 10µl TaqMan Universal PCR Master Mix (2X), 1µl TaqMan probes (20X) and 6.5µl nuclease free H_2O for each TaqMan man probe. Reaction mixes was pipetted into an optical 96 well plate and 3.5µl of cDNA template (final concentration of 8.75 ng/µl) was added with nuclease free water being substituted in as a negative control for each probe. The plate was sealed with an optical adhesive cover, spun at 4,000 x g for 30 s The qPCR was carried out in the Bio-Rad iQ5 using the following settings: 2 min at 50 °C (UNG incubation), 10 min at 95 °C (Polymerase activation) followed by 40 cycles of 15 secs at 95 °C and 1 min elongation at 60 °C using the FAM dye. Each

experiment was done in duplicates using 3 samples per genotype and 3 biological and 2 technical repeats were carried out per experiment. The standard delta-delta method was used to analyse the data (Livak and Schmittgen, 2001).

2.3 Biochemistry

2.3.1 Protein sample preparation

Ten early Third instar larvae were homogenised with a Konte pestle in 240µl RIPA buffer (Thermo Scientific), 3 µl protease inhibitors and 15 µl phosphatase inhibitors and left on ice for 10 min. Samples were centrifuged at 12,000 x g for 5 min at 4 °C. 200 µl supernatant was aspirated into a new tube and 40 µl 6x SDS loading buffer was added, mixed and boiled at 100 °C for 5 min. Samples were directly loaded into SDS-PAGE gels or stored at -20 °C.

2.3.2 SDS-PAGE

Proteins were separated by SDS-PAGE using a 12% separating gels. Frozen samples were heated for 5 min at 60 °C and 15µl of each sample was loaded into wells alongside 5µl PageRuler Plus Prestained Protein Ladder (Thermo Scientific) ladder. Samples were run at 70V for 10 min through the 6% stacking gel and then at 150V for 100 min through the separating gel in 1x running buffer (Geneflow) gel in an electrophoresis tank (Bio-Rad Laboratories). Gels underwent western blotting (continued in section 2.3.3) or a coomassie staining (Expedeon) to confirm successful running of protein sample.

2.3.3 Western Blotting

After samples were separated by SDS-PAGE, the separating gel was equilibrated in transfer buffer for 5 min, placed into a cassette sandwich consisting of sponges, filter papers and a MeOH activated-PDVF membrane. Proteins were transferred to the membrane by electrophoretic transfer at 0.4 amps for 90 min at 4 °C in 1x transfer buffer (GeneFlow) supplemented with 10% methanol. Ponceau S solution (Sigma) was used to confirm successful transfer of proteins and rinsed with excess running water. The membrane was blocked in 5% w/v dried skimmed milk (Marvel) in TBST (Recipe in appendix) for 60 min at room temperature to block nonspecific binding. Membranes were cut in between the expected sizes of the protein of interest and housekeeping protein. They were then incubated in their respective primary antibodies diluted in 1.5% milk in TBST overnight at 4 °C or 1 hour at room temperature. Rabbit-α-p62 was used 1:1,000 to detect p62 (*Drosophila* Ref (2) P) and was kindly provided by Dr Gabor Juhasz (Takats et al., 2013). The loading control, Mouse-α-actin IgM was diluted 1:20,000 and obtained from the Developmental Studies Hydridoma Bank (clone JLA20). Membranes were rinsed 2 times in TBST followed by 4x15 min washes, incubated in HRP-conjugated secondary antibodies diluted in 1.5% milk in TBST for 1 hour at room temperature followed by a similar washing regime. All steps from blocking to washing of secondary antibodies were done on a rotating platform. Bands were stained for 5 min with the SuperSignal West Pico Plus Chemiluminescence Substrate (ECL) kit (Thermo Scientific) as per instructions and then visualised on a Vilber Fusion Fx imager.

2.4 Histological

2.4.1 Larval NMJ fillet preparation and staining

Wandering third instar larvae was dissected in HL3.1 medium (Feng et al., 2004) (recipe in appendix) using a dissecting microscope. Larvae were left on cold HL3.1 on ice for 3 min to cold anesthetise them before using pins to immobilise and fillet them on sylgard dishes. Larvae were fixed in 4% methanol-free EM grade formaldehyde (Polysciences) in HL3.1 for 20 min at room temperature. Tissues were washed several times in HL3.1 then permeabilsed and washed with PBSTx (PBS containing 0.3% Triton X-100). Samples were blocked in 1% BSA in PBS/0.3% TritonX with 0.02% sodium azide for 30 min at room temperature. Samples were then incubated in primary antibody diluted in block overnight at 4 ^{o}C which included Alexa-488 Phalloidin (1:400, ThermoFisher) when staining of the plasma membrane was desired. Samples were rinsed twice followed by 3x15 min washes before incubation in secondary antibody diluted in block for 2 hours at room temperature. Samples were then washed a further twice rapidly followed by 3 x 15 min washes before mounting samples in Prolong Gold (Invitrogen). Samples were stored in the dark at 4 ^{o}C. All steps from blocking to secondary antibody washes were performed on a 360° nutator. A list of primary antibodies, suppliers and dilutions used are provided in table 2.3.

2.4.2 Larval tissue dissection and staining

The larval CNS was isolated by holding the larvae with a pair of forceps and then slowing pulling the mouth hooks away from the body with another pair of forceps. All other tissues were removed after dissecting the larvae. The salivary glands and

Malpighian tubules were permeabilsed and washed with PBST (PBS containing 0.1% Tween-20) and blocked in 1% BSA in PBS/0.1% Tween with 0.02% sodium azide as TritonX detergent was too strong. All others tissues used 0.3% TritonX and all subsequent fixation and staining steps followed NMJ staining procedure (section 2.4.1). Tissues were mounted in VectaShield (Vector Laboratories) using bridged slides to prevent samples being squashed.

2.5 Drosophila assays

2.5.1 Live autofluorescence build-up

Newly eclosed w^{1118} controls and *CLN7* mutant adult flies were collected and termed as day 0. Equal numbers of flies were kept per genotype with a maximum of 10 per vial. Flies were aged to 28 days of age in a 29 °C incubator on a 12 hour light/dark cycle on standard food. Flies were anathesised on a CO_2 pad. Flies were pinned in the abdomen on a sylgard dish with a dissecting pin and submerged PBS. The adult brain was carefully dissected using two fine pairs of forceps. The casing of the head was peeled off slowly in order to keep the lamina attached to the brain. The brains with the photoreceptors and lamina neurons attached were imaged immediately in PBS (all images taken within 1 hour of dissection) on an inverted Zeiss LSM780 confocal using excitation at 594 nm. Mutants were imaged first and then same settings were then used to image w^{1118} controls.

1° Antibody	Species	Dilution	Supplier (clone or product)
GFP (recognises Venus-YFP)	Rabbit	1:4000	AbCam (ab290)
Alexa-594 α-HRP	Goat	1:400	Jackson ImmunoResearch (123-585-021)
Elav	Rat	1:25	Developmental Studies Hybridoma Bank (7E8A10)
REPO	Mouse	1:5	DSHB (8D12)
Wrapper	Mouse	1:5	Dr Alicia Hidalgo, DSHB (10D3)
Prospero	Mouse	1:250	Dr Alicia Hidalgo, DSHB (MR1A)
Discs large (dlg)	Mouse	1:5	DSHB (4F3)
Na$^+$K$^+$ ATPase α-subunit	Mouse	1:5	DSHB (A5)
pMAD	Mouse	1:500	Professor Carl-Henrik Heldin (Uppsala)

Table 2.3: Details of primary antibodies used for Immunofluorescence microscopy

2.5.2 Autophagy assay

Accumulation of the *Drosophila* p62 homologue Ref(2)P (Takats et al., 2013) was quantified by western blot of total protein lysates from fed or starved 3IL instar stage larvae. *w^1118* control, *CLN7* mutants, and *atg18/*(Df(3L)Exel6112) (positive control) were used. 20 larvae 24-48 hph (hours post hatching) per genotype was transferred to fresh food supplemented with yeast paste. 24 hours later, protein samples were prepared from 10 larvae (fed state) (Section 2.3.1) and 10 larvae were removed from the food, rinsed twice in PBS and then transferred to 20% sucrose in PBS for 4 hrs (starved) before being protein prepped. Western blots were carried out on samples as described above (Section 2.3.3).

2.5.3 Phototaxis assay

A light dark arena was created by covering half of a 10 cm diameter petri dish lid and bottom with black duct tape and verified using a light meter. 25ml of 3% agar in ddH$_2$O was added and let to set at room temperature the night before. The following day, 30 early third instar larvae (72-96 hph) was removed from standard food, rinsed twice in water to remove attached food, blotted dry on tissue, transferred onto the agar dish and allowed to acclimatise for 5-10 min. The LED light source was placed approximately 15 to 20 cm above the dish to give uniform lighting, and calibrated to 550 lux using a light meter. After acclimatisation, larvae were lined up at the light dark border, covered with the lid and left under the light source in a dark area.

The number of larvae in the light half was manually counted every 30 sec for a total of 11 min. This was repeated 3 times per genotype and the mean was taken. This

was repeated 2 times per genotype. The light/dark index was calculated using: (number of larvae in the light – number of larvae in the dark) / total number of larvae. w^{1118} controls were used first, followed by the *CLN7* mutants. Assays were carried out between 9am and 5pm and fresh arenas were made each day. The room temperature was measured using a digital thermometer at 20.5-21 °C and was not affected by the light source.

2.5.4 Electroretinogram (ERGs)

ERG and SSVEP analysis was performed with the help of Dr. Chris Elliot (University of York). For ERGs, flies were reared at 29 °C in constant darkness. ERGs were carried out on 3 and 21 day old flies. A non-anesthetised fly was sucked into a trimmed p1000 pipette tip, and then blown into a trimmed p200 pipette tip. The fly was gently blown until only its head protruded from the tip and was fixed with nail varnish. The fly was placed into the ERG setup, and micromanipulators were used to place a recording electrode on one eye and the reference electrode on the proboscis. Each electrode contained *Drosophila* saline (130mM NaCl, 4.7mM KCl, 1.9mM $CaCl_2$). The fly was allowed to acclimatise to the dark for 2 min before undergoing ERGs. Blue LED light with 5 pulsed stimuli 8 seconds apart was used. The SSVEP (below) response was then recorded from the same fly.

2.5.5 Steady state visually evoked potential (SSVEP)

SSVEP was immediately carried out after Flash ERGs on the same fly. This measured responses to randomised contrast stimuli ranging from 0 to 69% and was done in the presence of a 30% contrast mask. Responses were measured at both

12 Hz and 15 Hz per fly. Data from flies not responding or producing background at 50 Hz were discarded.

2.6 Image acquisition and analysis

2.6.1 Neuromuscular junction quantification

The neuronal plasma membrane with Alexa-594 goat anti-HRP (Jackson ImmunoResearch) and active zones with mouse anti-Bruchpilot (nc82) of filleted wandering 3IL were stained. Type Ib boutons from muscle 4 on segments A3-A4 were manually counted at 40x using a widefield fluorescence microscope (Zeiss AxioScope). Then a lower 10x magnification image of muscle 4 was taken along with a graticle. ImageJ was used to quantify the muscle surface area (MSA) and then the absolute bouton number was normalised to MSA (Bouton number/MSA) (Figure 2.2). Boutons were counted double blinded.

2.6.2 Microscopy imaging

Images were acquired on a Zeiss LSM780 confocal using at 25x (LD LCI Plan-NEOFLUAR, water (W), 0.8 numerical aperture (NA)), 40x (C-ACHROMATIC, W, 1.2NA) and 63x (C-ACHROMAT, W, 1.2NA) or the LSM510 Meta confocal microscopes at 25x (LCI Plan-NEOFLUAR, W, 0.8NA) and 40x (C-ACHROMATIC, W, 1.2NA). Images were taken as z-stacks (z step sizes specified in results) and the LSM780 was used to tile scan and stich images when required. Images were optimised using Zen (Zeiss), Photoshop CS6 (Adobe) and Volocity (Perkin Elmer) software packages.
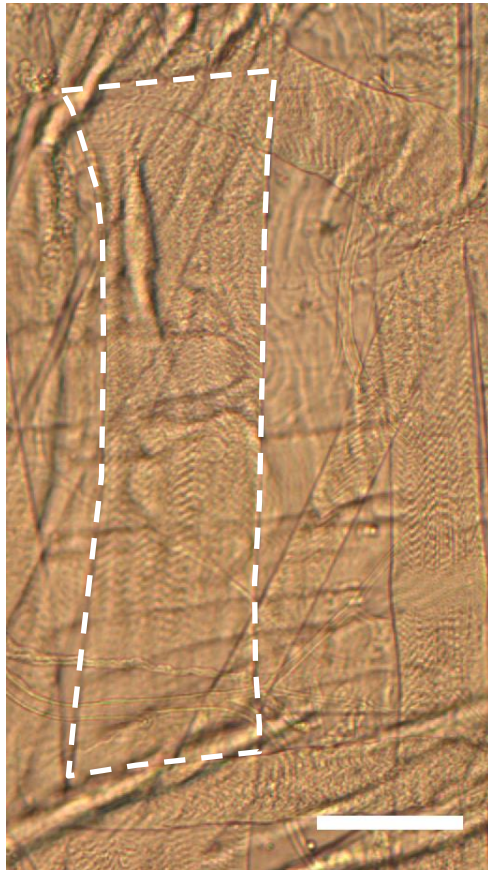
Figure 2.2: Quantification of boutons and muscle surface area. A bright field image showing several muscle walls from a region of the larval abdominal segment. Type Ib boutons were quantified from muscle 4 and normalised to its muscle surface area (dashed lines) using ImageJ. Scale bar = 100 μm.

2.6.3 Western blot analysis - Quantification of autophagy

Accumulation of the *Drosophila* p62 homologue Ref(2)P was quantified from western blots of total protein lysates from fed or starved mid-third instar stage larvae (section 2.4.2). Anti-p62 (Takats et al., 2013) pixel intensity was normalised to actin levels using anti-actin IgM (DSHB clone JLA20) from three biological replicates. Band Intensities were quantified on ImageJ by subtracting the mean pixel intensity from the surrounding background. P62 bands were normalised to its respective actin bands (loading control) and then compared relative to other genotypes. Standard errors were generated from three biological replicates.

2.6.4 Statistical analysis

GraphPad Prism 7 was used to perform statistical tests. Each group was tested for normality using the D'Agostino-Pearson omnibus normality test and parametric or non-parametric tests where then performed as appropriate. Unpaired t-tests (parametric) or Mann-Whitney tests (non-parametric) were used when comparing two groups and one way ANOVA (parametric) followed by Tukeys posthoc or Kruskal-Wallis test (non-parametric) followed by Dunns test posthoc was used when comparing more than two groups. Statistical significance was set as follows: non-significant (N.S) = $p>0.05$, * = $p<0.05$, ** = $p<0.01$, *** = $P<0.001$ and **** = $P<0.0001$.

2.7 Appendix

Name	Recipe
PBS buffer	137mM $NaCl_2$, 2.7mM KCl, 10mM Na_2HPO_4 and 1.8mM KH_2PO_4
TBS buffer	50 mM Tris-HCl, 150 mM NaCl, pH 7.6
TBST	TBS, 0.1% v/v Tween 20
SDS loading buffer	100 mM Tris-Cl (pH 6.8), 4% (w/v) SDS (sodium dodecyl sulfate), 0.2% (w/v) bromophenol blue, 20% (v/v) glycerol and 200 mM β-mercaptoethanol
TAE	40 mM Tris---HCl, 20 mM acetic acid, and 1mM EDTA
Squishing buffer	10 mM Tris-HCl pH8, 1 mM EDTA and 25 mM NaCl + 200μg/ml of fresh proteinase K (PK)
HL3.1	70mM NaCl, 5mM KCl, 20mM $MgCl_2$, 10mM $NaHCO_3$, 5mM trehalose, 115mM sucrose, 5mM HEPES, pH 7.3, 1.5mM $CaCl_2$.

Table 2.4: List of reagent recipes

3. GENOME EDITING OF *DROSOPHILA CLN7* USING THE CRISPR-CAS9 SYSTEM

Data presented in this chapter have been published in (Mohammed et al., 2017)

3.1.1 Introduction

Mutations in *CLN7/MFSD8* are responsible for a variant of late-infantile NCL (Siintola et al., 2007). Forty unique mutations, primarily resulting in missense mutations, have been identified from studies using 91 CLN7 diseased patients spanning 73 families (UCL – NCL mutation database) but how these mutations lead to disease and the function CLN7 remains unknown. One method to try elucidate functions of genes is the use of model organisms. I used *Drosophila melanogaster*, a well-established model organism particularly suited for monogenic human diseases, to examine the functions of CLN7. *Drosophila* is predicted to contain a single homologue of *CLN7* (Flybase, encoded by *CG8596*) with 3 possible annotated transcripts of the gene, each producing a protein with identical AA sequences. *Drosophila* CLN7 shares 56% amino acid sequence homology with human CLN7 and is predicted to contain a major facilitator superfamily domain (MFSD) (Muzaffar and Pearce, 2008), a conserved family of transporters that facilitate movement of small molecules across plasma membranes (Yan, 2013). However, the function or potential substrates CLN7 may transport remains unknown. Neurodevelopmental defects have been identified in *CLN7* null mutant *Drosophila* (O'Hare, Submitted), which will be discussed further in chapter 5, however how loss of *CLN7* results in these phenotypes remains unknown. Studying

the localisation pattern of CLN7 would help uncover potential functions but attempts to visualise endogenous CLN7 *in vivo* by generating antibodies against *Drosophila* CLN7 have proved unsuccessful (O'Hare, 2012). In this chapter, I used the CRISPR/Cas9 genome editing technique to generate a YFP-tagged CLN7 knock-in to overcome the need for antibodies against the poorly antigenic transmembrane protein to ultimately carry out the first *in vivo* localisation study of CLN7.

3.1.2 Advancements in genome editing

The discovery of natural transposable elements such as P-elements led the generation of semi-random mutations but the elements preferentially inserted in particular genomic regions. Subsequent to the completion of the *Drosophila* genome, the first method for specific genome editing was developed which utilised homologous recombination. However, this was limited by the very low efficiency. The discovery of introducing double strand breaks (DSBs) to substantially increase the efficacy advanced genome editing leading to the rise of nuclease-based editing techniques such as zinc finger nucleases (ZFNs) and transcription activator-like effector nucleases (TALENs). These contain non-specific chimeric nucleases bound to sequence specific DNA binding domains and require proteins to be redesigned for each new target. Further advancements occurred with the rise of Clustered Regulatory Interspaced Short Palindromic Repeats (CRISPR) (Ren et al., 2017). This technique promised bespoke genome editing at much higher efficiencies.

The CRISPR genome editing system was simplified from the immune system of *Streptococcus pyogenes* into two components, a Cas9 endonuclease and a

chimeric guide RNA (gRNA) (Jinek et al., 2012). The gRNA is made up of two domains, the trans-activating domain and a 20nt gRNA sequence which interacts with and guides Cas9 to the target sequence respectively. Cas9 can induce DSBs upstream of a protospacer adjacent motif (PAM), which contains a NGG motif. In contrast to ZFNs and TALENs, where new proteins have to be designed for each new target, CRISPR can target a new sequence readily by changing the 20nt gRNA sequence (Gupta and Musunuru, 2014).

In this chapter I utilised *Drosophila* Cas9 expressing transgenic lines in combination with gRNAs to fuse a YFP sequence into *CLN7* gene to generate a YFP-CLN7 fusion protein. This would allow a novel *in-vivo* localisation pattern of CLN7 to be examined to help uncover potential functions. Secondly, I attempted to generate a precise full length *CLN7* gene deletion using two gRNAs simultaneously.
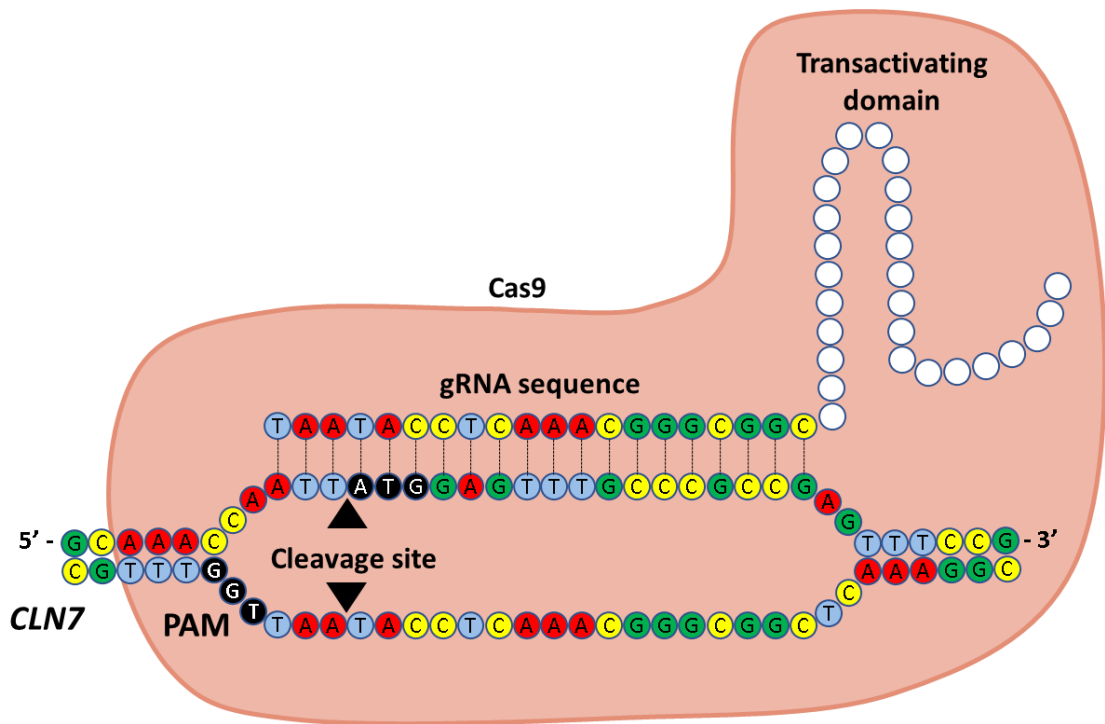
Figure 3.1: Schematic of CRISPR/Cas9 system. CRISPR is made up of two components, a Cas9 endonuclease and a guide RNA (gRNA). The gRNA has two domains, a 20nt gRNA sequence which guides Cas9 to the target DNA sequence and a transactivating domain that binds and activates Cas9. Cas9 induce DSBs between the third and forth base upstream of a NGG protospacer adjacent motif (PAM – depicted by arrowheads). gRNA1 was designed to cleave 5' of the ATG start codon of *CLN7*.

3.2 Results

3.2.1 Developing the CRISPR genome editing technique

To investigate the expression pattern and localisation of *Drosophila* CLN7, I developed and utilised the highly efficient genome editing technique, CRISPR/Cas9, to tag the N-terminus of the transmembrane protein, with YFP. This would allow me to determine the localisation of CLN7 *in vivo,* overcoming the need for antibodies against the poorly antigenic transmembrane protein. CRISPR would be used to insert a YFP sequence into the *CLN7* gene by HDR. Additionally, I planned to use the CRISPR system to generate a novel *CLN7* mutant via gene deletion in order to determine roles of CLN7 in neurodevelopment.

3.2.2 Designing the gRNAs

CLN7 is a putative lysosomal transmembrane protein with 12 membrane-spanning domains. It was therefore important to decide carefully where to tag the protein with YFP. I decided to tag the N-terminus of the protein which was predicted to be in the cytosol rather than intra-lumenal. The FlyCRISPR tool was used to generate a list of potential gRNA target sites of the *Drosophila CGC8596* gene, the homolog of mammalian *CLN7,* along with their potential off-target effects. Two gRNAs were designed: gRNA1 targeting the *CLN7* ATG start codon and gRNA2 targeting towards the end of the translating exon region. The gRNAs would guide the Cas9 nuclease towards these specific target sequence and induce DSBs. gRNA1 was used to generate a DSB immediately 3' of the ATG start codon and activate the DNA repair mechanism which can occur through NHEJ or HDR pathways. A template was also provided to take advantage of the HDR pathway to precisely insert the

YFP sequence into the 5' end of the CLN7 protein, generating a N-terminal YFP-CLN7 fusion protein. A combination of gRNA1 and gRNA2 was used in an attempt to generate a full gene deletion (section 3.2.8). The simultaneous DSBs at either ends of the *CLN7* would result in the removal of sequences in-between the two gRNAs.

The FlyCRISPR tool was used to design unmodified oligonucleotides, sense and anti-sense, with BbsI restriction sites for each gRNA (see table of primers 2.2). The 5' end of the oligos were phosphorylated with a T4 DNA kinase and then annealed to one another. The annealed oligos were then ligated into a BbsI-digested pCFD3 plasmid (Figure 3.2) and then sequenced to confirm successful ligation. The pCFD3 plasmid is ampicillin resistant and allows the expression of a single gRNA under a polymerase III dependant U6:3 promoter, the strongest U6 promoter in *Drosophila*.

Seven individual colonies were screened for the uptake of the gRNA contain pCFD3 plasmid via colony PCR (Figure 3.3). Colony PCR confirmed six out of seven colonies successfully incorporated the ligated plasmid with DNA being extracted and purified from two successful transformations, confirmed via sequencing and then diluted to 1000 ng/µl in ddH$_2$0. To complement the gRNA and utilise the specific genome editing capabilities of the CRISPR system I also designed a HDR template.
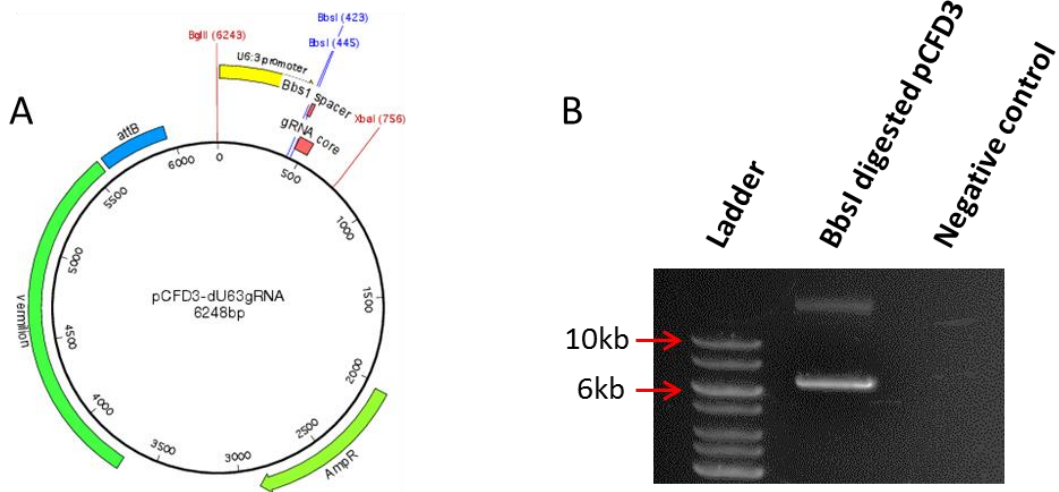
Figure 3.2: BbsI digestion. A – Schematic of pCFD3 plasmid containing BbsI restriction sites between the U6:3 promoter and gRNA core. B - The pCFD3 plasmid was digested and linearised by the BbsI enzyme. The lower band represents a linear plasmid (6248bp) and the higher band represents undigested supercoiled DNA. Schematic taken from http://www.crisprflydesign.org/plasmids/.
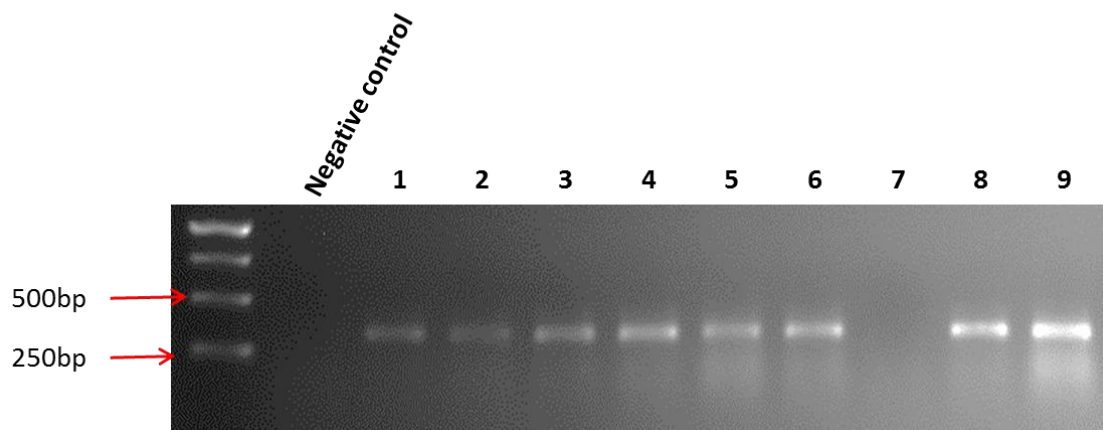
Figure 3.3: Colony PCR of pCFD3 and gRNA. Nine individual colonies were screened for the successful transformation of ligated gRNA and plasmid. PCR using a primer within the plasmid along a gRNA oligonucleotide as a primer confirmed 8/9 ligated transformations was successful.

3.2.3 Designing homology directed repair (HDR) template

The site of DSB induced by the gRNA guided Cas9 occurs between the third and forth base upstream of the PAM sequence and the HDR template was subsequently designed around the DSB site. The template included a Venus variant of YFP spilt with an artificial intron (taken from the *Drosophila white* gene) to reduce what would have been a very large first *YFP-CLN7* exon of 1108 bp (Figure 3.4b). The YFP sequence included a 5' FLAG-tag epitope, and a 3' short linker sequence to allow correct independent folding of the YFP and CLN7 proteins. 500bp homology arms were added to either side of the template, corresponding to either side of DSB site. The template sequence was insect codon-optimised using a GenScript algorithm to maximise expression, synthesised by GenScript and cloned by them into a pUC57 vector.

The HDR vector, containing an ampicillin resistance gene, was transformed into competent bacterial cells and grown on a carbenicillin LB agar plates. Several individual colonies were screened for the uptake of the vector by colony PCR and then sequenced after DNA extraction to ensure the *YFP-CLN7* gene was correctly aligned. DNA from a successfully sequenced colony was then extracted and purified on a larger scale via maxiprep and diluted to 1000 ng/μl.

3.2.4 Removal of the artificial intron

The purified HDR template contained an artificial intron within the YFP sequence to produce a smaller first *YFP-CLN7* exon. To measure the effects of the artificial intron on transcription and the CRISPR system, the artificial intron was also
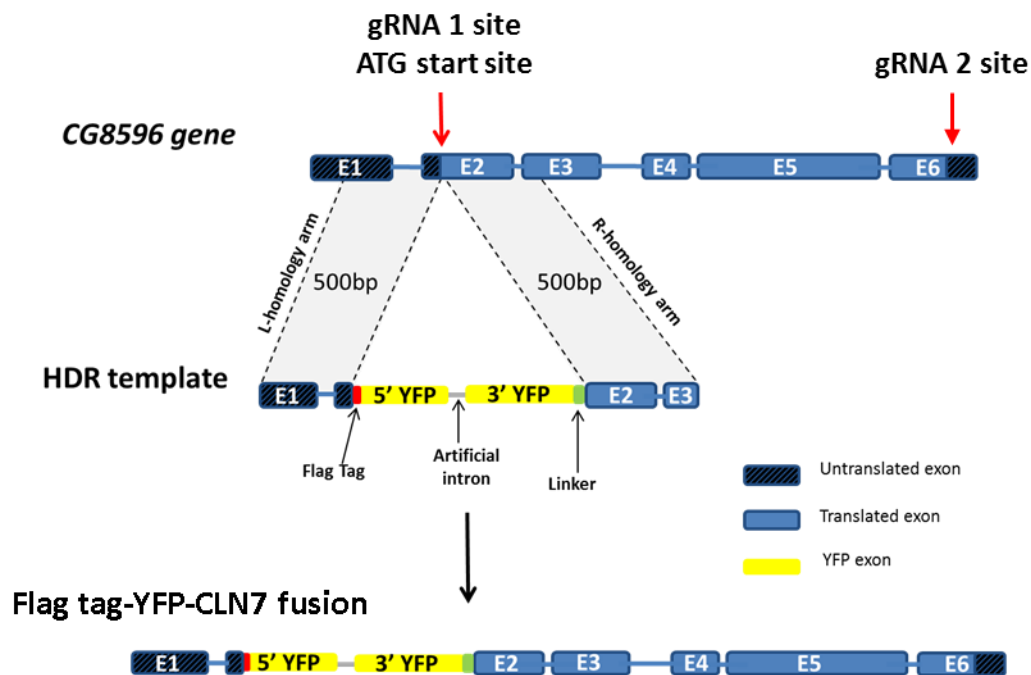
Figure 3.4a: Generation of a YFP-CLN7 by homology-directed repair. The HDR template consists of: a 5'Flag Tag, a Venus YFP sequence spilt with an artificial intron, a linker sequence and is surrounded by homology arms of 500bp corresponding to either sides of the gRNA 1 target site. The gRNA 1 can transport the cas9 nuclease to its target site resulting in a DSB. DSB repair mechanisms recognises the homology arms within the HDR template and uses it for HDR repair, copying the Flag Tag-YFP sequence into the gene. gRNA 1 and gRNA 2 were used to try generate a full gene deletion.

removed from the template using Gibson cloning. Two PCR fragments, 5' and 3' of the artificial intron, was generated from the HDR template (Figure 3.4b). Each fragment contained overlapping ends of approximately 20 bases aligning to the adjacent fragment and vector. The two fragments were ligated with the ampicillin resistant vector and transformed into competent bacteria. They were screened in similar fashion to the original HDR template: by colony PCR, miniprep (Figure 3.5) and sequenced to ensure the artificial intron was successfully removed. A maxiprep was also carried out and the template was diluted to 1000 ng/µl.

3.2.5 Embryo injections

The gRNA and template were mixed in a 250:750 ng/µl ratio respectively before being injected into Cas9-expressing *Drosophila* embryos. The mixtures (with or without the artificial intron) were injected into vasa::Cas9 and nanos::Cas9 embryos respectively (Gratz et al., 2014). The vasa::Cas9 and nanos::Cas9 lines localise the Cas9 nuclease to the presumptive gonad-forming region at the posterior of the embryo using vasa regulatory elements and a nanos promoter with a 3'UTR respectively. Once injected into embryos, the Cas9 nuclease would be guided to the *CLN7* gene by the gRNA where it would induce a DSB at the ATG start codon. The DSB repair mechanism would then use the provided HDR template for specific repair resulting in the incorporation of YFP into the start of the *CLN7* gene (Figure 3.3). Approximately 200 embryos were injected with each
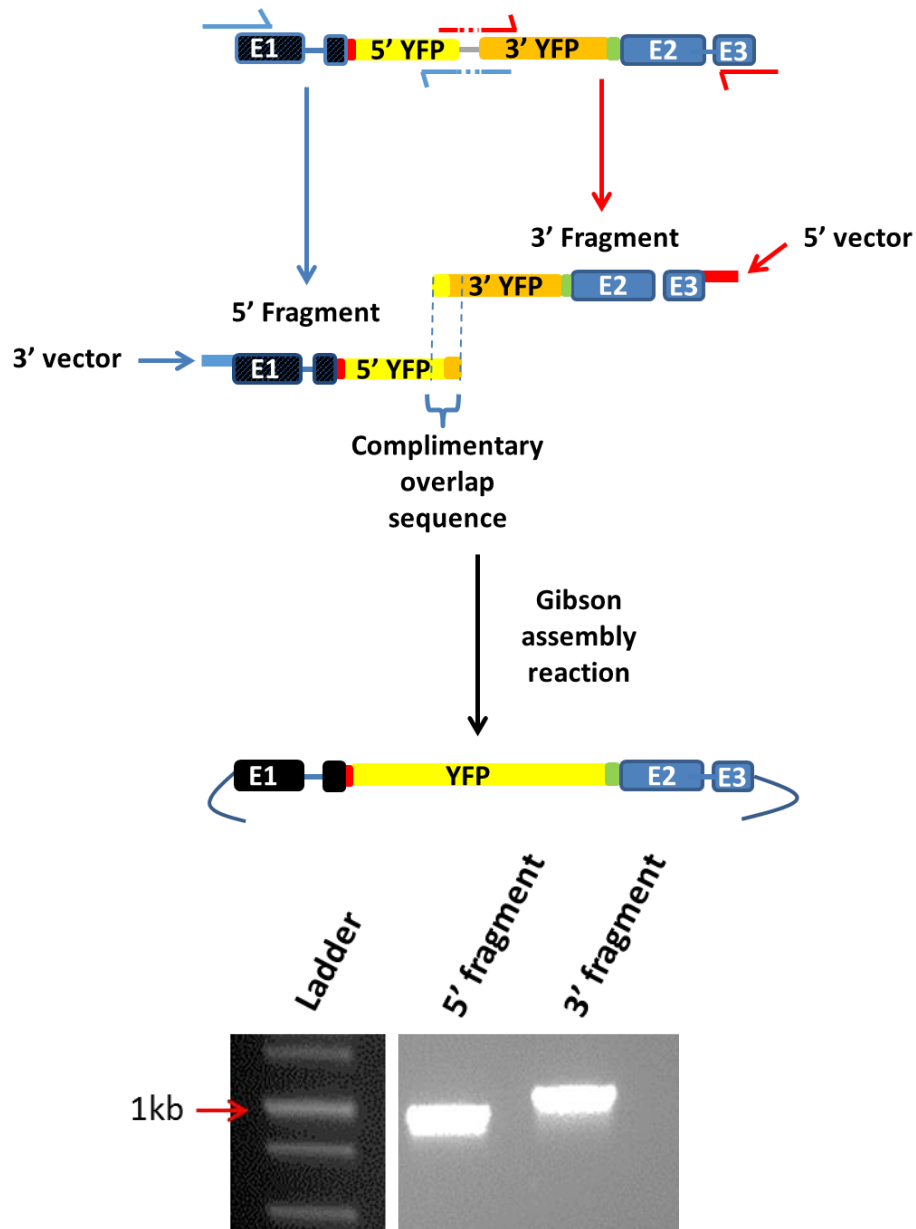
Figure 3.4b: PCR amplification of 5' and 3' fragments for Gibson cloning. A) Schematic of the 5' and 3' fragments amplified from YFP-CLN7 template (with artificial intron). Pair of primers (single headed arrows) are shown above and below the template. B) Gel electrophoresis of the amplified 5' (830bp) and 3' (905bp) fragments.
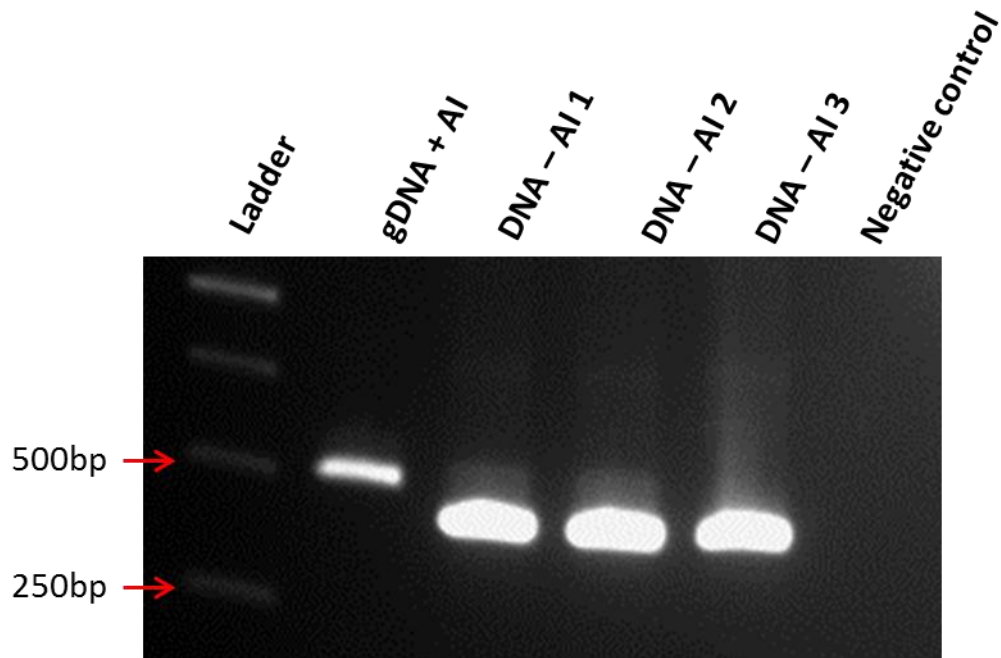
Figure 3.5: Removal of artificial intron Gibson cloning. DNA amplified across the AI of 3 Gibson cloned cultures (minus AI – 453bp) was smaller than gDNA including the AI (527bp). This shows successful removal of the AI.

mixture of gRNA and template. The insertion of Cas9 in the vasa::Cas9 and nanos::Cas9 lines were marked with 3xP3-GFP and 3xP3-RFP respectively on the X chromosome resulting in the expression of GFP/RFP in the CNS, intestine and anal plates of larvae and the eyes of adults. In order to screen for positive YFP-CLN7 expression the 3xP3-GFP and 3xP3-RFP markers had to be removed by via a crossing scheme. Embryos surviving and eclosing to adult flies were collected as either males or virgin females and then individually mated to a third chromosome balancer strain to propagate the transgenic chromosome (Figure 2.1). Vasa injected lines were crossed to the Dr, hs-hid/TM6B,Tb,Hu balancer on a white background, while nanos injected lines were crossed to the MKRS,Sb/TM6B,Tb,Hu balancer on a vermillion background.

3.2.6 PCR screening

Following the crossing scheme described in chapter 2 (Figure 2.1), genomic DNA (gDNA) was prepared from each injected parent. DNA was amplified using a set of primers across YFP to select for successful insertion of YFP. A set of control primers within the *CLN7* gene was also used as a PCR control and the success of gDNA preparation. PCR confirmed 74% (n=27) of the vasa-Cas9 embryos injected with HDR including the artificial intron had potentially incorporated the HDR template into the *CLN7* gene (Figure 3.6). One of the negative controls produced an unexpected band, however this band was smaller than an expected positive screen and was thought to be due to non-specific priming. PCR of 62 of the progeny from 8 different potential lines indicated a 60% transmission rate of the germline event. Additional attempts were made to tag CLN7 C-terminal using
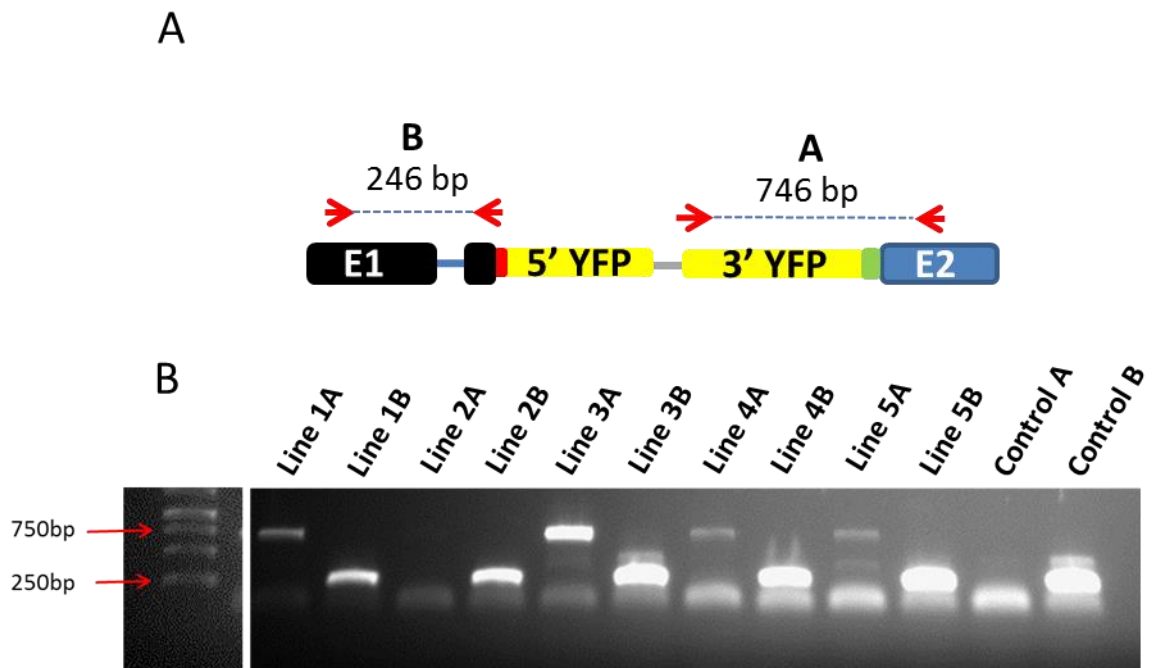
Figure 3.6: Screening of successful CRISPR event. A) Schematic of YFP-CLN7. Primer set A had a primers going from YFP into the *CLN7* gene while control primer set B were in the *CLN7* gene. B) Flies which incorporated the YFP-CLN7 sequence produced a band of 746 bp using primer set A while unsuccessful CRISPR events produced no band. Primer set B was used as a control producing a band of 246 bp in all flies.

gRNA2 and a newly designed C-terminal template, however PCR screening was unsuccessful.

The same process was carried out in 9 nanos::Cas9 lines injected with the HDR templated lacking the artificial intron. PCR confirmed 89% of injected line lines incorporated YFP into the *CLN7* gene. PCR from 20 progeny from 4 YFP positive lines indicated a 95% transmission rate of the germline event into the next generation. Two independent homozygous lines were generated and the P3-RFP marker removed by crossing.

Homozygous larvae from both templates were screened for YFP under a fluorescence dissection microscope but no obvious fluorescence was seen. To ensure that the band produced by PCR (Figure 3.7) was from successful incorporation of the HDR template into the *CLN7* gene, fresh preparations of gDNA from two independent homozygous lines was made and sequenced. Sanger sequencing indicated correct HDR and incorporation of Flag-YFP into the locus. The reasons for the lack of fluorescence were not clear at this stage but were attributed at this point to the low endogenous levels of *CLN7* expression (Flybase). Another possibility considered was that the artificial intron was being incorrectly spliced in the first template leading to a frame shift and truncated protein. The latter is less likely cause as the fluorescence was not seen in the line without an artificial intron but still warranted investigation. These were investigated by RT-PCR to check for transcription and correct splicing.
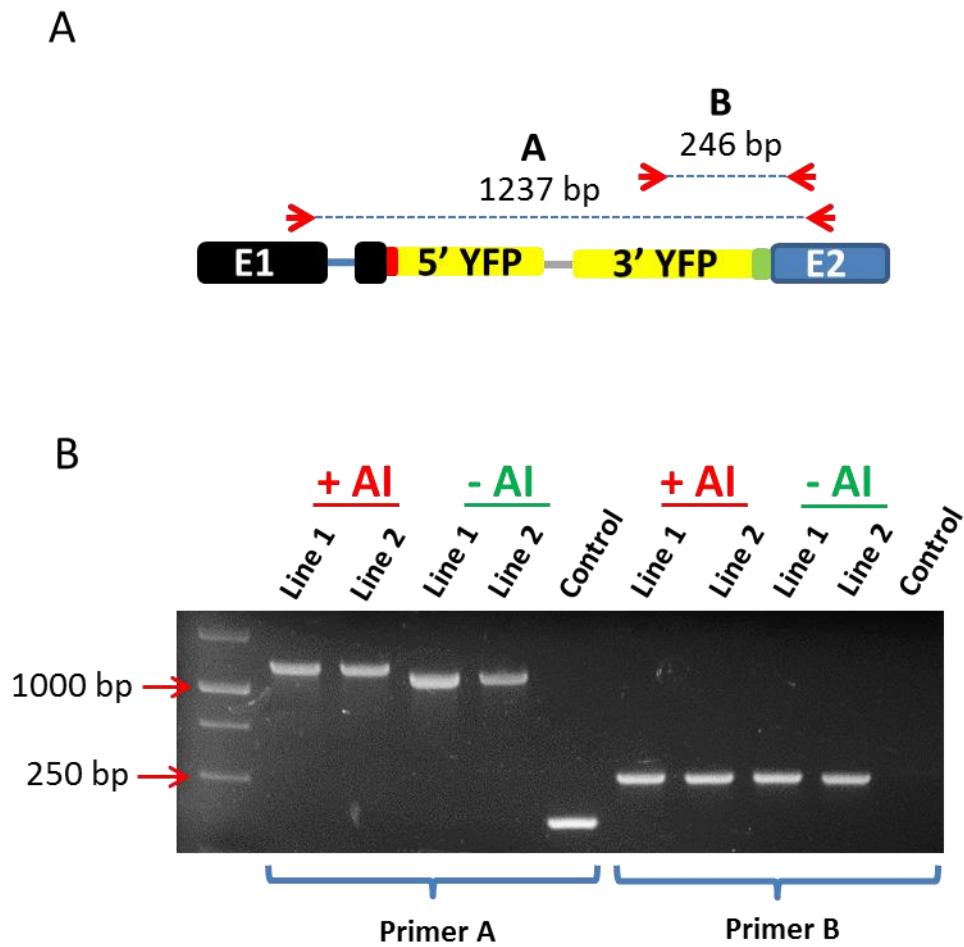
Figure 3.7: PCR screening of homozygous CRISPR lines. A) Schematic of YFP-CLN7. Primer set A spanned the YFP sequence while primer set B had a forward and reverse primer in YFP and *CLN7* respectively. B) Flies which incorporated the YFP-CLN7 sequence produced a band at 1237bp (with AI) or 1163 bp (without AI) using primer set A. Control flies lacking the insertion produced a band of 172 bp. Flies which had YFP-CLN7 produced a band 246bp, while the control flies did not produce a band.

3.2.7 Quantitative PCR of CRISPR lines

To determine if the *YFP-CLN7* gene was being transcribed, mRNA was extracted from adult flies in the 2 independent lines containing the artificial intron. RT-PCR was performed using random hexamer primers to generate cDNA. The YFP sequence was amplified across the artificial intron with intron spanning primers in gDNA and cDNA providing a readout at a genomic and transcriptional level respectively. This was done to firstly see if *YFP-CLN7* was being transcribed: this would be detectable by the presence of bands after cDNA amplification. Secondly, I would be able to compare the size of the PCR products in gDNA *vs.* cDNA to determine if the artificial intron (74bp) had been spliced out correctly in the mRNA (and the cDNA copy). gDNA from both lines with the artificial intron produced a larger band (527bp) when compared to cDNA (453bp) which splices out the artificial intron (Figure 3.8). This suggest the YFP-CLN7 gene was being expressed in the flies, and the artificial intron was spliced out. The successful splicing event was confirmed by Sanger sequencing of the purified cDNA fragment which ensured the gene correctly spliced.

PCR amplification of cDNA and gDNA showed the *CLN7* gene was being expressed in the knock-in, however, did not indicate the level of transcription. To quantify the level of transcripts, cDNA was made from 2 lines with and without the artificial intron along with their w^{1118} and v^1 controls respectively. A qPCR was carried out using intron-spanning TaqMan probes. *Drosophila* has 3 annotated transcripts of *CLN7* (http://flybase.org/reports/FBgn0035767.html). A probe was used to amplify across exons 3 and 4 in two transcripts (CLN7-A and CLN7-C) and
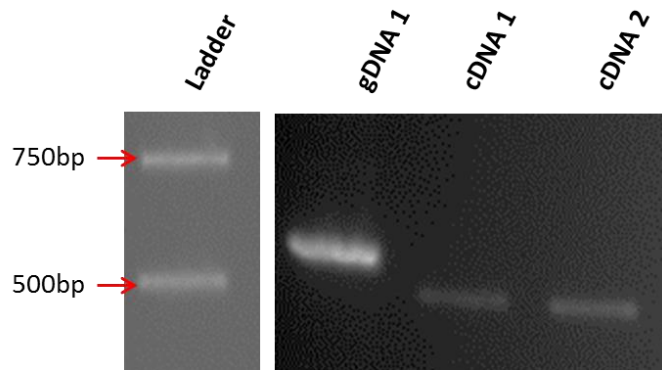
Figure 3.8: Artificial intron is correctly spliced out. Sizes of gDNA and cDNA were compared across the AI. cDNA bands (453bp) were smaller than gDNA (527bp) suggesting the AI was spliced during transcription.
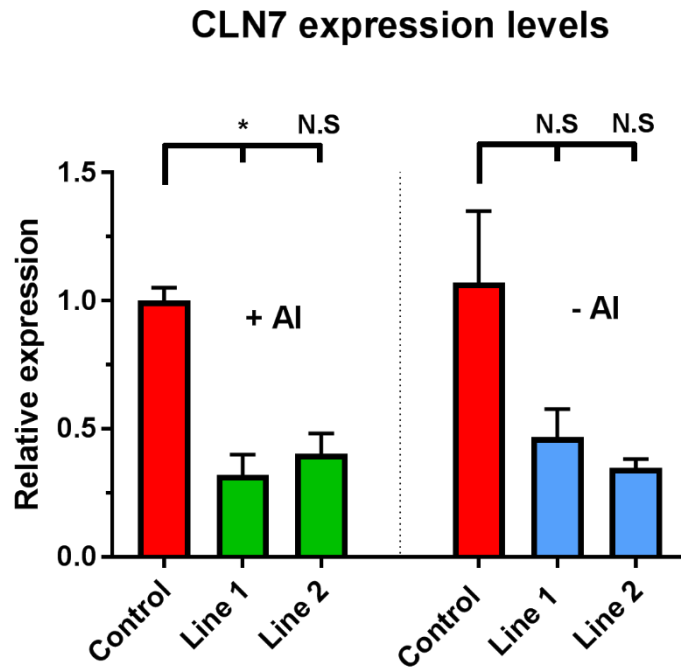
Figure 3.9: *CLN7* expression level of CRISPR generated YFP-CLN7. Quantitative PCR (qPCR) of two independent YFP-CLN7 lines with and without an artificial intron (AI) showed reduced expression *CLN7.* The CRISPR generated lines had approximately 30-40% expression relative to its control. A significant reduction was seen in Line 1 (p=0.0341) with an AI but not with Line 2 (p=0.2021). A similar reduction was seen with the removal of the AI, but was not significant for Line 1 (p=0.1473) or Line 2 (p=0.0507) compared to its control. Error bars represent standard deviation (n=3).

exons 2 and 3 (CLN7-B). A probe for the *RpL32* gene was used as a housekeeping control. qPCR analysis showed lines from both templates expressed *CLN7* at approximately 30-40% of the level of their respective controls (Figure 3.9). However this was only significantly lowered for Line 1 including an AI but not for the other 3 Lines compared to their respective controls. The lack of significance is likely due to the low number of repeats (n=3) with additional repeats most likely to make the data significant. This indicates that the presence of an artificial intron does not have a major impact on expression levels of *YFP-CLN7* and that the knock-in was affecting *CLN7* transcription. This may be the reason why YFP-CLN7 is undetectable under a fluorescence dissection microscope, but more likely due to the already low level endogenous expression of *CLN7*. However, I have demonstrated the high efficiency of using CRISPR for genome editing in *Drosophila* and will now attempt to generate a full length *CLN7* deletion with CRISPR.

3.2.8 Generation of the *CLN7* gene deletion

Reverse genetics, where a specific gene is disrupted and the resulting phenotypes are observed and measured is a powerful technique to study the function of genes. The CRISPR system has provided a highly efficient method to carry out reverse genetics. Here I planned to utilise CRISPR to try and generate a novel *CLN7* deletion to study its function. To generate a gene deletion, vasa::Cas9 embryos were injected with an equimolar mix of gRNA1 (used previously to in HDR repair) and gRNA2. Both gRNAs acting together will induce simultaneous DSB breaks at 2 locations removing the internal DNA sequence to create a gene
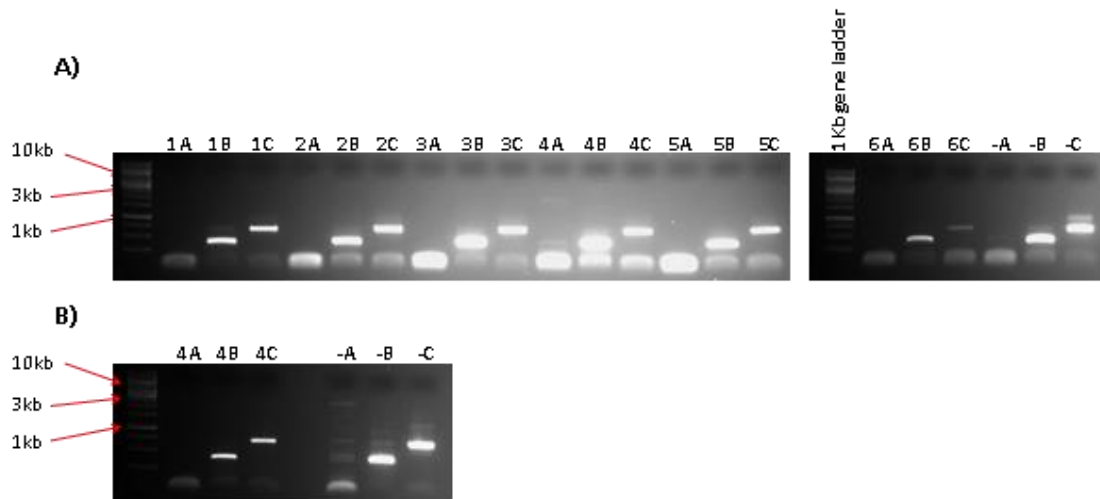
Figure 3.10: PCRs confirm unsuccessful *CLN7* deletion. gDNA was collectively made from a pool of 10 progenies produced from the cross between the injected parent and third chromosome balancer (Dr, Hs-Hid/TM6B, Tb, Hm). A: A further 6 injected flies were also prepped for gDNA. Each set of gDNA underwent a PCR reaction (64 °C annealing temperature) with 3 sets of primers: A) CLN7 KO FP + CLN7 KO RP, B) CLN7 KO FP + positive CLN7 RP and C) CLN7 KO RP + CLN7 positive FP. Control primer sets B and C produced the expected bands of 407 bp and 690 bp respectively. Reaction 3A produced a very faint band around 200 bp (Knockout band) and 2.7 kb (full primer length) for lane 4A. B: A second PCR was done using the same gDNA increasing the annealing temperature to 66 °C. This removed the faint bands seen at 64 °C but bands were still seen with primer sets B and C suggesting the KO was unsuccessful.

deletion. As before, surviving adult flies were then mated to a third chromosome balancer, gDNA was then prepared from each injected parent and PCRs of each gDNA was undertaken to identify successful gene deletion events (Figure 3.10). A single injected fly gDNA showed a potentially successful *CLN7* KO via a faint band, however this was also present in the negative controls. This individual prep was rerun at a higher annealing temperature for confirmation, however the bands were no longer present in the sample but persisted in the control sample suggesting the initial band was due to mispriming. As the CRISPR event would only occur in germline cells, the deletion event may have been difficult to detect in the injected parents. If *CLN7* was knocked out, the gene edit would have been passed on to some of their offspring. However, since the propagation of a gene deletion is dependent on the deletion event occurring in the germline and then being transmitted to the next generation, this was likely to be a relatively rare event and difficult to identify. Practically, it was impossible to PCR amplify gDNA from several thousand individual progenies in the F1 generation. Therefore, to try and determine if this event had occurred, groups of 20 gDNA preps was made, each from a pool of 10 F1 progeny from individual crosses. No collective prep showed a potential CLN7 KO band confirming that either the gene targeting strategy had been unsuccessful or that detection on the deletion was not possible by this method.

3.2.9 Random CLN7 indel detection

The successful generation of the HDR YFP-CLN7 fusion confirms the high efficiency of DSBs induced by gRNA1, which targets the ATG start codon. This suggests the unsuccessful event of generating a precise *CLN7* deletion was most likely due the

efficiency of gRNA2. Therefore, I screened flies for potential random mutations and indels around the ATG start site. gDNA amplified across the gRNA1 site were treated with T7 Endonuclease which recognises and cleaves mismatched DNA. The samples were then run on an agarose gel electrophoresis to look for multiple bands caused by a cleavage event. However, all samples produced a single product band indicating no mismatched DNA and random indels was present. This suggests no DSBs were induced by either gRNA in these lines.

3.3 Discussion

Mutations in the CLN7/MFSD8 gene cause late infantile NCL, an early onset neurodevelopmental disorder. To date, localisation studies of the transmembrane protein have been carried out using cell culture and overexpression assays. However, the function of CLN7 remains elusive. A single homologue of *CLN7* has been identified in *Drosophila* which may be used to help uncover potential functions of CLN7. Attempts to generate antibodies against the N-terminal and C-terminal regions of *Drosophila* CLN7 were made (Megan O'Hare, 2012) and were specific to the CLN7 protein when overexpressed, however, failed to detect low levels of endogenous CLN7. Here, I utilised the CRISPR genome editing system to create a method of studying the localisation of CLN7 at endogenous levels *in vivo*.

3.3.1 Efficiency of CRISPR system

The specificity and efficiency of genome editing has been greatly enhanced by the discovery and continual development of the CRISPR/Cas9 system. The use of transgenic cas9 flies have greatly increased the efficiency of CRISPR, which previously relied on co-injections of gRNA and Cas9 RNA or DNA producing variable results (Bassett et al., 2013, Gratz et al., 2013). In this study, I generated a YFP-CLN7 knock-in using both vasa::cas9 (with artificial intron) and nanos::cas9 (without artificial intron) transgenic flies. Vasa flies express cas9 in the germline cells and somatic cells while nanos flies predominate in the former. Both lines had a similar high rates of CRISPR events in injected embryos, and notably in the germline cells as depicted by their high transmission rate as previously reported (Port et al., 2014). This indicated the high efficiency of gRNA1 in inducing dsDNA breaks, and

the HDR repair mechanism in incorporating the template DNA into the *Drosophila* genome.

A second gRNA2 site was also targeted in order to try generate a full *CLN7* deletion. Two existing mutations for the CLN7 gene delete only a portion of the gene and, while unlikely, there is the possibility that residual function persists (O'Hare, Submitted). The function and the substrate being transported by the CLN7 protein remains unknown and this complete gene deletion would have given an opportunity to determine roles of the CLN7 protein without the possibility of residual function. However, co-injection of gRNA1 and gRNA2 failed to successfully generate a full gene deletion. The high level of success in generating the YFP-CLN7 knock-in using gRNA1 alone suggests gRNA2 may have a lower yield in producing dsDNA breaks. Using gRNA2 alone to attempt to generate a CLN7 fusion protein at the C-terminal was also unsuccessful. Therefore, the inability to generate a full-length deletion and C-terminal fusion may be attributed to the common factor, gRNA2, which may have been inefficient resulting in no dsDNA breaks, or at very low levels which were not detected. Due to the close proximity between the two gRNAs, differences in efficiencies is unlikely to be due to chromatin packaging which has been shown to impede efficiency *in vivo* and *in vitro* and is more likely related to the target sequence themselves (Horlbeck et al., 2016, Daer et al., 2017). Although the target sites of the gRNAs have been shown to have little effect on efficiency in *Drosophila*, with one study finding only 1 of 14 gRNAs (n=66) failing to induce dsDNA breaks. This was subsequently attributed to a single nucleotide polymorphism (SNP) in the gRNA

target site (Port et al., 2015). Sequencing of the gRNA2 target site in *vasa-cas9* flies being injected showed a lack of SNPs suggesting this was not the case with gRNA2.

The failure to detect dsDNA breaks at the gRNA1 site using the T7 endonuclease assay may have occurred due to the presence of two gRNAs. Inactive gRNAs (presumably gRNA2 in this instance) have been shown to compete with active gRNAs (gRNA1) to form complexes with cas9 (Thyme et al., 2016). This would result in decreased activity of the active gRNA. Although unlikely, as Cas9 should be abundant under a *vasa* promoter, this cannot be fully ruled out.

With the continual advancements in CRISPR, one way to potentially overcome detection of low efficiency may be to incorporate a 3xP3-dsRed eye reporter, which can be removed by ΦC31 recombinase-mediated cassette exchange (RMCE) after screening for red eyes (Venken et al., 2011, Zhang et al., 2014). This would increase the efficiency of screening process compared to relying on PCR based detection. This would allow thousands of flies to be screened more easily to detect low genome editing events and can be used for HDR or precise deletion using 2 gRNAs.

3.3.2 YFP-CLN7 knock-in

The YFP-CLN7 knock-in reporter overcomes the poorly antigenic nature of the putative lysosomal transmembrane protein and allows a localisation study of endogenous levels of CLN7 to be undertaken (chapter 4). As CLN7 is a putative lysosomal transporter, YFP was chosen to be inserted into the cytosolic side of the membrane to prevent quenching of YFP fluorescence by the low pH of the lysosome

and avoid potential artefacts (Shaner et al., 2005). Both the N-terminal and C-terminal regions of CLN7 are predicted to be on the cytoplasmic side making them ideal targets. However, the N–terminus was primarily chosen as previous work has shown tagging of a lysosomal transmembrane protein, CLN3, at the C-terminus resulted in retention of the fusion protein in the endoplasmic reticulum (ER)(Haskell et al., 1999).

A short linker separate was placed between YFP and the start of CLN7 to allow independent folding since direct tagging of the lysosomal protease, TPP1, with crmCherry resulted in a large proportion of TPP1-crmCherry localising outside of the lysosome, and with the addition of a linker improving lysosomal localisation (Huang et al., 2014). A 3x FLAG tag was directly fused to the N-terminal of YFP to provide an additional epitope for localisation studies, if needed. This could act as a second epitope to carry out a localisation study or used to detect protein-protein interactions via Tandem affinity purification (TAP) tag. The latter would be interesting as CLN7 has shown to form a complex with RHEB, a regulator of mTORC signalling, which has been implicated with phenotypes of mutants (O'Hare, Submitted).

3.3.3 Reduced expression of YFP-CLN7

PCR and sequencing confirmed the high efficiency and success of the CRISPR technique, however, even though the YFP sequence was placed under the endogenous *CLN7* promoter, qPCR suggested gene expression of the knock-in was dysregulated. Gene expression is regulated at many stages including, transcription

initiation, pre-mRNA splicing, mRNA stability, and chromatin packing. To initiate and complete RNA synthesis, a 5′ promoter element is found upstream of the transcription start site (Levine and Tjian, 2003). There are 3 annotated transcripts of the *CLN7* gene (CLN7-RA, RB and RC) in *Drosophila*. The insertion of the YFP at the *CLN7* start site may have disrupted the promoter element, or interfered with the binding of transcription factors in one or more of the transcripts resulting in the production and degradation of unstable mRNA. To determine if this is the cause, qPCR would have to be carried out to target each transcript using specifically designed primers.

Furthermore, an artificial intron was initially added to reduce what would have been a large first exon. This was done as the majority of exons in *Drosophila* are between 100-180 bp long, with only 15% of exons being longer than 550 bp (Hawkins, 1988). I was concerned that a large intron might effect expression. However, incorporating an artificial intron was shown to have no effect as firstly, it was spliced out correctly and secondly, flies which lacked the artificial intron exhibited a similar reduced expression level from the knock-in. This indicated another unknown mechanism was responsible for the reduced expression of *CLN7*. However, for the purpose of my studies, I would be able to utilise the YFP-CLN7 knock-in line to map CLN7 localisation *in vivo* (Chapter 4). I will also investigate whether low level expression of YFP-CLN7 has any functional consequences (Chapter 5).

4. *IN VIVO* LOCALISATION OF CLN7

Data presented in this chapter have been published in:

(Mohammed et al., 2017) and (O'Hare, Submitted)

4.1.1 Introduction

Patients with NCL disease present with symptoms including visual defects and psychomotor deterioration and are clinically characterised by the intralysosomal build-up of storage material (reviewed by Haltia, 2006). However, the cell biology behind CLN7, like the other NCLs, and why symptoms and pathology are restricted to the CNS irrespective of ubiquitous expression of the CLN proteins are not well understood. The CLN7 protein is predicted to contain twelve membrane spanning domains and shares homology with the MFSD family of transporters (Siintola et al., 2007). However, the function or potential substrates CLN7 may transport remains unknown. Proteomics using rat liver cells has identified CLN7 as a potential lysosomal transporter (Chapel et al., 2013) with GFP-tagged CLN7 protein in COS-1 and HeLa cells primarily localising to lysosomes (Siintola et al., 2007, Steenhuis et al., 2010, Sharifi et al., 2010).

4.1.2 Localisation of the CLN7 protein

Overexpression of GFP-CLN7 in a pan-neural pattern in *Drosophila* third instar larvae using the GAL4-UAS system (Brand and Perrimon, 1993) results in co-localisation with lysotracker, an acidic compartment marker, in the cell body of CNS neurons *in vivo*. Larval primary neuronal culture also showed GFP-CLN7 localises

in the soma and along the neuronal projections *ex-vivo* (O'Hare, 2012). However, this approach utilised ectopic overexpression of GFP-CLN7 in a pan-neuronal pattern which may have resulted in artefacts because of the high levels of expression of the transmembrane protein. Attempts to make antisera to CLN7 produced only non-specific antibodies so to overcome potential overexpression artefacts and the poor antigenic nature of CLN7, I generated an YFP::CLN7 knock-in by gene editing using the CRISPR/Cas9 system, as discussed in chapter 3, (Gokcezade et al., 2014, and reviewed by Bassett and Liu, 2014). In this chapter, I aimed to validate the YFP-CLN7 knock-in and use it to determine the localisation of pattern of CLN7 in various tissues in the fly, along with a *CLN7::RedStinger* promoter fusion construct generated as part of a collaboration in the laboratory of Prof. Guy Tear (KCL) (Figure 4.1). The *CLN7::RedStinger* line has the *CLN7* promoter fused to the fluorescent nuclear-localised RedStinger. This produces nuclear RedStinger protein expressed within tissues/cells that would normally express CLN7. The protein is strongly fluorescent and the signal is retained after fixation. The aim was to use the CLN7::RedStinger line as a method of confirming the localisation pattern seen with YFP-CLN7. Determining the localisation of CLN7 *in vivo* would give a better understanding of the functions and pathways CLN7 may be involved in.

From the *in-vivo* localisation study carried out using YFP-CLN7 knock-in I was able to determine that, unexpectedly, CLN7 was predominantly expressed in glial cells in the CNS, while neuronal expression was limited to regions of the developing visual system. My localisation study also showed CLN7 to localise to the

postsynaptic site at the developing NMJ. This reveals new ideas of how CLN7 may

function and regulate NMJ development.

A) YFP::Cln7
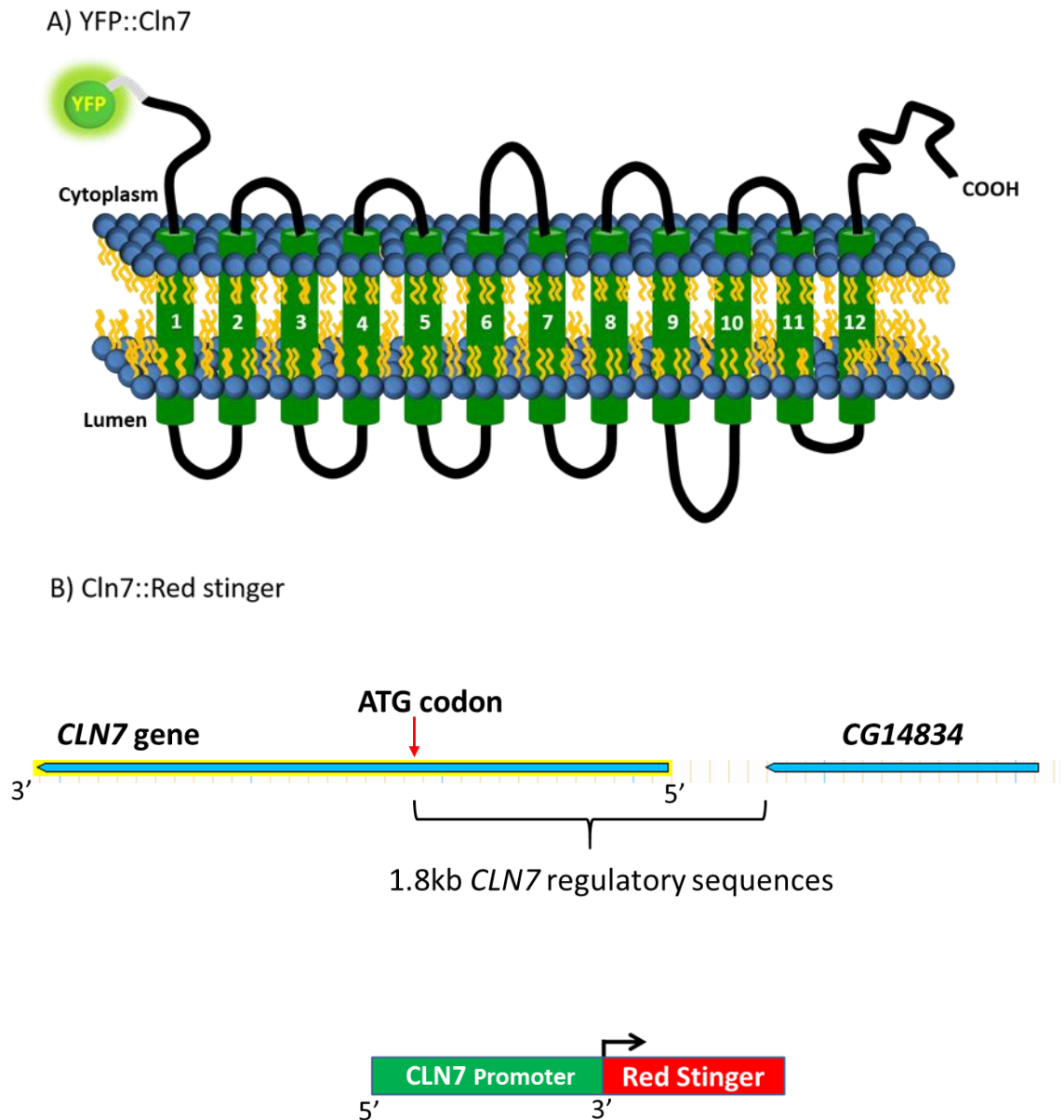
B) Cln7::Red stinger

Figure 4.1: Schematic of the YFP::CLN7 knock-in and CLN7::Red Stinger. A) Schematic of the topology of the CLN7 transmembrane protein. YFP was fused to the N-terminus via the CRISPR/Cas9 system. B) Schematic showing the 5' UTR regulatory sequence of *CLN7* (in-between *CLN7* and upstream gene) used to generate a CLN7::Red Stinger construct.

4.2 Results

4.2.1 Validation of YFP-CLN7 knock-in

Firstly, I validated the specificity anti-GFP in YFP-CLN7 *in vivo* using fixed larval tissues. Since pathologies of the NCLs are primarily restricted to the CNS, I examined expression of the *CLN7* construct in the nervous system of *Drosophila* third instar larvae. The third instar stage was used as various parallel studies have utilised this developmental stage to characterise neural development. Expression profiling of *CLN7* (encoded by *CG8596* in *Drosophila*) has suggested a low levels of *CLN7* transcripts in the larval nervous system (www.flyAtlas.org: (Chintapalli et al., 2007)).

The larval brain is made up of two main regions, the optic lobes and ventral nerve cord - the insect equivalent of the mammalian spinal cord. I dissected brains from YFP-CLN7 (containing the artificial intron) and control w^{1118} larvae, fixed them in 4% formaldehyde and carried out immunohistological staining using an anti-GFP antibody, which also recognises the YFP variant. Optical sections of the larval nervous system imaged by confocal microscopy showed YFP-*CLN7* along the edges of the nervous system (Figure 4.2). 3D rendering of the sections showed *CLN7* was expressed in cells ensheathing the whole nervous system. Additional staining was found along the midline of the VNC. In contrast, only residual background staining was visualised in w^{1118} controls across the whole tissue, indicating specificity of the anti-GFP antibody for YFP-CLN7 (Figure 4.2). This confirmed the YFP-CLN7 fusion was a success and able to maintain its
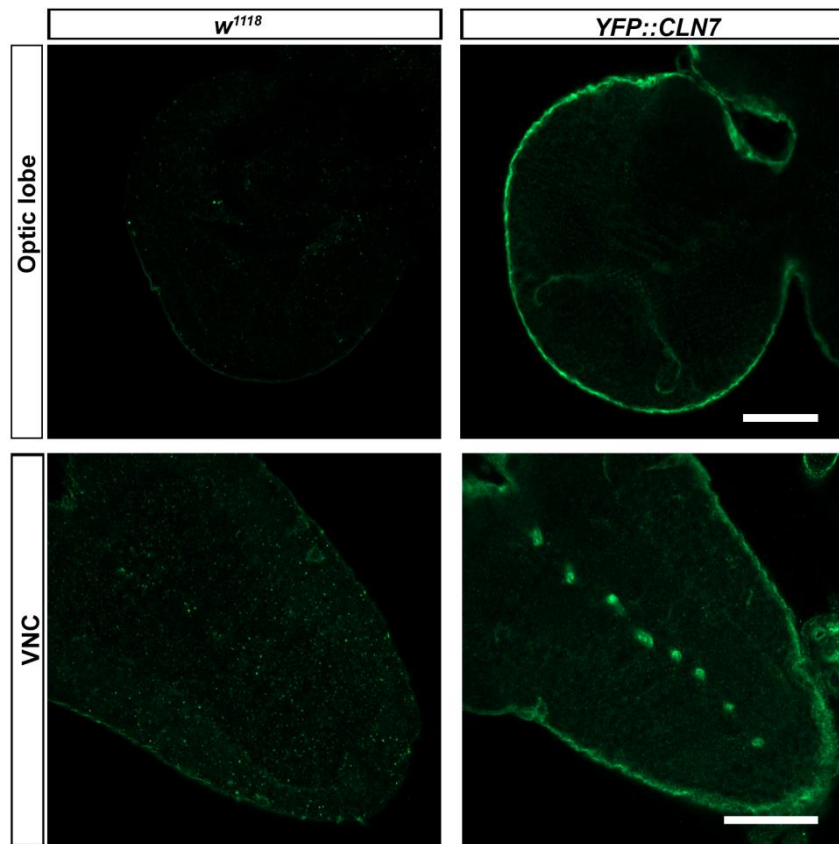
Figure 4.2: Anti-GFP specificity in YFP-CLN7 fusions. The optic lobe and ventral nerve cord (VNC) of third instar larvae were stained for GFP. Staining's between *w¹¹¹⁸* and *YFP::CLN7* lines show anti-GFP was staining specifically for YFP::CLN7. Scale bar = 50 µm.

epitopes. In addition, previous work in the lab which has been replicated in this thesis has shown re-expression of an YFP-CLN7 fused protein is able to fully rescue the mutant phenotype, which indicates the fluorescent protein is able to fold correctly. This validated the use of YFP-CLN7 and subsequently can be used to carry-out a thorough localisation study of CLN7 *in vivo*. Importantly, potential artefacts was avoided as the transmembrane protein was not overexpressed. The next step would be to identify the cell types that CLN7 is expressed in by counterstaining with different markers.

4.2.2 *in vivo* CLN7 localisation

4.2.2.1 CLN7 is expressed in glia that form the blood-brain-barrier

The larval nervous system is made up different types of cells including: neurons, glial cells, and neuronal/glial progenitor cells. To determine which cells were expressing CLN7, the nervous system was first counterstained with a pan glial marker, anti-REPO, which stains all glial cells except the midline glia. The YFP-CLN7 expression pattern overlapped with REPO staining along the surface of the nervous system suggesting CLN7 is expressed by surface glia (figure 4.3). The surface glia forms the blood-brain-barrier (BBB) in *Drosophila* and are analogous to the function of endothelial cells that form the vertebrate BBB. Two REPO positive nuclei were also found to localise and sit directly above the midline YFP-CLN7 staining in the VNC (Figure 4.3B – dotted box). This suggested these CLN7 expressing cells were channel glia, which are also a component of the BBB (Ito et al., 1995). To ensure the midline pattern was actually in channel glia and not
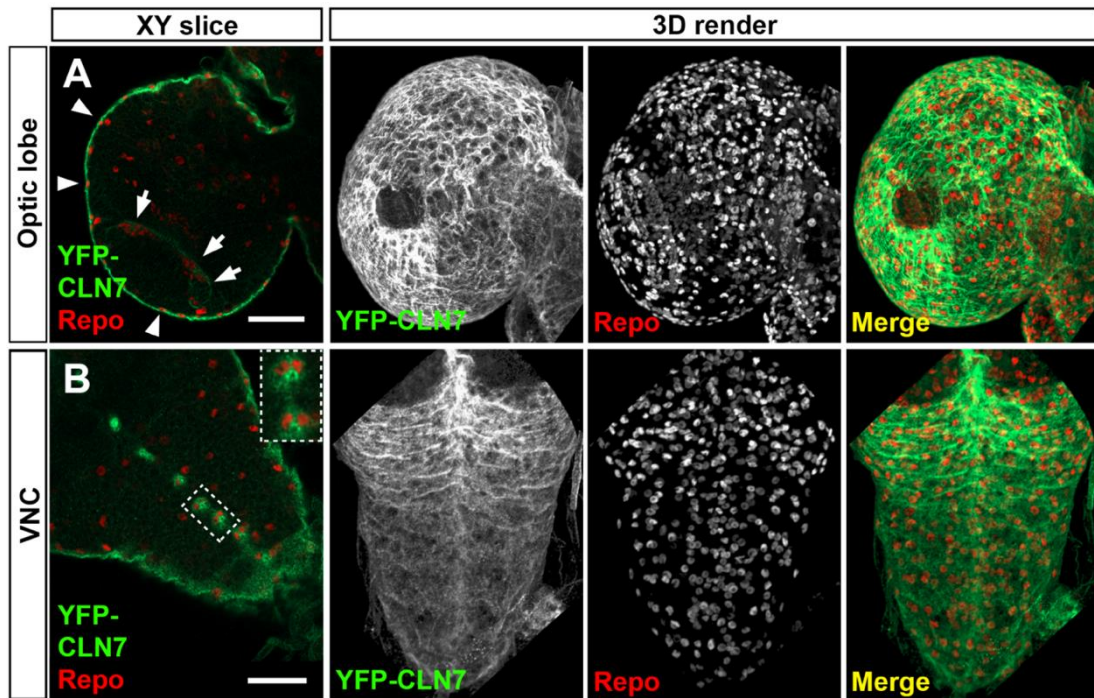
Figure 4.3: YFP::CLN7 is expressed by a subset of glia in the CNS. Cross sectional image of the optic lobe (A) and ventral nerve chord (VNC – B) and their corresponding 3D rendered image. A: Nuclear glial staining (red), stained with anti-REPO, are surrounded by YFP::CLN7 (green) in the optic lobe (arrows). CLN7 is expressed at the surface glia ensheathing the CNS in 3D rendered images. B: CLN7 is expressed in channel glia in the VNC, visualised by a pair of nuclear REPO markers (enlargement shown in dotted box). This indicates Cln7 expression is localised to a subset of glia. 50 µm scale shown. 3D rendered imaged have been rotated and do not include a scale bar.

midline glia, I additionally counterstained midline glia, which do not express REPO, with anti-Wrapper (Figure 4.4). YFP-CLN7 was found to be expressed in cells along the midline in an alternating pattern with midline glia. This confirmed the lack of CLN7 expression in midline glia as they stained different cell structures and indicated CLN7 was expressed by channel glia.

The larval CNS was also counterstained with the pan-neuronal marker, anti-Elav (post mitotic) and neural and glial precursor marker, anti-Prospero. A small subset of neurons in the optic lobes localised with YFP-CLN7 corresponding to lamina neurons (Figure 4.5A – dotted box) which form part of the developing visual system in flies. The neuronal staining on the edge of the nervous system was surrounded by YFP-CLN7 staining on the outer side, suggesting these are surface glia ensheathing the nervous system. No other cells were shown to express CLN7 in the larval CNS. Staining with Prospero suggested CLN7 was not expressed by any neuroblasts (Figure 4.6).

4.2.2 *CLN7::RedStinger* promoter fusion validates knock-in localisation

To verify the findings of the YFP-CLN7 localisation experiments, I used an alternative approach to reveal *CLN7* expressing cells. A *CLN7::RedStinger* promoter construct was generated in the group of Prof. Guy Tear (KCL) by fusing approximately 1.8 kb of *CLN7* gene regulatory sequences, found upstream of the *CLN7* start codon, to a fluorescent nuclear-localised RedStinger reporter (Barolo et al., 2004). This results in nuclear RedStinger expression in CLN7 expressing cells. The line had not been characterised before this study.
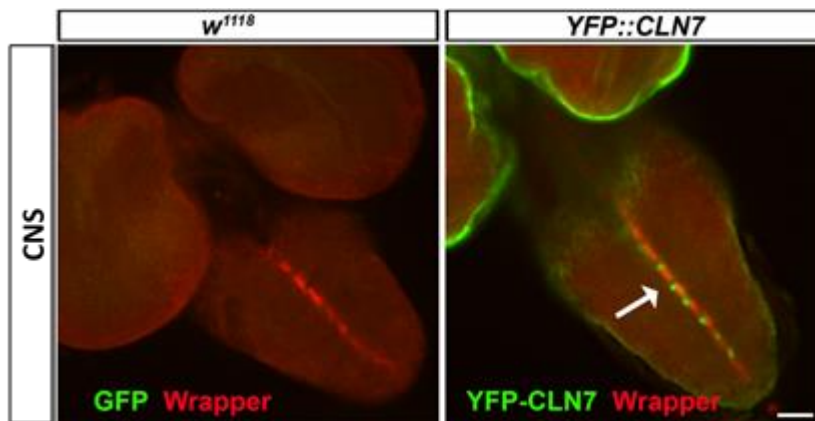
Figure 4.4: CLN7 is not expressed in midline glia. Larval CNS was stained for YFP-CLN7 (green) and midline glia with anti-Wrapper (Red). YFP-CLN7 did not co-localise with midline glia and was expressed in between midline glia cells (arrow). Scale bar = 25 μm.
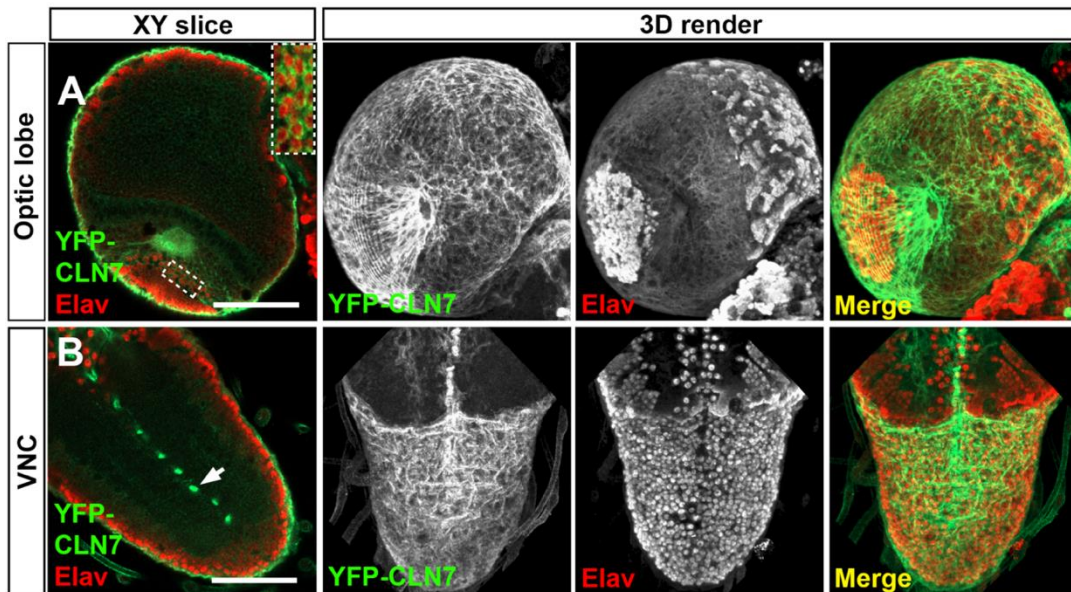
Figure 4.5: YFP::CLN7 is expressed in lamina neurons. Cross sectional image of the optic lobe (A) and ventral nerve chord (VNC – B) and their corresponding 3D rendered image. YFP-CLN7 (green) counterstained with the post-mitotic neuronal marker, anti-Elav (red), shows CLN7 is expressed in lamina neurons in the optic lobe (enlargement shown in box in A). CLN7 expressing cells surround the neuronal surface staining, indicating these are the surface glia. 50 µm scale shown. 3D rendered images have been rotated using Volocity and do not include a scale bar.
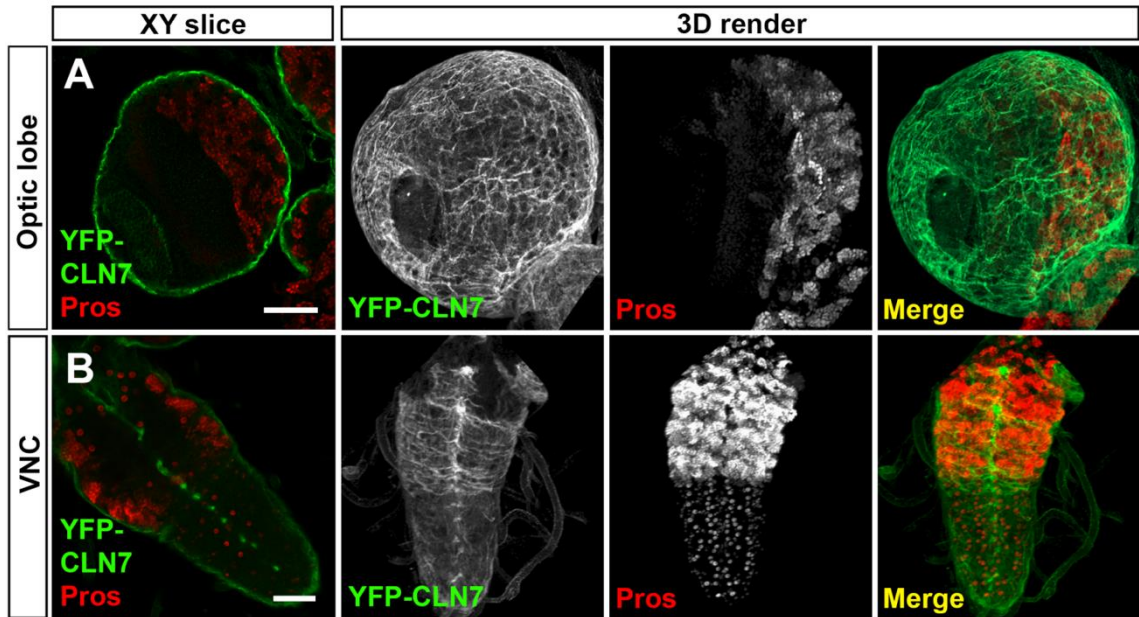
**Figure 4.6: YFP::CLN7 is not expressed in neuroblasts.** Cross sectional image of the optic lobe (A) and ventral nerve chord (VNC – B) and their corresponding 3D rendered image. YFP-CLN7 (green) counterstained with the neuroblast marker, prospero (red), shows CLN7 is not expressed in neuroblasts. Scale bar = 50 µm. 3D rendered images have been rotated using Volocity and do not include a scale bar.

Within the CNS, *CLN7::RedStinger* was predominantly expressed at the surface. This matched staining pattern of YFP-*CLN7*. However, additional cells were stained in the VNC which were not present in the knock-in line. CNSs were counterstained with anti-REPO which indicated that the peripheral RedStinger positive cells were glial cells (Figure 4.7), and therefore corresponded to surface glia. The insect BBB is made up of two glial cells, the apical perineurial glia and basal sub-perineurial glial cells. These can be distinguished by the size and shape of the nucleus, the morphology of the cells and their spatial positioning in the CNS. *CLN7::RedStinger* expression was limited to the perineurial glia, found on the apical side of the CNS and characterised by smaller oblong nuclei (Figure 4.7A'' – dotted box), but was absent from the more basal sub-perineurial glia which have larger circular nuclei. (Awasaki et al., 2008). *CLN7::RedStinger* also co-localised with anti-REPO along the midline of the VNC, supporting my finding of expression of CLN7 in channel glia (Figure 4.7B'' – dotted box).

Co-staining the *CLN7::RedStinger* lines with anti-Elav revealed no co-localisation (Figure 4.8) in any cells. This confirmed the lack of neuronal expression in the larval CNS of the YFP::CLN7 line. Some differences between the two CLN7 lines can be explained by the somewhat arbitrary length of the *CLN7* promoter sequence used to generate *CLN7::RedStinger*. 1.8kb of 5'UTR was included (corresponding to the interval between *CLN7* and the upstream gene) but presumably other regulatory sequences are absent leading to expression in other glia. In combination, my *YFP-CLN7* knock-in and the *CLN7::RedStinger* reporter
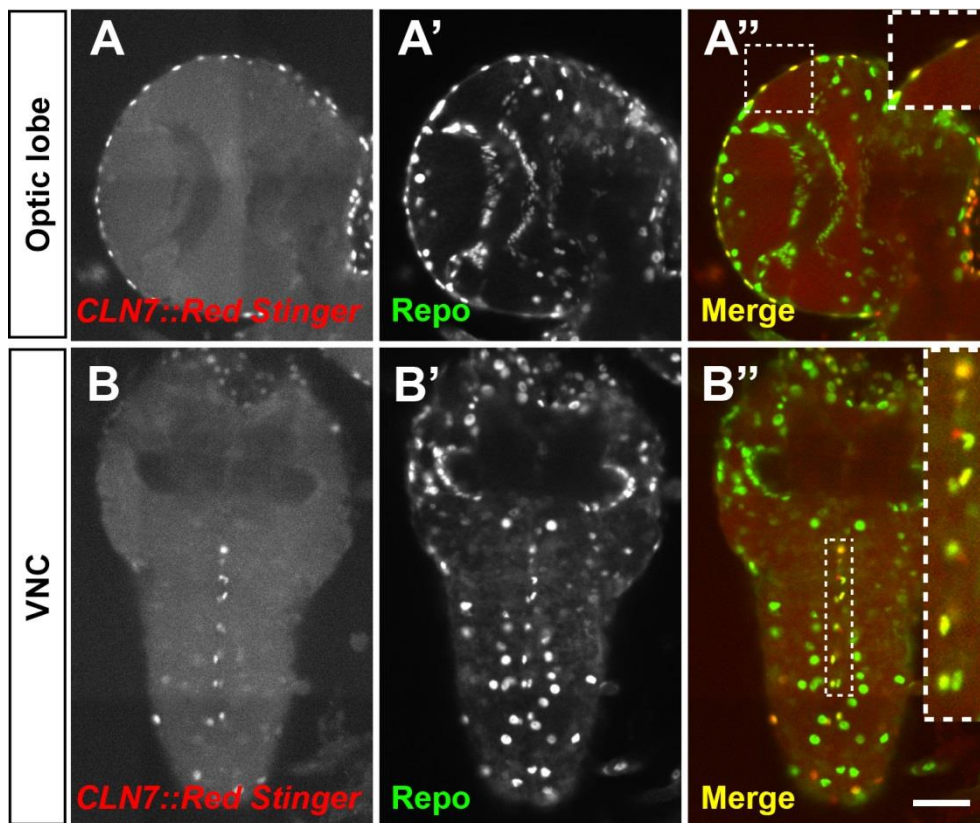
Figure 4.7: CLN7::RedStinger promoter fusion reporter confirms glial expression. RedStinger is a nuclear protein that retains its fluorescence after fixation requiring no antibody. Optic lobe (A-A'') and ventral nerve chord (VNC) (B-B'') from larvae were counterstained with the glial marker REPO (Green). CLN7::RedStinger expression (red) co-localises with perineurial glia (Yellow - enlargement of box in A'') which form the part of the insect blood brain barrier and the channel glia in the VNC (Yellow -enlargement of box in B''). Scale bar = 50 μm.
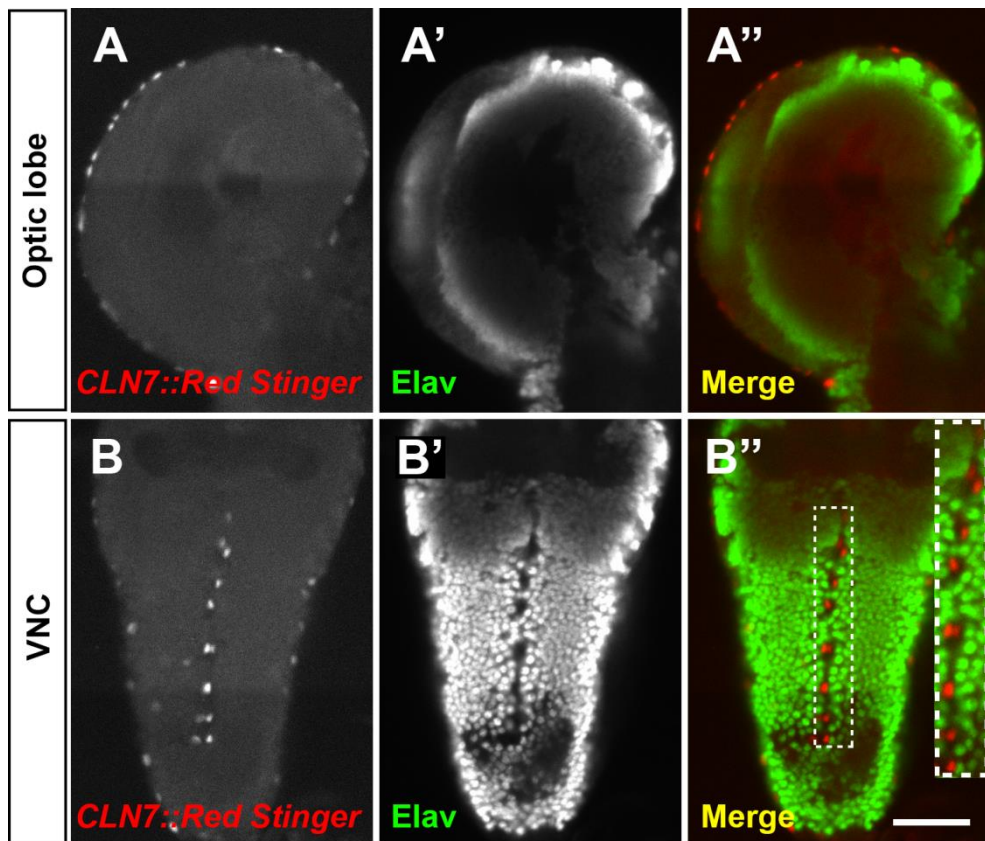
Figure 4.8: A CLN7::RedStinger is not expressed in neurons. Optic lobe (A-A'') and ventral nerve chord (VNC) (B-B'') from larvae were counterstained with the neuronal marker Elav (Green). CLN7::RedStinger expression (red) did not co-localises with Elav in either the optic lobe or VNC. Scale bar = 50 µm.

reveal that CLN7 is predominantly a glial protein in the CNS and neural expression is restricted to a small subset of neurons in the visual system only. Surprisingly, with deterioration in motor function being a key symptom of CLN7 disease, no CLN7 expression was detected in central neurons or motor neurons of the CNS.

4.2.3 CLN7 localises to the post-synaptic density

After early retinal pathology, NCL patients suffer seizures and a progressive decline in motor function. The *Drosophila CLN7* mutant exhibits atypical development in the larval neuromuscular junctions (NMJs) which indicates a crucial role for CLN7 in neural development (discussed further in chapter 5). Given that CLN7 is expressed in neurons in the mammalian CNS and the NMJ phenotypes in the CLN7 mutant, it appeared likely that Drosophila CLN7 would be expressed within the motor neurons that innervate the NMJ. Using both knock-in and *CLN7* promoter fusion lines, I found *CLN7* is surprisingly not expressed in the larval motor neuron cell bodies within the VNC. Therefore, I decided to examine expression of CLN7 at the NMJs.

Three tissues have been shown to be directly involved in NMJ development, pre-synaptic motor neurons, post-synaptic muscle and peripheral glia. I examined *CLN7* expression in these cells by dissecting and fixing NMJ fillets in late wandering stage larvae (Brent et al., 2009). YFP-CLN7 was found to be expressed in all post-synaptic body wall muscles, clusters of oenocytes in repeating segments and in epithelial cells surround the muscle walls (Figure 4.9B). In all muscles, CLN7 appears to be concentrated at the NMJ, around pre-synaptic terminal swelling (boutons) stained marked with anti-HRP, a pre-synaptic membrane marker (Figure 4.9C). YFP-CLN7

was found to localise around boutons and but the staining was distinct and separable from the HRP stain (Figure 4.9D). This confirms that CLN7 is not expressed in the pre-synaptic motor neurons. The post-synaptic site on muscles was then stained with anti-DLG, the fly homolog of mammalian PSD-95, and was found to co-localise with YFP-CLN7, indicating a concentration of CLN7 protein within the sub-synaptic reticulum membrane that envelopes the bouton (Figure 4.9E, (Hoang and Chiba, 2001)). This can be visualised in both type Ib and Is NMJs. The expression pattern of the YFP-CLN7 knock-in was corroborated with the *CLN7::RedStinger* fusion. Nuclear RedStinger expression was seen in oenocytes (Figure 4.10A – in dotted circle) and in all muscle walls (Figure 4.10B) suggesting they express CLN7. Combined, they indicate CLN7 is expressed in the muscle and then recruited or concentrated at the postsynaptic density.

4.2.4 CLN7 is expressed in principle cells of Malpighian tubule

FlyAtlas (Chintapalli et al., 2007) indicates the highest levels of *CLN7* transcription occurs in the Malpighian tubules, the excretory and osmoregulatory organ that forms the insect orthologue of the mammalian kidney. The Malpighian tubule is made up of two cells: principle cells and stellate cells. Malpighian tubules from YFP-*CLN7* expressing and wild-type larvae were stained with anti-GFP to visualise *CLN7* expression. The basal membrane of the tubules was counterstained with anti-Na$^+$/K$^+$ ATPase transporter (Figure 4.11A and B). The CLN7 protein was found to localise on the outer side of the ATPase transporter and form large peripheral vesicles (Figure 4.11B'), presumed to be lysosomes. The expression pattern also contained regular tubule regions that lacked YFP-CLN7 staining
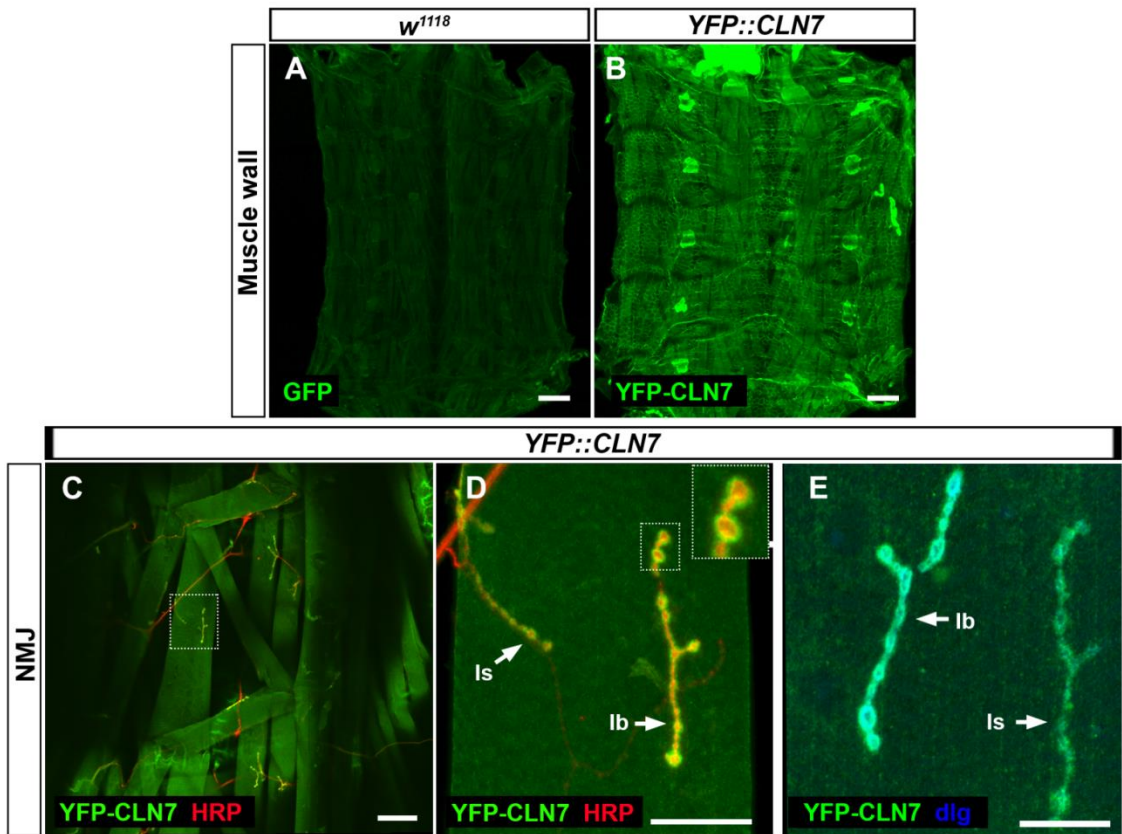
Figure 4.9: CLN7 is expressed in muscles and localises to the post synaptic density at the neuromuscular junction (NMJ). A and B: Muscle walls of w1118 and YFP::CLN7 third instar larvae were stained for GFP (green). Anti-GFP shows specificity for YFP-CLN7 compared to background staining in *w[1118]*. CLN7 is expressed in all body wall muscles, oenoctyes and in the epidermis. C: YFP-CLN7 (green) localises to all NMJs stained with anti-HRP (red). D: Higher magnification of muscle 4 shows CLN7 is recruited to both type Is and Ib boutons and surrounds anti-HRP (arrows and enlargement of boxed region).E: CLN7 colocalises with the postsynaptic marker, anti-dlg (blue). Scale bar= 250 µm (A and B); 100 µm (C); 50 µm (D) and 25 µm (E).
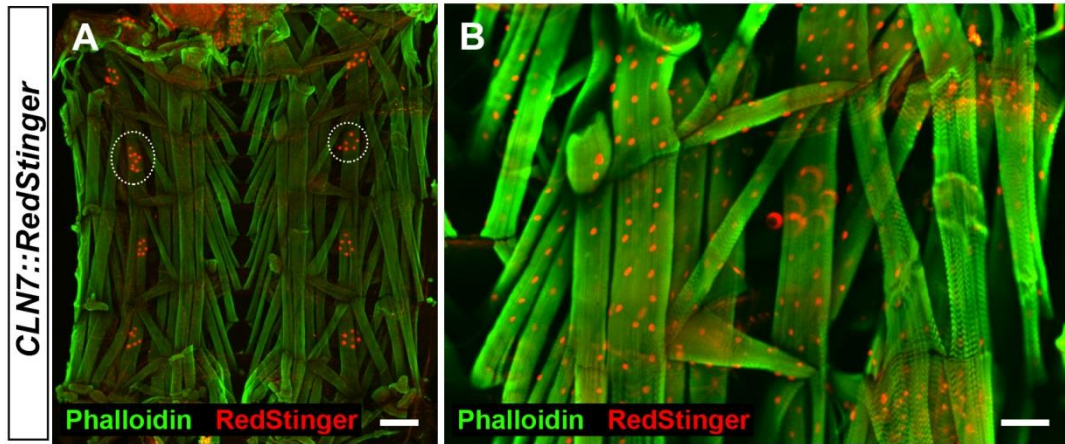
Figure 4.10: CLN7 is expressed in muscle and oenocytes. F-actin in muscle walls were stained with Alexa-488 phalloidin (green). A: CLN7::RedStinger is expressed in oenocytes (circled). B: A different focal plane and higher magnification of A show CLN7 is expressed in all muscle walls. Scale bar= 250 μm (A) and 100 μm (B).

suggesting CLN7 expression may be limited to one of the two tubule cell types. This was confirmed by counterstaining nuclei in *CLN7::RedStinger* tubules with DAPI. The nuclei of each cell type can be distinguished by cell numbers and morphology. CLN7::RedStinger was found to be co-localised exclusively with nuclei larger morphologically and greater in number suggesting CLN7 is only expressed in the principle cells.

4.2.5 Peripheral tissue staining

FlyAtlas also indicated moderate or low levels of CLN7 expression in the fat body and salivary glands of larvae. To determine if CLN7 could be detected in both tissues, fat body and salivary glands, the plasma membrane was counterstained with F-actin (Figure 4.12). YFP-CLN7 co-localised with F-actin in both sets of tissues suggesting CLN7 was present at the membrane (Figure 4.12A' and B'). YFP-CLN7 expression could not be detected in the cytoplasm of fat body cells, suggesting it is either expressed at undetectably low levels or absent (Figure 4.12A'). However, staining of the salivary gland produced a mesh-like pattern in the cytoplasm in addition to perinuclear staining (Figure 4.12B'). YFP-CLN7 also overlapped with F-actin at the basolateral membrane, but not at the apical membrane in salivary glands (Figure 4.12C'). The CLN7::RedStinger reporter confirmed CLN7 expression in the salivary glands, however was not detected in the majority of fat body cells (Figure 4.13). The CLN7::RedStinger reporter incorporated approximately 1.8 kb of gene regulatory sequences upstream of the CLN7 start codon. Therefore some promoter sequences may have been overlooked and resulted in a slight difference in expression pattern as YFP-CLN7 retains the endogenous promoter.
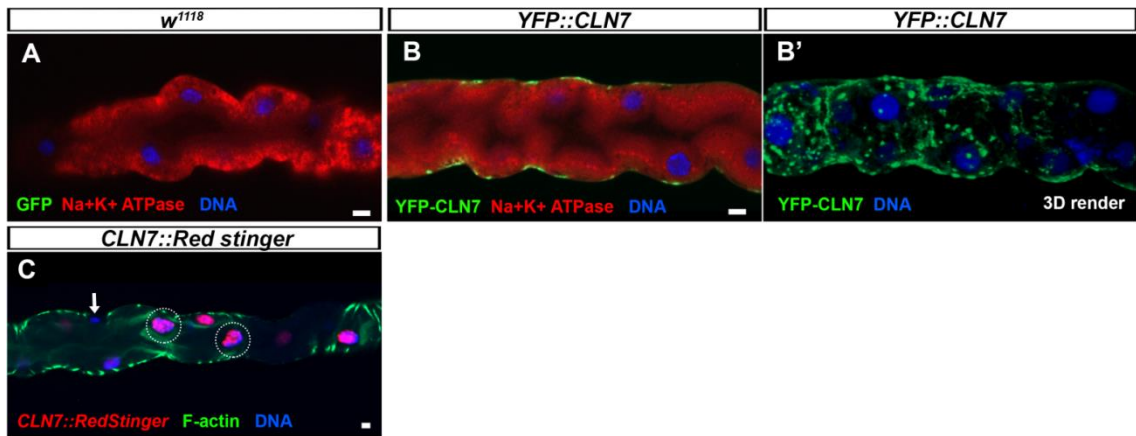
Figure 4.11: CLN7 is exclusively expressed in the Malpighian tubule principal cells.
A and B: Malpighian tubules basal membrane was stained with anti-Na+/K+ ATPase (red).
A single XY optical slice shows GFP specificity for YFP-CLN7. CLN7 is expressed apical of
the basal membrane and absent from the lumen. B': a 3D render of B show CLN7 is
localised to large peripheral vesicles, presumed to be lysosomes. C: CLN7::RedStinger
(red) is counterstained for F-actin with Alexa-488 phalloidin (green) and nuclear DAPI
(blue). RedStinger fails to co-localise with smaller nuclear staining (arrows) while co-
localising with larger nuclei (circled) which corresponds to stellate and principal respectively
which form the Malpighian tubule. Scale bar: 50 μm.
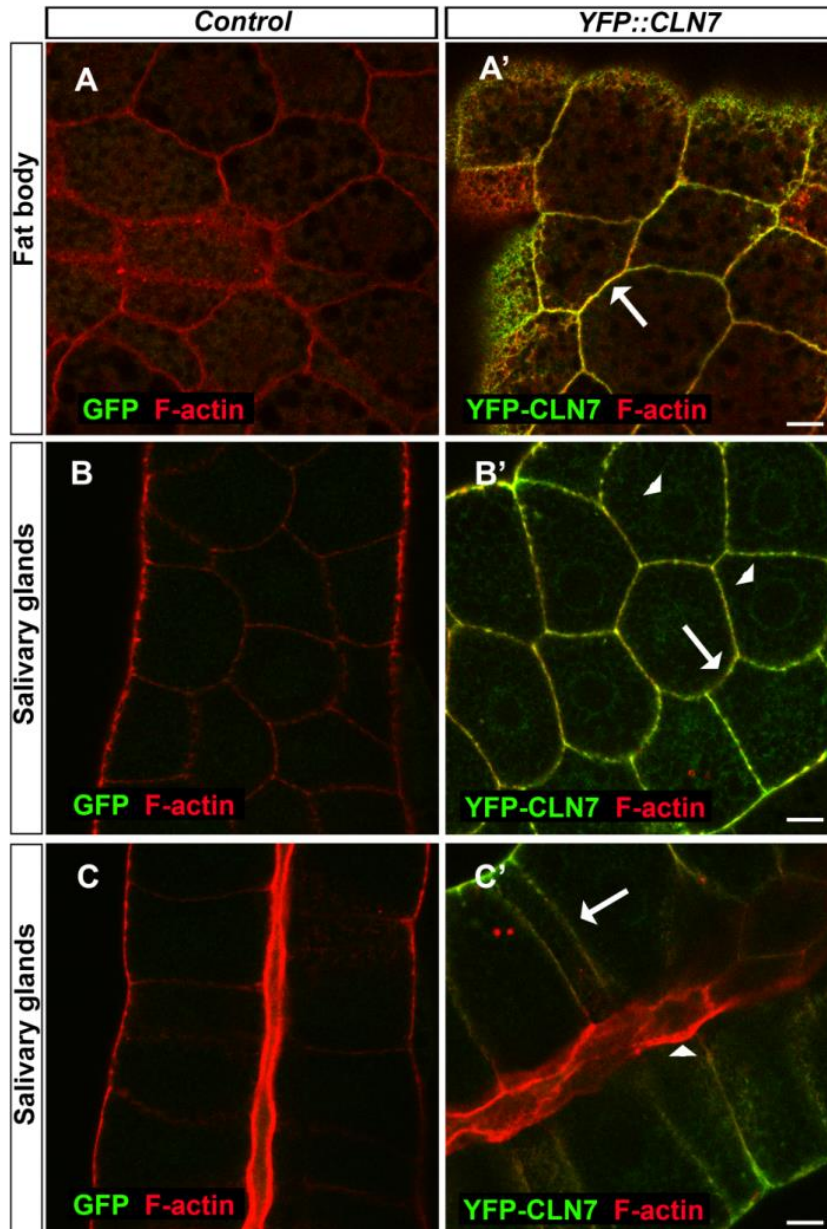
Figure 4.12: YFP-CLN7 is present at the plasma membrane but absent in apical membrane. Fat bodies and salivary glands were dissected from wandering YFP-CLN7 larvae, fixed and stained for YFP::CLN7 (green). The plasma membrane was counterstained with F-actin (red). A: CLN7 is expressed in plasma membrane in the fat body (arrow). B: CLN7 is expressed in plasma membrane in the salivary glands (arrow) and has low levels of perinuclear staining (arrowheads). C: CLN7 is present in the basolateral membrane (Arrow) of the salivary glands but absent from the apical membrane (arrowhead). Scale bar = 20 µm.
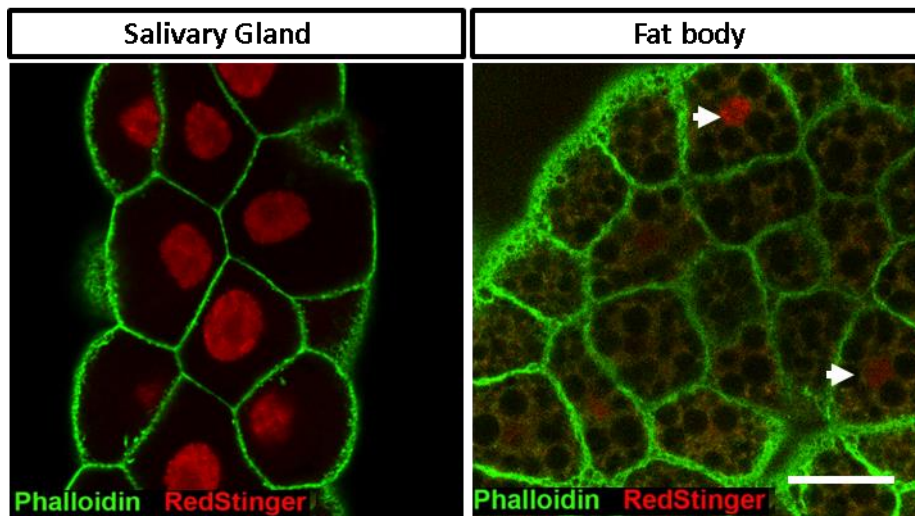
Figure 4.13: CLN7::RedStinger is expressed salivary glands but not fat body. Plasma membranes are visualised with Alexa-488 phalloidin (green) staining F-actin. *CLN7::RedStinger* is expressed salivary glands (Red). No *CLN7::RedStinger* was observed in fat body with nuclear red staining (arrows) regarded as background staining. Scale bar= 50 μm.

4.3 Discussion

4.3.1 CLN7 is predominantly a glial protein in *Drosophila*

I have used a CRISPR/Cas9-generated YFP-CLN7 knock-in reporter line (chapter 3) to carry out an *in vivo* localisation study of CLN7. Using a knock-in YFP-CLN7 line by-passed the poor antigenic nature of CLN7 that had prevented specific antibodies from being generated and allowed a study of its cellular expression and sub-cellular localisation. A few tissues were prioritised for this localisation study based on expression profiling data available on Flybase. The Malpighian tubules, the kidney mammalian orthologue and highest CLN7 expressing tissue in larvae, along with salivary glands, fat body were chosen to be studied along with parts of the CNS due to neurological defects associated with CLN7 disease. The specificity of the anti-GFP for YFP-CLN7 was demonstrated by the lack of, or very low levels of, background staining in w^{1118} controls in various tissues compared to the knock-in line. In each tissue, expression of YFP-CLN7 was confirmed with a promoter fusion line: CLN7::RedStinger.

Interestingly, in the CNS of flies CLN7 is predominantly expressed in glial cells which form the insect blood-brain barrier (BBB), with limited neuronal expression within the developing visual system. However, CLN7 is widely expressed in the mammalian CNS in both neurons and glia. In humans, CLN7 is detected in the Purkinje cells of the cerebellum, hippocampus, caudate and cerebral cortex, particularly in the neuropil of the latter (The Human Protein Atlas). CLN7 is expressed at similar levels in neurons and glia in the cerebral cortex, but at higher levels in neurons in the hippocampus and caudate (The Human Protein Atlas). In

mice, CLN7 is highest in the cerebral cortex and cerebellum and found at moderate levels in the hippocampus and medulla (Brandenstein et al., 2016). In rats, CLN7 mRNA is expressed at six times higher levels in neurons when compared to glia (Sharifi et al., 2010).

Activation of glial cells is the earliest marker of most neurodegenerative diseases and can be seen in several different animal models of NCLs (Cooper et al., 2015, Kay et al., 2006, Oswald et al., 2005, Pontikis et al., 2004). However, the cause of glial activation and the roles they play in disease progression remains unknown. Studying the function of CLN7 within glial cells may help to elucidate some of these roles and help uncover early NCL disease progression.

4.3.2 Potential functions of CLN7

CLN7 is predominantly expressed in surface glia which form the insect BBB (Stork et al., 2008). The BBB in Drosophila undertakes many functions including: the transport of metabolites, maintenance of water and ion homeostasis, chemoprotective roles, and metabolic and signalling roles, such as the regulation of organismal growth via insulin signalling (Hindle and Bainton, 2014, Limmer et al., 2014). Two types of cells form surface glia: the apical perineurial glia, and the underlying sub-perineurial glia. Perineurial glia contain various solute transporters while the sub-perineurial glia form tight junctions that are analogous to the endothelial tight junctions in the vertebrate BBB (Stork et al., 2008, Mayer et al., 2009, DeSalvo et al., 2011). CLN7 is specifically expressed in perineurial glia which is consistent with its likely role as a solute transporter. These expression patterns

match transcriptome data of adult *Drosophila* surface glia. This shows CLN7 (*CG8596*) is enriched approximately fifty times more in surface glia relative to the whole fly CNS, and has low neuronal expression (DeSalvo et al., 2014). Similarly, CLN7 is exclusively expressed in the principle cells of Malpighian tubules. The Malpighian tubule comprise of two cell types, principle cells and stellate cells, and both express numerous solute transporters for excretion, detoxification and osmoregulation (Jung et al., 2005, Dow, 2009). However, lack of CLN7 in the stellate cells suggests it is unlikely to be involved in chloride transport.

The only neuronal CLN7 expression in the CNS was limited to lamina neurons that form part of the developing visual system of third instar larvae. One possibility is that *Drosophila* exhibits an ancestral CLN7 expression pattern originating in surface glia and visual neurons and expands to include neurons outside the visual system in vertebrates. Visual neuron localisation is interesting as visual defects leading to blindness are one of the earliest symptoms of the NCLs. In the fly visual system, lamina neurons are secondary order neurons and a site of synaptic connections with primary order neurons. Within mice, CLN7 has been shown to predominantly localise to the outer plexiform layer of the retina, a region also highly enriched with synaptic connections (Khan et al., 2017), with loss of CLN7 in CLN7 mutant mice leading to atrophy of the visual system (Jankowiak et al., 2016). These suggest CLN7 plays an important role in the development/maintenance of synaptic homeostasis which may be conserved from flies to vertebrates. It would be interesting to see whether the visual system is similarly compromised in *Drosophila*

CLN7 mutants. This would help elucidate potentially conserved functions of CLN7 in the visual system and will be further investigated in chapter 6.

In addition to visual defects, NCL patients suffer from motor defects which are recapitulated in *CLN7* mutant *Drosophila* larvae. Mutant larvae exhibit an undergrowth phenotype at the NMJ and is accompanied by functional defects in larval motility (O'Hare, Submitted). This localisation study revealed CLN7 is not expressed in larval motor neurons. However, CLN7 is expressed in the muscle and has been shown to be recruited to the post synaptic density at the NMJs. CLN7 has recently been shown to be expressed and co-localise with the mammalian post synaptic marker postsynaptic density 95 (PSD-95) in murine retina (Khan et al., 2017). Therefore, CLN7 must play an important role in the development/regulation of synaptic homeostasis, potentially working in a retrograde fashion. Roles of CLN7 at the NMJ will be further discussed in the following chapter.

4.3.3 CLN7 along endo-lysosomal pathway

YFP-CLN7 is primarily localised to the plasma membrane in surface glia, fat body and salivary glands. Lysosomal membrane proteins can be recruited to the lysosome from the trans-Golgi network either directly to endosomes/late endosomes, or indirectly via the plasma membrane. The cytoplasmic mesh-like and perinuclear staining in salivary glands suggests CLN7 may be found along the trans-Golgi network (Huu et al., 2014). Cell culture studies using human and mouse found CLN7 to primarily be late/endosomal and lysosomal protein (Sharifi et al., 2010, Steenhuis et al., 2010) and has been identified as a lysosomal membrane protein

by proteomics (Chapel et al., 2013). Counterstaining the salivary glands with organelle specific antibodies: anti-KDEL (ER) and anti-KDEL receptor/anti-GM130 (Golgi) and lysosomal marker arl-8 would help identify the specific compartments CLN7 can be found in.

In human embryonic kidney cells (HEK293), 22% of CLN7 has been shown to localise at the plasma membrane and to indirectly incorporate into lysosomes (Steenhuis et al., 2010). However, another study using HeLa cells could not detect wild type CLN7 at the plasma membrane with the majority of CLN7 being localised to lysosomes (Sharifi et al., 2010). In my experiments, CLN7 was localised in large vesicles likely to be lysosomes in the principal cells of Malpighian tubules. One possible explanation for the differences in sub-cellular localisation of CLN7 in the various cell types may be differential requirements for solute transporter in the glial and tubule cells. Nevertheless, expression in both surface glia and Malpighian tubule, which regulate solute transport across the BBB and gut respectively, suggest CLN7 contributes to solute transport in both cell types.

The surface glia also regulates organismal growth indirectly via the secretion of a soluble insulin receptor inhibitor, secreted decoy of insulin receptor (SDR) (Okamoto et al., 2013). A decrease in SDR secretion causes increased insulin signalling in peripheral tissues and ultimately larger cells. Interestingly, CLN7 mutant flies exhibit an overgrowth phenotype (O'Hare, Submitted). It will be interesting to find out if SDR secretion is affected by loss of CLN7, potentially uncovering a substrate of the putative transporter.

The fat body, the tissue that has functions similar to both mammalian liver and adipose tissue, and the salivary glands respond well to starvation induced stress. Autophagy is dysregulated in most, if not all neurodegenerative diseases including a mouse model of CLN7 disease (Brandenstein et al., 2016). Expression of CLN7 in these tissues will provide an excellent opportunity to study autophagy *in vivo* (Nagy et al., 2015) (Lorincz et al., 2017).

5. ROLES OF CLN7 AT THE NEUROMUSCULAR JUNCTION

Data presented in this chapter have been published in (O'Hare, Submitted)

5.1 Introduction

Lysosomes have essential cellular functions including degradation and recycling macromolecules and regulation of mTORC signalling. Due to the longevity and high energy demand of neurons, these specialised cells are highly susceptible to lysosomal dysfunction. While lysosomes fail to remove protein aggregates in late onset neurodegenerative diseases such as Alzheimer's, Parkinson's and Huntington's disease, the reliance of neurons on lysosomes is exemplified by Lysosomal Storage Disorders (LSDs), a group of over 50 monogenic inherited diseases. LSDs arise from lysosomal dysfunction and generally exhibit early onset neuropathology. One subgroup of LSDs are the NCLs which present neurological symptoms and neuropathology.

Synaptopathology – pathology of the synapse – is a hallmark of many, if not all, neurodegenerative diseases and precedes neuronal loss in many disease models. CLN7 is a putative lysosomal transmembrane protein and can be found along the endo-lysosomal pathway. Lysosomes predominantly have been found at the soma although evidence suggests they can be found along the axon (LEE et al 2011) and also localise at the NMJ terminal (Sweeney and Davis, 2002). Early synaptopatholgy – preceding neuronal loss - has also been visualised in multiple NCL models

including CLN1 and CLN3 in *Drosophila* at the NMJ (Kim et al., 2008, Kielar et al., 2009a, Sharma et al., 2012, Bond et al., 2013, Koch et al., 2011, Partanen et al., 2008b). The early onset pathology indicates likely alterations to synaptic function and activity within the developing nervous system. However, it can be harder to study synaptic functions in larger models *in vivo*. The NMJ of *Drosophila* larvae provides a well-established model for quantifying and studying the development and function of synapses (Menon et al., 2013). The synapses are readily accessible and easily identifiable via immunofluorescence for high-resolution microscopy and functional electrical recordings (Faller et al., 2015, Andlauer and Sigrist, 2012b, Budnik et al., 2006, Ruiz-Canada and Budnik, 2006) making it a well-established system for examining and quantifying synaptic development, function and plasticity. The peripheral NMJ of insects are excitatory glutamatergic synapses that are structurally and functionally similar to central synapses in the vertebrate CNS. They share common fundamental processes and synaptic proteins (Menon et al., 2013) and thus can be used as an easily manipulated model to understand synapse function.

My localisation study described in chapter 4 revealed that *CLN7* is expressed in all body wall muscles that are innervated by the motor neurons in *Drosophila* larvae and that the CLN7 protein is recruited to and enriched at the postsynaptic site of both type Ib and Is boutons but not of type II and III motor neurons (unpublished observations) which lack the DLG-positive sub-synaptic reticulum. Boutons innervating muscle 4 were chosen for quantitative analysis to investigate the development of synapses. Muscle 4 is readily accessible muscle after dissection

and the Ib and Is boutons are spatially distinct. It has been also been characterised in many studies to allow comparisons. In this chapter, I investigate the possible roles of CLN7 in neurodevelopment as *CLN7* larvae exhibit a decrease in boutons – presynaptic swellings which house the release sites for neurotransmitter. Bouton formation can be regulated by signalling within the presynaptic neuron; by retrograde signal from the postsynaptic muscle into the neuron across the synapse; and from the supporting glial cells (Fuentes-Medel et al., 2012, Menon et al., 2013, Collins and DiAntonio, 2007). I set out to determine where CLN7 expression is required for synapse development and will use the GAL4-UAS system, within flies to study the effects of ectopic re-expression and RNAi knockdowns.

5.1.1 Preliminary *CLN7$^{-/-}$* data

To study the roles of CLN7, two loss of function *CLN7* mutations were generated in *Drosophila CLN7^{84D}* and *CLN7^{36H}* (O'Hare, Submitted). *CLN7* mutants were found to exhibit abnormal development of the NMJ in third instar larvae. Mutants had significantly fewer type Ib boutons compared to wild types, while type Is boutons remained unaffected. This was specific to loss of CLN7 as re-expression of CLN7 in the mutant background was sufficient to rescue the mutant phenotype. This suggested abnormal homeostatic balance between the presynaptic innervation and postsynaptic requirements of the muscle.

In addition, *CLN7* mutants may also share genetic interactions with autophagy related proteins as an *Atg/Df* autophagy mutant shows the same decrease in type
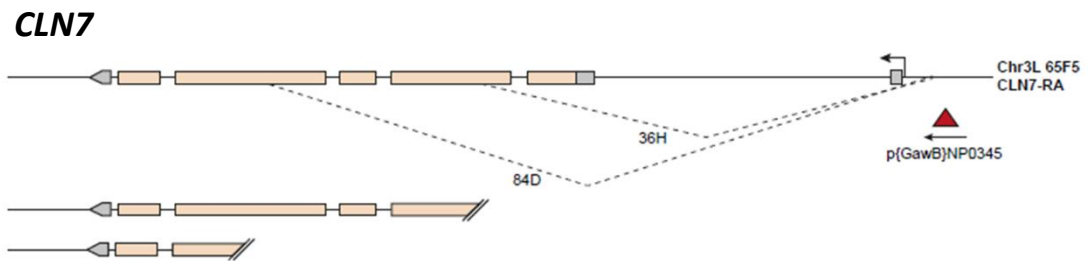
Figure 5.1: Schematic of *CLN7* mutations. Imprecise P-element excision was used to generate two deletions in the *CLN7* gene. A small deletion, 36H, and larger deletion, 84D, are shown.

Ib phenotype (Shen and Ganetzky, 2009). *CLN7* mutant adults were also shown to be larger in size, with larger cells accounting for the increase in wing span, not increased number of cells. The abnormal increase in size suggests a possible shift in the homeostatic TORC signalling, which is involved in the anabolic *vs.* catabolic pathways. In this chapter, I will firstly attempt to replicate the NMJ phenotype seen in *CLN7* mutants and then due to the similarities in phenotypes between *CLN7* and Autophagy mutants, and autophagy being regulated by TORC signalling – which is affected in CLN7 mice (Danyukova et al., 2018) and flies (personal communication with Richard and Kyle), I will determine if autophagy is affected in *CLN7* mutants. Lastly, due to the postsynaptic localisation of CLN7, I will determine if CLN7 is involved in the TGF-β signalling pathway, which regulates the development of the synapse in a retrograde manner, as downregulation of this pathway phenocopies *CLN7* larvae.

5.2 Results

5.2.1 Loss of CLN7 results in NMJ pathology

One simple readout of synaptopathology is to examine and quantify the development of boutons at the NMJ; boutons house most of active zones. Type Ib motorneurons were quantified on muscle 4. As the number of boutons in each NMJ is proportional to the size of muscle cell it is innervating and increases as the muscles grow 100-fold through larval development, all quantifications were normalised to muscle surface area. This is especially important as the *CLN7* flies have enlarged cells (Richard Tuxworth/Megan O'Hare, unpublished data). Both alleles of *CLN7* resulted in significantly fewer boutons compared to its isogenic w^{1118} control (Figure 5.2). *CLN7^{84D}* (306.4 ± 54.79, n=20) and *CLN7^{36H}* (267.7 ± 41.38, n=12) larvae had 24.10%, and 17.34% significantly fewer boutons compared to w^{1118} controls (403.7 ± 52.91, n=13, p=0.0001 and p=0.0204 respectively) replicating previous studies (Megan O'Hare, 2012). Interestingly, *CLN7$^{84D/+}$* (267.7 ± 41.38, n=21) and *CLN7$^{36H/+}$* (305.5 ± 60.83, n=16) heterozygotes also resemble mutant phenotypes indicating both alleles are haploinsufficent (Figure 5.3). A further reduction in boutons is seen in *CLN7$^{84D/36HD}$* transheterozygotes (256.6 ± 70.42, n=19) although this fails to reach statistical significance (p=0.1969 vs *CLN7^{84D};* p=0.0538 vs. *CLN7^{36H}*, figure 5.3). These results suggest development of the NMJ is critically dependent on levels of CLN7 and that any reduction in levels might potentially affect the stoichiometry of membrane complexes containing CLN7.
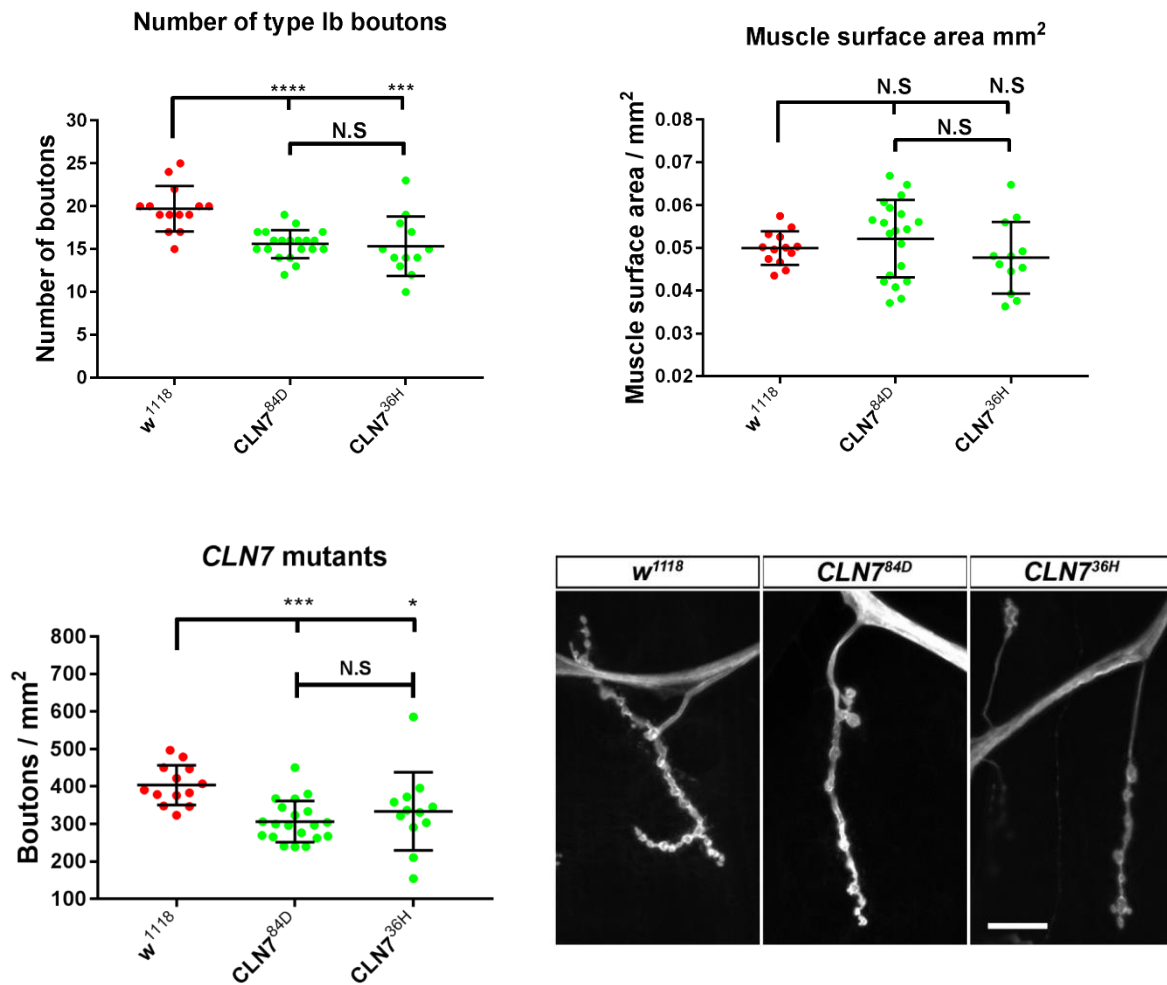
Figure 5.2: *CLN7* mutants have smaller synapses. Type Ib terminals on muscle 4 were quantified and normalised to the muscle surface area. Top left panel shows the *CLN7⁸⁴ᴰ* (15.6) and *CLN7³⁶ᴴ* (15.33) have significantly fewer boutons than *w¹¹¹⁸* controls (19.71, p<0.0001 and p=0.0002 respectively). There is no significant difference between the two *CLN7* alleles (p=0.9550). Top right panel shows no significant difference between muscle size between *CLN7⁸⁴ᴰ* (0.05215), *CLN7³⁶ᴴ* (0.04772) and *w¹¹¹⁸* controls (0.04996, p=0.7109 and p=0.7501 respectively). There is no difference between the two *CLN7* alleles (p=0.2714). Bottom left panel show both allelic *CLN7* mutants have significantly fewer boutons/mm². *w¹¹¹⁸* control larvae had 403.7 boutons compared to 306.4 in *CLN7⁸⁴ᴰ* (p=0.0001) and 267.7 in *CLN7³⁶ᴴ* (p=0.0204). This represents a significant 24.10% and 17.34% decrease respectively. There was no significant difference between *CLN7⁸⁴ᴰ* and *CLN7³⁶ᴴ*. Bottom right panel shows representative images of type Ib boutons found on muscle 4 for each genotype. ANOVA, N.S>0.05, * *p*<0.05, p<0.001 and **** *p*<0.0001). Plots represent mean ± standard deviation.
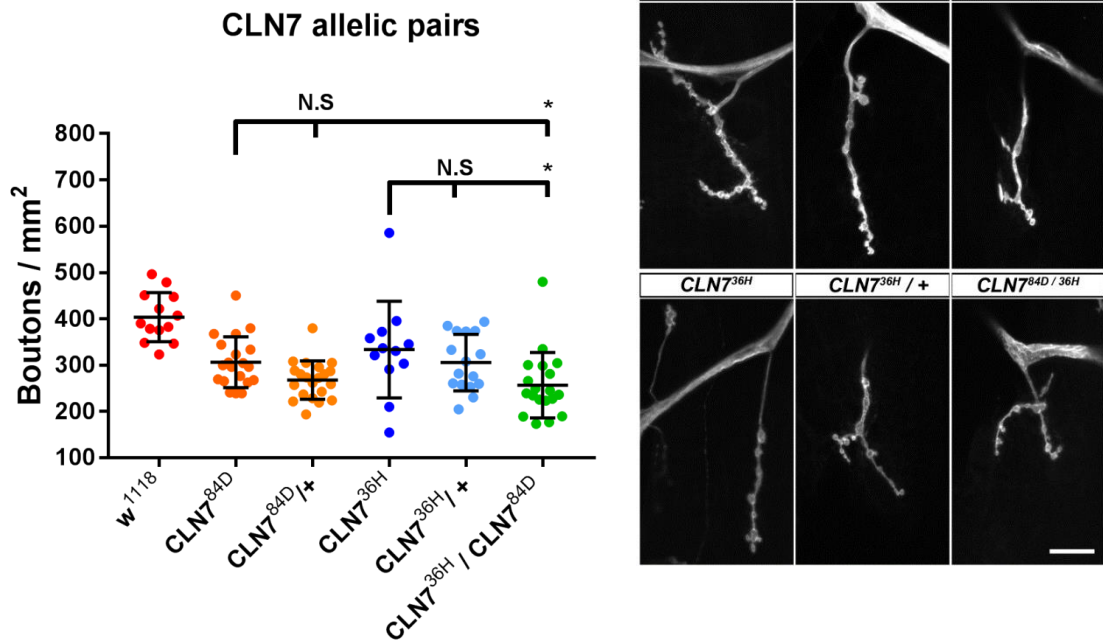
Figure 5.3: *CLN7* is haploinsufficent. Type Ib terminals on muscle 4 were quantified and normalised to the muscle surface area. Fewer boutons formed in *CLN7*^{84D/+} heterozygous (267.7) compared to the *CLN7*^{84D} mutant (306.4), however this was not significant (p=0.8892). Similarly, there was a slight reduction in boutons in *CLN7*^{36H/+} heterozygote (305.5) compared to the *CLN7*^{36H} mutant (333.7) but this was not significant (p>0.9999). The *CLN7*^{84D/36H} transheterozygote formed the fewest boutons (256.6) and was lower than both *CLN7*^{84D} (p=0.1969) and *CLN7*^{36H} mutants (p=0.0538). B: Representative images of type Ib boutons found on muscle 4 for each genotype. (Kruskal-Wallis test, N.S>0.05 and * *p*<0.05). Plots represent mean plus standard deviations.

5.2.3 CLN7 is required in the postsynaptic muscle for NMJ development

My localisation studies described in chapter 4 showed that CLN7 was expressed in muscles and recruited to the postsynaptic site. To determine which cell types require CLN7 for NMJ development, I utilised the UAS-GAL4 system. Tissue specific *CLN7* knockdown was introduced by the expression of dsRNA targeting the *CLN7* gene. Postsynaptic knockdown of CLN7 using Mef2-Gal4 (269.7 ± 45.89, n=14) resulted in a significant reduction of boutons at similar to the *CLN7* mutants compared to the UAS-CLN7^{RNAi} control (402.5 ± 74.55, n=12; p=0.0001) and Mef2-Gal4/+ (334.7 ± 44.82, n=13, p=0.0207; figure 5.4). This indicates that CLN7 expression in the muscles is crucial for NMJ development. Knockdown of *CLN7* pre-synaptically or in glial cells using Elav-Gal4 (383.9 ± 67.51, n=14; p>0.9999) and Repo-Gal4 (389.4 ± 59.07, n=15; p>0.9999) respectively resulted in no significant change in number of boutons compared to UAS-CLN7^{RNAi} control (402.5 ± 74.55, n=12; figure 5.4) and indicating no essential requirement for CLN7 in these cells. PG-Gal4 was used to knock down *CLN7* in the peripheral glial cells and perineurial glial of the BBB where CLN7 was shown to be expressed (Chapter 4, figure 4.3). This resulted in no significant changes (363.3 ± 93.79, n=19) compared to UAS-RNAi control (p=0.7465). These results were predicted given my expression studies indicate no expression of CLN7 in motor neurons or the glia that ensheath the motor neurons.

CLN7 RNAi knockdown
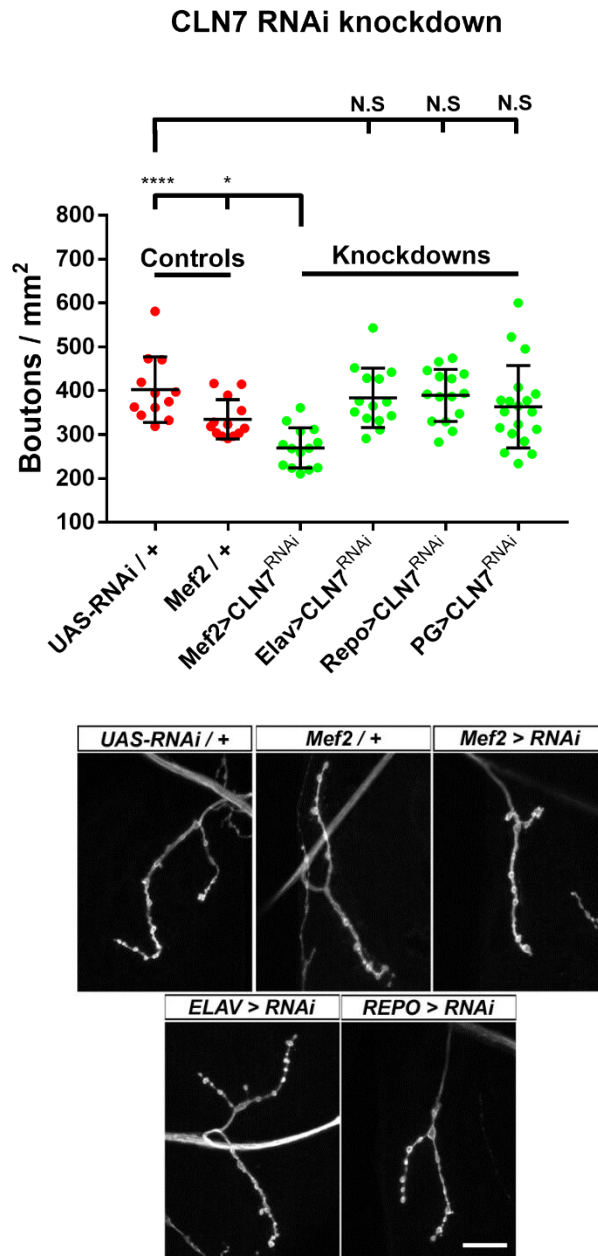
Figure 5.4: postsynaptic knockdown of CLN7 phenocopies *CLN7* mutant. Type Ib terminals on muscle 4 were quantified and normalised to the muscle surface area. Postsynaptic knockdown using a Mef2-Gal4 driver (269.7) caused a significant reduction in synapse size compared to the UAS-RNAi (402.5) and Gal4 driver (334.7) controls. Synapse sizes of pan-neuronal (presynaptic) and pan-glial knockdowns using ElavGal4 (383.9) and REPOGal4 (389.4) drivers respectively were similar to the UAS-RNAi control (402.5). B: Representative images of type Ib boutons found on muscle 4 for each genotype. Kruskal-Wallis test used, N.S>0.05, * $p<0.05$ and **** $p<0.0001$). Plots represent mean plus standard deviations.

5.2.4 CLN7 may be required in additional tissues for NMJ development

I next performed the converse experiments where I re-expressed an N-terminal fused YFP-CLN7 in a tissue-specific manner in a *CLN7[84D]* or *CLN7[84D/36H]* transheterozygote background. Ubiquitous re-expression of a YFP-CLN7 line driven by Actin-Gal4 (397.8 ± 90.12, n=16) fully rescued the mutant phenotype when compared a UAS-YFP-CLN7 control (289.1 ± 43.42, n=15; p=0.0072) and Actin-Gal4 (269.1 ± 96.38, n=96.38, p=0.0009) controls in a *CLN7[84D]* background (Figure 5.5). This showed the use of an N-terminal fused YFP-CLN7 is functional. Re-expressing YFP-CLN7 pre-synaptically (Elav-Gal4, 324.7 ± 62.7, n=13) or in glial cells (Repo-Gal4, 311.6 ± 78.84, n=18) independently resulted in no rescue of the *CLN7[84D]* phenotype (Figure 5.6). Re-expressing YFP-CLN7 in postsynaptic muscle cells (Mef2-Gal4, 307.7 ± 53.94, n=16) caused a significant rescue when compared to the Mef2-Gal4 control (245.2 ± 52.32, n=24, p=0.0021 ANOVA), but only a partial non-statistically significant rescue when compared to the UAS control (277.8 ± 62.71, n=15, p=0.2438 ANOVA) when re-expressed in a transheterozygote background (Figure 5.7). As muscle re-expression alone did not fully rescue the mutant phenotype like ubiquitous re-expression, YFP-CLN7 was re-expressed simultaneously pre- and post-synaptically as well as in peripheral glial cells using Spin-Gal4. Spin-Gal4 driven re-expression resulted in a significant rescue (324.7 ± 57.23, n=16) compared to the Spin-Gal4 control (277.3 ± 60.78, n=14, p=0.0372) but partial rescue when compared to the UAS-CLN7 control (289.1 ± 43.42, n=15, p=0.1518) (Figure 5.8). This was similar to muscle re-expression and indicates CLN7 is crucial in the muscle, but may additionally be required in other cells for NMJ development.
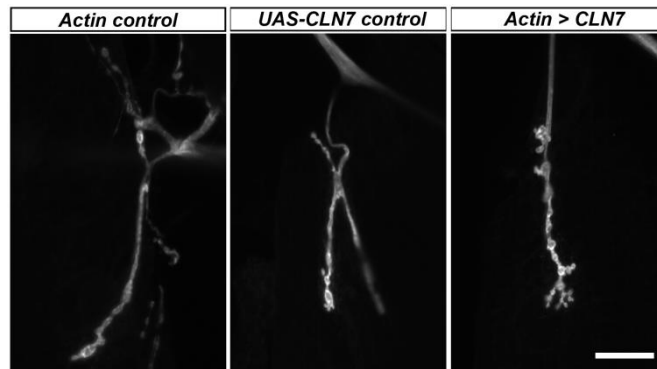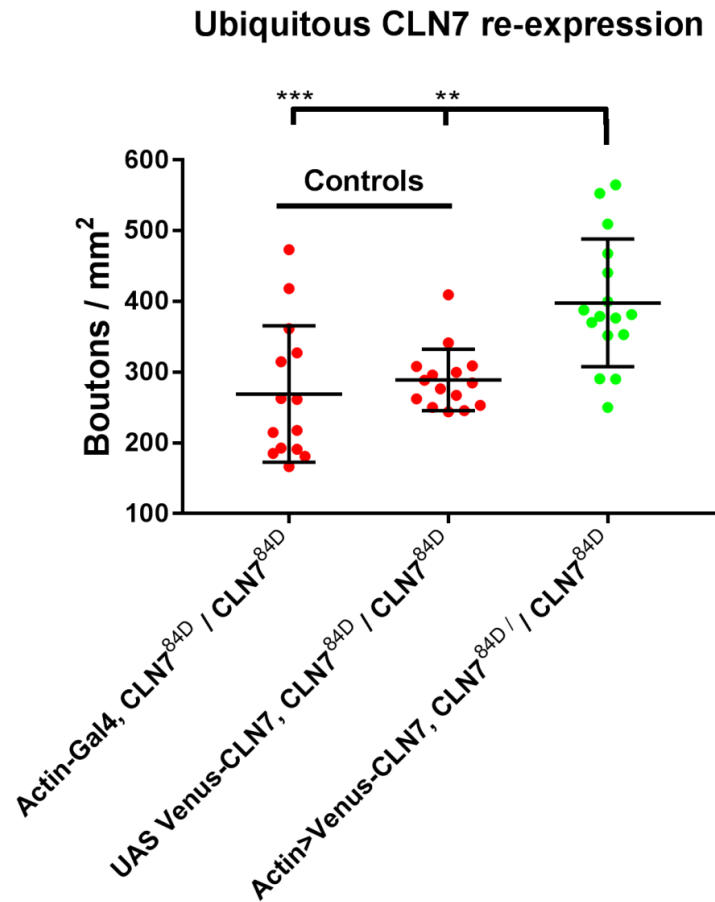
Figure 5.5: Ubiquitous re-expression of CLN7 in a mutant background rescues synaptopathology. Type Ib terminals on muscle 4 were quantified and normalised to the muscle surface area. Ubiquitous re-expression of CLN7 using ActinGal4 (397.8) caused a significant rescue in synapse size compared to the ActinGal4 (269.1) and UAS-venus-CLN7 (289.1) controls alone. A 37.60% increase compared to the UAS-CLN7 control. B: Representative images of type Ib boutons found on muscle 4 for each genotype. ANOVA test was used. ** p<0.01 and *** p<0.001). Plots represent mean plus standard deviations.
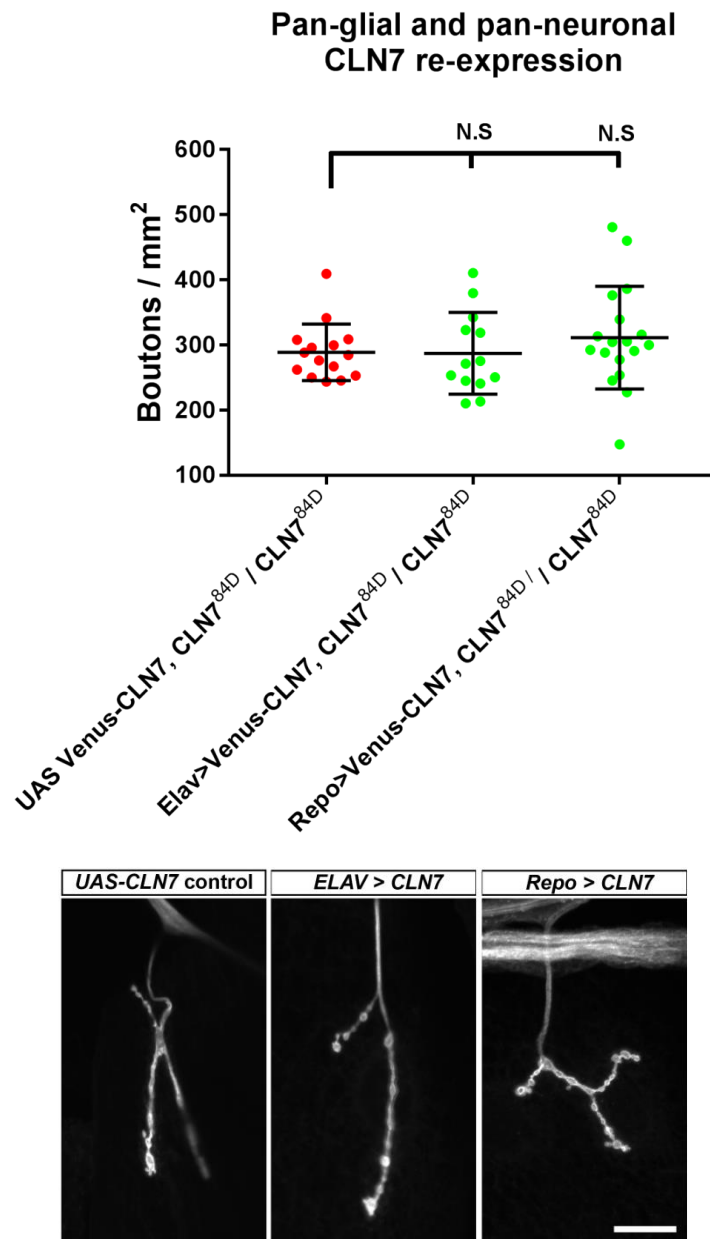
Figure 5.6: Pan neuronal and pan-glial re-expression of UAS-YFP-CLN7 does not rescue mutant phenotypes. Type Ib terminals on muscle 4 were quantified and normalised to the muscle surface area. Neuronal and glial re-expression of YFP-CLN7 using ElavGal4 (289.1) and RepoGAL4 (324.7) respectively did not rescue mutant phenotypes compared to the UAS-venus-CLN7 control (311.6). B: Representative images of type Ib boutons found on muscle 4 for each genotype. ANOVA was used. N.S>0.05. Plots represent mean plus standard deviations.
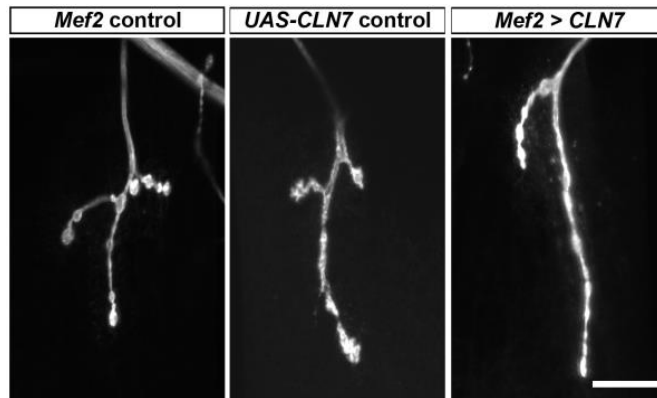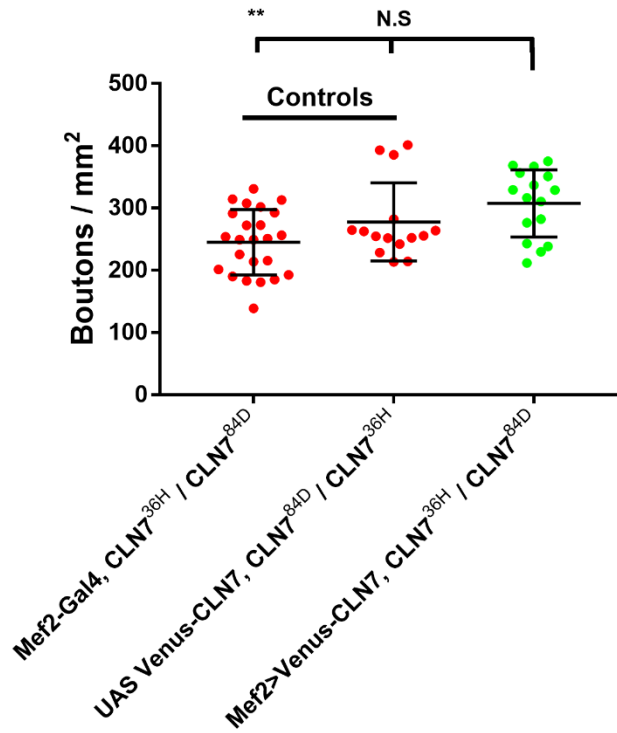
Figure 5.7: Postsynaptic re-expression of CLN7 causes a partial but not significant rescue. Type Ib terminals on muscle 4 were quantified and normalised to the muscle surface area. Postsynaptic re-expression of CLN7 using Mef2Gal4 (307.7) caused a significant rescue in synapse size compared to the MefGal4 (245.2, p=0.0021) and partial against UAS-venus-CLN7 controls (277.8, p=0.2438). B: Representative images of type Ib boutons found on muscle 4 for each genotype. ANOVA test was used. N.S>0.05. ** p<0.01 Plots represent mean plus standard deviations.
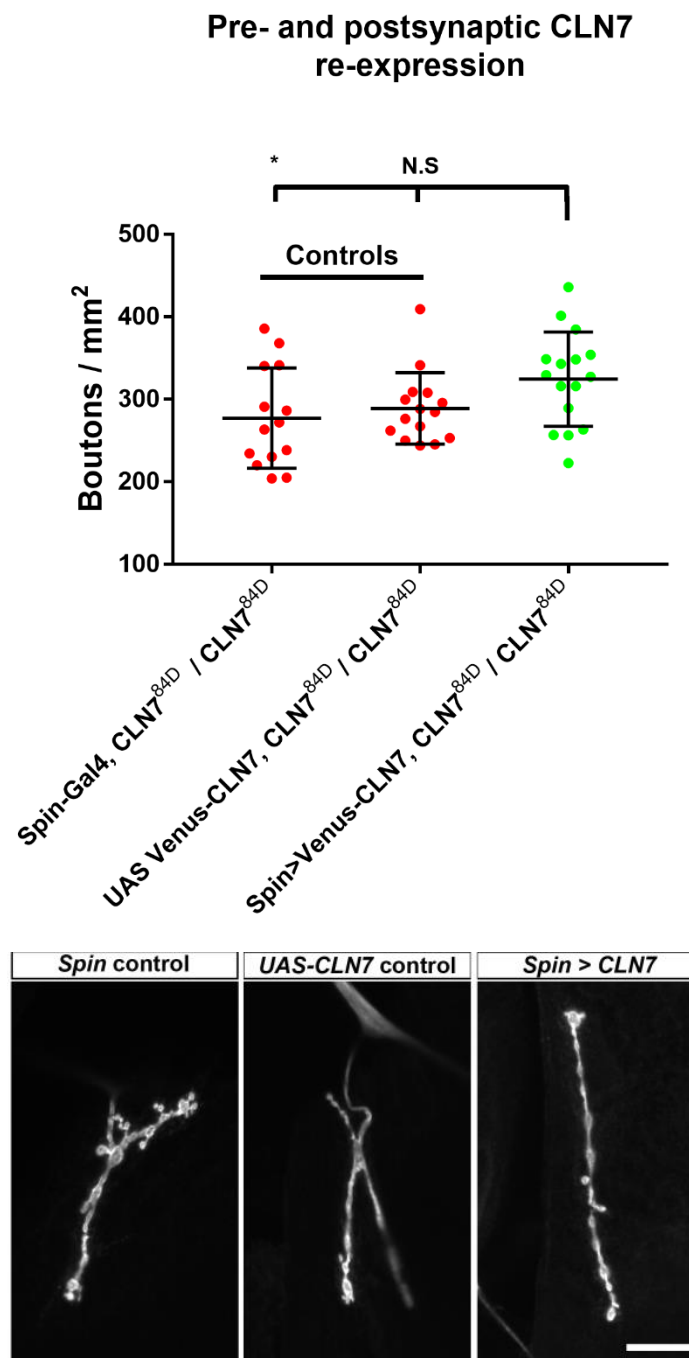
Figure 5.8: Pre-, post-synaptic and glia re-expression has partial rescue. Re-expression of CLN7 in the pre- and postsynaptic side and peripheral glia simultaneously with spin-Gal4 (324*) caused a significant rescue in synapse size compared to the SpinGal4 (277.3, p=0.0395) and partial rescue against UAS-venus-CLN7 controls (289.1, p=0.1315). B: Representative images of type Ib boutons found on muscle 4 for each genotype. ANOVA test was used. N.S>0.05. * p<0.05 Plots represent mean plus standard deviations.

5.2.2 YFP-CLN7 knock-in has pathology at the NMJ

The development of the NMJ seems to be sensitive to levels of CLN7 with both *CLN7* alleles being haploinsufficent. In chapter 3, I determined the YFP-CLN7 knock-in generated using CRISPR was expressed at approximately 30% of its isogenic controls. Therefore, I wanted to determine if the low levels of YFP-CLN7 from the knock-in construct would result in a phenotype at the NMJ. *YFP-CLN7* (with the artificial intron) larvae (299.7 ± 35.79, n=16) had a significant 25.76% decrease in boutons compared to control (403.7 ± 52.91, n=13, P=0.0001) and was at a similar level to *CLN7^{84D}* (306.4 ± 54.79, n=20, figure 5.9). The removal of the artificial intron had no effect as v^1*;YFP-CLN7* (plus AI) (386.5 ± 93.14, n=26) had a significant 19.16% decrease in boutons compared to the v^1 control (478.1 ± 67.99, n= 16, P=0.0015 unpaired t-test). This indicates that the YFP-CLN7 knock-in lines exhibits NMJ phenotypes similar to *CLN7* mutants. As ubiquitous re-expression of YFP-CLN7 in a mutant background is able to rescue the NMJ phenotype, indicating that a YFP-CLN7 fusion folds correctly (Figure 5.5), the phenotype is most likely caused by the low expression of the gene, and haploinsufficiency of *CLN7,* as opposed to the fusion of YFP to CLN7.

5.2.5 Autophagy not majorly effected in *CLN7* mutants

Defects in autophagy have been reported in the NCLs, including a mouse model of CLN7 disease (Brandenstein et al., 2016). Autophagy, regulated by mTOR, has been shown to act as a positive regulator of NMJ development in *Drosophila* with autophagy mutants having a reduction in boutons similar to that seen in *CLN7* mutants (Shen and Ganetzky, 2009). To investigate if a defect in autophagy was a

Figure 5.9: YFP-CLN7 exhibits mutant phenotype. Type Ib terminals on muscle 4 were quantified and normalised to the muscle surface area. *YFP-CLN7* knock-in lines express *CLN7* at approximately 30% of endogenous levels. *YFP-CLN7* larvae including the artificial intron (AI) (299.7) develop similarly few boutons as *CLN7*[84D] mutants (306.4) but is significantly lower than the *w*[1118] control (403.7, p<0.0001). A similar reduction is seen in the *YFP-CLN7 (-AI)* line (386.5) when compared to its *vermillion (v1)* control (478.5). B: Representative images of type Ib boutons found on muscle 4 for each genotype. ANOVA was used to compare the first three groups in A and an unpaired t test was used to compare remaining two groups. ** *p*<0.01 and **** p<0.0001). Plots represent mean plus standard deviations.

cause of the reduction of boutons in the *CLN7* flies, I quantified the accumulation of p62, which has been used as a readout of autophagic flux state. p62 is a multi-domain protein that recognises cellular waste and acts as a receptor to initiate autophagy (Katsuragi et al., 2015). A failure in autophagy or lysosomal function will lead to an accumulation of p62 in lysosomes. mTOR integrates information of the nutritional state of the cell and decides between cell growth and autophagy. In nutrient-rich conditions, mTOR is activated and drives cellular growth while inhibiting autophagy. However, in nutrient-deprived states, mTOR becomes inactive leading to the activation of autophagy. Under nutrient-rich conditions (fed), *w^{1118}* control larvae had no accumulation of p62 as it is continually degraded by lysosomes, but during starvation, low levels of p62 started to accumulate (Figure 5.10) as autophagy is activated by the inhibition of TORC signalling. In *CLN7* larvae, no p62 is detected in the fed state similar to controls (p=0.9831). During the fed state, there is a slight increase in p62 accumulation compared to controls, although this is not close to statistical significance (p=0.7750). An autophagy mutant, *atg18/Df*, was used as a positive control and exhibited significant (p=0.0063) low level p62 accumulation under fed states, and a dramatic increase in accumulation under starved states (p=0.0090) compared to *w^{1118}* control. Although no p62 build-up is visualised in *CLN7* mutants, one experiment is not enough to definitively rule out a defect in autophagy (Klionsky et al., 2016). As levels of p62 can be increased by transcriptional upregulation of p62 upon autophagy induction by prolonged starvation or with certain pharmacological inducers ((Sahani et al., 2014, Kuoa et al., 2015)), determining levels of p62 transcripts would also help investigate an autophagy defect. Additional
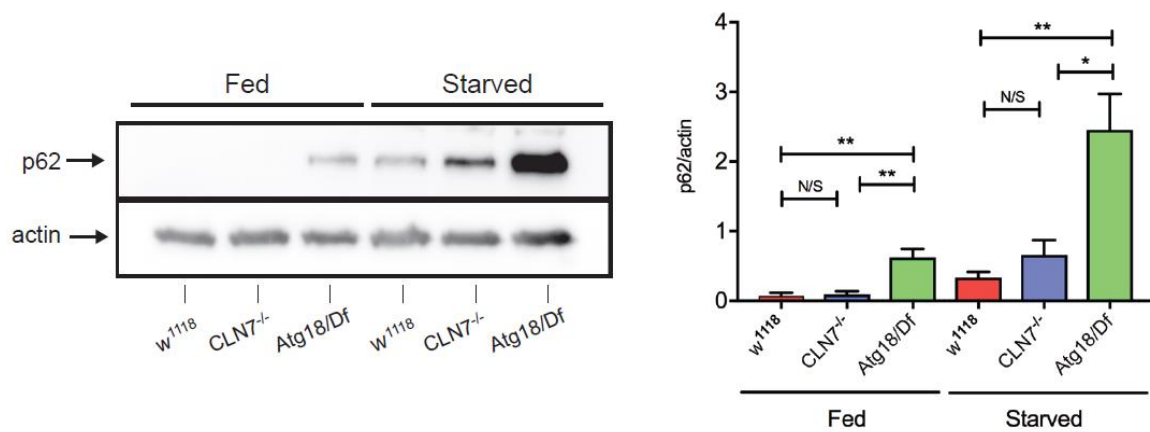
Figure 5.10: *CLN7* **mutants do not suffer major autophagy defects.** The lysosomal substrate, p62, accumulates when there is a block in autophagy and can be detected by western blots. A: When larvae are fed, p62 does not accumulate in w^{1118} controls or *CLN7* mutant larvae but does in *atg18* mutants. After 3-4 hours starvation, p62 accumulates in control animals and slightly more in *CLN7* larvae, but not significantly. However, p62 accumulates to higher levels in starved *atg18* mutants. B. Quantification of A. p62 intensities were normalised to respective actin bands. Error bars represent mean ± SEM (n=3 for each). N/S p>0.05, * p<0.05 and ** p<0.01.

experiments assessing autophagy is required to conclude whether autophagy is defective, which may include the use of tandem-tagging of LC3 (encoded by *atg8* in *Drosophila*) to monitor autophagic flux.

5.2.6 CLN7 is not involved in TGF-β signalling

As the localisation and genetic studies suggest CLN7 is required in the postsynaptic muscles, one possible hypothesis is CLN7 regulates retrograde signalling from the muscle to neuron that drives expansion of the pre-synaptic compartment. These retrograde signals are important for the homeostasic regulation controlling the relative sizes of post-synaptic muscle and pre-synaptic neuron. One retrograde mechanism known to regulate the development of the NMJ in both *Drosophila* and mammals is TGF-β signalling. Downregulating this pathway results in similar neuronal undergrowth phenotypes to the loss of *CLN7* (McCabe et al., 2003, Rawson et al., 2003). I asked whether the TGF- β pathway is still functional in the *CLN7* mutants. Sax encodes a type I TGF-β receptor in the pre-synaptic membrane. Along with thickveins, Sax binds the TGF-β ligand, glass bottomed boat and activates SMAD signalling in the neuron. Inhibiting the pathway with a *sax* mutant resulted in a decrease in boutons (296.3 ± 54.09, n=9) compared to w^{1118} controls (403.7 ± 52.91, n=13, p=0.0440) and at similar numbers to *CLN7* larvae (306.4 ± 54.79, n=20) (Figure 5.11). Upregulating this pathway using a *Dad* mutant, which encodes an inhibitory SMAD that functions in the neuron, resulted in a significant increase in boutons (562.8 ± 72.34, n=12) compared to w^{1118} controls (p=0.0263) and was accompanied by satellite boutons

CLN7 on the TGF-β signalling pathway
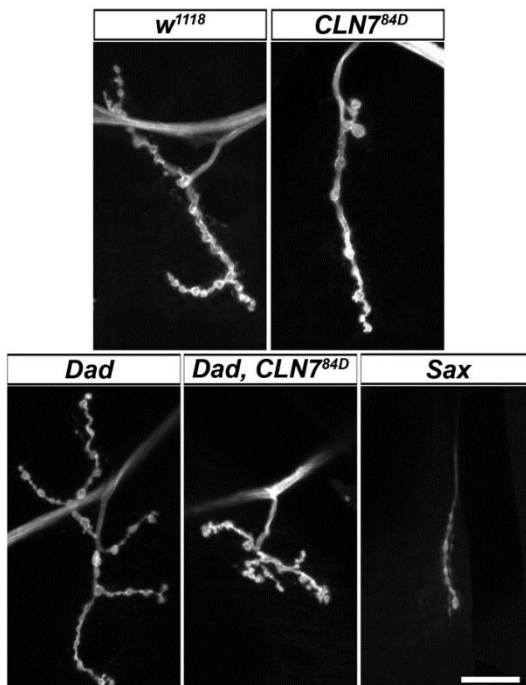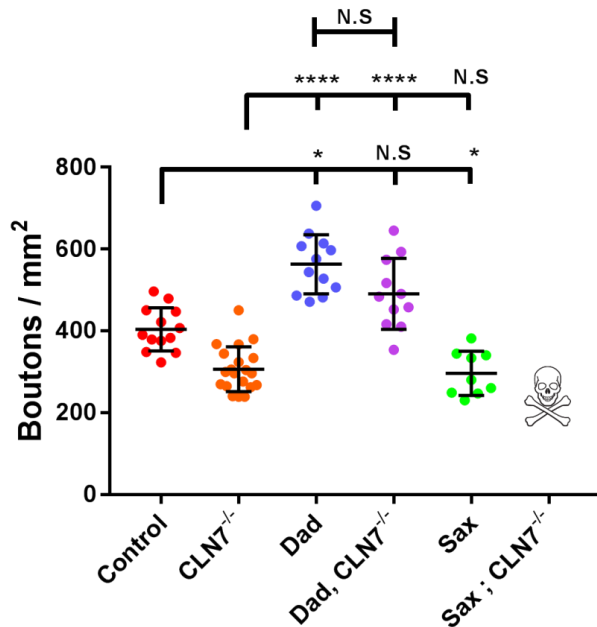
Figure 5.11: CLN7 is not involved in TGF-β signalling. Mutations along the TGF-β retrograde signalling pathway from the muscle affect NMJ development. A: Mutations in *Dad*, an inhibitory SMAD, causes an NMJ overgrowth of phenotype (562.8); mutations in *saxophone* (*sax*), a type I TGFβ receptor results in undergrowth phenotype (296.3) similar to *CLN7* mutants (306.4). Introducing a *CLN7* mutation into a *Dad;CLN7* double mutant results in a decrease in boutons compared to the Dad (490.4). A *sax;CLN7* double mutant is lethal early in development. B: Representative images of type Ib boutons found on muscle 4 for each genotype. (ANOVA was used. N.S>0.05, * p<0.05 and **** p<0.0001. Plots represent mean plus standard deviations.

(Figure 5.11). *CLN7/sax* and *CLN7/Dad* double mutant lines were made. If Sax or Dad, both of which are located at the pre-synaptic side, was epistatic to CLN7 a *CLN7/sax* would be expected to maintain *CLN7* or *sax* mutant phenotype, while a *CLN7/Dad* double mutant would show the Dad the overgrowth phenotype and satellite bouton formation. The *CLN7/sax* combination was lethal in early larval stages indicating a likely additive effect and that CLN7 and Sax operate in different pathways (Figure 5.11). The *CLN7/Dad* combination formed satellite boutons and resulted in an intermediate phenotype (490.4 ± 86.79, n=11) which was still significantly higher than *CLN7* larvae (306.4 ± 54.79, n=20, p<0.0001, Figure 5.11). This also indicated that CLN7 and Dad act in separate pathways.

To support these findings, anti-phosphorylated-MAD (pMAD) staining was carried out in presynaptic terminals at the NMJ and in motor neuron nuclei where pMAD is transported to. This can be used as a read-out of TGF-β signalling. Punctate pMAD staining is detected in the nuclei and at the NMJ in *w[1118]* controls but ablated in a *wit* mutant, which normally exhibits a reduction in boutons (Aberle et al., 2002), indicating specificity of the antibody (Figure 5.12). pMAD staining in *CLN7* was similar to *w[1118]* in both regions suggesting the phosphorylation of MAD at the NMJ and its subsequent transport to the nuclei was unaffected and not the cause of the reduction of boutons in *CLN7*.

5.2.7 CLN7 in Wnt signalling

Another well studied retrograde mechanism known to regulate NMJ development in mammals and *Drosophila* is Wnt signalling. Downregulating Wnt signalling using
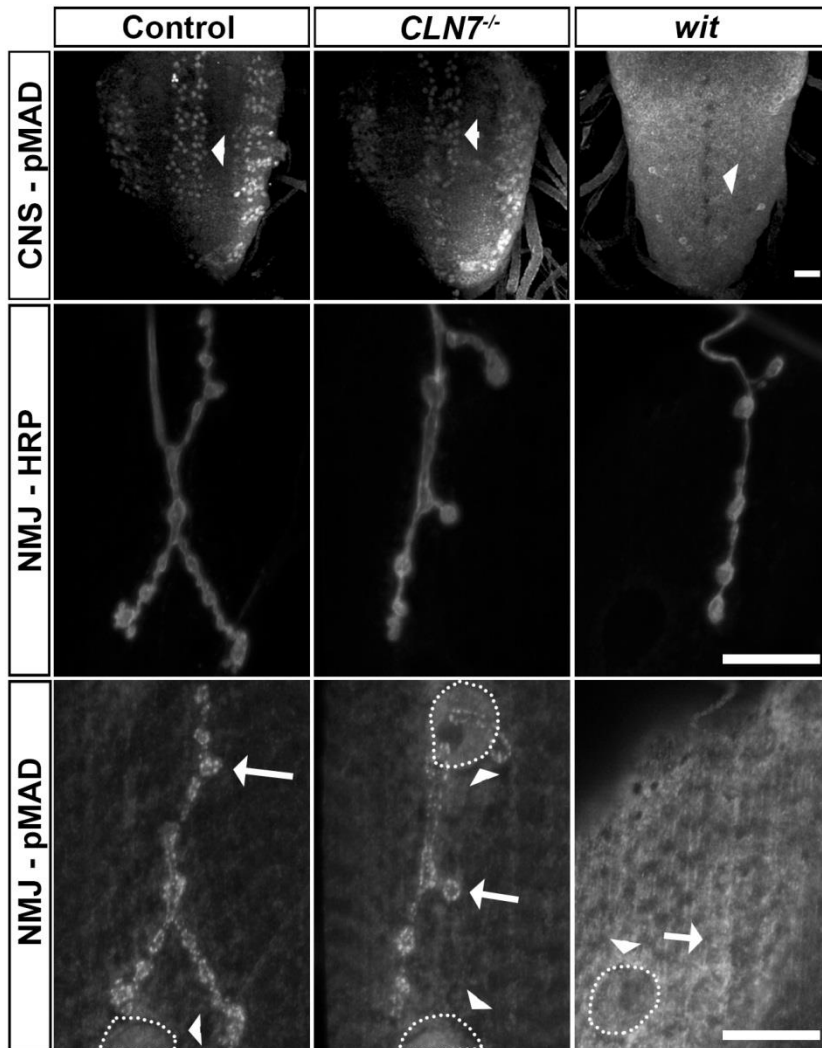
Figure 5.12: pMAD levels in CLN7 mutants are unaffected. Binding of Gbb to Tkv, Sax, and Wit receptors results in the phosphorylation of Mad (pMAD) in the presynaptic side before being transported to the motor neuron nuclei. pMAD staining is visible in motor neurons in the w^{1118} positive control and *CLN7* mutant CNS but is absent in wit mutant CNS, a negative control (arrowheads). The neuronal plasma membrane was counterstained with anti-HRP. pMad staining at the NMJ is also visible in the positive control and *CLN7* mutant, but absent in the wit mutant (arrows). Similarly, pMad is localised within muscle nuclei but absent in wit mutants (dashed circles and arrowheads). Scale bar = 20μM.

various mutants results in a reduction of boutons like *CLN7* (Budnik and Salinas, 2011, Packard et al., 2002)*.* Quantifying boutons of a *wnt5* mutant, which encodes a Wnt ligand, resulted in a significant reduction in boutons (278 ± 54.61, n=16) compared to w^{1118} controls (403.7 ± 52.91, n=13, p<0.0001) as reported by others, and was similar to *CLN7* larvae (306.4 ±54.79, n=20, figure 5.13). Attempts were made to make a *wnt5/CLN7* double mutant which would have allowed a genetic epistatic study to be carried out, however this was unsuccessful as a result of unstable intermediate lines for unknown reasons and due to time constraints could not be investigated further. Further investigations is needed to determine if CLN7 is involved in Wnt signalling by generating other double mutant combinations with *CLN7* or via additional methods.
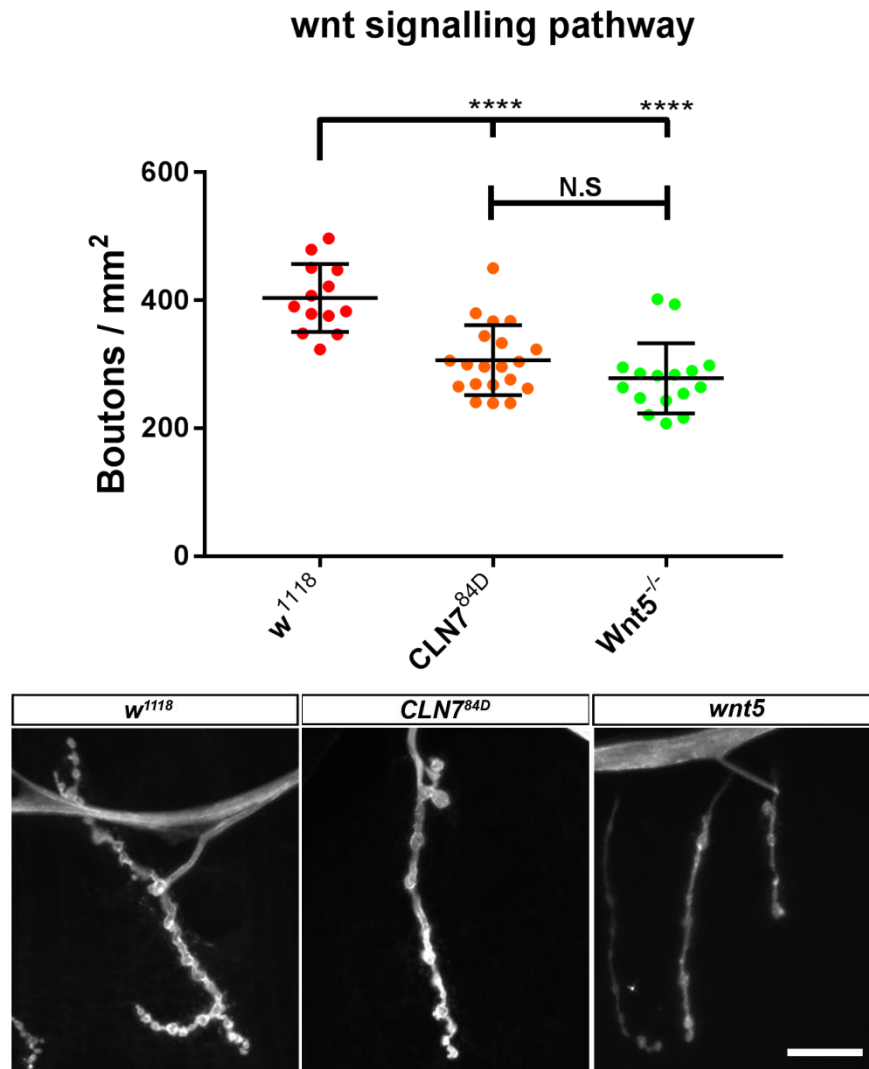
Figure 5.13: *CLN7* **mutants resemble** *wnt* **mutants.** The wnt signalling pathway is involved in retrograde NMJ development. A: Mutations in *wnt5*, results in a significant undergrowth phenotype (278) compared to *w1118* controls (403.7, p<0.0001) and similar to *CLN7* mutants (306.4, p=0.2723). B: Representative images of type Ib boutons found on muscle 4 for each genotype. (ANOVA) test was used. N.S>0.05 and **** p<0.0001. Plots represent mean plus standard deviations.

5.4 Discussion

Here, I have used the *Drosophila* model system to establish how mutations in *CLN7*, responsible for a childhood onset neurodegenerative disease, affect the development of the nervous system. These questions are difficult to answer in mouse models of CLN7 disease. Instead, I have used the NMJ of *Drosophila* to look for role for CLN7 in the growth and homeostasic development of the nervous system. The *Drosophila* NMJ is a simple, genetically tractable model for studying the development of the synapse. It provides ease of access to microscopy and electrical recording, stereotyped development which can be readily quantified, and is structurally similar to central excitatory synapses of the mammalian CNS. Hence, the NMJ can be used to look at the mechanisms of synaptopathology which occur in most or all forms of neurodegeneration, including the NCLs (Kielar et al., 2009a, Sharma et al., 2012, Bond et al., 2013, Koch et al., 2011, Partanen et al., 2008b, Henstridge et al., 2016, Bae and Kim, 2017, Aby et al., 2013, Kim et al., 2008). I have shown loss of CLN7 in *Drosophila* results in the development of significantly fewer boutons indicating an essential role for CLN7 in NMJ development. Type Ib boutons were solely quantified in my study as type Is boutons have previously been shown within the lab to be unaffected by the loss of CLN7, even though localisation data in chapter 3 indicates CLN7 localises to both type Is and Ib boutons and not type II or type III boutons (unpublished observations). This may arise due to the different functional roles as in the phasic type Is synaptic terminals vs the tonic type Ib terminals respectively (Lnenicka and Keshishian, 2000) and suggests there may

be some functional redundancy for regulating type Is boutons or that CLN7 is particularly crucial to the development of type Ib boutons.

5.4.1 CLN7 is required in muscle for NMJ development

The development of the NMJ is regulated by the presynaptic neurons, postsynaptic muscle and peripheral glia (Menon et al., 2013). Knocking down CLN7 in each of these tissues indicated CLN7 expression is crucial in the muscles (Mef2-Gal4) as opposed to presynaptic neuronal (Elav-Gal4) or glial (Repo-Gal4) expression. This correlates with the localisation study carried out in chapter 4 which shows that CLN7 is specifically expressed in muscles and localises to the postsynaptic density but appears to be absent from the motor neurons and enseathing glia. However re-expression of CLN7 in *CLN7* muscles (Mef2-Gal4) is unable to fully rescue the mutant phenotype along with re-expressing in all three cell types simultaneously using Spin-Gal4 (Sweeney and Davis, 2002). This suggests CLN7 may also be required elsewhere to regulate the NMJ as ubiquitous (Actin-Gal4) re-expression is able to fully recue the mutant phenotype. The knockdown and localisation data combined also suggest CLN7 may regulate neural growth development in a retrograde manner from the muscle.

5.4.2 No major autophagy defect observed in *CLN7*$^{-/-}$

CLN7 is a putative lysosomal transmembrane protein required on the postsynaptic side of the NMJ. One of the key functions of lysosomes is the regulation of TOR signalling and its downstream target autophagy. Defects in autophagy is common in many if not all neurodegenerative diseases (Kiriyama and Nochi, 2015) and seen

in mouse models of CLN2, CLN3, CLN5, CLN6 and CLN10 disease (Cao et al., 2006, Thelen et al., 2012, Koike et al., 2000, Leinonen et al., 2017, Micsenyi et al., 2013). Dysregulation of both have also been observed in mouse models of CLN7 disease with mutants experiencing impaired mTORC1 reactivation after prolonged starvation and autophagy defects (Seranova et al., 2017, Danyukova et al., 2018, Brandenstein et al., 2016).

Postsynaptic regulation of TOR signalling in mammals and flies have also been shown to effect synaptic activity in central and peripheral synapses in vertebrates and *Drosophila*, (Henry et al., 2018, Penney et al., 2012) with defects in TOR signalling being implicated in decline of cognitive functions and autism (Lipton and Sahin, 2014). However, changes in TORC1 signalling does not alter the number of boutons (Penney et al., 2012). In *Drosophila*, autophagy, specifically in the presynaptic side, regulates neural development at the NMJ with autophagy mutants producing a similar reduction of boutons phenotype as *CLN7* larvae (Shen and Ganetzky, 2009). Therefore, as CLN7 has been implicated in TORC signalling, in combination with the postsynaptic localisation and NMJ phenotype, it was hypothesised that loss of CLN7 may cause defects in autophagy via impaired retrograde TOR signalling resulting in the reduction of boutons in *CLN7*. However, no significant p62 build-up was observed suggesting autophagy may be majorly intact within the fly. This was supported by studies carried out within the lab which demonstrated upregulation of autophagy via pharmacological inhibition of mTOR using rapamycin and Torin, resulted in an increase in boutons in both *CLN7* and control larvae reflecting an increase in autophagy (Katelyn 2016, personal

communication, (Shen and Ganetzky, 2009)). This indicated there was no block in the autophagy process and that is mTOR epistatic of CLN7. However, additional experiments are required to determine if autophagy is truly intact in *CLN7* flies because no single experiment is able to conclude if autophagy is functional.

5.4.3 CLN7 forms a complex with RHEB

My data suggest CLN7 that is haploinsufficient with abnormal development of the NMJ being observed in *CLN7* heterozygotes where CLN7 is expressed at 50%. The CRISPR generated *YFP-CLN7* knock-in was found to be expressed at only 30% of wildtype levels in chapter 3 for reasons that are unclear and this also exhibited mutant phenotype at the NMJ. This is likely due to the haploinsufficient nature of the protein as opposed to having an YFP fused to the N-terminal because all Gal4-UAS re-expression experiments utilised an N-terminal YFP-CLN7 and re-expressing YFP-CLN7 ubiquitously (Actin-Gal4) fully rescues the mutant phenotype. A similar phenotype was observed when CLN7 was overexpressed ubiquitously. Co-immunoprecipitation data indicates CLN7 forms a complex with RHEB, a known upstream regulator of mTOR (Personal communication with Richard Tuxworth and Kyle Connolly, UoB), indicating a potential TORC regulatory signalling mechanism. This indicates normal development of NMJ is sensitive to levels of CLN7 which may be regulated by the stoichiometry of a multimeric-complex. As under- and over-expression both lead to potential alterations in stoichiometry, this suggest CLN7 is likely to form a multimeric complex with RHEB and more yet to be identified proteins.

5.4.4 Potential roles in NMJ development

The lysosome is important to neuronal health and the development of NMJs and seems to be required predominantly on the presynaptic neuronal side. Within neurons, lysosomes generally reside in the cell body, but on rare occasions can also be found at the synaptic terminal. The importance of lysosomes in NMJ development have been shown by LSD models which include mutations in Spinster (also known as benchwarmer), a MFS lysosomal transmembrane protein, and Trpml, a lysosomal Ca^{2+} channel which regulates the storage and release of lysosomal Ca^{2+} when required (McGuinness et al., 2007, Morgan et al., 2011). Mutations in both are used as models for LSDs with mutations in the human homologue of *Trpml* the cause of Mucolipodosis type IV (MLIV), a LSD. Both proteins localise to late endosomes and lysosomes in the pre-synaptic side while Spinster also being expressed on the postsynaptic side (Wong et al., 2012, Sweeney and Davis, 2002). *Trpml* mutants present an undergrowth phenotype similar to *CLN7* (Wong et al., 2014). This is due to an imbalance in Ca^{2+} homeostasis which also regulates TOR signalling resulting in a defect in autophagy (Wong et al., 2012). However, in both of these models, the defect is based predominantly in the pre-synaptic compartment. This contrasts with CLN7 which is exclusively post-synaptic. Although autophagy is not majorly dysregulated in *CLN7*, a small contribution cannot be ruled out due to the slight increase in p62 build-up when starved. To further investigate potential defects in autophagy, the localisation and morphology of mitochondria at the NMJ can be determined *in vivo* using *mito::GFP* lines or MitoTracker. However, roles for CLN7 on TORC signalling and its localisation suggest potentially a unique mechanism in NMJ development involving

TORC signalling. New data within the lab indicate CLN7 may affect TORC2 signalling (personal communication with Richard) which has also been shown to regulate NMJ development (Natarajan et al., 2013).

Loss of Spinster mutations lead to an NMJ overgrowth phenotype caused by an increase in neuronal reactive oxygen species (Milton et al., 2011) and also due to an increase in the TGF-β retrograde signalling pathway (Sweeney and Davis, 2002). Response to oxidative stress in *CLN7* remains intact and is unlikely to affect NMJ development, unlike a model of juvenile NCL with mutations in *Cln3,* which has a similar neuronal undergrowth phenotype as CLN7 mutants, but which fails to respond to increased oxidative stress (Tuxworth et al., 2011a) (personal communication with Richard Tuxworth and Katelyn Aitchison). TGF-β signalling has also been implicated in several neurodegenerative diseases including, multiple sclerosis (MS), amyotrophic lateral sclerosis (ALS) and spinal muscular atrophy (SMA). Lower levels of pMad are found in an SMA (Chang et al., 2008) and ALS (Ratnaparkhi et al., 2008) fly models, while an increase is found in MS (Kim et al., 2010) which can be used as a readout of TGF-β signalling, however no detectable changes was detected in *CLN7.* While the NMJ in *CLN7* larvae resemble a downregulation of the TGF-β pathway (Aberle et al., 2002, Rawson et al., 2003, McCabe et al., 2003), CLN7 was shown to act independent to this pathway with a *sax-CLN7* double mutant resulting in developmental lethality.

The other major retrograde signalling known to regulate NMJ development is Wnt signalling. *Wnt* larvae were shown to have a smaller synapse as reported by others,

and this was found to match *CLN7.* Unlike the TGF-β pathway, the Wnt pathway requires further investigation as balancer lethality during generation of double mutants hindered experiments. A *wnt5, CLN7* double mutant would have been able to identify if CLN7 functioned alone this pathway. In addition, the Frizzled Nuclear Import (FNI) pathway, regulated by Wnt signalling, in the postsynaptic muscle has been shown to regulate the NMJ (Budnik and Salinas, 2011, Speese and Budnik, 2007, Mathew et al., 2005). Wingless (Wg) released by the pre-synaptic terminal binds to the postsynaptic Frizzled receptor (dFz) causing it to be endocytosed and then transported to the nucleus where the C-terminal domain is cleaved and translocate into the nucleus. Antibodies against the C-terminus of the Frizzled receptor (Mathew et al., 2005) can be used to determine if this pathway is intact in *CLN7* mutants but despite several requests could not be obtained from the group that developed them. If given the time, another trans-synaptic homeostatic signalling mechanism which regulates neural development in both mammals and *Drosophila* is the fibroblast growth factor (FGF) pathway could also be investigated (Fox et al., 2007, Sen et al., 2011). In contrast to the TGF-β and Wnt pathways, transmitter release at the presynaptic terminal activates the postsynaptic FGF pathway in the muscle downstream Ras/Raf/MAP kinase signalling. Downregulation of this pathway in *Drosophila* results in a reduction of boutons similar to *CLN7.* Given the postsynaptic localisation of CLN7, carrying out epistatic assays would determine if CLN7 is involved in this pathway.

6. PHYSIOLOGICAL ROLES OF CLN7 IN THE VISUAL SYSTEM

Parts of this chapter have been published: (Mohammed et al., 2017)

Functional work was done in collaboration with Dr Chris Elliott

6.1 Introduction

The NCLs, as a group, share a similar progression of disease even though the age of onset varies. Some symptoms of NCLs include epilepsy and a decrease of visual acuity which can ultimately lead to blindness. Visual failure is one of the earliest symptoms in CLN7 disease and has been modelled in a mouse model of CLN7 disease (Jankowiak et al., 2016). The *Drosophila* larval visual system is made up of an imaginal eye disc, containing photoreceptors, which develop into structures of the eye in adult flies and the optic lobe, which is the site of photoreceptor projections and synapse. In the localisation study (chapter 4), CLN7 was determined to be expressed in the lamina neurons of the larval CNS which forms part of the developing visual system. Given pathology of the visual system in patients, it was of interest to look more closely at the expression of CLN7 in the Drosophila visual system.

Build-up of autofluorescent material is the hallmark of the NCLs. This is not present in the central brain regions of CLN7 mutant flies consistent with no neural expression of CLN7 in these regions (not shown). However, given CLN7 expression in the visual system, here I asked whether there is autofluorescent material present

in the visual system in ageing *CLN7* mutant flies. Secondly, I investigated the roles of CLN7 within the developing visual system in larvae via a phototaxis assay and using two functional assays – electroretinograms (ERGs) and steady state visual evoked system (SSVEP) – on adult flies to assess visual acuity and determine if loss of CLN7 has functional consequences in the visual system. The ERG assay responds to luminescence and various components of an ERG trace can be analysed (Figure 6.1) providing a readout of synaptic transmission between the photoreceptors and underlying lamina neurons. The SSVEP is used to measure neuronal response amplitudes in the human visual system in adults and infants. This assay measures response to randomised flickering light at differing frequencies providing a comprehensive measurements of contrast response.

The visual system is more sensitive to contrast than to luminescence, therefore neurons have to persistently adapt to their visual environment depending on level of contrast (Priebe and Ferster, 2002). Neurons can be affected by visual stimuli in neighbouring neurons with overlay making an example of this (Busse et al., 2009, Tsai et al., 2011). In SSVEP experiments, each frequency (F) stimulus generates peaks at multiples of F. For example, a 12 Hz stimulus would produce peaks at 12 Hz (first harmonic) and 24 Hz (second harmonic). In this chapter, two frequency inputs will be used one at 12 Hz (input 1) and a second at 15Hz (input 2) used as a mask at constant 30% contrast. Frequency components will be identified as [harmonic]F[input] as characterised in a previous paper (Afsari et al., 2014b). The first harmonic and second harmonic of the first input, 1F1 and 2F1 reflect photoreceptor responses and neuronal signalling in lamina neurons respectively

(figure 6.1). In addition, when two frequencies are fired simultaneously (masking), they generate responses at frequencies that are low-order sum and differences known as intermodulations (1F1 + 1F2 and 2F1 +2F2) which reflect signalling in deeper visual structures, the medulla and lobular plate (Afsari et al., 2014b, Tsai et al., 2011). SSVEPs have been used in to study many aspects of humans including, Parkinson disease (Afsari et al., 2014b), autism (Belmonte and Yurgelun-Todd, 2003) and epilepsy (Birca et al., 2008, Tsai et al., 2011) and provides higher sensitivity than ERGs.

Both ERGs and SSVEP have been used to study a *Drosophila* model of early onset Parkinson's disease. These studies found neurons in the visual system were hyperactive from an early age which resulted in early pathology of the visual system (Hindle et al., 2013). These phenotypes were attributed to an imbalance in Ca^{2+} homeostasis in the visual neurons could be fully rescued by removing excess Ca^{2+} using a continuously active Ca^{2+} transporter (CalX). Given the visual symptoms of CLN7 disease patients and dysregulation of Ca^{2+} seen at the NMJ the ERG and SSVEP will help elucidate some of the roles of CLN7 within neurons.
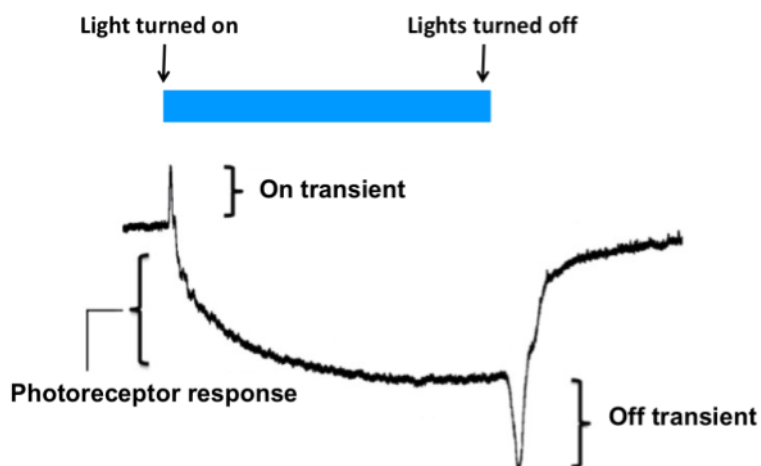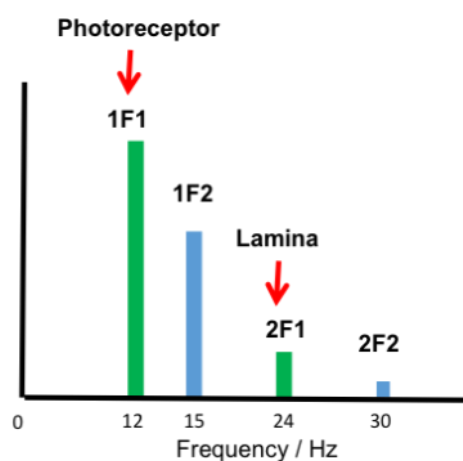
Figure 6.1: Schematic of an ERG and SSVEP response. A: The ERG is made up of 5 main elements: the on- and off-transients, the recovery of each transient back to baseline and the photoreceptor response. The on- and off-transients are produced in response to lights on and lights off phases. B: The SSVEP response is shown after undergoing a Fourier transform. Peaks can be seen at multiples of the frequency stimuli (12 and 24 Hz in green and 15 and 30 Hz in blue, known as first and second harmonics respectively). 1F1 and 2F1 reflects responses from the photoreceptors and lamina neurons respectively. Adapted from (Vilinsky and Johnson, 2012).

6.2 Results

6.2.1 CLN7 is expressed in the developing visual system

Early retinal degeneration is found in most NCL patients and has been modelled in a mouse model of CLN7 disease. I have previously detected expression of YFP-CLN7 (Figure 6.2) in the lamina neurons in the larval optic lobe, therefore I wanted to determine if CLN7 was also expressed within the developing photoreceptors as well. Staining the larval eye discs showed expression of YFP-CLN7 protein in the neurons of each ommatidium which were counterstained with Elav (Figure 6.2) confirming expression of CLN7 in the photoreceptors. The CLN7 protein appears in a membrane-like localisation. Additionally, CLN7 was expressed in glia stained with Repo which corresponds to retinal basal glial (Chotard and Salecker, 2007). YFP-CLN7 can also be seen in the lamina neurons and neuronal projections in the optic lobes (Figure 6.2).

6.2.2 CLN7 is expressed in the adult visual system

The *Drosophila* adult visual system is developed in the third instar larval stage in the imaginal eye disc and within the optic lobe of the brain. In adult the CNS, photoreceptors, first order neurons mature and project onto second-order lamina and third-order medulla neurons. I used the YFP-CLN7 knock-in to look at CLN7 expression within the CNS. I found CLN7 was expressed in the photoreceptors of the optic lobe containing part of the visual system (Figure 6.3). CLN7 was also found to ensheath the whole CNS, most likely representing the BBB but no expression was found within CNS. This indicated the sole neuronal expression of CLN7 was limited to the visual neurons of the visual complex suggesting a role in
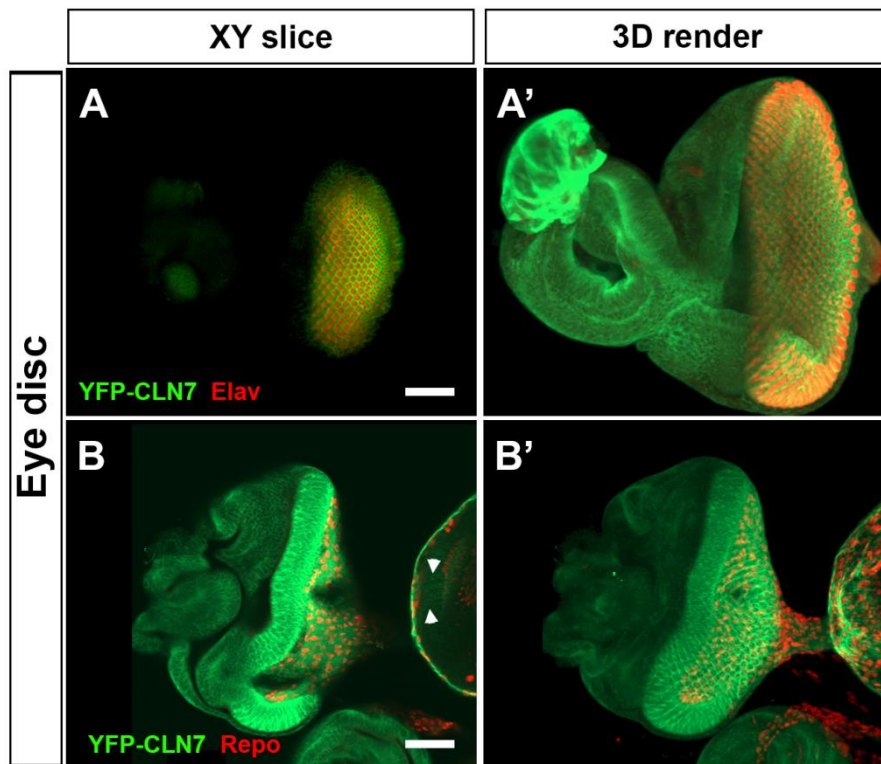
Figure 6.2: CLN7 is expressed in neurons and glia in the developing visual system in third instar larvae. Imaginal eye discs from YFP-CLN7 larvae were stained with anti-GFP (green). A and A': Photoreceptors were counterstained with the neuronal anti-Elav (red) marker which localises with CLN7. B and B': Glial cells were counterstained with anti-Repo (red) marker indicate some localisation with CLN7. A and B show single XY sections; A' and B' show 3D renders of z-stacks. Scale bar = 50 μm.
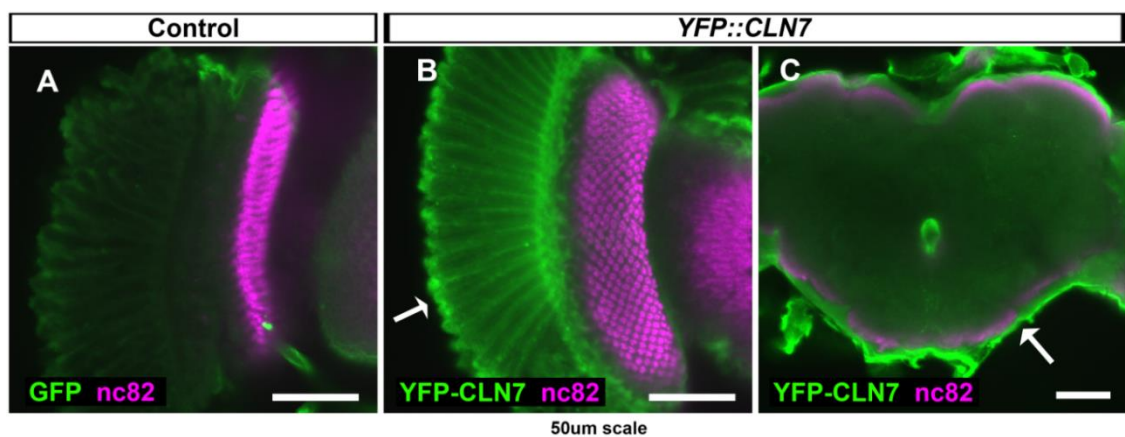
Figure 6.3: CLN7 in adult visual system. A, B and C: The visual system and brain of adult flies from *w1118* and *YFP-CLN7* lines were stained with anti-GFP (green) with the neuropil stained by anti- Bruchpilot (nc82 - magenta). B: CLN7 is expressed in the photoreceptors (arrow) of the adult visual system. C: CLN7 is expressed in cells ensheathing the brain (arrows) but not within the CNS. Scale bar = 50 µm.

visual transduction.

6.2.3 *CLN7* flies develop build-up of autofluorescent material

The LSDs and NCLs are clinically characterised by the build-up of storage material in lysosomes. Different NCL sub-types have different compositions of storage material, although each is characteristically autofluorescent and known as ceroid lipofuscin. As CLN7 was found to be expressed in the surface glia of the CNS and in the primary and secondary order of the visual neurons of the fly, I wanted to determine if loss of CLN7 in the fly would model the clinical build-up of ceroid lipofuscin in patients. At 28 days of age, a significant build-up of autofluorescent material can be seen in *CLN7* flies compared to w^{1118} controls (Figure 6.4). The build-up of autofluorescent material is localised to the photoreceptors while no build-up was seen within the CNS which correlates with the YFP-CLN7 expression data. This indicates the *CLN7* fly model has a similar build-up of autofluorescent storage material and supports its use to study CLN7 function.

6.2.4 *CLN7$^{-/-}$ adult flies* exhibit abnormal synaptic signalling in the visual system

A common symptom of the NCLs is a decrease in visual acuity. Given the ceroid lipofuscin build up in the fly visual system, it was of interest to see whether the loss of CLN7 results in functional physiological consequences within the fly visual system. ERGs, using blue LED lights, were performed to measure visual response to light in a dark-adapted state to see if mutants exhibit abnormal ERGs as seen in CLN7 disease patients (Kousi et al., 2009).
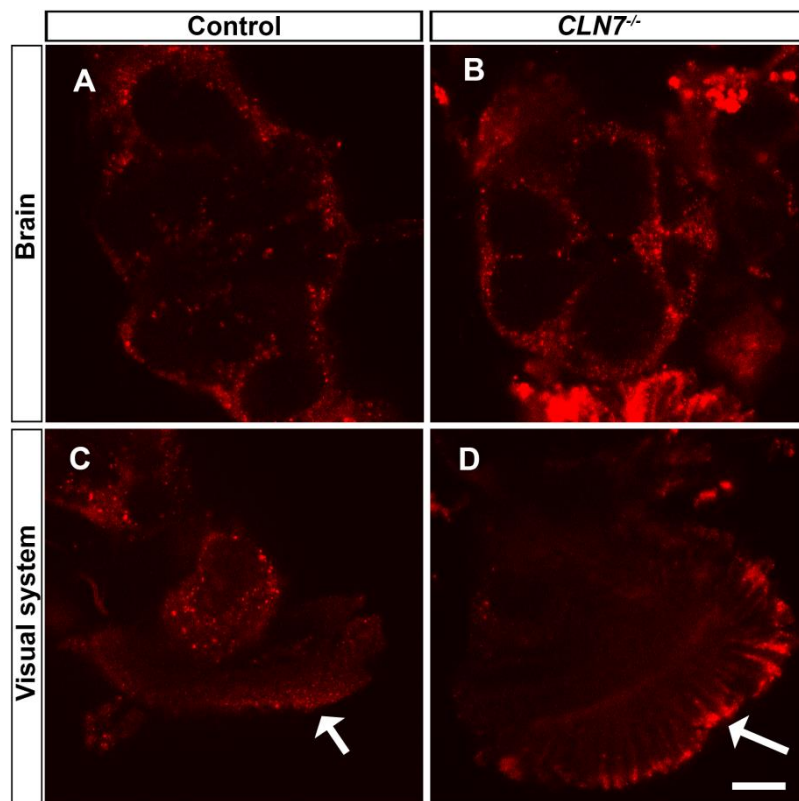
Figure 6.4: Build-up of autofluorescent material in *CLN7*. The CNS and optic lobe of Control w^{1118} and *CLN7* mutant flies were dissected and imaged live. A and B: No clear build-up was seen in the CNS between genotypes. C and D: Qualitative analysis showed *CLN7* have an increase build-up of autofluorescent material in the photoreceptor (arrows). Representative images shown. Scale bar = 50 μm.

ERGs of the fly visual system were recorded at 3 and 28 days of ages. *CLN7* heterozygotes were also examined as they exhibit pathology at the NMJ similar to *CLN7* larvae (chapter 5, figure 5.3). The first component of the ERG to be analysed was the on-transient peak, which reflects synaptic activity between R1–R6 photoreceptors and lamina neurons and hyperpolarisation of the latter. *CLN7* flies have a statistically significant reduction in the on-transient peak (557.9 ± 127.7, n=17) compared to controls (839.5 ± 183, n=16, p=0.0003, figure 6.5). *CLN7* heterozygote flies had an intermediate peak (691.2 ± 273.2, n=10) between *CLN7* and controls, but was non-statistically significant from the control flies (p=0.1401). 28 days old aged flies exhibit a similar phenotype: with *CLN7* flies (532.7 ± 256.2, n=13) having a statistically significant smaller peak compared to w^{1118} controls (839.1 ± 287.4, n=25, p= 0.0001, figure 6.5). *CLN7* heterozygotes produced an intermediate peak (663.1 ± 259.6, n=13) which was non-statistically different from control flies (p=0.1369). Overall, this suggests a possible gene dosage dependant phenotype within the visual system which is contrasts with the haploinsufficient phenotype of CLN7 heterozygotes in NMJ development (Chapter 5, figure 5.3). It also indicates dysregulation in synaptic signalling between the photoreceptors and lamina neurons, depicted as reduced hyperpolarisation of lamina neurons, occurs at an early age and is maintained in aged flies.
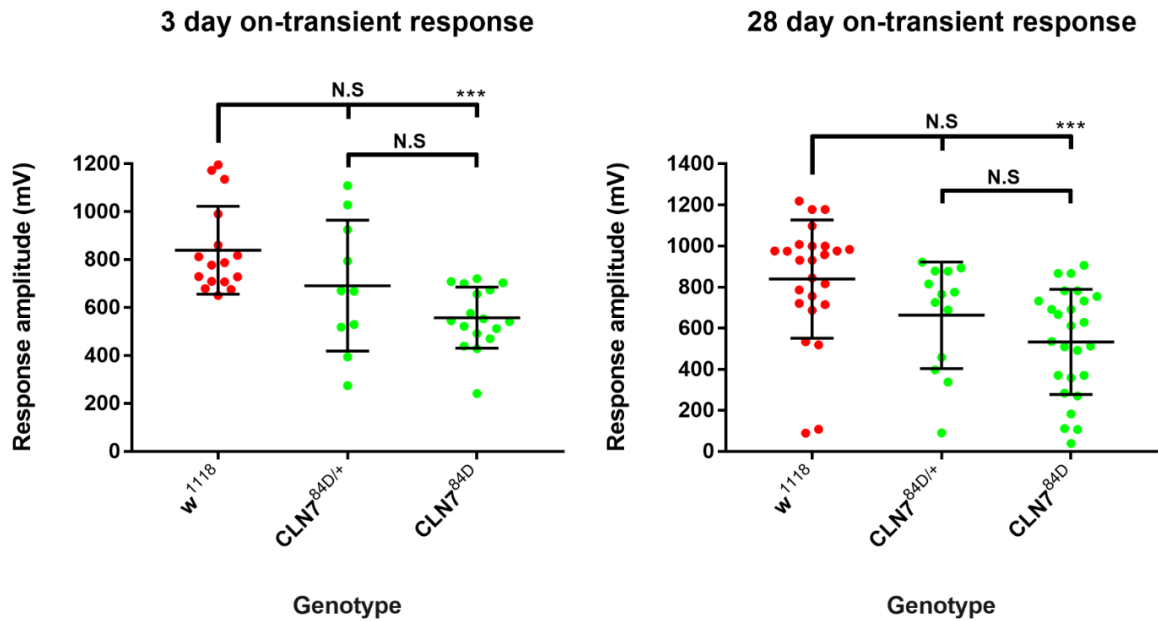
Figure 6.5: *CLN7* flies have abnormal visual responses in visual synapses. At 3 days of age, w^{1118} controls have a significantly larger response amplitude to the lights on lights on phase, on-transient, compared to *CLN7* (p=0.0003). *CLN7^{84D/+}* heterozygotes had an intermediate amplitude that was neither significantly different to control (p=01401) or *CLN7* (p=0.1340). At 28 days of age, a similar pattern is seen, as *CLN7* flies have a significantly reduced amplitude compared to control flies (p=0.0001). *CLN7^{84D/+}* heterozygotes had an intermediate phenotype but was non-statistically significant from control (p=0.1369) and *CLN7* (p=0.5022). (ANOVA, Tukey's post hoc analysis was used at 3 day, Kruskal-Wallis, Dunns post hoc was used at 28 days, N.S p>0.05 and *** *p*<0.001). Plots represent mean ± standard deviation. (Data provided by Dr Chris Elliott).

6.2.5 Defect on lights recovery

The time constant was also quantified which is used as a proxy for the rate of recovery back to baseline following the on-transient peak (lamina neuron hyperpolarisation). The recovery to baseline after the on-transient peak follows an exponential decay formula $(t) = N_0 e^{-\pi t}$: where $N(t)$ is the size of the amplitude at time t, N_0 is the amplitude size at t=0 (maxima peak), π= time constant, and t= time. The time taken for the on-transient peak to return towards baseline by approximately 63.2% (π= 1/e which is approximately 0.368) is referred to as the time constant. As the time constant is a measure of rate as opposed to time/duration, it will not be affected by the size of the on-transient peak as smaller peaks as seen in *CLN7* mutants would be expected to, under normal conditions, to return to baseline faster. *CLN7* flies, had a time constant of -0.005683 ± 0.0004425 (n=17) which was significantly lower than w^{1118} flies (0.004294 ± 0.0007301, n=16, p<0.0001, figure 6.6). As the time constant is inversely proportional to the rate of recovery, a larger modular time constant value, like *CLN7* flies, represents a shorter recovery time. *CLN7* heterozygotes had an intermediate time constant of -0.004811 ± 0.0008018 (n=10), which was statistically significantly higher than *CLN7* flies (p=0.0047) but not from w^{1118} flies (p=0.1320). At 28 days of age, a similar correlation is seen as w^{1118} flies had a significantly higher time constant (-0.003401 ±0.001189, n=25) compared to *CLN7* (-0.005334 ± 0.0023, n=23, p<0.0001), however *CLN7* heterozygotes were also significantly lower than control (-0.005053 ± 0.001175, n=13, p=0.0055, figure 6.6). There was no significant difference between *CLN7* and *CLN7/+* (p>0.9999) at 28 days of age.
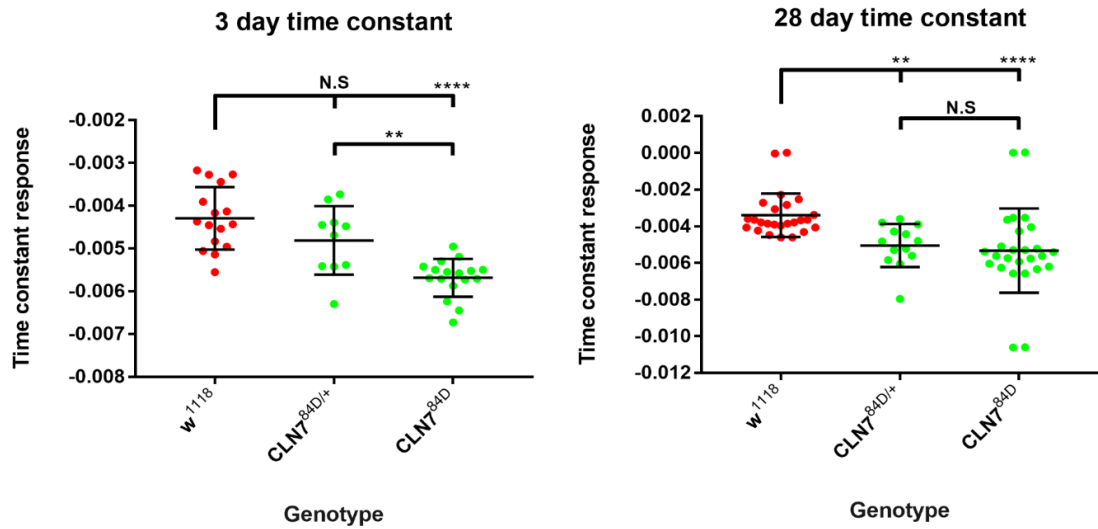
Figure 6.6: *CLN7* flies have smaller time constants. At 3 days of age, w^{1118} controls have a significantly larger time constant to the lights on phase, compared to *CLN7* (p<0.0001). *CLN7^{84D/+}*heterozygotes had an intermediate amplitude that was not significantly different to controls (p=01312) but was from *CLN7* (p=0.0047). At 28 days of age, a similar pattern is seen, as *CLN7* flies have a significantly reduced time constant compared to control flies (p<0.0001). *CLN7^{84D/+}* heterozygotes again had an intermediate phenotype but was now statistically significant from control flies (p=0.0055) but not from and *CLN7* (p>0.9999). (ANOVA, Tukey's post hoc analysis used at 3 day, Kruskal-Wallis, Dunns post hoc was used at 28 days, N.S p>0.05, ** p<0.01 and **** *p*<0.0001). Plots represent mean ± standard deviation. (Data provided by Dr Chris Elliott).

6.2.6 Age dependant photoreceptor response

The photoreceptor response is characterised by the difference between the baseline and start of the off-transient peak. w^{1118} controls produced a photoreceptor response of 1056 ± 608 (n=17) which was similar to *CLN7* (1087 ± 404.2, n=19, p=>0.9999) and *CLN7* heterozygotes (1058 ± 442.8, n=10, p>0.9999) at 3 days of age (Figure 6.7). By 28 days of age, the response in controls reduce to 733.8 ± 419.5 (n=25) which is matched by *CLN7* heterozygotes (718.9 ± 374.6, n=13, p>0.9999). However, the response amplitude did not decrease in 28 day old *CLN7* flies (1200 ± 525.8, n=26), and is statistically significant from w^{1118} (p=0.0015) and *CLN7* heterozygotes. This suggests that there is no gene dosage dependant phenotype and long-term loss of CLN7 results in increased depolarisation of photoreceptors as a phenotype is only seen in aged flies.

6.2.7 *CLN7* flies have normal lights off phase

Turning off the lights produces an off-transient peak which reflects the termination of histamine neurotransmitter release by photoreceptors synapsing onto lamina neurons and repolarisation of the latter. During the lights-off phase at 3 days of age, the off-transient amplitude was similar between control flies (-590.4 ± 528.5, n=16), *CLN7* (*-776* ± 310.1 n=17, p=0.6159) and *CLN7* heterozygotes (-747.7 ± 621.3, n=10, p=0.6643, figure 6.8). By 28 days of age, a gene dosage dependant phenotype starts to appear with loss of CLN7 resulting in a smaller peak. However, the response of control flies (-1056 ± 636.3, n=25) was non- significantly different from *CLN7* (-700.8± 470.9, n=26, p=0.0861) and *CLN7* heterozygotes (-907.9 ± 614.4, n=13, p=0.4940, figure 6.8). Phototransduction signalling needs to be able to
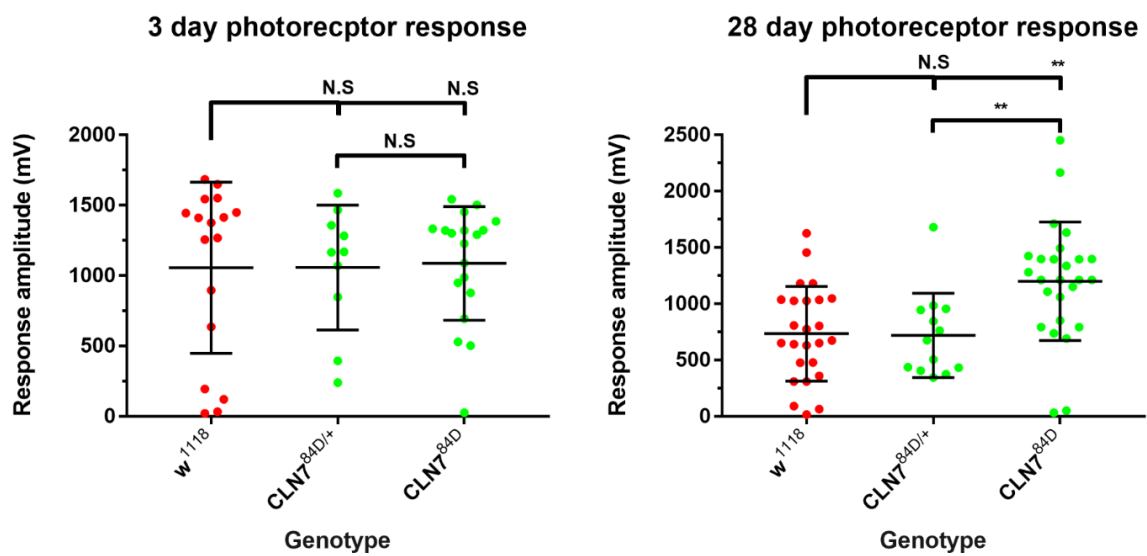
Figure 6.7: significant photoreceptor response in ages *CLN7* flies. At 3 days of age, there is no significant difference between the peak-peak amplitude of w^{1118} controls, *CLN7* (p>0.9999) and *CLN7^{84D/+}* heterozygotes (p>0.9999). There was no significant difference between *CLN7* and *CLN7^{84D/+}* (p>0.9999). At 28 days of age, w^{1118} controls and *CLN7* heterozygotes have smaller responses compared to 3 day-old flies. However, the response in *CLN7* flies do not reduce and are significantly different to w^{1118} (p=0.0015) and heterozygotes (p=0.0057). (Kruskal-Wallis, Dunn's post hoc was used, N.S p>0.05, **p<0.01). Plots represent mean ± standard deviation. (Data provided by Dr Chris Elliott).

3 day off-transient response

28 day off-transient response
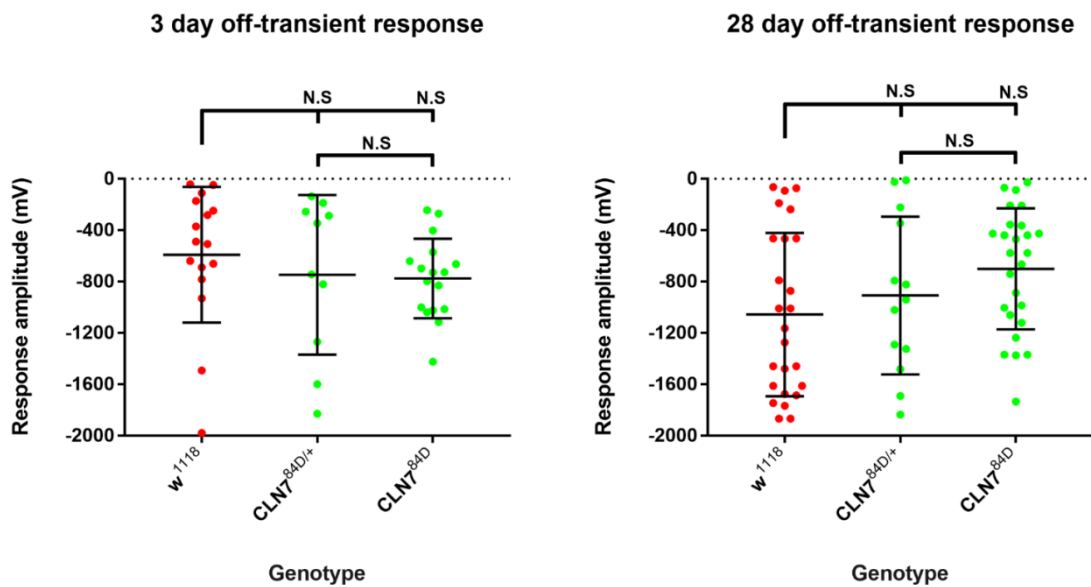
Figure 6.8: *CLN7* **have no defect in off-transient response.** At 3 days of age, there is no significant difference between the off-transient amplitude of *w^1118* controls, *CLN7* (p=0.1774) and *CLN7^84D/+* heterozygotes (p>0.9999). There was no significant difference between *CLN7* and *CLN7^84D/+* (p>0.9999). At 28 days of age, a slight trend appears as loss of CLN7 decreases the amplitude size, however, there is no significant difference between the off-transient amplitude between *w^1118* controls and *CLN7* (p=0.1028) or *CLN7^84D/+* heterozygotes (p>0.9999). There was no significant difference between *CLN7* and *CLN7/+* (p>0.9999). (Kruskal-Wallis, Dunn's post hoc was used, N.S p>0.05). Plots represent mean ± standard deviation. (Data provided by Dr Chris Elliott).

adapt rapidly to changes in light and it is just as essential that the signal be able to be reset ready for the next light stimuli. This can quantified as the time taken to recover back to baseline following the off-transient peak. The initial recovery phase of the off transient is calculated by the time taken for the off-transient to recover half way back to baseline. At 3 days of age, w^{1118} controls have a similar recovery period (705.7 ± 278.1ms, n=16) as *CLN7* flies (744.9 ± 215.7ms, n=17, p=0.9220) and *CLN7* heterozygotes (739.5 ± 411.5ms, n=17, p=0.9558, figure 6.9). At 28 days of age, the time taken to recover to baseline rises to 975.9 ± 452.2ms (n=25) in w^{1118} controls but remains low in *CLN7* (714.7 ± 340.8ms, n=26) and *CLN7* heterozygotes flies (781 ± 409.1ms, n=13, p=0.3372) and is almost statistically significantly lower in *CLN7* (p=0.0602, figure 6.9).The faster recovery time is expected as it correlates with the smaller off-transient response suggesting there is no defect in the termination of histamine release by photoreceptors and recovery.

6.2.8 Early defects in phototransduction signalling

The ERGs gives a measure of luminescence response, but is unable to provide information to changes in contrast which generally shares an inverse trade-off – as one increases the other decreases. Therefore, to identify whether CLN7 mutant flies show defects in contrast perception, a more sensitive assay, steady-state visually evoked potential (SSVEP), was carried out. The increased sensitivity is due to an averaged response to hundreds of stimuli and the removal of out-of-band noise (Norcia et al., 2015). The first harmonic 1F1 represents the photoreceptor response. At 3 days of age, a gene dosage dependant phenotype was visible. *CLN7* flies had a significantly higher mean response amplitude (61.85 ± 28.16mV, n=17) compared
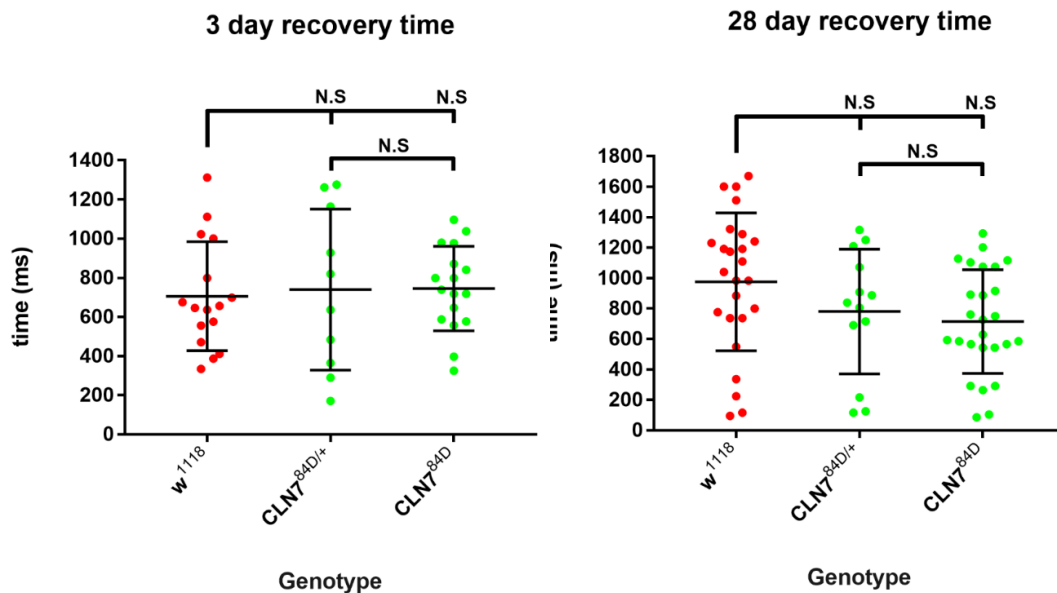
Figure 6.9: There is no defect in recovery time during the lights off phase. At 3 days of age, there is no significant difference between the recovery time of *w*^{*1118*} controls, *CLN7* (p=0.9220) and *CLN7*^{*84D/+*} heterozygotes (p=0.9558). There was no significant difference between *CLN7* and *CLN7*^{*84D/+*} (p=0.9988). At 28 days of age, a slight trend appears as loss of CLN7 decreases the recovery time. However, there is no significant difference between the recovery time between *w*^{*1118*} controls, *CLN7* (p=0.0602) and *CLN7*^{*84D/+*} heterozygotes (p=0.3372). There was no significant difference between *CLN7* and *CLN7*^{*84D/+*} (p=0.8784). (ANOVA, Tukey's post hoc analysis was used, N.S p>0.05). Plots represent mean ± standard deviation. (Data provided by Dr Chris Elliott).

to w^{1118} flies (41.01± 16.52mV, n=15, p=0.0333, figure 6.10).   *CLN7* hetrozygotes had an intermediate phenotype (56.33 ± 19.05, n=10) however, this was non-statistically significant from control (p=0.2307) or *CLN7* flies (p=0.8132). At 28 days of age, the spread of the data becomes a lot random which may potentially be attributed to the old age of the flies. The response amplitude in w^{1118} flies increases to 57.03 ±18.1mV (n=19), which is similar to *CLN7* flies (53.89 ± 26.62, n=21, p=0.9037).   *CLN7* hetrozygotes flies also has a similar response amplitude (51.75 ± 23.72mV, n=12) as control (p=8108).

The second harmonic 2F1 represents signalling in lamina neurons. At 3 days of age, *CLN7* flies had a significantly higher mean response amplitude (4.146 ± 1.654mV, n=17) compared to w^{1118} flies (2.436 ± 1.232mV, n=15, p=0.0102, figure 6.11). *CLN7* heterozygote flies produced the highest response amplitude (4.695 ± 1.843, n=10) which was significantly higher than control flies (p=0.0030) but not *CLN7* flies (p=0.6568). At 28 days of age, the response amplitude in w^{1118} flies increases to 4.846 ± 4.249 mV (n=19), which is similar to *CLN7* flies (4.708 ± 4.28, n=21, p>0.9999). *CLN7* hetrozygotes flies produced a similar response amplitude (3.312 ± 2.497mV, n=12) as control (p=0.8318). Lower order intermodulations (2F1+2F2) can also be extracted from response in the SSVEP assay. These have been shown to most likely reflect interactions between lamina and medulla neurons and reflect where higher levels of visual processing occurs. At 3 days of age, the 2F1+2F2 response (medulla response) in w^{1118} controls (0.4606 ± 0.2221 mV), *CLN7* (0.4665 ± 0.245, p=0.9972) and *CLN7* heterozygotes (0.4477 ± 0.2457 mV, p=0.99) were
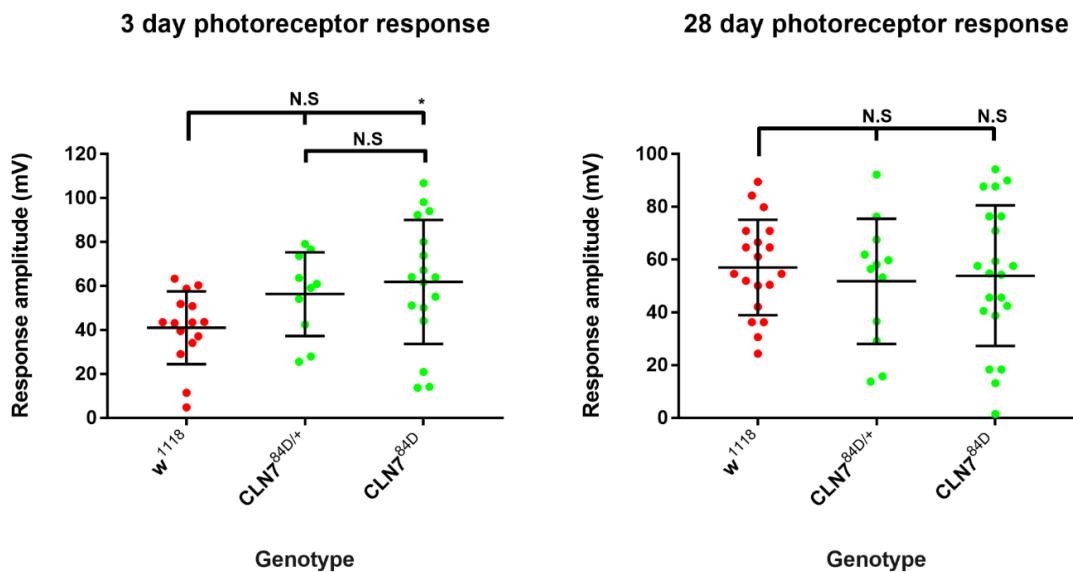
Figure 6.10: Abnormal early onset in photoreceptor response. SSVEP was used to quantify the 1F1 response amplitude to measure photoreceptor response to contrast. At 3 days of age, *CLN7* flies produce a significantly higher 1F1 response compared to *w*[1118] controls (p=0.0333). *CLN7*[84D/+] heterozygotes produced an intermediate response but was not significantly different from control (p=0.2307) or *CLN7* flies (p=0.8132). At 28 days of age there is no significant difference between the 1F1 response between *w*[1118] controls and *CLN7* (p=0.9037) or *CLN7*[84D/+] heterozygotes (p=0.8108). (ANOVA, Tukeys post hoc analysis was used, N.S p>0.05, *p<0.05). Plots represent mean ± standard deviation. (Data provided by Dr Chris Elliott).
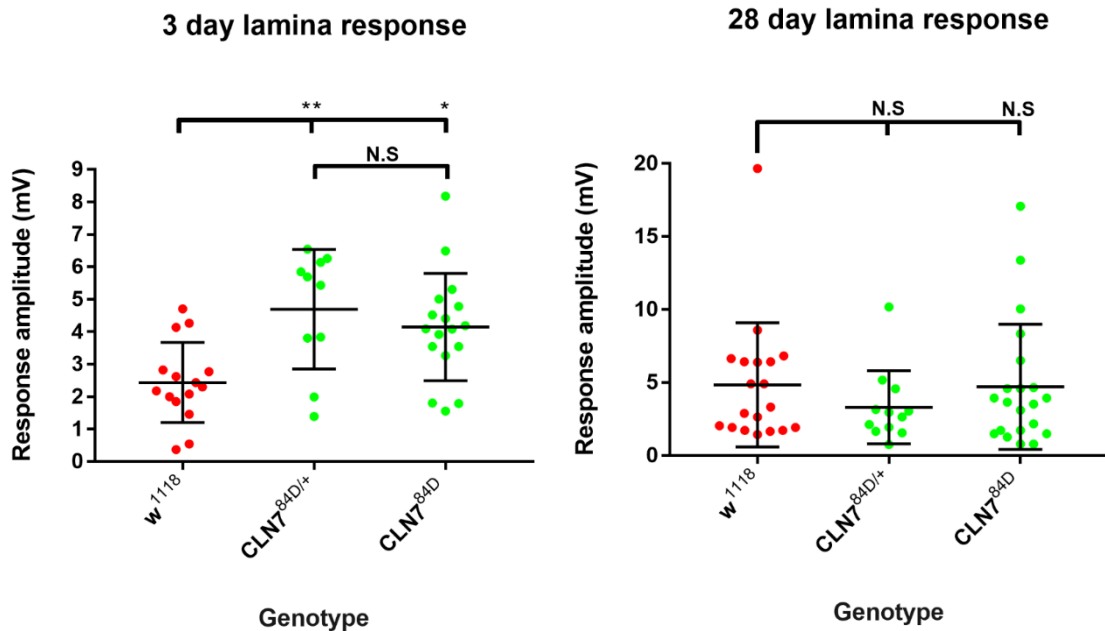
Figure 6.11: Abnormal early onset lamina signalling. SSVEP was used to quantify the 2F1 response amplitude to measure the lamina response to contrast. At 3 days of age, *CLN7* and *CLN7^{84D/+}* heterozygote flies produce a significantly higher 2F1 response compared to *w^{1118}* controls (p=0.0102 and p=0.0030 respectively). *CLN7^{84D/+} heterozygotes* produced a slightly higher non-statistically significant response than *CLN7* (p=0.6568). At 28 days of age there is no significant difference between the 2F1 response between *w^{1118}* controls and *CLN7* (p>0.9999) or *CLN7^{84D/+}* heterozygotes (p=0.8318). (ANOVA, Tukey's post hoc analysis used at 3 day and Kruskal-Wallis, Dunn's post hoc used at 28 days of age. N.S p>0.05, * p<0.05 and ** p<0.01), *p<0.05. Plots represent mean ± standard deviation. (Data provided by Dr Chris Elliott).

similar (Figure 6.12). No difference was also observed in 28 day old flies, w^{1118} controls (0.5068 ± 0.3009 mV), *CLN7* (0.4853 ± 0.3482, p=0.9999) and *CLN7* heterozygotes (0.3771 ± 0.1593 mV, p=0.9999, figure 6.12). This suggests neural signalling in deeper complexes are unaffected by the loss of CLN7. As both the second harmonic 2F1 and the forth order intermodulation 2F1+2F2 are affected by neurotransmitter released by photoreceptors (Afsari et al., 2014b), this implies increased activity of photoreceptors are likely resulting in increased neurotransmitter release and subsequently increase signalling in second-order lamina neurons.

6.2.9 *CLN7* larvae fail to respond to light

As *CLN7* mutant adult flies exhibit defective signalling, I next investigated whether a similar defect is present in the larval stage. During the larval stages, the visual system has not fully formed and larvae respond to light. A phototaxis assay was carried out using larvae in a light/dark dish. Larvae were exposed to 550 lux of light for 11 minutes and their movement were recorded. A light response index was calculated (response index = (Number of larvae in dark – number of larvae in light)/total number of larvae). Values of: -1<-0.5 indicate strong preference for light, -0.5<0 indicate low preference for light, 0<0.5 indicate low light avoidance and 0.5<1 indicates high light avoidance. w^{1118} larvae exhibited a high level of light avoidance with a response index of 0.51 at 11 minutes (Figure 6.13). *CLN7* larvae failed to respond to light like control larvae and had a low avoidance to light with a response index of 0.1 at 11 minutes, however this was not significantly different from controls (p=0.100).
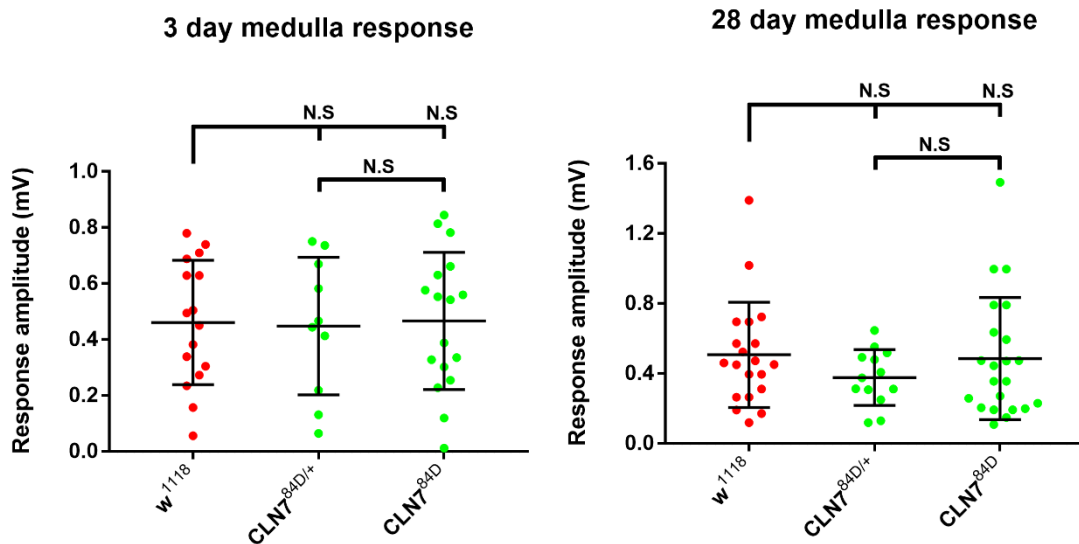
Figure 6.12: No defect in signalling in medulla neurons. SSVEP was used to quantify the 2F1+2F2 response amplitude to measure the lamina/medulla interactions to contrast. At 3 days of age, *CLN7* and *CLN7*^{84D/+} heterozygote flies produce a similar response to *w*¹¹¹⁸ controls (p=0.9972 and p=0.99 respectively). There was no significant difference between *CLN7*^{84D/+} heterozygotes and *CLN7* (p=0.6568). At 28 days of age there is no significant difference between *w*¹¹¹⁸ controls and *CLN7* (p=0.9999) or *CLN7*^{84D/+} heterozygotes (p=0.9999). (ANOVA, Tukey's post hoc analysis used at 3 day and Kruskal-Wallis, Dunn's post hoc used at 28 days of age. N.S p>0.05. Plots represent mean ± standard deviation. (Data provided by Dr Chris Elliott).
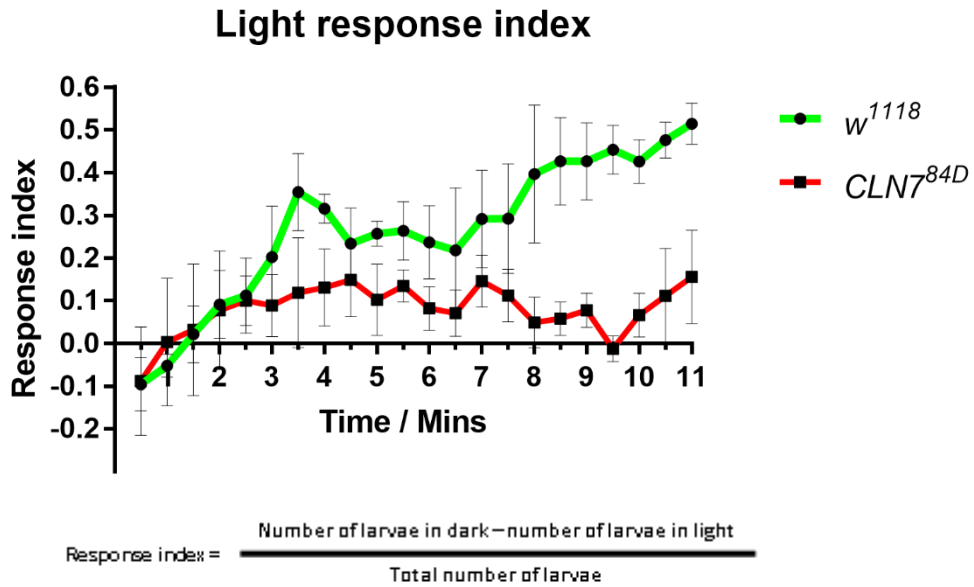
Figure 6.13: *CLN7* **mutants exhibit altered phototactic behaviour.** 20 Larvae placed in a round dark/light petri dish. 550 lux of light was shone over the entire dish and movements of larvae are tracked every 30 seconds for 11 minutes. A graph showing the light response index of w^{1118} controls and *CLN7* mutants. Controls move to the dark side over time as expected, however *CLN7* larvae do not exhibit a preference for either the light or dark sides. However, at 11 minutes, the difference between genotypes are not significant (P=0.100, n=3, Mann Whitney U Test) Means ± SEM was plotted.

6.3 Discussion

Here I have used the *Drosophila* model system to determine how the loss of CLN7, responsible for late infantile NCL, affects phototransduction signalling. Defects within the visual system are common within the NCLs which can lead to blindness (Haltia, 2003). I observed defects in both ERGs and SSVEP functional assays in *CLN7* flies which suggest abnormal synaptic function between the photoreceptor and second-order lamina neurons, but responses in aged flies suggest *CLN7* flies do not succumb to blindness.

6.3.1 CLN7 comparable to mammals

I have shown that CLN7 is expressed within the developing visual system in larvae and in the adult visual system. In both stages of the *Drosophila* life cycle, CLN7 localised primarily to the photoreceptors and in second order lamina neurons. In murine models, MFSD8/CLN7 predominantly localised to the outer plexiform layer (OPL) of the retina (Khan et al., 2017). The OPL is a layer of neuronal synapses within the retina and is the site, rich in synaptic connections, where primary order photoreceptors forms connections with second order neurons, bipolar and horizontal cells. In contrast to this study, they found CLN7 predominantly co-localised with the presynaptic photoreceptor terminal marker, PSD-95, indicating CLN7 localises to the photoreceptor terminals in mice. A lack of co-immunostaining with the SNAP-25 indicated CLN7 was not expressed in the second-order neurons.

The effects of loss of CLN7 on the visual system has been modelled in *mfsd8* (*CLN7*) deficient mouse. A hypomorphic mice model (*Mfsd8*^{tm1a/tm1a}) of CLN7 disease in which a *LacZ* gene-trap cassette was inserted between exons 1 and 2 showed many clinical symptoms of human CLN7 disease (Damme et al., 2014). One such pathology in 8.5 month old mice was the severe or complete degeneration of the photoreceptors cell layers in central and peripheral regions of the retina. The degeneration of the retina was accompanied by increased astrogliosis and Muller cells detected by GFAP immunoreactivity. Another study using a *CLN7* knockout mouse model which recapitulated key phenotypes of human CLN7 disease was used to determine the progression of retinal pathology (Jankowiak et al., 2016, Brandenstein et al., 2016). Retinal morphology was found to be normal at 0.5 months of age, but at 1- 2- and 4-months of age, the outer nuclear layer (ONL) of photoreceptors started to thin in mutants. The thinning of the ONL correlated with an increase in astrogliosis in Muller cells detected by anti-GFAP (Jankowiak et al., 2016). It would be interesting to determine whether loss of CLN7 in flies also lead to neuropathology of the photoreceptors and underlying visual components and if so, place it in the disease progression timeline. This could be determined by histopathological staining and sectioning of the fly visual system to look for neurodegeneration.

The build-up of autofluorescent lipofuscin in postmitotic cells, including neurons, occurs naturally with the aging process (Porta, 2002). One of the hallmarks of LSDs is the premature accumulation of autofluorescent pigments, predominantly lipofuscin in NCLs, within lysosomes of all cells. Autofluorescent build-up has been

observed in *Ppt1* (CLN1) and *Cathepsin D* (CLN10) deficient *Drosophila* models (Hickey et al., 2006, Myllykangas et al., 2005). In the INCL model (*Ppt1*), significant autofluorescent build-up was started at 72 hours after pupation and persisted post eclosion in the CNS of young (1 day) and aged (58 day) adult flies (Hickey et al., 2006). In the Congenital NCL model (*CathD*), autofluorescent build-up was detected in the CNS of flies 15 days post eclosion and become more prevalent as flies were aged to 30- and 45 days (Myllykangas et al., 2005). In addition, vertebrate models of *CLN7* including mouse and a dog model exhibit significant build-up of autofluorescent material within the CNS which recapitulates a key phenotype of CLN7 patients (Siintola et al., 2007). This was localised to the cerebellum and cerebral cortex in the Chinese Crested dog model, and can additionally be found in the hippocampus, thalamus and olfactory bulb in mouse models (Guo et al., 2015, Damme et al., 2014, Brandenstein et al., 2016). In this study, I found *CLN7* flies recapitulated the NCL disease phenotype, as a significant autofluorescent build-up was observed in 28 day old *CLN7* flies compared to controls. This was localised to the photoreceptors of visual system, but unlike NCL patients and other models, was not prevalent within the CNS. This correlates with the localisation pattern of CLN7 which was found predominantly to be expressed in the BBB, photoreceptors and lamina neurons while being absent from the central CNS. It would be interesting to determine if the composition of the storage material matches the clinical phenotype of CLN7 patients and at what stage of development the build-up begins.

6.3.3 Early dysfunction in synaptic signalling in *CLN7*

Due to the early onset of visual acuity patients suffer in late infantile CLN7, in addition to the clinical build-up of autofluorescent material in *CLN7* flies, I wanted to determine if the flies also exhibited physiological defects. In this study, two assays, ERGs and SSVEP, were employed to characterise phototransduction and responses within fly visual system. The ERG characterised the synaptic transmission between the photoreceptors and lamina neurons. The SSVEP has been used to show functional homology between the *Drosophila* and vertebrate visual systems (Afsari et al., 2014a) and is able to distinguish between the individual components visual system: responses in first-order photoreceptors (1F1), and signalling in second-order lamina (2F1) and third-order medulla neurons (1F2 + 2F2). SSVEP has been used to show hyperactive responses in the photoreceptor and increased signalling lamina neurons in a *Drosophila* model of early onset PD (Afsari et al., 2014b).

Both assays indicated early defects in synaptic transmission between photoreceptors and lamina neurons. The ERG measures a luminance response, while the SSVEP measures contrast response, and a trade-off between the two has been shown - when the luminance response gets better, the contrast response gets worse and vice versa (Nippe et al., 2017)**.** This can be seen in 3 day old *CLN7* flies, which experience a decrease in the ERG on-transient response (Figure 6.5) but an increase in SSVEP contrast response (Figure 6.11). This suggests a defect in phototransduction signalling in lamina neurons of *CLN7* flies which have reduced response to light and increased response to contrast. However, at 28 days of age,

CLN7 flies maintains a significantly lower on-transient response compared to controls flies, but the contrast response in lamina neurons (2F1) did not increase. This may indicate a late onset defect in a trade-off between the two responses. However, it may also be attributed to the general poor health of aged *CLN7* flies which may have yielded smaller responses. *CLN7* flies generally moved a lot less and remained at the bottom of the vials instead of climbing along the sides. Locomotion defects have been reported in 1-5 day old *CLN7* flies, performing 20% worse than control flies in a negative geotaxis assay (Personal communication with Katelyn Aitchison and Richard Tuxworth). It is likely the climbing ability of the flies would deteriorate with age, potentially more so in the mutants. It was also previously reported that *CLN7* flies maintained in a constant light/dark cycle at 25 ᵒC have significantly longer life spans compared to its respective controls (O'Hare, Submitted). In this study, *CLN7* flies aged to 28 days in constant darkness at increased temperatures (29 ᵒC) were not as healthy as controls. These factors may be attributed to some of the particularly low SSVEP lamina responses, however, they could not be omitted as the flies were still alive and produced a functional readout. To overcome this, a more robust reading can be obtained by taking an additional SSVEP recording at 21 days of age, where the aged flies are healthier.

Defects in the on- or off-transients have been shown to indicate impaired synaptic transmission between first-order photoreceptors and large monopolar cells of second-order in the lamina neurons (Coombe and Heisenberg, 1986, Heisenberg, 1971). The ERG on-transient reflects the release of histamine neurotransmitter and subsequent hyperpolarisation of lamina neurons, and along with the increased rate

of recovery which suggests there may be a defect in this synaptic transmission, either by having roles in neurotransmitter release or synaptic recycling. However, there seem to be no defects in the termination of histamine release by photoreceptors as shown by normal off-transient response which reflects repolarisation of the lamina neurons.

After the off-transient peaks, a biphasic recovery occurs which returns the potential towards baseline. The initial recovery is characterised by the time taken to recover halfway from the off-transient peak back to baseline and represents a feedback mechanism from the optic lobe back to the photoreceptors (Scott and Zuker, 1997). The recovery time can be positively correlated to the size of the off-transient peak, therefore larger peaks generally take longer to recover. *CLN7* and *CLN7* heterozygotes produce a similar off-transient response at 3 days of age and as anticipated the recovery time is not affected by a decrease of CLN7 levels in 3 day old flies. However, by 28 days of age, a slight trend started to appear - a decrease in *CLN7* levels resulted in a smaller off transient peak which correlated to a decrease in recovery time. These trends were close to being significant between control and *CLN7* flies (off-transient, $p=0.1028$ and recovery, $p=0.0602$) which suggests lower levels or a lack of CLN7 expression may result in defects in synaptic transmission retrograde signalling from the optic lobe back to the photoreceptors overtime. The feedback mechanism from the optic lobe to the photoreceptors use histaminergic and cholinergic neurotransmitters to terminate responses to lights off (Rajaram et al., 2005). Therefore, a potential defect in this pathway suggests CLN7 may be involved in the regulation of histamine and acetylcholine synaptic transmission.

Increasing the number of flies analysed would be able to determine if this potential defect is real.

To determine if these defects were present during developmental stages, a phototaxis assay was used. Active photoreceptors within the larval system can be find in the Bolwig organ (BO) and class IV dendritic arborisation neurons, which are present in the head and tile each body segment in larvae, respectively (Xiang et al., 2010). w^{1118} control larvae portrayed negative phototactic behaviour as expected (Gong and Gong, 2012, Gong, 2009). However, *CLN7* showed a neutral behaviour neither preferring the light or dark sides potentially indicating the start of an abnormal light response. CLN7 has been shown to be present in all muscle walls and the epidermis of larvae but did not follow any neuronal arborisation pattern. Whether CLN7 is expressed in active photoreceptors can be determined using the *YFP::CLN7* knock-in.

6.3.4 Visual defects in CLN7 patients

Pathology of the visual system is a prominent feature of the NCLs, but are not present in all cases. Patients of an adult onset NCLs did not suffer from visual defects (Goebel and Wisniewski, 2004, Wisniewski et al., 2001). In addition, a study of a consanguineous Egyptian family suffering from *CLN7* disease did not present visual impairment (Stogmann et al., 2009), however underlying defects in phototransduction signalling could not be ruled out as ERGs could not be carried out. In contrast, two families with mutations in *CLN7* present a non-syndromic macular dystrophy (Roosing et al., 2015). Patients did not present with classical

NCL symptoms and were able to survive longer than symptomatic LINCL CLN7 disease, with patient ages ranging from 27-65 years of age. Patients were found to predominantly exhibit normal ERG readings, which is a reading of summed electrical response of the entire retina upon light stimulation. However, patients exhibited a reduced response with a multifocal ERG (mfERG). Here, many areas of the retina are stimulated at the same time with electrical responses being recorded from each location simultaneously (Azarmina, 2013). In addition, optic coherence imaging, which examines morphological changes showed loss of central photoreceptors at later stages of life (Roosing et al., 2015). As mfERG and OCT have recently been used as diagnostics tools, no tests have been carried out in early stages of the disease. This indicates that while some tests/assays may indicate normal responses in patients/mutants, more specialised/sensitive techniques may be needed to uncover subtle differences as done with SSVEP.

6.3.5 LSD models

In addition to *Drosophila* models of INCL (*Ppt1*) and congenital NCL (*CathD*), models of other LSD have been established which include: a *saposin* deficient model and a *spinster* (*Spin* -formerly known as benchwarmer) (Hindle et al., 2017, Dermaut et al., 2005). Spin is a late endosomal/lysosomal transmembrane protein with 8-12 membrane spanning domains. Like CLN7, it is a part of the MFS family of transporters and thought to transport sugar. On the other hand, pro-saposin is cleaved into its active form in by CathD, and under the acidic pH of the lysosome, it promotes hydrolases involved in the degradation of sphingolipid. Models of each diseases has been shown to recapitulate key features of the human disease,

including the build-up of sphingolipid and carbohydrate storage materials respectively, neurodegeneration of the CNS and visual system and defects in phototransduction and synaptic transmission using ERGs. Unlike the *CLN7* model, both *Saposin* and *Spin* models, ERGs did not detect any early defects within the visual system. However, all ERG components (ERG response and on- and off-transients) were compromised in the *Saposin* and *Spin* mutants by 22 and 40 days of age respectively, with the former also requiring a longer recovery period upon light off response.

6.3.4 Dysregulation of Ca^{2+}

A genetic link has been established between Saposin and a potential role in Ca^{2+} regulation. Interestingly, Ca^{2+} homeostasisis is affected at the NMJ of *CLN7* larvae which leads to the question: is abnormal Ca^{2+} levels responsible for defects in the visual system in *CLN7?* Ca^{2+} has been shown to play crucial roles in phototransduction and, crucially, is regulated by lysosomes, which act as an internal store. *Saposin* was combined with a plasma membrane Ca^{2+} exchanger (CalX) which pumps Ca^{2+} out the cytosol of photoreceptor in exchange for an influx of Na^+. CalX was overexpressed as it was under NinaE (rhodopsin 1) promoter, and the excess removal of Ca^{2+} from the photoreceptor cytosol had no effect in 5 day old flies, but exacerbated the deterioration of ERGs by 22 days of age compared to *Saposin* mutants alone, therefore loss of Saposin may lead to decreased Ca^{2+}levels. Abnormal Ca^{2+} has been observed at the NMJ of *CLN7* larvae, which suffers from synaptopatholgy, and this may also be the case within the visual system. There are constant improvements of tools available to monitor and study effects of Ca^{2+} within

the visual system including GCaMP calcium sensors and channelrhodopsins along with the availability of genetic and pharmacological means to control levels of Ca^{2+}. These can all be utilised to help elucidate potential roles of CLN7 in Ca^{2+} homeostasis and phototransduction. If more time was available, I would also try and determine where CLN7 expression was crucial for functional phototransduction by re-expressing CLN7 in a mutant background ubiquitously, and in combinations of surface glia, photoreceptors and lamina neurons and measure Ca^{2+} levels in the visual system directly.

6.3.5 The visual system in *CLN7* is hyperactive like an early onset PD model

The ERG assay found no defect in the photoreceptor response to light in 3 day old flies (Figure 6.7). However, the more highly sensitive SSVEP assay indicated photoreceptors (1F1) were hyperactive at early stages (Figure 6.10). The opposite was seen in aged flies, *CLN7* flies produced a significantly increase response to light, but produced an indifferent contrast response (1F1). ERG photoreceptor amplitude found photoreceptors to be hyperactive in *CLN7* flies. This indicates the hyperactivity of photoreceptors start from early age, initially to contrast, and then eventually to light as flies age.

Interestingly, the responses seen in *CLN7* flies are similar to a *Drosophila* model of early onset Parkinson's disease (PD). PD flies produced a higher response in the SSVEP assay in photoreceptors (1F1) and lamina (2F1) in 1 day old flies (Afsari et al., 2014b), but the ERG components: on-transient, off-transient and peak-peak amplitude, were normal at 3-days of age (Hindle et al., 2013). The ERG components

became significantly reduced by 28 days of age which correlated with onset of neuropathology of the visual system in PD flies determined by vascularisation of the retina, lamina and lobula. This was attributed to increased activity of the visual system (Hindle et al., 2013). As *CLN7* flies have hyperactive photoreceptors and lamina signalling at 3 days of age in response to contrast, along with an increased rate of recovery following lights on on-transient, it would be interesting to see if neuropathology occurs within the visual system of *CLN7* flies as seen in other *Drosophila* models of LSDs (Dermaut et al., 2005, Hindle et al., 2017, Hickey et al., 2006, Myllykangas et al., 2005). This could be achieved by simply counting surviving photoreceptors labelled with GFP and visualised through the deep psuedopupil, or by histological methods after sectioning the eyes.

7. GENERAL DISCUSSION

7.1 Developing the CRISPR/Cas9 system in *Drosophila*

In this thesis, my aims were to carry out the first *in vivo* localisation study of CLN7 using the *Drosophila* model and determine potential roles for CLN7. Previous localisation studies of the CLN7 protein have utilised an overexpressed version of the protein which can lead to mis-localisation of the transmembrane protein. Using the CRISPR/Cas9 system, I was able to generate a YFP-CLN7 knock-in under the endogenous *CLN7* promoter. This overcome the poor antigenicity of the CLN7 and allowed the cellular localisation of CLN7 to be investigated. Generating this line twice, once with the artificial intron and once without, have shown using the HDR CRISPR technique can be successful at highly efficient in *Drosophila*. However, the success depends on the ability of the gRNA to induce dsDNA breaks, as I was unable to generate a complete gene knockout or tag the C-terminus of the protein with another gRNA. In future, the efficiency of gRNAs can be tested in S2 cells before going *in vivo*, multiple gRNAs could be used simultaneously or the gRNAs could be integrated into the genome rather than injected.

Although I was able to generate knock-ins, both lines resulted in a reduction of *CLN7* expression to approximately 30% of their respective controls. This was not due to improper folding of YFP as the re-expression of an N-terminal fused YFP-CLN7 in a mutant background was able to fully rescue the mutant phenotype. Therefore, the insertion of YFP at the ATG start site is more likely to have affected one of several processes regulating transcription, potentially due to 3 annotated transcripts of

CLN7. If one or more transcripts were unstable, which could be identified by qPCR using transcript specific primers. This suggests an additional step should be taken into consideration when designing HDR templates for future knock-ins. Nonetheless, as this did not lead to an overexpression of the transmembrane protein, which would potentially have resulted mis-localisation, I was able to successfully carryout an *in vivo* localisation study of CLN7.

7.2 CLN7 is predominantly a glial protein

Due to the neurodevelopmental and neuropathology seen in CLN7 patients, it was surprising to find neuronal expression of CLN7 restricted to the visual system while predominantly being expressed in surface glia which form the insect BBB. CLN3 expression was also determined to be a restricted to the surface glia in the *Drosophila* CNS (Mohammed et al., 2017). This likely reflects an ancestral expression pattern in glial cells, which later expanded into neurons in mammals. Activation of glial cells is one of the earliest markers in NCLs, preceding neurodegeneration, as seen in various models, (Cooper et al., 2015, Kay et al., 2006, Oswald et al., 2005) however, the role glial cells play in disease progression remains unknown. As *CLN7* flies exhibit an overgrowth phenotype, it was thought CLN7 may potentially regulate organismal growth via the transport of an insulin antagonist, secreted decoy of insulin receptor (SDR). A reduction in SDR secretion results in increased growth similar to *CLN7.* The lack of CLN7 expression in stellate cells indicate it is unlikely to regulate chloride transport, however to investigate if CLN7 regulates SDR release, levels of SDR in the hemolymph would have to be quantified and compared to controls via western blotting using anti-SDR.

7.3 Characteristic build-up of autofluorescent material

Loss of CLN7 in humans leads to a neurodegenerative disease with visual failure and motor defects being prominent symptoms. Therefore it was essential to determine if loss of CLN7 had functional consequences on these processes using a *Drosophila* model of CLN7 disease. I helped further validate the use of the *Drosophila* model by identifying the characteristic build-up of autofluorescent material in *CLN7* flies. This mimics observations made in human CLN7 disease and mice models of CLN7 disease and NCLs in general helping validate its use as model of the late infantile disease. SMCAS is the main component of storage material in most of the NCLs, including CLN7 disease. It would be interesting to determine how closely the *Drosophila* model resembles the human and mammalian models of CLN7 disease.

7.4 CLN7 regulates synaptic function from post-synaptic side

Using the loss of function models, defects were observed in the development of boutons in the late larval NMJ A reduction in boutons highlighted the imbalance in the homeostatic needs between the innervating presynaptic motor neuron and postsynaptic muscle. Interestingly, my YFP-CLN7 knock-in reported that CLN7 is expressed in the muscle and, importantly, localises to the postsynaptic site. A similar reduction in boutons has been observed in *CLN3* flies although the expression pattern of CLN3 at the NMJ has yet to be characterised.

To support my localisation study, genetic studies using the GAL4-UAS system for tissue specific RNAi knockdowns and re-expressions determined CLN7 expression was crucial in the muscles for the development of the NMJ. In comparison, loss of CLN7 in motor neurons and peripheral glial cells, which also regulate NMJ development had no effect. Electrophysiological analysis of the *Drosophila* NMJ showed continuous stimulation of motor neurons in *CLN7* larvae lead to increased depression of nerve-evoked excitatory junction potentials compared to controls (O'Hare, Submitted). This suggests a defect in synaptic vesicle recycling or the ability to utilise the reserve pool of neurotransmitter vesicles. With the post synaptic localisation of CLN7, suggests CLN7 has some sort of retrograde functional consequence.

7.5 CLN7 regulates synaptic function in visual system

A common symptom in the group of NCL disorders is visual impairment, which leads to blindness. To see if flies exhibit a similar disturbance in the visual system, adult flies underwent ERGs, which measures luminescence response, and SSVEP, which measures contrast response in *CLN7* flies. The reduction in on-transient response seen in ERGs also highlighted defects in the synaptic signalling between first order photoreceptors and second order lamina neurons. In addition, the SSVEP showed an increase in photoreceptor activity and lamina signalling at 3 days of age, similar to an early onset PD model (Afsari et al., 2014a). However, unlike the PD model, *CLN7* flies still elicited a response at 28 days of age indicating the lack of visual blindness (Hindle et al., 2013). In combination with the NMJ data, this indicates a crucial role for CLN7 in synaptic functions of both processes. My localisation study

indicated CLN7 carried out its function in the photoreceptors and lamina neurons of the visual system. However, the function CLN7 carries out in the photoreceptor and its postsynaptic target (lamina neuron) remains unknown. Due to time constraints, a similar genetic study using RNAi knockdowns and re-expressions could not be carried out but would be interesting to quantify the effects on the on-transient responses following tissue specific RNAi knockdowns and re-expressions of CLN7 in the photoreceptor and lamina neurons. The on-transient response reflects photoreceptor release of histamine neurotransmitter and subsequent hyperpolarisation of lamina neurons. If a photoreceptor specific knockdown of *CLN7* still resulted in an on-transient phenotype, it would suggest CLN7 regulates synaptic transmission from the presynaptic side and conversely if the phenotype persisted in a lamina specific knowndown, this would suggest a postsynaptic regulation similar to the NMJs. These may reveal ways CLN7 regulates synaptic function and what roles CLN7 plays in the photoreceptor and lamina neurons within the visual system

7.6 CLN7 regulates TORC signalling

Several signalling pathways and processes have been shown to be involved in the neural development. One main process known to regulate the development of the NMJ and also be abnormal in the models of NCLs, including CLN7 disease, was autophagy (Shen and Ganetzky, 2009). A lack of p62 build-up in *CLN7* flies determined that autophagy in was not majorly affected as seen in a mouse model of CLN7 disease (Brandenstein et al., 2016). However, as no single experiment can rule out an autophagy defect, further investigations into autophagy in flies are required to determine if *CLN7* flies have an autophagy defect. Nonetheless, the

phenotype observed at the NMJ seemed to be independent of autophagy due to pharmacological induction of autophagy increasing boutons in controls and mutants suggesting CLN7 is likely involved a different process. It was also shown not to be involved in the trans-synaptic TGF-β pathway and due to time constraints other pathways could not be fully investigated and requires further investigations.

CLN7 has recently been found to regulate TORC signalling in mice and *Drosophila* models of CLN7 disease (Danyukova et al., 2018, O'Hare, Submitted). In flies, CLN7 was found to form a protein complex with Rheb, a key regulator of TORC signalling, but how it exactly regulates TORC signalling remains to be identified. While autophagy, regulated by TORC1 signalling regulates NMJ growth, TORC2 activity is required to prevent overgrowth and loss of Rictor, a TORC2 component, leads to an expansion of NMJs (Natarajan et al., 2013). As a *CLN7/Rictor* double mutant also lead to an expansion of the NMJ, CLN7 was determined to function upstream of TORC2 signalling (O'Hare, Submitted). As both TORC signalling seems to function in the presynaptic neurons to regulate NMJ, it is possible CLN7 may regulate TORC signalling in a retrograde fashion. To further investigate functions of CLN7 functions additional partners which forms complexes with CLN7 could be identified. This could be achieved *in vivo* by using the YFP-CLN7 knock-in (which contains a 3x FLAG tag and YFP epitopes) to carryout tandem affinity purification (TAP) tagging followed by NMR spectroscopy.

7.7 Summary

The work carried out in this thesis has helped uncover potential roles and functions of CLN7 within neurodevelopment, to help understand disease progression of a late infantile neurodegenerative disease. This study has shown the importance of CLN7 and functional consequences of losing CLN7 in both the visual system and NMJ. My data show loss of CLN7 leads to hyperactivation of the visual system, although this has yet to shown to lead to early neuropathology of visual neurons. CLN7 was also identified to regulate the development and growth the NMJ via the post-synaptic muscle suggesting some form of retrograde signalling.

8. References

ABERLE, H., HAGHIGHI, A. P., FETTER, R. D., MCCABE, B. D., MAGALHAES, T. R. & GOODMAN, C. S. 2002. wishful thinking encodes a BMP type II receptor that regulates synaptic growth in Drosophila. *Neuron,* 33**,** 545-58.

ABY, E., GUMPS, K., ROTH, A., SIGMON, S., JENKINS, S. E., KIM, J. J., KRAMER, N. J., PARFITT, K. D. & KOREY, C. A. 2013. Mutations in palmitoyl-protein thioesterase 1 alter exocytosis and endocytosis at synapses in Drosophila larvae. *Fly,* 7**,** 267-279.

ACHARYA, J. K., JALINK, K., HARDY, R. W., HARTENSTEIN, V. & ZUKER, C. S. 1997. InsP3 receptor is essential for growth and differentiation but not for vision in Drosophila. *Neuron,* 18**,** 881-7.

AFSARI, F., CHRISTENSEN, K. V., SMITH, G. P., HENTZER, M., NIPPE, O. M., ELLIOTT, C. J. & WADE, A. R. 2014a. Abnormal visual gain control in a Parkinson's disease model. *Hum Mol Genet,* 23**,** 4465-78.

AFSARI, F., CHRISTENSEN, K. V., SMITH, G. P., HENTZER, M., NIPPE, O. M., ELLIOTT, C. J. H. & WADE, A. R. 2014b. Abnormal visual gain control in a Parkinson's disease model. *Human Molecular Genetics,* 23**,** 4465-4478.

ANDLAUER, T. F. & SIGRIST, S. J. 2012a. In vivo imaging of Drosophila larval neuromuscular junctions to study synapse assembly. *Cold Spring Harb Protoc,* 2012**,** 407-13.

ANDLAUER, T. F. & SIGRIST, S. J. 2012b. Quantitative analysis of Drosophila larval neuromuscular junction morphology. *Cold Spring Harb Protoc,* 2012**,** 490-3.

ARSOV, T., SMITH, K. R., DAMIANO, J., FRANCESCHETTI, S., CANAFOGLIA, L., BROMHEAD, C. J., ANDERMANN, E., VEARS, D. F., COSSETTE, P., RAJAGOPALAN, S., MCDOUGALL, A., SOFIA, V., FARRELL, M., AGUGLIA, U., ZINI, A., MELETTI, S., MORBIN, M., MULLEN, S., ANDERMANN, F., MOLE, S. E., BAHLO, M. & BERKOVIC, S. F. 2011. Kufs Disease, the Major Adult Form of Neuronal Ceroid Lipofuscinosis, Caused by Mutations in CLN6. *American Journal of Human Genetics,* 88**,** 566-573.

AWASAKI, T., LAI, S. L., ITO, K. & LEE, T. 2008. Organization and postembryonic development of glial cells in the adult central brain of Drosophila. *J Neurosci,* 28**,** 13742-53.

AZARMINA, M. 2013. Full-Field versus Multifocal Electroretinography. *J Ophthalmic Vis Res,* 8**,** 191-2.

BAE, J. R. & KIM, S. H. 2017. Synapses in neurodegenerative diseases. *BMB Rep,* 50**,** 237-246.

BAROLO, S., CASTRO, B. & POSAKONY, J. W. 2004. New Drosophila transgenic reporters: insulated P-element vectors expressing fast-maturing RFP. *Biotechniques,* 36**,** 436-40, 442.

BASSETT, A. R., TIBBIT, C., PONTING, C. P. & LIU, J. L. 2013. Highly efficient targeted mutagenesis of Drosophila with the CRISPR/Cas9 system. *Cell Rep,* 4**,** 220-8.

BELLETTATO, C. M. & SCARPA, M. 2010. Pathophysiology of neuropathic lysosomal storage disorders. *Journal of Inherited Metabolic Disease,* 33**,** 347-362.

BELMONTE, M. K. & YURGELUN-TODD, D. A. 2003. Functional anatomy of impaired selective attention and compensatory processing in autism. *Brain Res Cogn Brain Res,* 17**,** 651-64.

BENNETT, M. J. & RAKHEJA, D. 2013. The Neuronal Ceroid-Lipofuscinoses. *Developmental Disabilities Research Reviews,* 17**,** 254-259.

BETZ, C. & HALL, M. N. 2013. Where is mTOR and what is it doing there? *Journal of Cell Biology,* 203**,** 563-574.

BIRCA, A., CARMANT, L., LORTIE, A., VANNASING, P. & LASSONDE, M. 2008. Gamma frequency SSVEP components differentiate children with febrile seizures from normal controls. *Epilepsia,* 49**,** 1946-9.

BOLLEPALLI, M. K., KUIPERS, M. E., LIU, C. H., ASTERITI, S. & HARDIE, R. C. 2017. Phototransduction in Drosophila Is Compromised by Gal4 Expression but not by InsP3 Receptor Knockdown or Mutation. *eNeuro,* 4.

BOND, M., HOLTHAUS, S. M., TAMMEN, I., TEAR, G. & RUSSELL, C. 2013. Use of model organisms for the study of neuronal ceroid lipofuscinosis. *Biochim Biophys Acta,* 1832**,** 1842-65.

BRAND, A. H. & PERRIMON, N. 1993. Targeted gene expression as a means of altering cell fates and generating dominant phenotypes. *Development,* 118**,** 401-15.

BRANDENSTEIN, L., SCHWEIZER, M., SEDLACIK, J., FIEHLER, J. & STORCH, S. 2016. Lysosomal dysfunction and impaired autophagy in a novel mouse model deficient for the lysosomal membrane protein Cln7. *Hum Mol Genet,* 25**,** 777-91.

BRENT, J. R., WERNER, K. M. & MCCABE, B. D. 2009. Drosophila larval NMJ dissection. *J Vis Exp*.

BUDNIK, V., GORCZYCA, M. & PROKOP, A. 2006. Selected methods for the anatomical study of Drosophila embryonic and larval neuromuscular junctions. *Int Rev Neurobiol,* 75**,** 323-65.

BUDNIK, V. & SALINAS, P. C. 2011. Wnt signaling during synaptic development and plasticity. *Curr Opin Neurobiol,* 21**,** 151-9.

BUSSE, L., WADE, A. R. & CARANDINI, M. 2009. Representation of concurrent stimuli by population activity in visual cortex. *Neuron,* 64**,** 931-42.

CAO, Y., ESPINOLA, J. A., FOSSALE, E., MASSEY, A. C., CUERVO, A. M., MACDONALD, M. E. & COTMAN, S. L. 2006. Autophagy is disrupted in a knock-in mouse model of juvenile neuronal ceroid lipofuscinosis. *J Biol Chem,* 281**,** 20483-93.

CARCEL-TRULLOLS, J., KOVACS, A. D. & PEARCE, D. A. 2015. Cell biology of the NCL proteins: What they do and don't do. *Biochimica Et Biophysica Acta-Molecular Basis of Disease,* 1852**,** 2242-2255.

CHAN, C. H., MITCHISON, H. M. & PEARCE, D. A. 2008. Transcript and in silico analysis of CLN3 in juvenile neuronal ceroid lipofuscinosis and associated mouse models. *Hum Mol Genet,* 17**,** 3332-9.

CHANG, H. C., DIMLICH, D. N., YOKOKURA, T., MUKHERJEE, A., KANKEL, M. W., SEN, A., SRIDHAR, V., FULGA, T. A., HART, A. C., VAN VACTOR, D. & ARTAVANIS-TSAKONAS, S. 2008. Modeling spinal muscular atrophy in Drosophila. *PLoS One,* 3**,** e3209.

CHAPEL, A., KIEFFER-JAQUINOD, S., SAGNE, C., VERDON, Q., IVALDI, C., MELLAL, M., THIRION, J., JADOT, M., BRULEY, C., GARIN, J., GASNIER, B. & JOURNET, A. 2013. An extended proteome map of the lysosomal membrane reveals novel potential transporters. *Mol Cell Proteomics,* 12**,** 1572-88.

CHINTAPALLI, V. R., WANG, J. & DOW, J. A. T. 2007. Using FlyAtlas to identify better Drosophila melanogaster models of human disease. *Nature Genetics,* 39**,** 715-720.

CHOTARD, C. & SALECKER, I. 2007. Glial cell development and function in the Drosophila visual system. *Neuron Glia Biol,* 3**,** 17-25.

COLLINS, C. A. & DIANTONIO, A. 2007. Synaptic development: insights from Drosophila. *Curr Opin Neurobiol,* 17**,** 35-42.

COOMBE, P. E. & HEISENBERG, M. 1986. The structural brain mutant Vacuolar medulla of Drosophila melanogaster with specific behavioral defects and cell degeneration in the adult. *J Neurogenet,* 3**,** 135-58.

COOPER, J. D. 2003. Progress towards understanding the neurobiology of Batten disease or neuronal ceroid lipofuscinosis. *Curr Opin Neurol,* 16**,** 121-8.

COOPER, J. D., RUSSELL, C. & MITCHISON, H. M. 2006. Progress towards understanding disease mechanisms in small vertebrate models of neuronal ceroid lipofuscinosis. *Biochim Biophys Acta,* 1762**,** 873-89.

COOPER, J. D., TARCZYLUK, M. A. & NELVAGAL, H. R. 2015. Towards a new understanding of NCL pathogenesis. *Biochim Biophys Acta,* 1852**,** 2256-61.

DAER, R. M., CUTTS, J. P., BRAFMAN, D. A. & HAYNES, K. A. 2017. The Impact of Chromatin Dynamics on Cas9-Mediated Genome Editing in Human Cells. *ACS Synth Biol,* 6**,** 428-438.

DAMME, M., BRANDENSTEIN, L., FEHR, S., JANKOWIAK, W., BARTSCH, U., SCHWEIZER, M., HERMANS-BORGMEYER, I. & STORCH, S. 2014. Gene disruption of Mfsd8 in mice provides the first animal model for CLN7 disease. *Neurobiol Dis,* 65**,** 12-24.

DANYUKOVA, T., ARIUNBAT, K., THELEN, M., BROCKE-AHMADINEJAD, N., MOLE, S. E. & STORCH, S. 2018. Loss of CLN7 results in depletion of soluble lysosomal proteins and impaired mTOR reactivation. *Hum Mol Genet,* 27**,** 1711-1722.

DAS, A. M., VON HARLEM, R., FEIST, M., LUCKE, T. & KOHLSCHUTTER, A. 2001. Altered levels of high-energy phosphate compounds in fibroblasts from different forms of neuronal ceroid lipofuscinoses: further evidence for mitochondrial involvement. *Eur J Paediatr Neurol,* 5 Suppl A**,** 143-6.

DERMAUT, B., NORGA, K. K., KANIA, A., VERSTREKEN, P., PAN, H., ZHOU, Y., CALLAERTS, P. & BELLEN, H. J. 2005. Aberrant lysosomal carbohydrate storage accompanies endocytic defects and neurodegeneration in Drosophila benchwarmer. *J Cell Biol,* 170**,** 127-39.

DESALVO, M. K., HINDLE, S. J., RUSAN, Z. M., ORNG, S., EDDISON, M., HALLIWILL, K. & BAINTON, R. J. 2014. The Drosophila surface glia transcriptome: evolutionary conserved blood-brain barrier processes. *Front Neurosci,* 8**,** 346.

DESALVO, M. K., MAYER, N., MAYER, F. & BAINTON, R. J. 2011. Physiologic and anatomic characterization of the brain surface glia barrier of Drosophila. *Glia,* 59**,** 1322-40.

DI FABIO, R., MORO, F., PESTILLO, L., MESCHINI, M. C., PEZZINI, F., DOCCINI, S., CASALI, C., PIERELLI, F., SIMONATI, A. & SANTORELLI, F. M. 2014. Pseudo-Dominant

Inheritance of a Novel Ctsf Mutation Associated with Type B Kufs Disease. *Neurology,* 83**,** 1769-1770.

FALLER, K. M. E., GUTIERREZ-QUINTANA, R., MOHAMMED, A., RAHIM, A. A., TUXWORTH, R. I., WAGER, K. & BOND, M. 2015. The neuronal ceroid lipofuscinoses: Opportunities from model systems. *Biochimica Et Biophysica Acta-Molecular Basis of Disease,* 1852**,** 2267-2278.

FENG, Y. F., UEDA, A. & WU, C. F. 2004. A modified minimal hemolymph-like solution, HL3.1, for physiological recordings at the neuromuscular junctions of normal and mutant Drosophila larvae. *Journal of Neurogenetics,* 18**,** 377-402.

FOSSALE, E., WOLF, P., ESPINOLA, J. A., LUBICZ-NAWROCKA, T., TEED, A. M., GAO, H., RIGAMONTI, D., CATTANEO, E., MACDONALD, M. E. & COTMAN, S. L. 2004. Membrane trafficking and mitochondrial abnormalities precede subunit c deposition in a cerebellar cell model of juvenile neuronal ceroid lipofuscinosis. *BMC Neurosci,* 5**,** 57.

FOX, M. A., SANES, J. R., BORZA, D. B., ESWARAKUMAR, V. P., FASSLER, R., HUDSON, B. G., JOHN, S. W., NINOMIYA, Y., PEDCHENKO, V., PFAFF, S. L., RHEAULT, M. N., SADO, Y., SEGAL, Y., WERLE, M. J. & UMEMORI, H. 2007. Distinct target-derived signals organize formation, maturation, and maintenance of motor nerve terminals. *Cell,* 129**,** 179-93.

FUENTES-MEDEL, Y., ASHLEY, J., BARRIA, R., MALONEY, R., FREEMAN, M. & BUDNIK, V. 2012. Integration of a retrograde signal during synapse formation by glia-secreted TGF-beta ligand. *Curr Biol,* 22**,** 1831-8.

GIBSON, D. G., YOUNG, L., CHUANG, R. Y., VENTER, J. C., HUTCHISON, C. A. & SMITH, H. O. 2009. Enzymatic assembly of DNA molecules up to several hundred kilobases. *Nature Methods,* 6**,** 343-U41.

GILLINGWATER, T. H. & WISHART, T. M. 2013. Mechanisms underlying synaptic vulnerability and degeneration in neurodegenerative disease. *Neuropathol Appl Neurobiol,* 39**,** 320-34.

GLASER, R. L., HICKEY, A. J., CHOTKOWSKI, H. L. & CHU-LAGRAFF, Q. 2003. Characterization of Drosophila palmitoyl-protein thioesterase 1. *Gene,* 312**,** 271-9.

GOEBEL, H. H. & WISNIEWSKI, K. E. 2004. Current state of clinical and morphological features in human NCL. *Brain Pathol,* 14**,** 61-9.

GONG, Z. 2009. Behavioral dissection of Drosophila larval phototaxis. *Biochem Biophys Res Commun,* 382**,** 395-9.

GONG, Z. & GONG, Z. 2012. A molecular diffusion based utility model for Drosophila larval phototaxis. *Theor Biol Med Model,* 9**,** 3.

GRATZ, S. J., CUMMINGS, A. M., NGUYEN, J. N., HAMM, D. C., DONOHUE, L. K., HARRISON, M. M., WILDONGER, J. & O'CONNOR-GILES, K. M. 2013. Genome engineering of Drosophila with the CRISPR RNA-guided Cas9 nuclease. *Genetics,* 194**,** 1029-35.

GRATZ, S. J., UKKEN, F. P., RUBINSTEIN, C. D., THIEDE, G., DONOHUE, L. K., CUMMINGS, A. M. & O'CONNOR-GILES, K. M. 2014. Highly Specific and Efficient CRISPR/Cas9-Catalyzed Homology-Directed Repair in Drosophila. *Genetics,* 196**,** 961-+.

GRIFFEY, M. A., WOZNIAK, D., WONG, M., BIBLE, E., JOHNSON, K., ROTHMAN, S. M., WENTZ, A. E., COOPER, J. D. & SANDS, M. S. 2006. CNS-directed AAV2-mediated

gene therapy ameliorates functional deficits in a murine model of infantile neuronal ceroid lipofuscinosis. *Mol Ther,* 13**,** 538-47.

GUO, J., O'BRIEN, D. P., MHLANGA-MUTANGADURA, T., OLBY, N. J., TAYLOR, J. F., SCHNABEL, R. D., KATZ, M. L. & JOHNSON, G. S. 2015. A rare homozygous MFSD8 single-base-pair deletion and frameshift in the whole genome sequence of a Chinese Crested dog with neuronal ceroid lipofuscinosis. *BMC Vet Res,* 10**,** 960.

GUPTA, R. M. & MUSUNURU, K. 2014. Expanding the genetic editing tool kit: ZFNs, TALENs, and CRISPR-Cas9. *J Clin Invest,* 124**,** 4154-61.

HALTIA, M. 2003. The neuronal ceroid-lipofuscinoses. *J Neuropathol Exp Neurol,* 62**,** 1-13.

HALTIA, M. 2006. The neuronal ceroid-lipofuscinoses: From past to present. *Biochimica Et Biophysica Acta-Molecular Basis of Disease,* 1762**,** 850-856.

HALTIA, M. & GOEBEL, H. H. 2013. The neuronal ceroid-lipofuscinoses: A historical introduction. *Biochimica Et Biophysica Acta-Molecular Basis of Disease,* 1832**,** 1795-1800.

HARDIE, R. C. & RAGHU, P. 2001. Visual transduction in Drosophila. *Nature,* 413**,** 186-93.

HASKELL, R. E., CARR, C. J., PEARCE, D. A., BENNETT, M. J. & DAVIDSON, B. L. 2000. Batten disease: evaluation of CLN3 mutations on protein localization and function. *Hum Mol Genet,* 9**,** 735-44.

HASKELL, R. E., DERKSEN, T. A. & DAVIDSON, B. L. 1999. Intracellular trafficking of the JNCL protein CLN3. *Mol Genet Metab,* 66**,** 253-60.

HAWKINS, J. D. 1988. A survey on intron and exon lengths. *Nucleic Acids Res,* 16**,** 9893-908.

HEISENBERG, M. 1971. Separation of receptor and lamina potentials in the electroretinogram of normal and mutant Drosophila. *J Exp Biol,* 55**,** 85-100.

HENRY, F. E., WANG, X., SERRANO, D., PEREZ, A. S., CARRUTHERS, C. J. L., STUENKEL, E. L. & SUTTON, M. A. 2018. A Unique Homeostatic Signaling Pathway Links Synaptic Inactivity to Postsynaptic mTORC1. *J Neurosci,* 38**,** 2207-2225.

HENSTRIDGE, C. M., PICKETT, E. & SPIRES-JONES, T. L. 2016. Synaptic pathology: A shared mechanism in neurological disease. *Ageing Res Rev,* 28**,** 72-84.

HICKEY, A. J., CHOTKOWSKI, H. L., SINGH, N., AULT, J. G., KOREY, C. A., MACDONALD, M. E. & GLASER, R. L. 2006. Palmitoyl-protein thioesterase 1 deficiency in Drosophila melanogaster causes accumulation of abnormal storage material and reduced life span. *Genetics,* 172**,** 2379-90.

HINDLE, S., AFSARI, F., STARK, M., MIDDLETON, C. A., EVANS, G. J. O., SWEENEY, S. T. & ELLIOTT, C. J. H. 2013. Dopaminergic expression of the Parkinsonian gene LRRK2-G2019S leads to non-autonomous visual neurodegeneration, accelerated by increased neural demands for energy. *Human Molecular Genetics,* 22**,** 2129-2140.

HINDLE, S. J. & BAINTON, R. J. 2014. Barrier mechanisms in the Drosophila blood-brain barrier. *Front Neurosci,* 8**,** 414.

HINDLE, S. J., HEBBAR, S., SCHWUDKE, D., ELLIOTT, C. J. H. & SWEENEY, S. T. 2017. A saposin deficiency model in Drosophila: Lysosomal storage, progressive neurodegeneration and sensory physiological decline. *Neurobiol Dis,* 98**,** 77-87.

HOANG, B. & CHIBA, A. 2001. Single-cell analysis of Drosophila larval neuromuscular synapses. *Dev Biol,* 229**,** 55-70.

HORLBECK, M. A., WITKOWSKY, L. B., GUGLIELMI, B., REPLOGLE, J. M., GILBERT, L. A., VILLALTA, J. E., TORIGOE, S. E., TJIAN, R. & WEISSMAN, J. S. 2016. Nucleosomes impede Cas9 access to DNA in vivo and in vitro. *Elife,* 5.

HUANG, L., PIKE, D., SLEAT, D. E., NANDA, V. & LOBEL, P. 2014. Potential pitfalls and solutions for use of fluorescent fusion proteins to study the lysosome. *PLoS One,* 9, e88893.

HUU, N. T., YOSHIDA, H., UMEGAWACHI, T., MIYATA, S. & YAMAGUCHI, M. 2014. Structural characterization and subcellular localization of Drosophila organic solute carrier partner 1. *BMC Biochem,* 15, 11.

ITO, K., URBAN, J. & TECHNAU, G. M. 1995. Distribution, Classification, and Development of Drosophila Glial-Cells in the Late Embryonic and Early Larval Ventral Nerve Cord. *Rouxs Archives of Developmental Biology,* 204, 284-307.

JALANKO, A. & BRAULKE, T. 2009. Neuronal ceroid lipofuscinoses. *Biochim Biophys Acta,* 1793, 697-709.

JANKOWIAK, W., BRANDENSTEIN, L., DULZ, S., HAGEL, C., STORCH, S. & BARTSCH, U. 2016. Retinal Degeneration in Mice Deficient in the Lysosomal Membrane Protein CLN7. *Invest Ophthalmol Vis Sci,* 57, 4989-4998.

JINEK, M., CHYLINSKI, K., FONFARA, I., HAUER, M., DOUDNA, J. A. & CHARPENTIER, E. 2012. A programmable dual-RNA-guided DNA endonuclease in adaptive bacterial immunity. *Science,* 337, 816-21.

KATSURAGI, Y., ICHIMURA, Y. & KOMATSU, M. 2015. p62/SQSTM1 functions as a signaling hub and an autophagy adaptor. *FEBS J,* 282, 4672-8.

KATZ, B. & MINKE, B. 2009. Drosophila photoreceptors and signaling mechanisms. *Front Cell Neurosci,* 3, 2.

KAY, G. W., PALMER, D. N., REZAIE, P. & COOPER, J. D. 2006. Activation of non-neuronal cells within the prenatal developing brain of sheep with neuronal ceroid lipofuscinosis. *Brain Pathol,* 16, 110-6.

KESHISHIAN, H., BROADIE, K., CHIBA, A. & BATE, M. 1996. The drosophila neuromuscular junction: a model system for studying synaptic development and function. *Annu Rev Neurosci,* 19, 545-75.

KHAN, K. N., EL-ASRAG, M. E., KU, C. A., HOLDER, G. E., MCKIBBIN, M., ARNO, G., POULTER, J. A., CARSS, K., BOMMIREDDY, T., BAGHERI, S., BAKALL, B., SCHOLL, H. P., RAYMOND, F. L., TOOMES, C., INGLEHEARN, C. F., PENNESI, M. E., MOORE, A. T., MICHAELIDES, M., WEBSTER, A. R., ALI, M., FOR, N. B.-R. D. & CONSORTIUM, U. K. I. R. D. 2017. Specific Alleles of CLN7/MFSD8, a Protein That Localizes to Photoreceptor Synaptic Terminals, Cause a Spectrum of Nonsyndromic Retinal Dystrophy. *Invest Ophthalmol Vis Sci,* 58, 2906-2914.

KIELAR, C., WISHART, T. M., PALMER, A., DIHANICH, S., WONG, A. M., MACAULEY, S. L., CHAN, C. H., SANDS, M. S., PEARCE, D. A., COOPER, J. D. & GILLINGWATER, T. H. 2009a. Molecular correlates of axonal and synaptic pathology in mouse models of Batten disease. *Human Molecular Genetics,* 18, 4066-4080.

KIELAR, C., WISHART, T. M., PALMER, A., DIHANICH, S., WONG, A. M., MACAULEY, S. L., CHAN, C. H., SANDS, M. S., PEARCE, D. A., COOPER, J. D. & GILLINGWATER, T. H. 2009b. Molecular correlates of axonal and synaptic pathology in mouse models of Batten disease. *Hum Mol Genet,* 18, 4066-80.

KIM, S., WAIRKAR, Y. P., DANIELS, R. W. & DIANTONIO, A. 2010. The novel endosomal membrane protein Ema interacts with the class C Vps-HOPS complex to promote endosomal maturation. *J Cell Biol,* 188**,** 717-34.

KIM, S. J., ZHANG, Z. J., SARKAR, C., TSAI, P. C., LEE, Y. C., DYE, L. & MUKHERJEE, A. B. 2008. Palmitoyl protein thioesterase-1 deficiency impairs synaptic vesicle recycling at nerve terminals, contributing to neuropathology in humans and mice. *Journal of Clinical Investigation,* 118**,** 3075-3086.

KIRIYAMA, Y. & NOCHI, H. 2015. The Function of Autophagy in Neurodegenerative Diseases. *Int J Mol Sci,* 16**,** 26797-812.

KITZMULLER, C., HAINES, R. L., CODLIN, S., CUTLER, D. F. & MOLE, S. E. 2008. A function retained by the common mutant CLN3 protein is responsible for the late onset of juvenile neuronal ceroid lipofuscinosis. *Hum Mol Genet,* 17**,** 303-12.

KLIONSKY, D. J., ABDELMOHSEN, K., ABE, A., ABEDIN, M. J., ABELIOVICH, H., AROZENA, A. A., ADACHI, H., ADAMS, C. M., ADAMS, P. D., ADELI, K., ADHIHETTY, P. J., ADLER, S. G., AGAM, G., AGARWAL, R., AGHI, M. K., AGNELLO, M., AGOSTINIS, P., AGUILAR, P. V., AGUIRRE-GHISO, J., AIROLDI, E. M., AIT-SI-ALI, S., AKEMATSU, T., AKPORIAYE, E. T., AL-RUBEAI, M., ALBAICETA, G. M., ALBANESE, C., ALBANI, D., ALBERT, M. L., ALDUDO, J., ALGUL, H., ALIREZAEI, M., ALLOZA, I., ALMASAN, A., ALMONTE-BECERIL, M., ALNEMRI, E. S., ALONSO, C., ALTAN-BONNET, N., ALTIERI, D. C., ALVAREZ, S., ALVAREZ-ERVITI, L., ALVES, S., AMADORO, G., AMANO, A., AMANTINI, C., AMBROSIO, S., AMELIO, I., AMER, A. O., AMESSOU, M., AMON, A., AN, Z. Y., ANANIA, F. A., ANDERSEN, S. U., ANDLEY, U. P., ANDREADI, C. K., ANDRIEU-ABADIE, N., ANEL, A., ANN, D. K., ANOOPKUMAR-DUKIE, S., ANTONIOLI, M., AOKI, H., APOSTOLOVA, N., AQUILA, S., AQUILANO, K., ARAKI, K., ARAMA, E., ARANDA, A., ARAYA, J., ARCARO, A., ARIAS, E., ARIMOTO, H., ARIOSA, A. R., ARMSTRONG, J. L., ARNOULD, T., ARSOV, I., ASANUMA, K., ASKANAS, V., ASSELIN, E., ATARASHI, R., ATHERTON, S. S., ATKIN, J. D., ATTARDI, L. D., AUBERGER, P., AUBURGER, G., AURELIAN, L., AUTELLI, R., AVAGLIANO, L., AVANTAGGIATI, M. L., AVRAHAMI, L., AWALE, S., AZAD, N., BACHETTI, T., BACKER, J. M., BAE, D. H., BAE, J. S., BAE, O. N., BAE, S. H., BAEHRECKE, E. H., BAEK, S. H., BAGHDIGUIAN, S., BAGNIEWSKA-ZADWORNA, A., et al. 2016. Guidelines for the use and interpretation of assays for monitoring autophagy (3rd edition). *Autophagy,* 12**,** 1-222.

KOCH, S., MOLCHANOVA, S. M., WRIGHT, A. K., EDWARDS, A., COOPER, J. D., TAIRA, T., GILLINGWATER, T. H. & TYYNELA, J. 2011. Morphologic and functional correlates of synaptic pathology in the cathepsin D knockout mouse model of congenital neuronal ceroid lipofuscinosis. *J Neuropathol Exp Neurol,* 70**,** 1089-96.

KOHN, E., KATZ, B., YASIN, B., PETERS, M., RHODES, E., ZAGURI, R., WEISS, S. & MINKE, B. 2015. Functional cooperation between the IP3 receptor and phospholipase C secures the high sensitivity to light of Drosophila photoreceptors in vivo. *J Neurosci,* 35**,** 2530-46.

KOIKE, M., NAKANISHI, H., SAFTIG, P., EZAKI, J., ISAHARA, K., OHSAWA, Y., SCHULZ-SCHAEFFER, W., WATANABE, T., WAGURI, S., KAMETAKA, S., SHIBATA, M., YAMAMOTO, K., KOMINAMI, E., PETERS, C., VON FIGURA, K. & UCHIYAMA, Y.

2000. Cathepsin D deficiency induces lysosomal storage with ceroid lipofuscin in mouse CNS neurons. *J Neurosci,* 20**,** 6898-906.

KOLLMANN, K., UUSI-RAUVA, K., SCIFO, E., TYYNELA, J., JALANKO, A. & BRAULKE, T. 2013. Cell biology and function of neuronal ceroid lipofuscinosis-related proteins. *Biochim Biophys Acta,* 1832**,** 1866-81.

KOREY, C. A. & MACDONALD, M. E. 2003. An over-expression system for characterizing Ppt1 function in Drosophila. *BMC Neurosci,* 4**,** 30.

KOUSI, M., SIINTOLA, E., DVORAKOVA, L., VLASKOVA, H., TURNBULL, J., TOPCU, M., YUKSEL, D., GOKBEN, S., MINASSIAN, B. A., ELLEDER, M., MOLE, S. E. & LEHESJOKI, A. E. 2009. Mutations in CLN7/MFSD8 are a common cause of variant late-infantile neuronal ceroid lipofuscinosis. *Brain,* 132**,** 810-9.

KUOA, S. Y., CASTORENO, A. B., ALDRICH, L. N., LASSEN, K. G., GOEL, G., DANCIK, V., KUBALLA, P., LATORRE, I., CONWAY, K. L., SARKAR, S., MAETZEL, D., JAENISCH, R., CLEMONS, P. A., SCHREIBER, S. L., SHAMJI, A. F. & XAVIER, R. J. 2015. Small-molecule enhancers of autophagy modulate cellular disease phenotypes suggested by human genetics. *Proceedings of the National Academy of Sciences of the United States of America,* 112**,** E4281-E4287.

LEINONEN, H., KEKSA-GOLDSTEINE, V., RAGAUSKAS, S., KOHLMANN, P., SINGH, Y., SAVCHENKO, E., PURANEN, J., MALM, T., KALESNYKAS, G., KOISTINAHO, J., TANILA, H. & KANNINEN, K. M. 2017. Retinal Degeneration In A Mouse Model Of CLN5 Disease Is Associated With Compromised Autophagy. *Sci Rep,* 7**,** 1597.

LEVINE, M. & TJIAN, R. 2003. Transcription regulation and animal diversity. *Nature,* 424**,** 147-51.

LIMMER, S., WEILER, A., VOLKENHOFF, A., BABATZ, F. & KLAMBT, C. 2014. The Drosophila blood-brain barrier: development and function of a glial endothelium. *Front Neurosci,* 8**,** 365.

LIPTON, J. O. & SAHIN, M. 2014. The neurology of mTOR. *Neuron,* 84**,** 275-91.

LIVAK, K. J. & SCHMITTGEN, T. D. 2001. Analysis of relative gene expression data using real-time quantitative PCR and the 2(-Delta Delta C(T)) Method. *Methods,* 25**,** 402-8.

LNENICKA, G. A. & KESHISHIAN, H. 2000. Identified motor terminals in Drosophila larvae show distinct differences in morphology and physiology. *J Neurobiol,* 43**,** 186-97.

LORINCZ, P., MAUVEZIN, C. & JUHASZ, G. 2017. Exploring Autophagy in Drosophila. *Cells,* 6.

MAHMOOD, F., FU, S., COOKE, J., WILSON, S. W., COOPER, J. D. & RUSSELL, C. 2013. A zebrafish model of CLN2 disease is deficient in tripeptidyl peptidase 1 and displays progressive neurodegeneration accompanied by a reduction in proliferation. *Brain,* 136**,** 1488-507.

MANCINI, C., NASSANI, S., GUO, Y. R., CHEN, Y. L., GIORGIO, E., BRUSSINO, A., DI GREGORIO, E., CAVALIERI, S., LO BUONO, N., FUNARO, A., PIZIO, N. R., NMEZI, B., KYTTALA, A., SANTORELLI, F. M., PADIATH, Q. S., HAKONARSON, H., ZHANG, H. & BRUSCO, A. 2015. Adult-onset autosomal recessive ataxia associated with neuronal ceroid lipofuscinosis type 5 gene (CLN5) mutations. *Journal of Neurology,* 262**,** 173-178.

MATHEW, D., ATAMAN, B., CHEN, J., ZHANG, Y., CUMBERLEDGE, S. & BUDNIK, V. 2005. Wingless signaling at synapses is through cleavage and nuclear import of receptor DFrizzled2. *Science,* 310**,** 1344-7.

MAYER, F., MAYER, N., CHINN, L., PINSONNEAULT, R. L., KROETZ, D. & BAINTON, R. J. 2009. Evolutionary conservation of vertebrate blood-brain barrier chemoprotective mechanisms in Drosophila. *J Neurosci,* 29**,** 3538-50.

MCCABE, B. D., MARQUES, G., HAGHIGHI, A. P., FETTER, R. D., CROTTY, M. L., HAERRY, T. E., GOODMAN, C. S. & O'CONNOR, M. B. 2003. The BMP homolog Gbb provides a retrograde signal that regulates synaptic growth at the Drosophila neuromuscular junction. *Neuron,* 39**,** 241-54.

MCGUINNESS, L., BARDO, S. J. & EMPTAGE, N. J. 2007. The lysosome or lysosome-related organelle may serve as a Ca2+ store in the boutons of hippocampal pyramidal cells. *Neuropharmacology,* 52**,** 126-35.

MENON, K. P., CARRILLO, R. A. & ZINN, K. 2013. Development and plasticity of the Drosophila larval neuromuscular junction. *Wiley Interdiscip Rev Dev Biol,* 2**,** 647-70.

MICSENYI, M. C., SIKORA, J., STEPHNEY, G., DOBRENIS, K. & WALKLEY, S. U. 2013. Lysosomal membrane permeability stimulates protein aggregate formation in neurons of a lysosomal disease. *J Neurosci,* 33**,** 10815-27.

MILTON, V. J., JARRETT, H. E., GOWERS, K., CHALAK, S., BRIGGS, L., ROBINSON, I. M. & SWEENEY, S. T. 2011. Oxidative stress induces overgrowth of the Drosophila neuromuscular junction. *Proc Natl Acad Sci U S A,* 108**,** 17521-6.

MOHAMMED, A., O'HARE, M. B., WARLEY, A., TEAR, G. & TUXWORTH, R. I. 2017. in vivo localization of the neuronal ceroid lipofuscinosis proteins, CLN3 and CLN7, at endogenous expression levels. *Neurobiol Dis,* 103**,** 123-132.

MONTELL, C. 2012. Drosophila visual transduction. *Trends Neurosci,* 35**,** 356-63.

MORGAN, A. J., PLATT, F. M., LLOYD-EVANS, E. & GALIONE, A. 2011. Molecular mechanisms of endolysosomal Ca2+ signalling in health and disease. *Biochem J,* 439**,** 349-74.

MUZAFFAR, N. E. & PEARCE, D. A. 2008. Analysis of NCL Proteins from an Evolutionary Standpoint. *Curr Genomics,* 9**,** 115-36.

MYLLYKANGAS, L., TYYNELA, J., PAGE-MCCAW, A., RUBIN, G. M., HALTIA, M. J. & FEANY, M. B. 2005. Cathepsin D-deficient Drosophila recapitulate the key features of neuronal ceroid lipofuscinoses. *Neurobiol Dis,* 19**,** 194-9.

NAGY, P., VARGA, A., KOVACS, A. L., TAKATS, S. & JUHASZ, G. 2015. How and why to study autophagy in Drosophila: it's more than just a garbage chute. *Methods,* 75**,** 151-61.

NAKANO, Y., FUJITANI, K., KURIHARA, J., RAGAN, J., USUI-AOKI, K., SHIMODA, L., LUKACSOVICH, T., SUZUKI, K., SEZAKI, M., SANO, Y., UEDA, R., AWANO, W., KANEDA, M., UMEDA, M. & YAMAMOTO, D. 2001. Mutations in the novel membrane protein spinster interfere with programmed cell death and cause neural degeneration in Drosophila melanogaster. *Molecular and Cellular Biology,* 21**,** 3775-3788.

NATARAJAN, R., TRIVEDI-VYAS, D. & WAIRKAR, Y. P. 2013. Tuberous sclerosis complex regulates Drosophila neuromuscular junction growth via the TORC2/Akt pathway. *Hum Mol Genet,* 22**,** 2010-23.

NIPPE, O. M., WADE, A. R., ELLIOTT, C. J. H. & CHAWLA, S. 2017. Circadian Rhythms in Visual Responsiveness in the Behaviorally Arrhythmic Drosophila Clock Mutant Clk(Jrk). *J Biol Rhythms,* 32**,** 583-592.

NITA, D. A., MOLE, S. E. & MINASSIAN, B. A. 2016. Neuronal ceroid lipofuscinoses. *Epileptic Disord,* 18**,** 73-88.

NORCIA, A. M., APPELBAUM, L. G., ALES, J. M., COTTEREAU, B. R. & ROSSION, B. 2015. The steady-state visual evoked potential in vision research: A review. *J Vis,* 15**,** 4.

NOSKOVA, L., STRANECKY, V., HARTMANNOVA, H., PRISTOUPILOVA, A., BARESOVA, V., IVANEK, R., HULKOVA, H., JAHNOVA, H., VAN DER ZEE, J., STAROPOLI, J. F., SIMS, K. B., TYYNELA, J., VAN BROECKHOVEN, C., NIJSSEN, P. C. G., MOLE, S. E., ELLEDER, M. & KMOCH, S. 2011. Mutations in DNAJC5, Encoding Cysteine-String Protein Alpha, Cause Autosomal-Dominant Adult-Onset Neuronal Ceroid Lipofuscinosis. *American Journal of Human Genetics,* 89**,** 241-252.

O'HARE, M. B. 2012. Examining CLN7 function in Drosophila. *KCL PhD Thesis*.

O'HARE, M. B. M., ALAMIN ; CONNOLLY, KYLE J; AITCHISON, KATELYN M; ANTHONEY, NIKI C; ROBERTS, AMY L; TAYLOR, MATTHEW J; STEWART, BRYAN A; TUXWORTH, RICHARD I; TEAR, GUY Submitted. The neuronal ceroid lipofuscinosis protein, Cln7, regulates neural development from the post-synaptic cell.

OKAMOTO, N., NAKAMORI, R., MURAI, T., YAMAUCHI, Y., MASUDA, A. & NISHIMURA, T. 2013. A secreted decoy of InR antagonizes insulin/IGF signaling to restrict body growth in Drosophila. *Genes Dev,* 27**,** 87-97.

OSWALD, M. J., PALMER, D. N., KAY, G. W., SHEMILT, S. J., REZAIE, P. & COOPER, J. D. 2005. Glial activation spreads from specific cerebral foci and precedes neurodegeneration in presymptomatic ovine neuronal ceroid lipofuscinosis (CLN6). *Neurobiol Dis,* 20**,** 49-63.

PACKARD, M., KOO, E. S., GORCZYCA, M., SHARPE, J., CUMBERLEDGE, S. & BUDNIK, V. 2002. The Drosophila Wnt, wingless, provides an essential signal for pre- and postsynaptic differentiation. *Cell,* 111**,** 319-30.

PALMER, D. N. 2015. The relevance of the storage of subunit c of ATP synthase in different forms and models of Batten disease (NCLs). *Biochim Biophys Acta,* 1852**,** 2287-91.

PALMER, D. N., BARRY, L. A., TYYNELA, J. & COOPER, J. D. 2013. NCL disease mechanisms. *Biochim Biophys Acta,* 1832**,** 1882-93.

PALMER, D. N., BAYLISS, S. L., CLIFTON, P. A. & GRANT, V. J. 1993. Storage bodies in the ceroid-lipofuscinoses (Batten disease): low-molecular-weight components, unusual amino acids and reconstitution of fluorescent bodies from non-fluorescent components. *J Inherit Metab Dis,* 16**,** 292-5.

PARTANEN, S., HAAPANEN, A., KIELAR, C., PONTIKIS, C., ALEXANDER, N., INKINEN, T., SAFTIG, P., GILLINGWATER, T. H., COOPER, J. D. & TYYNELA, J. 2008a. Synaptic changes in the thalamocortical system of cathepsin D-deficient mice: a model of human congenital neuronal ceroid-lipofuscinosis. *J Neuropathol Exp Neurol,* 67**,** 16-29.

PARTANEN, S., HAAPANEN, A., KIELAR, C., PONTIKIS, C., ALEXANDER, N., INKINEN, T., SAFTIG, P., GILLINGWATER, T. H., COOPER, J. D. & TYYNELA, J. 2008b. Synaptic changes in the thalamocortical system of cathepsin D-deficient mice: A model of human congenital neuronal ceroid-lipofuscinosis. *Journal of Neuropathology and Experimental Neurology,* 67**,** 16-29.

PENNEY, J., TSURUDOME, K., LIAO, E. H., ELAZZOUZI, F., LIVINGSTONE, M., GONZALEZ, M., SONENBERG, N. & HAGHIGHI, A. P. 2012. TOR is required for the retrograde regulation of synaptic homeostasis at the Drosophila neuromuscular junction. *Neuron,* 74**,** 166-78.

PERRIMON, N., NI, J. Q. & PERKINS, L. 2010. In vivo RNAi: today and tomorrow. *Cold Spring Harb Perspect Biol,* 2**,** a003640.

PONTIKIS, C. C., CELLA, C. V., PARIHAR, N., LIM, M. J., CHAKRABARTI, S., MITCHISON, H. M., MOBLEY, W. C., REZAIE, P., PEARCE, D. A. & COOPER, J. D. 2004. Late onset neurodegeneration in the Cln3-/- mouse model of juvenile neuronal ceroid lipofuscinosis is preceded by low level glial activation. *Brain Res,* 1023**,** 231-42.

PORT, F., CHEN, H. M., LEE, T. & BULLOCK, S. L. 2014. Optimized CRISPR/Cas tools for efficient germline and somatic genome engineering in Drosophila. *Proceedings of the National Academy of Sciences of the United States of America,* 111**,** E2967-E2976.

PORT, F., MUSCHALIK, N. & BULLOCK, S. L. 2015. Systematic Evaluation of Drosophila CRISPR Tools Reveals Safe and Robust Alternatives to Autonomous Gene Drives in Basic Research. *G3 (Bethesda),* 5**,** 1493-502.

PORTA, E. A. 2002. Pigments in aging: an overview. *Ann N Y Acad Sci,* 959**,** 57-65.

PRIEBE, N. J. & FERSTER, D. 2002. A new mechanism for neuronal gain control (or how the gain in brains has mainly been explained). *Neuron,* 35**,** 602-4.

RAGHU, P., COLLEY, N. J., WEBEL, R., JAMES, T., HASAN, G., DANIN, M., SELINGER, Z. & HARDIE, R. C. 2000. Normal phototransduction in Drosophila photoreceptors lacking an InsP(3) receptor gene. *Mol Cell Neurosci,* 15**,** 429-45.

RAJARAM, S., SCOTT, R. L. & NASH, H. A. 2005. Retrograde signaling from the brain to the retina modulates the termination of the light response in Drosophila. *Proc Natl Acad Sci U S A,* 102**,** 17840-5.

RANTA, S. & LEHESJOKI, A. E. 2000. Northern epilepsy, a new member of the NCL family. *Neurol Sci,* 21**,** S43-7.

RATNAPARKHI, A., LAWLESS, G. M., SCHWEIZER, F. E., GOLSHANI, P. & JACKSON, G. R. 2008. A Drosophila model of ALS: human ALS-associated mutation in VAP33A suggests a dominant negative mechanism. *PLoS One,* 3**,** e2334.

RAWSON, J. M., LEE, M., KENNEDY, E. L. & SELLECK, S. B. 2003. Drosophila neuromuscular synapse assembly and function require the TGF-beta type I receptor saxophone and the transcription factor Mad. *J Neurobiol,* 55**,** 134-50.

REN, X., HOLSTEENS, K., LI, H., SUN, J., ZHANG, Y., LIU, L. P., LIU, Q. & NI, J. Q. 2017. Genome editing in Drosophila melanogaster: from basic genome engineering to the multipurpose CRISPR-Cas9 system. *Sci China Life Sci,* 60**,** 476-489.

ROOSING, S., VAN DEN BORN, L. I., SANGERMANO, R., BANFI, S., KOENEKOOP, R. K., ZONNEVELD-VRIELING, M. N., KLAVER, C. C., VAN LITH-VERHOEVEN, J. J., CREMERS, F. P., DEN HOLLANDER, A. I. & HOYNG, C. B. 2015. Mutations in MFSD8,

encoding a lysosomal membrane protein, are associated with nonsyndromic autosomal recessive macular dystrophy. *Ophthalmology,* 122**,** 170-9.

RUIZ-CANADA, C. & BUDNIK, V. 2006. Introduction on the use of the Drosophila embryonic/larval neuromuscular junction as a model system to study synapse development and function, and a brief summary of pathfinding and target recognition. *Int Rev Neurobiol,* 75**,** 1-31.

SAFTIG, P. & KLUMPERMAN, J. 2009. Lysosome biogenesis and lysosomal membrane proteins: trafficking meets function. *Nature Reviews Molecular Cell Biology,* 10**,** 623-635.

SAHA, A., KIM, S. J., ZHANG, Z., LEE, Y. C., SARKAR, C., TSAI, P. C. & MUKHERJEE, A. B. 2008. RAGE signaling contributes to neuroinflammation in infantile neuronal ceroid lipofuscinosis. *FEBS Lett,* 582**,** 3823-31.

SAHANI, M. H., ITAKURA, E. & MIZUSHIMA, N. 2014. Expression of the autophagy substrate SQSTM1/p62 is restored during prolonged starvation depending on transcriptional upregulation and autophagy- derived amino acids. *Autophagy,* 10**,** 431-441.

SAJA, S., BUFF, H., SMITH, A. C., WILLIAMS, T. S. & KOREY, C. A. 2010. Identifying cellular pathways modulated by Drosophila palmitoyl-protein thioesterase 1 function. *Neurobiol Dis,* 40**,** 135-45.

SANTAVUORI, P., LINNANKIVI, T., JAEKEN, J., VANHANEN, S. L., TELAKIVI, T. & HEISKALA, H. 1993. Psychological symptoms and sleep disturbances in neuronal ceroid-lipofuscinoses (NCL). *J Inherit Metab Dis,* 16**,** 245-8.

SARA MOLE, R. W., AND HANS GOEBEL 2011. Appendix 1: NCL Incidence and Prevalence Data. *The Neuronal Ceroid Lipofuscinoses (Batten Disease) (2 ed.)***,** 361-365.

SCHULZ, A., KOHLSCHUTTER, A., MINK, J., SIMONATI, A. & WILLIAMS, R. 2013. NCL diseases - clinical perspectives. *Biochim Biophys Acta,* 1832**,** 1801-6.

SCOTT, K. & ZUKER, C. 1997. Lights out: deactivation of the phototransduction cascade. *Trends Biochem Sci,* 22**,** 350-4.

SEEHAFER, S. S., RAMIREZ-MONTEALEGRE, D., WONG, A. M., CHAN, C. H., CASTANEDA, J., HORAK, M., AHMADI, S. M., LIM, M. J., COOPER, J. D. & PEARCE, D. A. 2011. Immunosuppression alters disease severity in juvenile Batten disease mice. *J Neuroimmunol,* 230**,** 169-72.

SEN, A., YOKOKURA, T., KANKEL, M. W., DIMLICH, D. N., MANENT, J., SANYAL, S. & ARTAVANIS-TSAKONAS, S. 2011. Modeling spinal muscular atrophy in Drosophila links Smn to FGF signaling. *J Cell Biol,* 192**,** 481-95.

SERANOVA, E., CONNOLLY, K. J., ZATYKA, M., ROSENSTOCK, T. R., BARRETT, T., TUXWORTH, R. I. & SARKAR, S. 2017. Dysregulation of autophagy as a common mechanism in lysosomal storage diseases. *Essays Biochem,* 61**,** 733-749.

SHANER, N. C., STEINBACH, P. A. & TSIEN, R. Y. 2005. A guide to choosing fluorescent proteins. *Nat Methods,* 2**,** 905-9.

SHARIFI, A., KOUSI, M., SAGNE, C., BELLENCHI, G. C., MOREL, L., DARMON, M., HULKOVA, H., RUIVO, R., DEBACKER, C., EL MESTIKAWY, S., ELLEDER, M., LEHESJOKI, A. E., JALANKO, A., GASNIER, B. & KYTTALA, A. 2010. Expression and lysosomal targeting of CLN7, a major facilitator superfamily transporter associated with variant late-infantile neuronal ceroid lipofuscinosis. *Hum Mol Genet,* 19**,** 4497-514.

SHARMA, M., BURRE, J., BRONK, P., ZHANG, Y., XU, W. & SUDHOF, T. C. 2012. CSPalpha knockout causes neurodegeneration by impairing SNAP-25 function. *EMBO J,* 31**,** 829-41.

SHEN, W. & GANETZKY, B. 2009. Autophagy promotes synapse development in Drosophila. *Journal of Cell Biology,* 187**,** 71-79.

SIINTOLA, E., PARTANEN, S., STROMME, P., HAAPANEN, A., HALTIA, M., MAEHLEN, J., LEHESJOKI, A. E. & TYYNELA, J. 2006. Cathepsin D deficiency underlies congenital human neuronal ceroid-lipofuscinosis. *Brain,* 129**,** 1438-1445.

SIINTOLA, E., TOPCU, M., AULA, N., LOHI, H., MINASSIAN, B. A., PATERSON, A. D., LIU, X. Q., WILSON, C., LAHTINEN, U., ANTTONEN, A. K. & LEHESJOKI, A. E. 2007. The novel neuronal ceroid lipofuscinosis gene MFSD8 encodes a putative lysosomal transporter. *Am J Hum Genet,* 81**,** 136-46.

SMITH, K. R., DAHL, H. H. M., CANAFOGLIA, L., ANDERMANN, E., DAMIANO, J., MORBIN, M., BRUNI, A. C., GIACCONE, G., COSSETTE, P., SAFTIG, P., GROTZINGER, J., SCHWAKE, M., ANDERMANN, F., STAROPOLI, J. F., SIMS, K. B., MOLE, S. E., FRANCESCHETTI, S., ALEXANDER, N. A., COOPER, J. D., CHAPMAN, H. A., CARPENTER, S., BERKOVIC, S. F. & BAHLO, M. 2013. Cathepsin F mutations cause Type B Kufs disease, an adult-onset neuronal ceroid lipofuscinosis. *Human Molecular Genetics,* 22**,** 1417-1423.

SPEESE, S. D. & BUDNIK, V. 2007. Wnts: up-and-coming at the synapse. *Trends Neurosci,* 30**,** 268-75.

STEENHUIS, P., HERDER, S., GELIS, S., BRAULKE, T. & STORCH, S. 2010. Lysosomal targeting of the CLN7 membrane glycoprotein and transport via the plasma membrane require a dileucine motif. *Traffic,* 11**,** 987-1000.

STEINFELD, R., REINHARDT, K., SCHREIBER, K., HILLEBRAND, M., KRAETZNER, R., BRUCK, W., SAFTIG, P. & GARTNER, J. 2006. Cathepsin D deficiency is associated with a human neurodegenerative disorder. *Am J Hum Genet,* 78**,** 988-98.

STENGEL, C. 1862. [Account of a singular illness among four siblings in the vicinity of Røraas] - Beretning om et mærkeligt Sygdomstilfælde hos fire Sødskende i Nærheden af Røraas. *Eyr et Medicinsk Tidskrift,* 1**,** 347-352.

STEPHENSON, R. M., NH 2013. Drosophila melanogaster: a fly through its history and current use. 43**,** 70-5.

STOGMANN, E., EL TAWIL, S., WAGENSTALLER, J., GABER, A., EDRIS, S., ABDELHADY, A., ASSEM-HILGER, E., LEUTMEZER, F., BONELLI, S., BAUMGARTNER, C., ZIMPRICH, F., STROM, T. M. & ZIMPRICH, A. 2009. A novel mutation in the MFSD8 gene in late infantile neuronal ceroid lipofuscinosis. *Neurogenetics,* 10**,** 73-7.

STORK, T., ENGELEN, D., KRUDEWIG, A., SILIES, M., BAINTON, R. J. & KLAMBT, C. 2008. Organization and function of the blood-brain barrier in Drosophila. *J Neurosci,* 28**,** 587-97.

SWEENEY, S. T. & DAVIS, G. W. 2002. Unrestricted synaptic growth in spinster-a late endosomal protein implicated in TGF-beta-mediated synaptic growth regulation. *Neuron,* 36**,** 403-16.

TAKATS, S., NAGY, P., VARGA, A., PIRCS, K., KARPATI, M., VARGA, K., KOVACS, A. L., HEGEDUS, K. & JUHASZ, G. 2013. Autophagosomal Syntaxin17-dependent

lysosomal degradation maintains neuronal function in Drosophila. *J Cell Biol,* 201**,** 531-9.

THELEN, M., DAMME, M., SCHWEIZER, M., HAGEL, C., WONG, A. M., COOPER, J. D., BRAULKE, T. & GALLICIOTTI, G. 2012. Disruption of the autophagy-lysosome pathway is involved in neuropathology of the nclf mouse model of neuronal ceroid lipofuscinosis. *PLoS One,* 7**,** e35493.

THYME, S. B., AKHMETOVA, L., MONTAGUE, T. G., VALEN, E. & SCHIER, A. F. 2016. Internal guide RNA interactions interfere with Cas9-mediated cleavage. *Nat Commun,* 7**,** 11750.

TOPCU, M., TAN, H., YALNIZOGLU, D., USUBUTUN, A., SAATCI, I., AYNACI, M., ANLAR, B., TOPALOGLU, H., TURANLI, G., KOSE, G. & AYSUN, S. 2004. Evaluation of 36 patients from Turkey with neuronal ceroid lipofuscinosis: clinical, neurophysiological, neuroradiological and histopathologic studies. *Turk J Pediatr,* 46**,** 1-10.

TSAI, J. J., NORCIA, A. M., ALES, J. M. & WADE, A. R. 2011. Contrast gain control abnormalities in idiopathic generalized epilepsy. *Ann Neurol,* 70**,** 574-82.

TUXWORTH, R. I., CHEN, H., VIVANCOS, V., CARVAJAL, N., HUANG, X. & TEAR, G. 2011a. The Batten disease gene CLN3 is required for the response to oxidative stress. *Hum Mol Genet,* 20**,** 2037-47.

TUXWORTH, R. I., CHEN, H. Y., VIVANCOS, V., CARVAJAL, N., HUANG, X. & TEAR, G. 2011b. The Batten disease gene CLN3 is required for the response to oxidative stress. *Human Molecular Genetics,* 20**,** 2037-2047.

TUXWORTH, R. I., VIVANCOS, V., O'HARE, M. B. & TEAR, G. 2009. Interactions between the juvenile Batten disease gene, CLN3, and the Notch and JNK signalling pathways. *Hum Mol Genet,* 18**,** 667-78.

TYYNELA, J., COOPER, J. D., KHAN, M. N., SHEMILTS, S. J. & HALTIA, M. 2004. Hippocampal pathology in the human neuronal ceroid-lipofuscinoses: distinct patterns of storage deposition, neurodegeneration and glial activation. *Brain Pathol,* 14**,** 349-57.

UMBACH, J. A., ZINSMAIER, K. E., EBERLE, K. K., BUCHNER, E., BENZER, S. & GUNDERSEN, C. B. 1994. Presynaptic dysfunction in Drosophila csp mutants. *Neuron,* 13**,** 899-907.

VENKEN, K. J., SCHULZE, K. L., HAELTERMAN, N. A., PAN, H., HE, Y., EVANS-HOLM, M., CARLSON, J. W., LEVIS, R. W., SPRADLING, A. C., HOSKINS, R. A. & BELLEN, H. J. 2011. MiMIC: a highly versatile transposon insertion resource for engineering Drosophila melanogaster genes. *Nat Methods,* 8**,** 737-43.

VILINSKY, I. & JOHNSON, K. G. 2012. Electroretinograms in Drosophila: a robust and genetically accessible electrophysiological system for the undergraduate laboratory. *J Undergrad Neurosci Educ,* 11**,** A149-57.

WAGER, K., ZDEBIK, A. A., FU, S., COOPER, J. D., HARVEY, R. J. & RUSSELL, C. 2016. Neurodegeneration and Epilepsy in a Zebrafish Model of CLN3 Disease (Batten Disease). *PLoS One,* 11**,** e0157365.

WHEELER, R. B., SHARP, J. D., MITCHELL, W. A., BATE, S. L., WILLIAMS, R. E., LAKE, B. D. & GARDINER, R. M. 1999. A new locus for variant late infantile neuronal ceroid lipofuscinosis-CLN7. *Mol Genet Metab,* 66**,** 337-8.

WISHART, T. M., PARSON, S. H. & GILLINGWATER, T. H. 2006. Synaptic vulnerability in neurodegenerative disease. *J Neuropathol Exp Neurol,* 65**,** 733-9.

WISNIEWSKI, K. E., ZHONG, N. & PHILIPPART, M. 2001. Pheno/genotypic correlations of neuronal ceroid lipofuscinoses. *Neurology,* 57**,** 576-81.

WONG, C. O., CHEN, K., LIN, Y. Q., CHAO, Y., DURAINE, L., LU, Z., YOON, W. H., SULLIVAN, J. M., BROADHEAD, G. T., SUMNER, C. J., LLOYD, T. E., MACLEOD, G. T., BELLEN, H. J. & VENKATACHALAM, K. 2014. A TRPV channel in Drosophila motor neurons regulates presynaptic resting Ca2+ levels, synapse growth, and synaptic transmission. *Neuron,* 84**,** 764-77.

WONG, C. O., LI, R., MONTELL, C. & VENKATACHALAM, K. 2012. Drosophila TRPML is required for TORC1 activation. *Curr Biol,* 22**,** 1616-21.

WU, H. T., XIONG, W. C. & MEI, L. 2010. To build a synapse: signaling pathways in neuromuscular junction assembly. *Development,* 137**,** 1017-1033.

XIANG, Y., YUAN, Q., VOGT, N., LOOGER, L. L., JAN, L. Y. & JAN, Y. N. 2010. Light-avoidance-mediating photoreceptors tile the Drosophila larval body wall. *Nature,* 468**,** 921-6.

YAN, N. 2013. Structural advances for the major facilitator superfamily (MFS) transporters. *Trends Biochem Sci,* 38**,** 151-9.

ZEMAN, W. & DYKEN, P. 1969. Neuronal Ceroid-Lipofuscinosis (Battens Disease) - Relationship to Amaurotic Family Idiocy. *Pediatrics,* 44**,** 570-&.

ZHANG, X., KOOLHAAS, W. H. & SCHNORRER, F. 2014. A versatile two-step CRISPR- and RMCE-based strategy for efficient genome engineering in Drosophila. *G3 (Bethesda),* 4**,** 2409-18.

ZINSMAIER, K. E., EBERLE, K. K., BUCHNER, E., WALTER, N. & BENZER, S. 1994. Paralysis and early death in cysteine string protein mutants of Drosophila. *Science,* 263**,** 977-80.